

COMPARATIVE STUDY AND SELECTION CRITERIA OF LINEAR MOTORS

THÈSE N° 3569 (2006)

PRÉSENTÉE LE 3 JUILLET 2006

À LA FACULTÉ SCIENCES ET TECHNIQUES DE L'INGÉNIEUR

Laboratoire d'actionneur intégrés

PROGRAMME DOCTORAL EN SYSTÈMES DE PRODUCTION ET ROBOTIQUE

ÉCOLE POLYTECHNIQUE FÉDÉRALE DE LAUSANNE

POUR L'OBTENTION DU GRADE DE DOCTEUR ÈS SCIENCES

PAR

Samuel CHEVAILLER

ingénieur électricien diplômée EPF
de nationalité suisse et originaire de L'Abergement

acceptée sur proposition du jury:

Prof. H. Bleuler, président du jury

Prof. M. Jufer, directeur de thèse

Dr M. C. Espanet, rapporteur

Dr N. Macabrey, rapporteur

Prof. N. Wavre, rapporteur



ÉCOLE POLYTECHNIQUE
FÉDÉRALE DE LAUSANNE

Suisse, EPFL

2006

La phrase la plus excitante à entendre en science, celle qui annonce de nouvelles découvertes, n'est pas "Eureka" (j'ai trouvé!), mais plutôt "Tiens, c'est marrant..."

The most exciting phrase to hear in science, the one that heralds new discoveries, is not 'Eureka!' but 'That's funny...'

Asimov, Isaac
(1920-1992)

Remerciements

Un tel travail ne s'effectue pas seul et un grand nombre de personnes ont contribué à l'élaboration de ce mémoire. Leur soutien, aussi bien scientifique que moral a été d'une grande aide et je tiens tout particulièrement à les en remercier.

Mes remerciements vont au Professeur Marcel Jufer qui a bien voulu diriger ma thèse. Je le remercie pour tous les conseils, les discussions et la liberté qu'il m'a laissé tout au long de ces quatre années.

Je tiens à exprimer ma vive reconnaissance à Alain Cassat pour être venu me proposer ce doctorat un après-midi de printemps au fin fond du Val de Travers, mais aussi pour les connaissances qu'il a bien voulu me transmettre tout au long des deux projets CTI.

Je remercie aussi les membres du jury d'avoir accepté de lire ce présent travail et de l'avoir intelligemment critiqué.

Je tiens aussi à remercier chaleureusement :

- Christophe Besson et Christian Koechli qui ont bien voulu lire et commenter mon travail;
- mon collègue de bureau José pour avoir supporté mes deux vélos, mes affaires de course, de natation, mes linges et toutes les odeurs qui vont avec;
- la joyeuse équipe du LAI-LEME et plus particulièrement les " anciens " et les " encore plus anciens " : Matteo, Igor, Mika, Jan, Laurent, Christian, Paolo et M. Crivii pour les agréables moments passés en leur compagnie;
- tous les copains et amis qui sont sur le site de l'EPFL avec lesquels j'ai passé de bons moments soit sportifs, soit beaucoup moins sportifs...

Comment ne pas aussi penser à mes Amis proches qui m'ont soutenu par leurs encouragements (Quand est-ce que tu vas enfin travailler ?, 30 ans toujours étudiant, ...). Je pense évidemment au Gé, au Jul, au Steph, à Laurent et à Stefan... que la vie serait monotone sans eux !

Des remerciements tout particulier vont à ma femme Jelena qui a su me soutenir durant la fin de ma thèse. Je pense aussi à notre fille Lena qui est venue apporter de la joie en fin de thèse.

Je pense aussi à ma famille proche, ma mère et mon frère qui m'ont continuellement soutenu durant ces années d'étude. Ils ont su, dans les moments difficiles, trouver les mots qu'il fallait.

Finalement, je tiens à dédier ma thèse à mon père, Pierre-Alain, qui n'a malheureusement pas eu la chance de voir l'aboutissement de mon travail.

Que chacun trouve ici l'expression de ma profonde gratitude.

Abstract

Initially, linear motors have been particularly dedicated to transportation systems. Nowadays, linear motors are meant to replace a system using a rotating motor and a transmission to realize a linear movement. With linear motors the performances increase considerably since the mechanical limitations are removed. This leads to a better precision, a higher acceleration and a higher speed of the moving part. Therefore, direct drives with linear motors are increasingly used in industrial applications although these solutions need often more investment costs.

Different linear motor structures and technologies exist. They can be either induction or synchronous motors with a transverse or a longitudinal flux. Furthermore, linear motors may have several topologies. They can be either long or short stator and double or single sided. All these variants may be combined giving therefore numerous possibilities to perform a linear movement. Hence, to make the best choice for a given application, a global methodology based on the comparison of optimized motors is presented in the thesis. This design methodology is based on figure of merits which are bound to the specifications of the studied application. This method differs from a conventional one since optimized motors with the same objective function are compared. The optimized motors are obtained by an indirect method based on an optimization algorithm (Sequential Quadratic Programming, SQP). An indirect approach differs from the conventional deterministic one for which at least one parameter must be fixed to obtain a motor pre design, since there are constraints and validity domain which are introduced. The proposed methodology can be applied either to rotating or to linear motor design.

The use of an optimization program to perform motor designs requires analytical motor models. The models developed in this thesis take into account the thermal behavior of the motors in order to achieve more realistic results. Furthermore, the analytical models of synchronous motors are thoroughly studied leading to several interesting conclusions. They are based on well known algorithms developed for rotating motors. The proposed models are very accurate in comparison with the FEM program, except for a transversal flux linear motor for which the obtained results are not worthwhile enough to be optimized. This is caused by the structure of the motor which is close to a reluctant motor and imposes to model the motor by a lumped magnetic scheme. Moreover, a global analysis of the windings due to the particularity of linear motor to have an even or odd number of poles is presented in the thesis.

The methodology proposed in the thesis is successfully used for an innovative application which deals with a multi mobile system for a lift. For this lift, several cabins travel in the same shaft implying linear motors to move autonomously each cabin. First, by comparing the different motor technologies, the best motor type is selected. Afterwards, the motor windings for the selected motors are analyzed and compared in order to find the most adapted one for this application. The motor is finally optimized, leading to a motor design proposal. This motor design takes into account the thermal behavior, the material cost and the electrical characteristic of the linear motor.

Keywords: Linear motors, analytical models, design methodology, comparison methodology, optimization processes, lift system, multi mobile system.

Résumé

Le développement des moteurs linéaires s'est d'abord fait en relation avec des applications liées aux systèmes de transport. Actuellement, les moteurs linéaires sont de plus en plus amenés à remplacer les systèmes composés d'un moteur rotatif et d'une transmission. L'utilisation d'entraînements directs augmente considérablement les performances du système puisque les limitations mécaniques sont supprimées. Les entraînements directs avec moteurs linéaires, bien que plus coûteux, sont caractérisés par une plus grande précision, une plus grande accélération et une plus grande vitesse.

Les moteurs linéaires peuvent être soit synchrone ou asynchrone avec un flux transversal ou longitudinal. Ils sont caractérisés par plusieurs topologies; stator court ou stator long, tubulaire ou non. Ces différentes variantes offrent une multitude de possibilités pour effectuer un mouvement linéaire. Par conséquent, afin de sélectionner le moteur le plus approprié, une méthodologie de dimensionnement basée sur la comparaison de moteurs optimisés est présentée. Elle utilise des facteurs de mérite qui sont associés à l'application. Cette méthode diffère d'une conventionnelle de part le fait que des moteurs optimisés avec la même fonction objective sont comparés. Les optimums sont obtenus par une méthode indirecte qui utilise un algorithme dédié d'optimisation. Le choix de l'approche indirecte diffère d'une approche déterministe où au minimum un paramètre doit être fixé pour réaliser un dimensionnement puisque ce sont des domaines et des contraintes qui sont introduits. Le moteur obtenu peut, par la suite, être amélioré par un processus itératif. La méthodologie introduite dans cette thèse se veut globale et peut sans autre être appliquée au dimensionnement d'un moteur rotatif ou linéaire.

L'utilisation d'un programme d'optimisation exige le développement de modèles analytiques. Les modèles développés dans cette thèse tiennent compte du comportement thermique des moteurs afin d'obtenir des solutions proches de la réalité. Les modèles analytiques des moteurs synchrones sont étudiés plus en détail et apportent certaines conclusions pertinentes. Les modèles analytiques présentés sont très précis, à l'exception du modèle d'un moteur linéaire à flux transversal pour lesquels les résultats obtenus ne sont pas assez précis pour permettre une optimisation. Tous les modèles ont été validés par un programme d'éléments finis. De plus, une analyse globale des bobinages due à la particularité des moteurs linéaires de pouvoir avoir un nombre impair ou pair de pôles est proposée.

La méthodologie présentée est utilisée avec succès à une application innovante qui propose un système multi-mobile pour un ascenseur. Pour cet ascenseur, il est prévu de faire circuler de manière autonome plusieurs cabines dans la même cage d'ascenseur. Dans ce cas, la cabine ne peut pas bénéficier d'un système de câble et contre-poids, ce qui impose le moteur linéaire comme moyen de locomotion. Dans un premier temps, les différentes technologies de moteurs linéaires sont comparés afin de déterminer le moteur le mieux adapté. Ensuite, les bobinages relatifs à ces moteurs sont étudiés et comparés. Une fois le bobinage choisi, l'optimisation peut être réalisée afin de proposer une motorisation pour cette application. Ce dimensionnement de moteur prend en compte les aspects thermiques, de coût de matériel ainsi que des caractéristique électrique du moteur.

Mots clés : Moteurs linéaires, modèles analytiques, méthodologie de dimensionnement et de comparaison, processus d'optimisations, technologie pour ascenseur.

Contents

Abstract	i
Résumé	iii
Contents	v
1 Introduction	1
1.1 Research Context	1
1.2 Objectives and Expected Contributions	2
1.3 Structures of Linear Motors	3
1.3.1 Linear Motor Classification and Topologies	3
1.3.2 Magnetic Ways with PM	5
1.3.3 Toothless Linear Motor	5
1.3.4 Toothed PM Synchronous Motor	7
1.3.5 Transverse Flux Linear Motor	8
1.3.6 Reluctance Linear Motor	9
1.3.7 Induction Linear Motor	9
1.3.8 Motor Structures Conclusions	10
1.4 Writing Conventions	11
2 Theory of Magnetism Applied to Linear Motors	13
2.1 Introduction	13
2.2 Review of the Maxwell's Theory	13
2.2.1 Differential Form	13
2.2.2 Integral Form	14
2.2.3 Complement to the Maxwell Equations	14
2.3 Thrust Calculation	16
2.3.1 Energy Derivation Method	16
2.3.2 Laplace's Law	16
2.3.3 Maxwell's Stress Tensor	17
2.4 Magnetic Materials	17
2.4.1 Magnet Properties and Modelling	17
2.4.2 Iron Properties and Modelling	20
3 Motor Design Methodology	23
3.1 State of the Art, Choice of a Design Method	23
3.1.1 Design Software Using a Procedural Approach	24
3.1.2 Design Software Using Optimization Technics	24

3.1.3	Design Software Based on Expert Systems	25
3.1.4	Design Methodology Choice	25
3.2	Introduction to Motor Design	26
3.3	Specifications and Objectives	29
3.4	Variant Possibilities and First Choice due to the Application	29
3.5	Introduction to Optimization Problems	29
3.5.1	Mathematical Definition of an Optimization Problem and Various Algorithms	30
3.5.2	Optimization Methodology	30
3.6	Comparison Methodology	35
3.6.1	Conditions for a Relevant Motor Comparison	35
3.6.2	List of Main Figures of Merit	35
3.6.3	Motor Comparison	37
3.7	Conclusions	37
4	Linear Motor Models	39
4.1	Introduction	39
4.2	Magnetic Way Models, mmf Calculation	39
4.2.1	Flux Distribution in the Air Produced by a Point Current	40
4.2.2	Flux Density in the Air Produced by a Lineic Current	42
4.2.3	Single Sided Magnetic Way with Mounted PM	42
4.2.4	Single Sided Magnetic Way with Opposite Yoke	47
4.2.5	Double Sided Magnetic Ways	50
4.2.6	Halbach Array	51
4.2.7	Conclusion	54
4.3	Winding Configurations and Models	55
4.3.1	Winding Factors	55
4.3.2	Winding Possibilities	57
4.3.3	Impact on the Cogging Force	63
4.3.4	Impact on the Copper Losses	64
4.3.5	Impact on the Attractive Force Distribution	65
4.3.6	Winding Constraints Leading to Winding Choice	66
4.3.7	Winding Choice - Discussion	66
4.4	Toothless Linear Motor	67
4.4.1	Winding Possibilities	68
4.4.2	Model for the Induced Voltage Calculation	70
4.4.3	Model for Inductances and Mutuals Determination	72
4.4.4	Force Determination	73
4.4.5	Special Cases	75
4.5	Toothed Synchronous Motor With Permanent Magnets	76
4.5.1	Winding Choice and Motor Geometry	76
4.5.2	Propulsion Force Determination	77
4.5.3	Attractive Force at No Load	83
4.5.4	Iron Part Model and Design	84
4.5.5	Induced Voltage Model	87
4.5.6	Self Inductance and Mutual Inductance Determination	87
4.5.7	Special Cases	88
4.6	Transverse Flux Linear Motor	91
4.6.1	Introduction	91

4.6.2	Motor Performances	95
4.6.3	Conclusions and Discussions	97
4.7	Motor Power Supply	97
4.7.1	Motor Electrical Model	98
4.7.2	Differences Between ShS Supply and LS Supply	99
4.7.3	Motor Working Domain	100
4.8	Motor Cost Estimation	100
4.8.1	Material Cost	101
4.8.2	Winding Cost	101
4.9	Motor Mechanical Model	101
4.9.1	Horizontal Motion	101
4.9.2	Vertical Motion	102
4.9.3	Low Energy Displacement Profile	102
4.10	Conclusions	103
5	Thermal Model of a Motor	105
5.1	Introduction	105
5.2	Theory of Thermal Transfers	105
5.2.1	Conduction	105
5.2.2	Radiation	106
5.2.3	Convection	107
5.3	Heating Sources	109
5.3.1	Joule Losses	109
5.3.2	Iron Losses	110
5.3.3	Magnet Losses	111
5.4	Impact of the Motor Duty Cycle on the Motor Design	113
5.5	Experiments	114
5.5.1	Heated Iron Plate	114
5.5.2	Fictive Toothless Motor	117
5.6	Motor Thermal Model	121
5.6.1	Example: Thermal Model of a Short Stator Toothed Motor	123
5.6.2	Influence of the Thermal Model on the Magnetic Model	125
5.7	Conclusions	126
6	Motor Design Analysis and Comparison	127
6.1	Introduction	127
6.2	Magnetic Ways, Air Gap MMF	127
6.2.1	Single Magnetic Ways without Opposite Iron Part	127
6.2.2	Single Magnetic Ways with Opposite Iron Part with Small Air gap	128
6.2.3	Magnetic Ways for Ironless Motors	135
6.2.4	Magnetic Ways Comparison: Conclusions	137
6.3	Toothless and Ironless Motors	138
6.3.1	Ironless Single Sided Motor	139
6.3.2	Toothless Motor	142
6.3.3	Ironless Double Sided Motor	145
6.3.4	Toothless Motor Comparison - Conclusion	148
6.4	Toothed Motors	150
6.4.1	Winding Choice	150

6.4.2	Maximum Propulsion Force	151
6.4.3	Motor Design, Parameter Sensitivity.	154
6.5	Motor Comparison - Conclusions	155
7	Application - Linear Motor for a Lift	159
7.1	Introduction	159
7.2	Specifications and Objectives	160
7.3	Design Methodology	161
7.4	Linear Motor Type Possibilities for an MMS	162
7.5	Linear Motor Preselection	163
7.5.1	First Motor Choice Imposed by the MMS	163
7.5.2	Second Choice Imposed by Additional Choice Criteria	167
7.6	Considered Motor Topologies	168
7.6.1	Double or Single Sided	168
7.6.2	Short Stator Topologies	169
7.6.3	Long Stator Topologies	170
7.6.4	Motor Topology Choice	171
7.7	Motor Heating and Cooling System	171
7.8	Supply Part	171
7.9	Preselected Motor Design	174
7.9.1	Assumptions and Constraints Relative to the Application	175
7.9.2	First Optimization - First Selection	176
7.9.3	Second Optimization - Winding Selection	177
7.10	Final Motor Choice	179
7.11	Final Motor Design	183
7.11.1	Final Motor Design - FEM Comparison	186
7.11.2	Mechanical Integration	187
7.12	Conclusions	189
8	Conclusions	191
	Appendices	194
A	Fourier Transformation	195
B	BH Curve Model	197
C	Winding Factors	199
D	Modulation Functions	205
E	TFM Geometry Parameters	207
F	List of Symbols	215
	References	219
	Curriculum Vitae	225

Chapter 1

Introduction

1.1 Research Context

This thesis is result of the collaboration between the laboratory of integrated actuators (LAI) and the company Schindler SA, active in the domain of elevators.

Nowadays, the development of elevator systems is mainly based on access control, information and entertainment (infotainment) or remote services for maintenance personnel. All these services however are not connected directly to the fundamental functionality of the elevator; the vertical transportation of passengers in a building. This aspect is described in [1, 2, 3].

In traction drive, the next step in elevator technology is a multiple use of the shaft room with the following goals: increasing the transportation capacity of the elevator installation and at the same time reducing the cross section required by the elevator system in the building. Another relevant goal regarding the passengers is the reduction of waiting- and travelling-time. The solution to achieve all these goals is a Multi Mobile System (MMS). This is a system with several cars in the same shaft as presented on Fig. 1.1. Depending on the traffic demand, several shafts can be dedicated to the same up or down directions to optimize the traffic exploitation. Furthermore, a horizontal transfer of the cars is needed to allow them to change shafts. Extending this concept, the same system can be used to transport passengers in horizontal direction inside a building. Such a system can be called a horizontal-vertical-transportation-system (HVT). The demands for such an HVT-system are much higher than for a system providing only vertical transportation due to the horizontal movement of passengers. The horizontal transportation of people is not a subject of this project.

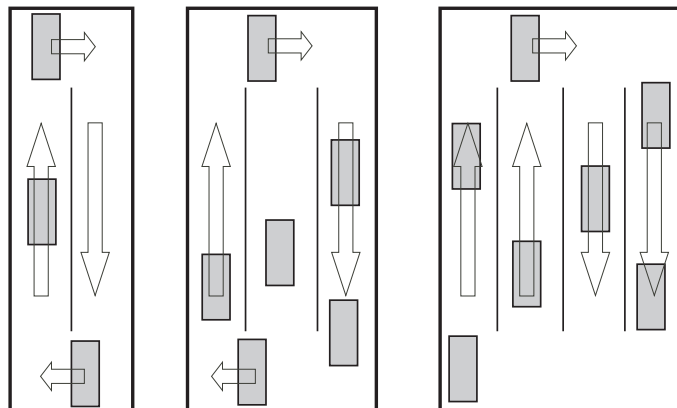


Figure 1.1: MMS principle, configurations with 2, 3 and 4 shafts [4].

In the future MMS, the individual cars can move autonomously. This requires a ropeless elevator system with self-propelled cars.

For the drive system a linear motor is the most promising concept. It is however crucial to reach the highest force-density since the cars are moved without counterweight. The selection of the appropriate motor concept and the optimal design of the motor are therefore crucial. The expected advantages of a linear motor are the following:

- no space needed in top and bottom of the shaft neither for the drive and other mechanical systems nor as safety space for the maintenance personnel. This is how the main idea of the machine-roomless elevator can be achieved gaining more space savings in the building;
- reduced cross-section of the shaft due to a flat construction of the linear motor;
- the different required brake-systems can be an integral part of the linear drive making the system simpler and cheaper;
- very high positioning accuracy of the car on the landings.

Although induction and synchronous linear motor technologies are known, there is no published scientific work analyzing completely the advantages and disadvantages in a comparative approach. Furthermore, due to volume and cost constraints the motor configurations must be considered: longitudinal flux linear motors and transverse flux linear motors, short stator and long stator. These options must be studied in a comparative perspective requesting method developments and design software tools. Furthermore, the design methodology should satisfy certain mathematical conditions in order to be useful in non-deterministic optimization methods. Such approach developments are new. The key scientific aims of this thesis are defined as follows:

- to make the synthesis of linear motor variants;
- to analyze and to determine the characteristics of the variants, versus long track applications;
- to define the optimization criteria and design process;
- to determine the best linear motor solution and its spatial integration in the lift available space.

1.2 Objectives and Expected Contributions

When designing an electromechanical system, the choice of a motor type is often dominating for the viability of the project. Therefore, in industrial applications implying a linear movement of the load, the choice of a linear motor type permits to optimize the characteristics of the system, like e.g., minimal costs, maximum efficiency, etc.

There are three main types of linear motors: the induction linear motor, the synchronous linear motor with permanent magnets (PM) and reluctance motor. All these motors can be designed with a longitudinal or a transverse flux linkage. Although each type of linear motor was the subject of scientific and industrial developments, there is no methodology allowing an objective comparison of these different motor types and their alternatives. The definition and the choice of figures of merit can allow the classification of each motor alternative and thus to realize the best technical choices. This systemic approach is based on the application of linear motors for lift, the subject of a CTI (Innovation Promotion Agency) project in the LAI [5, 6].

The principal objective of this thesis is to develop such a comparison method as well as a methodology to find the best motor for a given application. To set up this methodology, it is necessary to build

analytical models of linear motors. Thereafter, the concept of specific figures of merit is introduced, which are the principal tools for the motor choice. Figures of merit can be either electric factors, mechanical factors or even manufacturing cost factors. Furthermore, a comparative analysis can be applied to compare different motor types for a given application.

The innovating scientific aspects brought by this thesis are at the level of the methodology of comparison. To our knowledge, there is no reliable and structured method developed in this direction. Another interesting aspect is the development of analytical motor models. Indeed, some analytical problems will be investigated and thereafter they will be validated by finite elements simulations. This thesis will also allow to set up a parametric study based on the figures of merit. Such a methodology of comparison and optimization will also permit to find the physical limits of the motors studied in this thesis (surface force, etc.)

1.3 Structures of Linear Motors

This chapter gives a brief classification of linear motors in order to present an overview of the various possibilities to perform a linear movement [7, 8]. Several linear motors and their topologies which are of the interest of this thesis are briefly introduced.

1.3.1 Linear Motor Classification and Topologies

It is not straightforward to give a general classification since each author has its own approach and a divergence regarding the excitation, the supply part or other considerations can appear. In this section, only the motors studied in this thesis are introduced. Various linear motor topologies are presented on Fig. 1.2. A choice was made to focus only on direct drive motors and a system consisting of a rotative motor and a ball screw to perform a linear movement is not studied. A linear motor classification is presented on Fig. 1.3.

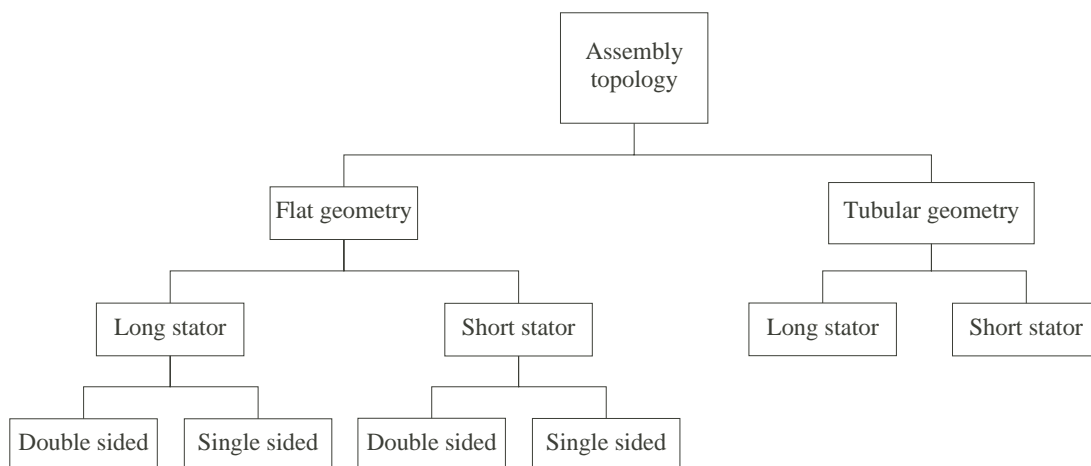


Figure 1.2: Linear motor topologies.

There are mainly four different approaches to produce a linear movement by an electrical way. The first solution is to use the electrostatic properties to move a glass way. A maximum force density of about 16 N/m^2 can be obtained [9]. The second solution on Fig.1.3, which is of the interest for this thesis is to produce a movement by an electromagnetic way. The third and fourth solutions based on mechanical friction use the piezoelectric or magnetostrictive properties to interact with a mover. The two variants

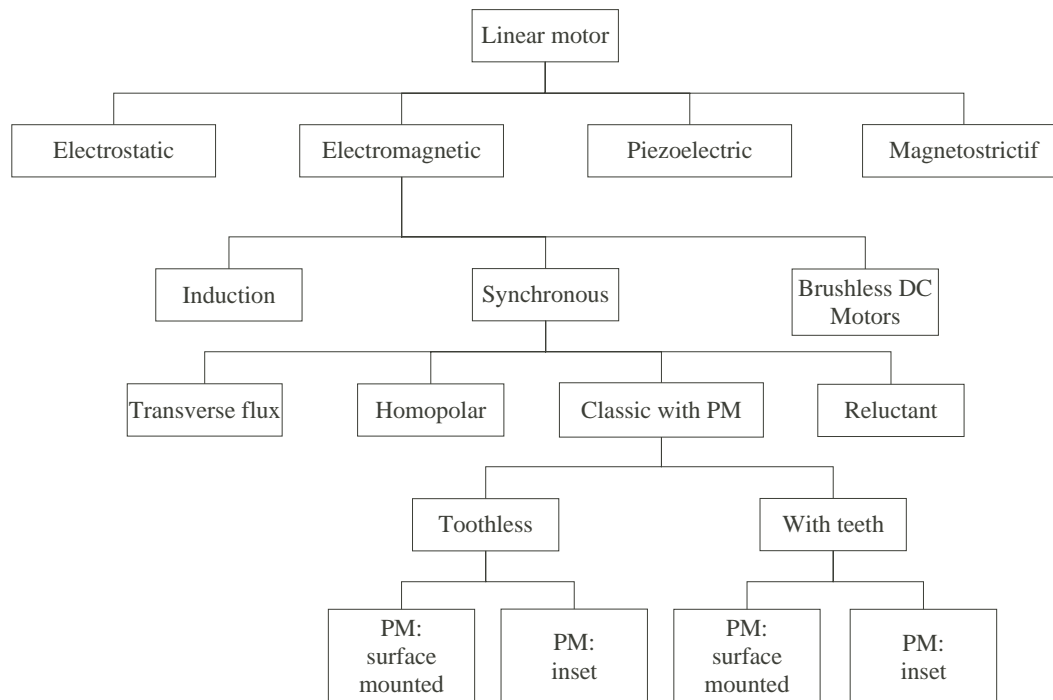


Figure 1.3: Linear motor classification.

differ by their respective material. For the first one, the force is produced under an electric field source (piezoelectric) and for the other one under a magnetic field source. The maximum force developed by these two motors can be very high [10] and depends on the topology. However, the stroke of these motors is very small.

Electromagnetic motors can be divided in three main groups; induction motors, synchronous motors and DC motors. The main difference between them is the excitation mode, which is generally produced by magnets except for the induction motor where it is self-induced. Indeed, for an induction motor the excitation is self induced by the supply part in a conducting plate forming the secondary. The winding arrangement produces a travelling field in the air gap, which induces currents in the conductive plane of the secondary part of the machine. The interaction between the primary field and the secondary currents produces the force. If the moving part has the same speed as the travelling field, the force is zero and the motor reaches its synchronous speed. For the two other motor variants the excitation is generated by an independent source such as magnets or brushless DC coils. The difference between a DC motor and a synchronous motor is in the supply part. The former generates a trapezoidal electro magnetic force (emf) waveform and is supplied with a rectangular phase current. It is generally controlled like a motor with brushes, since a position sensor produces commutating DC-currents in the stator winding, based on the position of the magnetic poles. On the other hand, the synchronous motor produces a sinusoidal emf waveform and is supplied with a sinewave phase current.

Furthermore, all linear motors can be build in various topologies. Figure 1.2 introduces possible topologies. A main topology distinction is due to their structure geometry which can be either tubular or flat. These two geometries can be build in a long stator (LS) or in a short stator (ShS) topology. For flat geometry, motors can be either single sided or assembled in opposite to constitute a double sided motor.

Definitions of LS and ShS are :

- Long Stator: the length of the supply part is longer than the excitation way, in most cases the excitation part is mobile.
- Short Stator: the supply part is shorter (or equal) than the excitation way. The supply part is, in most cases, mobile.

To conclude this section, Table 1.1 summarizes the force ranges for the listed motors.

Table 1.1: Nominal force range for linear motors with a continuous duty cycle and without additional cooling.

Induction linear motor	1-2 N/cm ²
Slotted PM synchronous linear motor	up to 6 N/cm ²
Slotless PM synchronous linear motor	up to 3 N/cm ²
Reluctance linear motor	1.5 N/cm ²
Transverse flux linear motor	3 N/cm ²
Piezoelectric linear motor	depending on the topology
Magnetostrictif linear motor	depending on the topology
Electrostatic linear motor	16 N/m ²

1.3.2 Magnetic Ways with PM

Magnetic ways produce the excitation flux in the air gap. Magnets, which are the magnetic source, can be either mounted or inserted in a magnetic yoke or combined to form an Halbach array [11]. These three families of magnetic ways are presented on Fig. 1.4. The first group consists of magnets mounted on a yoke (Fig. 1.4 a, b, c). As it is presented in Section 4.2, where the model of the magnetic way is introduced, magnets are substituted by a current density if there is no opposite yoke or by a sum of point currents, in presence of an opposite yoke.

Furthermore, double sided magnetic ways (Fig. 1.4 c, e, g) are used with a supply part without iron. These motors types are sometimes called ironless motors.

Halbach array have a particularity due to the magnet placing, since they have a magnetic flux enhanced on one side (strong side) and cancelled on the other side (weak side).

All magnetic ways are presented in a short stator configuration i.e. the magnetic ways are fixed. However these magnetic ways can also be mobile and therefore used in a long stator configuration.

1.3.3 Toothless Linear Motor

Toothless motors have the particularity to have a winding without teeth and therefore no cogging and no reluctance forces. The supplied part is composed either by a distributed winding, a concentrated winding or a Gramme's winding [12]. Depending on the motor design specifications, the distributed and concentrated windings can optionally be stuck to a yoke. For instance, if a motor with a high acceleration and low force is required, the tendency will be to lighten as much as possible the moving weight in order to reach the high acceleration. Two topologies are presented on Fig. 1.5 and Fig. 1.6. The first one is a long stator tubular motor with two poles and the second one is a short stator double sided motor. The latter has the particularity to have high acceleration and a higher force density compared to other toothless motors. However, this motor needs a high number of magnets which increases its overall cost.

Regarding winding, only polyphase windings with adjacent coils will be studied in this thesis; in particular three phase windings. The maximum coil length can not be higher than 360 edeg, as it is discussed in detail in Section 4.4.1. Nevertheless, the presented method to model these motors can be extended to other winding possibilities.

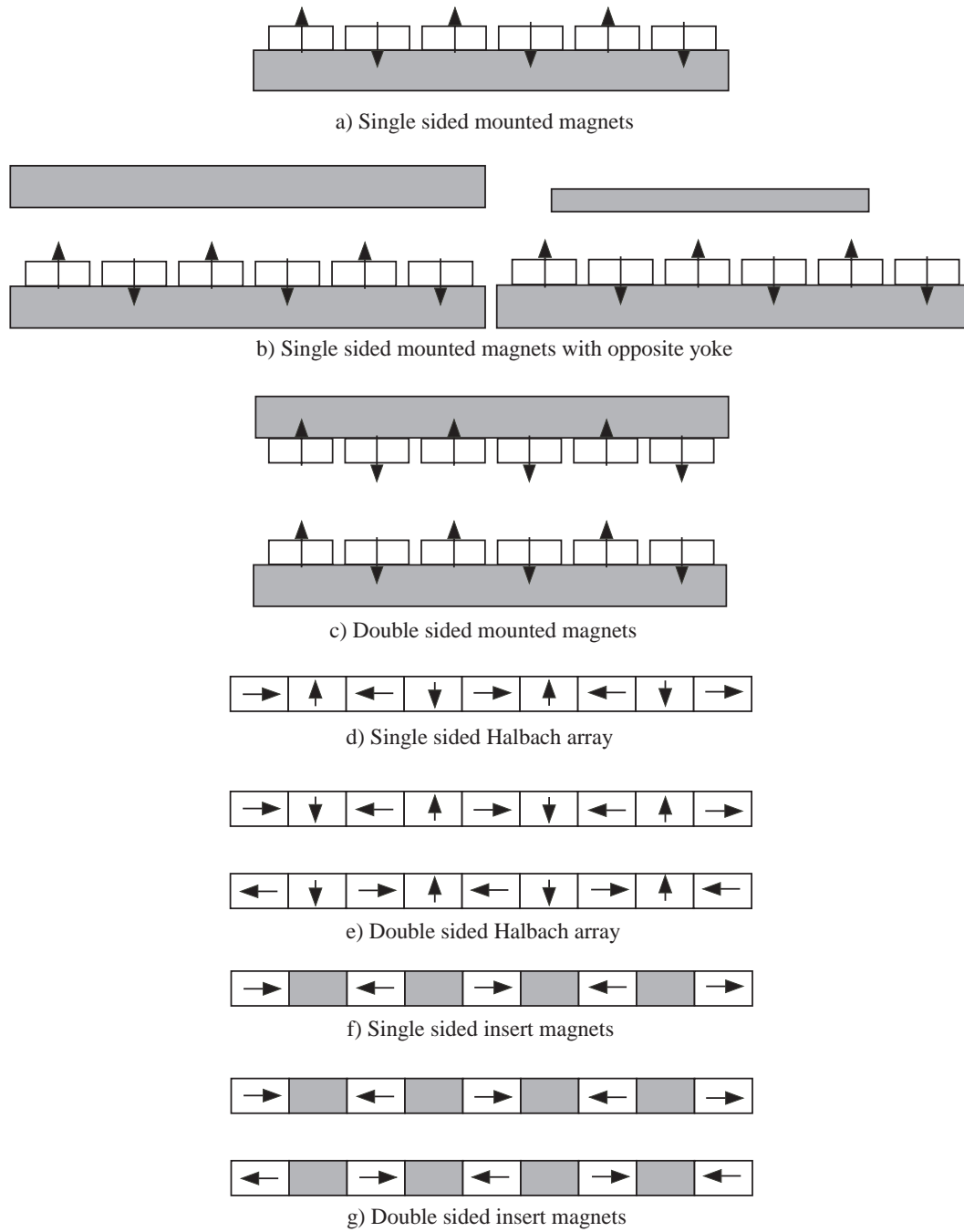


Figure 1.4: Different magnetic ways.

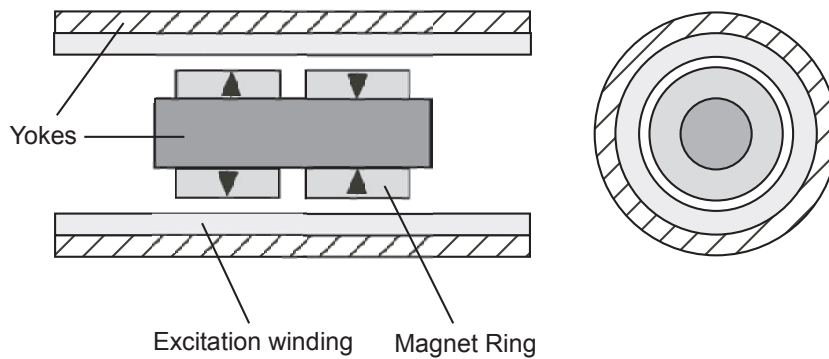


Figure 1.5: Long stator tubular linear motor.

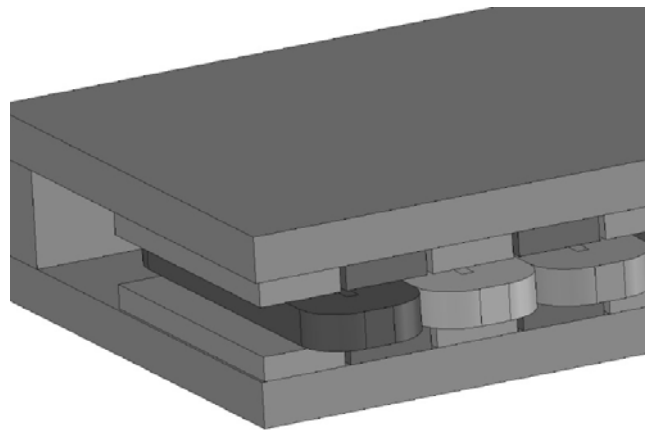


Figure 1.6: Short stator double sided linear motor.

This motor type is characterized, when it is supplied, by a low attractive force and low iron losses. On the other hand they have a lower efficiency than motors with teeth because of their high magnetic air gap which is the sum of the coil height and magnet(s) height. Generally due to their lightness, these motors are often used for applications requiring a high dynamic.

In this thesis, a difference will be made between a mover made only of coils and a mover which consists of coils stuck to a yoke. The former are called *the ironless motor* and the later *the toothless motor*.

1.3.4 Toothed PM Synchronous Motor

This type of motor is common in the industry applications since the rare earth magnets have an attractive price and interesting magnetic properties [13], as explained in Section 2.4.1. Compared to the toothless motor, the supply part is in this case composed of iron laminations and winding in slots. The supply part is normally assembled with magnetic ways like shown on Fig. 1.4 b, d, f.

Slotted synchronous motor is very powerful and compact. Unfortunately, due to magnets, a high attractive force between the supply part and the magnetic ways appears. For the same propulsion force, the ratio between the attractive force and the propulsion force is about 3 times with a water cooling and about 5 times without additional cooling. Due to the high attractive force, a robust mechanical guidance system is required to guide the moving part and to keep the air gap precise. To minimize the problem, a double sided motor can be used. In this case, each side of the double sided motor produces two opposite

attractive forces which cancel each other. This solution reduces the attractive force between the two motor parts but does not eliminate the problem since only when both upper and lower air gap heights are equal, the attractive force is cancelled. A small difference between these two heights unbalance the attractive forces leading to an unstable system. Furthermore, due to the teeth, this motor can have a high cogging force.

Several windings, concentrated or distributed, will be introduced in section 4.5.1.

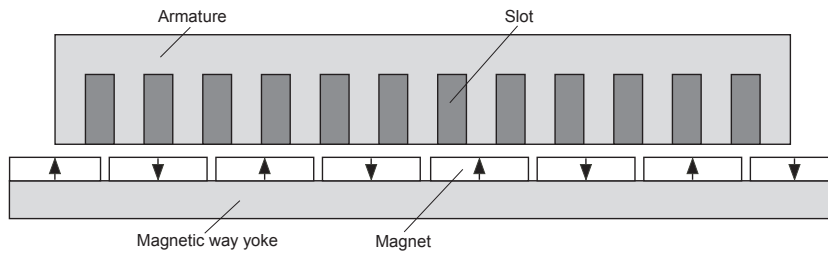


Figure 1.7: Toothed single sided synchronous motor.

1.3.5 Transverse Flux Linear Motor

Most linear motors can be classified as longitudinal flux machines because they have their flux flowing in a plane parallel to the direction of motion. If the end windings are not considered, longitudinal flux machines (Fig. 1.8) have essentially a 2D main flux pattern.

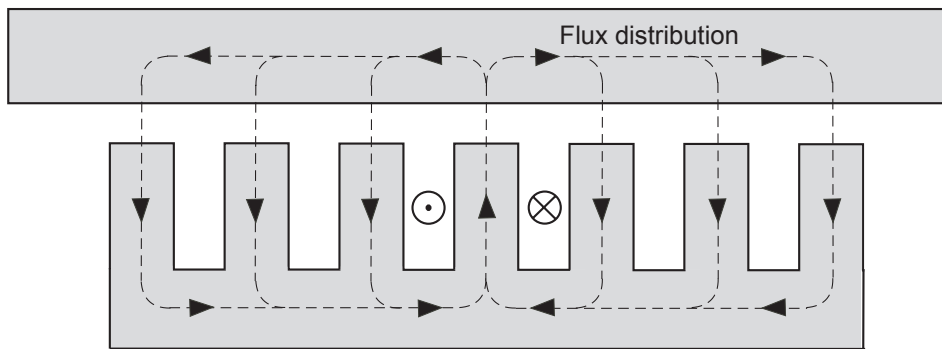


Figure 1.8: Longitudinal flux linear motor.

On the other hand, transverse flux motor (TFM), have a flux flow in a plane perpendicular to the motion direction and in this case a 3D model is required to design the motor (Fig. 1.9). This technology has been introduced more than 100 years ago¹. Recently the emergence of high remanence magnets has contributed to its development [14, 15].

Due to their structure, TFM are often phase independent and several motor modules must be added to form a polyphase motor. In addition to the propulsion force, TFM often have a high cogging and reluctance force. These two additional force components impose, when a constant force is needed, to supply the motor with a specific current form.

¹First patent in 1895 by W.M. Morday.

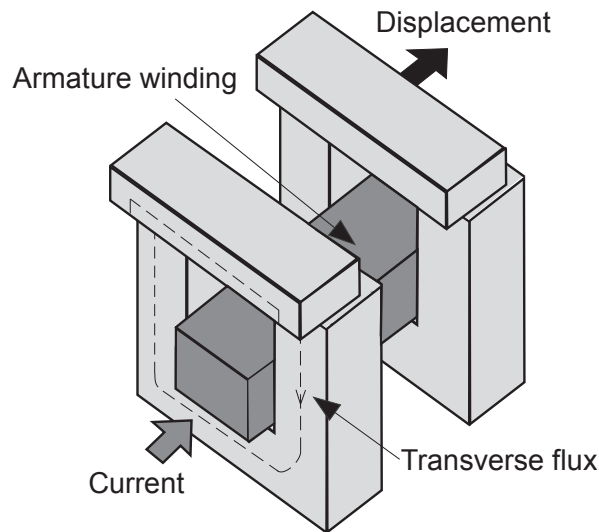


Figure 1.9: Transverse flux linear motor.

1.3.6 Reluctance Linear Motor

Compared to the other motors, reluctance motor generates the propulsion force by means of the permeance variation due to salient poles in both sides of the way and the supply part [13]. Therefore, without magnetic saturation, the force is proportional to the current square and a high variation of the permeance is needed to achieve a high force. Figure 1.10 represents a single sided reluctance linear motor. All the magnetic parts are made of lamination stack to reduce the iron losses as much as possible.

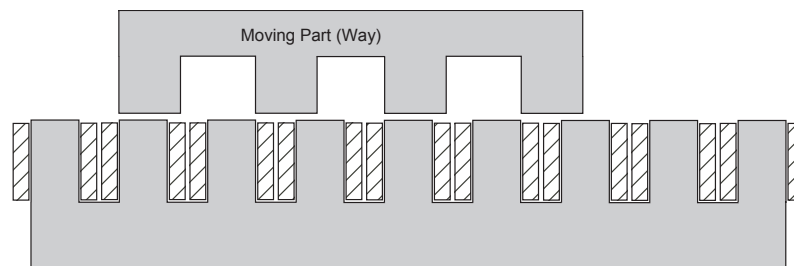


Figure 1.10: Single sided reluctance motor.

The principal difficulty to design these motors is to estimate the flux path, i.e. the permeance in the air gap between two opposite structures, and therefore to have a good model of the saturation. One of the main disadvantages resides in the fact that this motor type is relatively noisy during its operation and has a low efficiency for a large air gap.

1.3.7 Induction Linear Motor

This motor is mechanically very simple and consequently less expensive than the previous presented motors. Its great advantage is its robustness coming from the simplicity of its construction. The supply part is similar to that of a toothed synchronous motor and the difference between them is in the reaction part. For induction motors, the way is composed of an aluminium or copper layer covering eventually a ferromagnetic part. This electrical conducting layer or squirrel cage allows the circulation of induced

currents produced by the stator winding MMF. The interaction of these induced currents with the winding create a propulsion force. If the translator moves at the same speed of the travelling magnetic field in the air gap no force is produced because no current is induced in the electrical conducting layer.

Figure 1.11 and Fig. 1.12 show a single and a double sided induction motor, respectively [16].

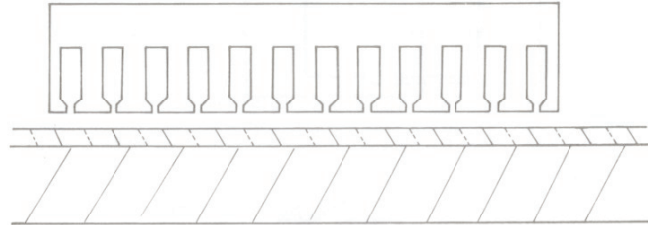


Figure 1.11: Single sided induction motor.

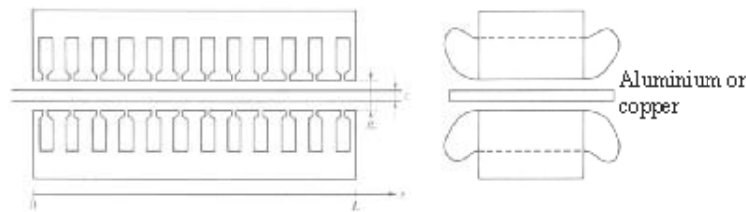


Figure 1.12: Double sided induction motor.

To achieve good performances in term of efficiency, induction motors must have a rather small air gap (about 1 mm). Moreover, compared to a linear motor with permanent magnets, this motor needs more energy to produce the same force.

1.3.8 Motor Structures Conclusions

To complete this chapter, Table 1.2 summarizes the advantages and disadvantages of presented motors. This first comparison between the motors shows a tendency and is not the result of a systematic analysis.

Table 1.2: Comparative table.

	Toothless Motor	Toothed Motor	TF Motor	Reluctance Motor	Induction Motor
Attractive Force ($I=0$)	small	high	high	no	no
Attractive Force ($I \neq 0$)	small	high	high	high	negative
Cogging force	no	yes	yes	no	no
Efficiency	good	very good	very good	less good	less good
Energy recovery	easy	easy	easy	less good	less good
Air gap sensitivity	low	high	high	very high	very high ²

²not the case in a double sided configuration

1.4 Writing Conventions

In order to be as rigorous as possible, The CEI writing convention is adapted in the thesis. The main typing conventions are:

- | | | |
|--------------------------|--------------------------------|--|
| • vectors | bold type | (Magnetic field in 2D : \mathbf{H}) |
| • complex number | underline | (complex number : $\underline{c}=a+jb$) |
| • RMS value | capital letter | (RMS current : I) |
| • instantaneous value | small letter | (instantaneous current : i) |
| • peak value | capital letter with circumflex | (peak current : \hat{I}) |
| • dimension nomenclature | small letter | (width : w) |
| • fields | capital letter | (Magnetic field : H) |

The mathematical operators are represented as follows:

- laplacian ∇^2
- curl $\nabla \times$
- divergence $\nabla \cdot$
- gradient ∇

Furthermore, to avoid possible errors or confusion, the three dimensions for linear motors are defined as follows (Fig. F.1, in Appendix):

- the length is defined in the direction of motion. This dimension takes part to the active surface;
- the width is the second dimension on the active surface;
- the height is the third dimension and does not take part to the active surface.

Furthermore, a terminology inherent to linear motor must be introduced. To increase the propulsion force several same linear motors are often mounted in series, using the same magnetic way. Therefore, a terminology was adopted to differentiate the complete motor (number of motor in series) from the smallest possible motor segment for a given winding. Indeed, for linear motors, a motor segment (or module) is designed which can be multiplied to build a complete motor in order to reach the specified propulsion force. In this way, the *motor segment* is defined being the smallest possible motor for a given winding and the *complete motor* represents the final motor design. For all analytical models only designs of motor segments are presented. This distinction between motor segment and complete motor differs compared to rotative motors. It permits to have a winding configuration distributed along $k \cdot 180$ electrical degrees (edeg) with k integer, whereas a rotative motor must have an even number of poles. For this reason, linear motors can have an odd number of poles N_p permitting more winding possibilities

The list of symbols and abbreviations can be found in appendix.

Chapter 2

Theory of Magnetism Applied to Linear Motors

2.1 Introduction

This chapter presents a theoretical approach to electromagnetism, which will be further applied in motor design. A brief review of Maxwell's laws together with their simplifications due to the specific domain of motor design are presented in Sections 2.2.1 and 2.2.3. Furthermore, Section 2.3 introduces several ways to calculate the forces generated by an electrical motor and Section 2.4 discusses properties of magnetic materials used in electrical motors.

The goal of this chapter is just to summarize the main formulas important for a motor design and not to introduce the magnetism theory in details. For more complete information, [17, 18] can be consulted.

2.2 Review of the Maxwell's Theory

The important contribution in the field of magnetism done by J.C. Maxwell was to regroup a set of equations which allows to join together the electrostatic and electromagnetic theories. These equations, reduced thereafter to four by means of the vector calculation, are presented both in differential and integral form.

2.2.1 Differential Form

The general differential form of the Maxwell's equations is:

$$\nabla \times \mathbf{H} = \mathbf{J} + \frac{\partial \mathbf{D}}{\partial t} + \rho_c \cdot \mathbf{v}, \quad (2.1)$$

$$\nabla \cdot \mathbf{D} = \rho_c, \quad (2.2)$$

$$\nabla \times \mathbf{E} = -\frac{\partial \mathbf{B}}{\partial t}, \quad (2.3)$$

$$\nabla \cdot \mathbf{B} = 0. \quad (2.4)$$

\mathbf{E} is the electric field, \mathbf{D} is the electric displacement, \mathbf{H} is the magnetic field, \mathbf{B} is the magnetic flux density, \mathbf{J} is a current density, \mathbf{v} the velocity of a fluid or plasma and ρ_c is the volume charge density.

In motor design only quasi-static electromagnetic problems are studied and the time-derivate of current displacement can be neglected compared to the current density. Therefore, (2.1) can be simplified to:

$$\nabla \times \mathbf{H} = \mathbf{J}, \quad (2.5)$$

implying:

$$\nabla \cdot \mathbf{J} = 0. \quad (2.6)$$

Furthermore, the study of electrical field in dielectric material is not of the main interest in a motor design, except when the insulation material is defined. Hence, (2.2) is not often used in motor design.

In addition to this set of equations, the properties of materials have to be introduced by set of constitutive equations. The first equation puts in relation the flux induction \mathbf{B} and the magnetic field \mathbf{H} in a material:

$$\mathbf{B} = \mu_0 \cdot (\mathbf{H} + \mathbf{M}). \quad (2.7)$$

Here, μ_0 is a proportional constant called the permeability of the air, equal to $4\pi \cdot 10^{-7}$ and \mathbf{M} is the magnetization, which can be interpreted as an internal source of flux density in a material.

The second constitutive equation puts in relation the current density and the electric field in a conducting medium of a conductivity σ :

$$\mathbf{J} = \sigma \mathbf{E}. \quad (2.8)$$

This equation is known as the generalized Ohm's law and it permits to define the electrical resistance.

Furthermore, from (2.4) by applying one property of vector calculation (the divergence of the rotational of a vector is null) a magnetic potential vector \mathbf{A} is defined as:

$$\mathbf{B} = \nabla \times \mathbf{A}. \quad (2.9)$$

2.2.2 Integral Form

Maxwell's equations (2.3), (2.4) and (2.5) can be formulated in the integral form as follows:

$$\oint_c \mathbf{E} \cdot d\mathbf{l} = - \int_s \frac{\partial \mathbf{B}}{\partial t} \cdot d\mathbf{S}, \quad (2.10)$$

$$\oint_s \mathbf{B} \cdot d\mathbf{S} = 0,$$

$$\oint_c \mathbf{H} \cdot d\mathbf{l} = \int_s \mathbf{J} \cdot d\mathbf{S}. \quad (2.11)$$

Equation (2.11), is called circuital law. It is deduced from (2.5) using Stoke's theorem [19]. The path c for the line integral is the contour bounding the surface s . To deduce (2.10), the Stoke's theorem is also applied to (2.3). Equation (2.11), known as the law of conservation of magnetic flux, is obtained from (2.4) using the divergence theorem.

2.2.3 Complement to the Maxwell Equations

The magnetic flux Φ through a surface S is obtained using (2.11). Substituting (2.9) into (2.11) and applying Stokes's theorem the magnetic flux through a surface S is given by:

$$\Phi = \int_s \mathbf{B} \cdot d\mathbf{S} = \oint_c \mathbf{A} \cdot d\mathbf{l}. \quad (2.12)$$

Moreover, the voltage U which is the difference between two electrical potentials is defined as:

$$U_{12} = V_2 - V_1 = \int_1^2 \mathbf{E} \cdot d\mathbf{l}. \quad (2.13)$$

Integrating the generalized Ohm's equation (2.8) along a particular streamline between two points 1 and 2 will define the electrical resistance R , as shown below:

$$U_{12} = \int_1^2 \mathbf{E} \cdot d\mathbf{l} = \int_1^2 \frac{\mathbf{J}}{\sigma} \cdot d\mathbf{l} = I \int_1^2 \frac{1}{\sigma S} \cdot d\mathbf{l} = R_{12} I. \quad (2.14)$$

$$(2.15)$$

Another simplification can be made on the right term of (2.10). This equation is very difficult to integrate on account of the partial derivate term of the time. This equation solved in [20] is equal to:

$$emf = \oint_c \mathbf{E} \cdot d\mathbf{l} = -\frac{d}{dt} \int_S \mathbf{B} \cdot d\mathbf{S} - \oint_c (\mathbf{v} \times \mathbf{B}) \cdot d\mathbf{l}. \quad (2.16)$$

In most motor designs, the circuit can often be studied as stationary and therefore the second term on the right part in (2.16) is zero. Therefore, the electromagnetic force emf , which is the induced voltage, is given by:

$$emf = \oint_c \mathbf{E} \cdot d\mathbf{l} = -\frac{d}{dt} \int_S \mathbf{B} \cdot d\mathbf{S} = -\frac{d\Psi}{dt}. \quad (2.17)$$

Ψ is the total magnetic flux.

The last interesting simplification of Maxwell's laws for the motor design is applied to (2.11). This simplification is introduced by an example. Figure 2.1 shows a coil with 4 turns wound around a toroidal ferromagnetic core. The coil wires have a current density J .

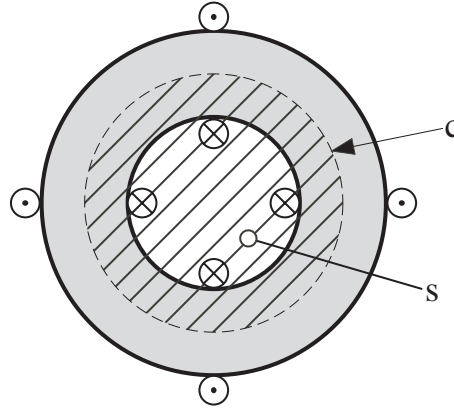


Figure 2.1: Toroidal coil with 4 turns wound around a ferromagnetic core.

A path c is defined as a circle in the middle of the ring. This path defines the surface s (hatch part). The integral on the surface s of the current density J is given by:

$$\int_S \mathbf{J} \cdot d\mathbf{S} = \int_S \frac{\mathbf{I}}{S_{cu}} \cdot d\mathbf{S} = \frac{4 \cdot I \cdot S_{cu}}{S_{cu}} = 4I \quad (2.18)$$

S_{cu} is the surface of one conductor carrying a current I . Applying (2.18) to a coil with N turns, a general form of the Ampere's circuital law (2.11) is given by:

$$\oint_c \mathbf{H} \cdot d\mathbf{l} = NI. \quad (2.19)$$

This equation, combined with (2.12), is the basis of the lumped equivalent magnetic circuit [13].

2.3 Thrust Calculation

In electromagnetic problems, the total force used to produce a movement is in most cases composed of three components: a cogging force (interaction PM/iron), a reluctance force (interaction iron + coil/iron) and an electromagnetic force (interaction coil + iron/PM).

The cogging force is a parasite force which can generate vibration and noise. This force is produced by interaction of the rotor (magnetic way) magnetic flux and variation of the stator magnetic reluctance, i.e. the stator excitation is not involved in generating cogging force. In addition to the tooth ripple component of cogging force, which exists in equivalent rotary PM machines, it exists an end component owing to the finite length of the armature. The reluctance force is produced by interaction of stator magnetomotive forces (mmf) and a reluctance variation produced by a toothed reactive part. This force can be either a parasite force or the main part of the propulsion force (reluctance motor). The electromagnetic force is due to the interaction of the fluxes created either by rotor excitation magnets and by coils or by rotor excitation coils and stator coils. This force is the main force in synchronous motors.

In the following sections, three approaches to calculate the forces are introduced. The goal is to give only the key points of the methods and more details about forces calculation can be found in [18].

2.3.1 Energy Derivation Method

This method is based on a virtual work [21]. The force distribution in an electromechanical problem is solved by using the energy or the co-energy of the whole system. The principle is to assume the electric sources (current) constant regarding an infinitesimal displacement of the electromechanical structure. Therefore, the force is equal to:

$$\mathbf{F} = \nabla W_{co}(x, y, z), \quad (2.20)$$

$$\mathbf{F} = -\nabla W_m(x, y, z) \quad (2.21)$$

if the magnetic co-energy W_{co} or the magnetic energy W_m are known, respectively.

To calculate the force by using this method the magnetic energy in each part of the motor must be calculated. The magnetic energy stored in magnetic fields is [22]:

$$W_m = \int_V \int_0^B H(B) \cdot dB \cdot dV \quad (2.22)$$

while the co-energy is:

$$W_{co} = \int_V \int_0^H B(H) \cdot dH \cdot dV. \quad (2.23)$$

The use of a lumped magnetic scheme permit to calculate forces by using the energy derivation method. By simplifying as much as possible a lumped magnetic scheme, the force can be calculated following [22]:

$$\mathbf{F} = \frac{1}{2} \nabla \Lambda_e(x, y, z) \cdot \theta_e^2, \quad (2.24)$$

Λ_e is the equivalent permeance and θ_e is the equivalent magnetic source.

2.3.2 Laplace's Law

The electromagnetic force applied on a particle of charge q and velocity \mathbf{v} in the presence of both magnetic and electric fields is given by the Lorentz force law:

$$\mathbf{F}(x, y) = q(\mathbf{E}(x, y) + \mathbf{v} \wedge \mathbf{B}(x, y)). \quad (2.25)$$

In electrical machines, the right part of the equation is predominant and defines the force acting on a conductor with current in a magnetic field by the relation:

$$\mathbf{F} = \int (I d\mathbf{l} \wedge \mathbf{B}), \quad (2.26)$$

l is the length of the conductor. This force is known as Laplace's force.

The Laplace's force is very useful to calculate the force acting on a coil in a flux density as it is the case for toothless motors. For toothed motor, the stator mmf must be replaced by a current distribution along the air gap to allow the use of (2.26).

2.3.3 Maxwell's Stress Tensor

Maxwell's stress tensor T_m gives a force per unit area produced by the magnetic field on a surface S . Therefore, the force F acting on a surface S is given by:

$$\mathbf{F} = \oint_S \mathbf{T}_m dS \quad (2.27)$$

The stress tensor T_m is composed of nine functions of space and time [20, 22]. By applying the stress tensor to an electromagnetic problem and performing some simplifications, the normal and tangential components (T_n, T_t) of the stress tensor acting on a surface S are defined by:

$$T_n = \frac{1}{2} \mu (H_n^2 - H_t^2) \quad (2.28)$$

$$T_t = \mu \cdot H_n \cdot H_t. \quad (2.29)$$

Thereafter, these components are integrated in order to determine the resulting forces. H_n and H_t are the components of the magnetic field acting on a surface S and μ is the permeability of the material where H_n and H_t are calculated.

This method must be used with care following the chosen assumptions. For example, if fringing are neglected ($H_t = 0$), the tangential force will be equal to zero.

2.4 Magnetic Materials

Motors consist of three types of material; ferromagnetic material, electrical conductor material and electrical insulator material. The goal of this section is to give the main characteristics of ferromagnetic materials, i.e. the magnets and the iron. The other materials, which are more commons, are not introduced in this section.

2.4.1 Magnet Properties and Modelling

Electrical motors use mainly rare-earth permanent magnets. These materials are characterized by a large hysteresis cycle and have a high coercitive magnetic field H_c . The magnetization M of PM can be assumed constant for a given temperature if the relative permeability is assumed equal to 1. Therefore, the characteristic of the magnet is approximated by a straight line in the B-H plane and the flux density inside the PM is equal to:

$$B = B_r + \mu_0 \cdot \mu_{r \text{ pm}} \cdot H_0, \quad (2.30)$$

B_r is the remanent induction of the PM and $\mu_{r \text{ pm}}$ its relative permeability.

Figure 2.2 shows the linear demagnetization curve characterized by the remanent induction B_r , the coercitive magnetic field H_c and the magnetic field H_0 . Furthermore, Fig. 2.3 shows the flux density function of the magnetic field and its dependance on the temperature [23]. This graph shows also the polarization dependence on the temperature. Generally the working point of the magnet must always be above it, in order to avoid a magnet demagnetization.

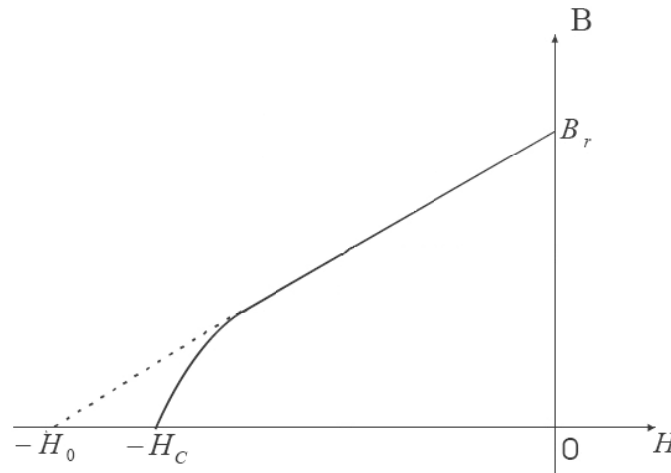


Figure 2.2: Permanent magnet demagnetization curve.

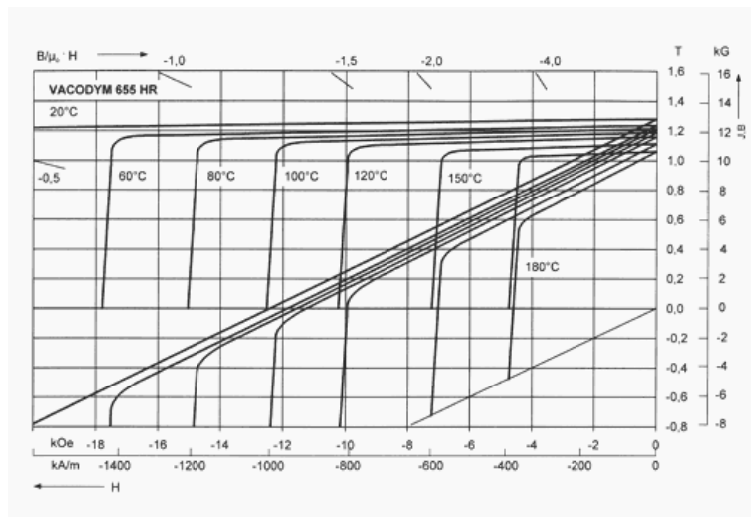


Figure 2.3: Demagnetization curve for a 655HR permanent magnet from Vacuumschmelze. The flux density is function of the magnetic field.

Rare-earth permanent magnets are characterized by a constant relative permeability $\mu_{r\ pm}$ close to 1. In practice, NdFeB permanent magnets (discovered in the 1980s) are more frequently used than SmCo (discovered in the 1960s). As shown in Table 2.1, NdFeB magnets have a higher remanent flux density but are more temperature dependent (TC). Actually, permanent magnets with a B_r higher than 1.4 T can be found on the market, which permits to increase the motor performances.

Table 2.1: Various properties of magnets.

Grade	B_r [T]	H_c [kA/m]	μ_r [-]	$H_c \cdot B_r$ [kJ/m ³]	TC (B_r) [%/°C]	TC (H_c) [%/°C]	Manufacturer
Vacodym 745HR (NdFeB)	1.44	1115	1.03	400	-0.115	-0.73	VAC
Vacodym 655HR (NdFeB)	1.28	990	1.03	315	-0.09	-0.61	VAC
N50 (NdFeB)	1.42	960	1.17	375	-0.12	-0.60	MMC
N45 (NdFeB)	1.32	955	1.1	345	-0.12	-0.60	OeMag
Vacomax 225HR (SmCo)	1.1	820	1.07	225	-0.03	-0.035	VAC
RCS28H (SmCo)	1.05	655	1.28	210	-0.035	-0.29	OeMag

To model a magnet, two different approaches are considered. The first one is to use equivalent currents or current densities and the second one is to model the magnet by an equivalent source of magnetic pe latter model is useful if a magnet should be added in a lumped equivalent magnetic circuit.

Equivalent Currents Approach

The goal of this method is to substitute the magnet by some equivalent currents or equivalent current densities, as shown on Fig. 2.4. In linear motors, only parallelepiped shape magnets are used and therefore they can be replaced by equivalent currents or currents densities along the faces parallel to the magnetization. Values of the equivalent current density J_s and the equivalent point currents I_s are defined as follows:

$$J_s = \frac{B_r}{\mu_0}, \quad (2.31)$$

$$I_s = \frac{J_s \cdot h_{pm}}{N_{Ipm}}. \quad (2.32)$$

Here, h_{pm} is the magnet height and N_{Ipm} is the number of equivalent current. This approximation can be made only if the relative permeability of the magnet is assumed equal to 1. An example of this model for $N_{Ipm} = 4$ is shown on Fig. 2.4).

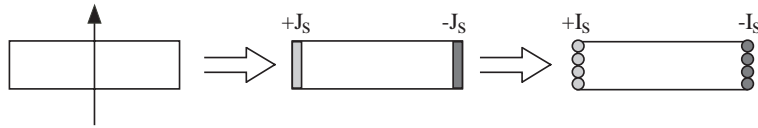


Figure 2.4: Model of a magnet using equivalent current densities or point currents.

A more general approach which considers non parallelepiped magnets can be found in [24].

Permeance Network Approach

PM can also be modelled by a magnetic scheme composed of a magnetic source θ_{pm} (2.33) and a permeance Λ_{pm} in series, as presented on Fig.2.5 [22].

The magnetic source θ_{pm} and the permeance Λ_{pm} are given by:

$$\theta_{pm} = H_0 \cdot h_{pm} \quad (2.33)$$

$$\Lambda_{pm} = \frac{\mu_0 \cdot \mu_{rpm} \cdot S_{pm}}{h_{pm}}. \quad (2.34)$$

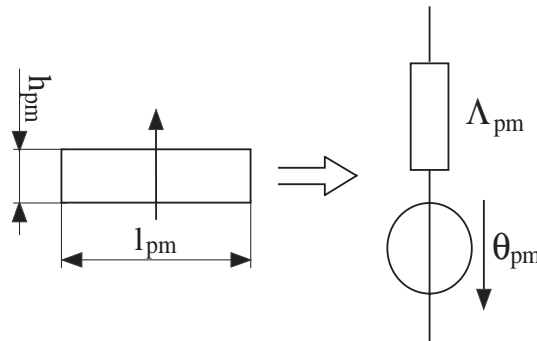


Figure 2.5: Permeance network model of PM.

S_{pm} is the surface of the magnet perpendicular to its magnetization vector. The magnetic field H_0 is equal to:

$$H_0 = \frac{B_r}{\mu_0 \cdot \mu_{r\ pm}}. \quad (2.35)$$

2.4.2 Iron Properties and Modelling

In an electric motor, the magnetic flux is guided by elements made of iron. If the magnetic flux to guide has only a DC component the magnetic material can be mainly a non laminate iron alloy. However, if the magnetic flux has a high amplitude AC component and a high frequency, the magnetic material must be laminated in order to decrease as much as possible the Eddy current losses. Furthermore, these materials must have the property to guide a high level of flux density, as some alloys (FeSi, FeCo or FeNi) permit it. Saturation curves of these materials are illustrated on Fig. 2.6 and the relative permeabilities are shown on Fig. 2.7 [25]. FeSi sheets are very widespread in the motor production because of their low price compared to the others. FeCo is often used in applications for which the motor weight has to be minimized and where the costs are not a restrictive factor (space applications for example).

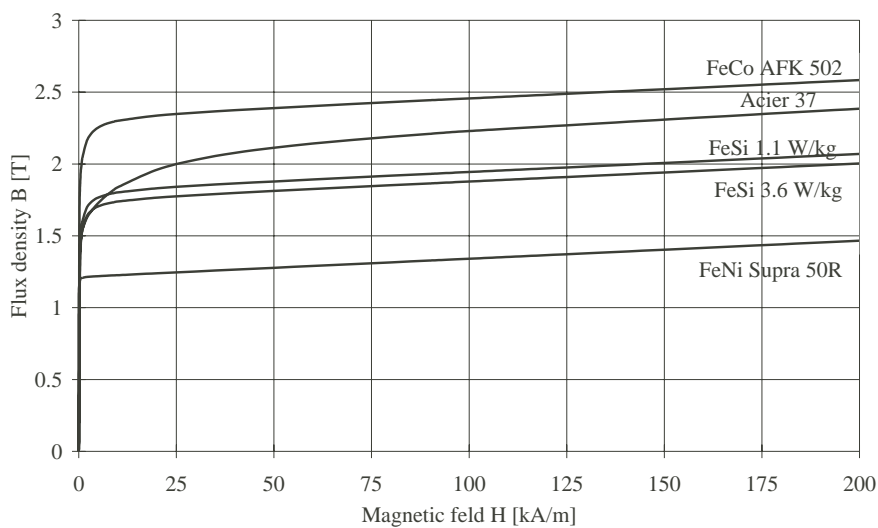


Figure 2.6: Saturation curves of materials used in motors.

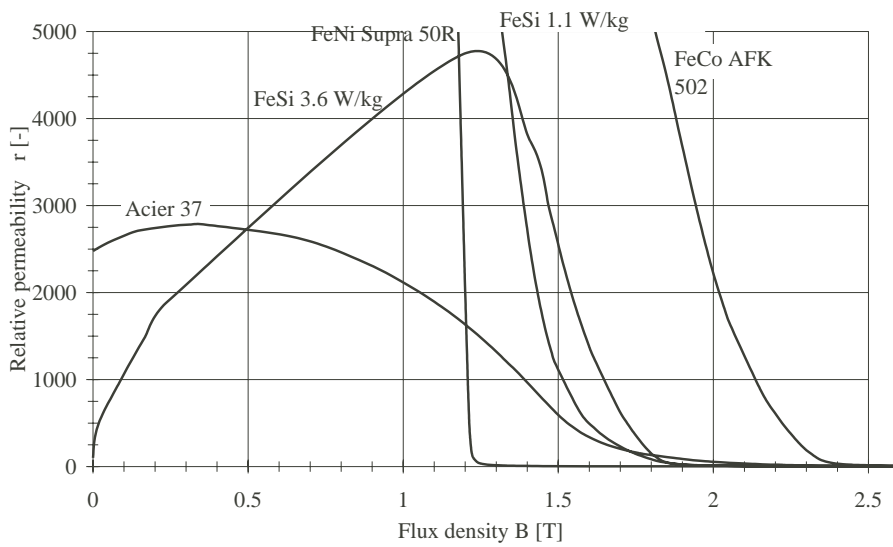


Figure 2.7: Relative permeability of materials used in motor.

For a linear magnetic material the magnetization is parallel and proportional to the magnetic field \mathbf{H} . Hence, (2.7) can be written as:

$$\mathbf{B} = \mu_0 \cdot \mu_r \cdot \mathbf{H}. \quad (2.36)$$

μ_r is the relative permeability of the material.

The saturation can be taken into account and modelled by various ways. A good overview of different modelization approaches is given in [26]. Two models are interesting: the first one is an exponential model [27] and the second one described in [28] which consists in dividing the saturation curve in three different parts. This model will be explained more in detail in Appendix B since it is used for this thesis.

Chapter 3

Motor Design Methodology

3.1 State of the Art, Choice of a Design Method

The recent developments in computer science offer new assistance possibilities in motor design by introducing adapted softwares. These programs solve in most cases *direct problems* (also called determinist approaches), i.e. the motor performances are calculated for a given motor geometry. The tendency is now to transform the direct problems to *indirect problems*, for which the goal is to determine the motor quantities (e.g. propulsion force, resistance, inductance, etc.) and geometry for required performances. This approach is more complex since several motors which fulfill the specifications can be designed.

Specific programs developed to design motors can be grouped in three categories [29]:

1. conception software using a procedural approach;
2. conception software using optimization technics;
3. conception software based on expert systems.

These design *methods* are briefly discussed in Sections 3.1.1 to 3.1.3, in order to make a choice concerning the methodology to apply.

To perform a design, the use of a *model* is compulsory. A model is a mathematical description of the problem to solve and it can deal with various phenomena in order to build a multi physical model. In this thesis, mechanical models are used in order to describe the dynamic of the motor; thermal models in order to explain the heat transfer in the motor and magnetic models to determine the electrical quantities and the forces (propulsion and attractive).

All these models can be separated in two groups:

- analytical models;
- numerical models.

Analytical models regroup explicit equations, which have the particularity to conserve an analytical expression after their resolution, i.e. that all parameters of the model can be written as a function of the other parameters. These analytical models are based on integral equations of Maxwell laws, image theory or equivalent currents and on Fourier laws or on empirical formulae for thermal motor models.

On the contrary, numerical models are used when the set of equations are impossible to solve directly. Therefore, iterative numerical methods (e.g. Monte Carlo) are used to obtain the solution (number). Most representative examples using numerical models are the FEM.

- *a program calculating the sensibility.* It permits to know the evolution of the model parameters and therefore of the motor performances. This program permits to give an optimization direction by varying some parameters in order to find the optimized solution.

This method has the advantage, using the program calculating the sensibility, to find an optimized design without exploring the complete problem space.

3.1.3 Design Software Based on Expert Systems

Expert systems are also often used to optimize a problem. A computer dictionary [31] gives the following definition:

"An expert system is regarded as the embodiment within a computer of a knowledge-based component from an expert skill in such a form that the system can offer intelligent advice or take an intelligent decision about a processing function. Some expert systems are designed to take the place of human experts, while others are designed to aid them. Expert systems are part of a general category of computer applications known as artificial intelligence . To develop an expert system, one needs a knowledge engineer, an individual who studies how human experts make decisions and translates the rules into terms that a computer can understand".

For this method, the direction taken to find the optimal solution is more or less stochastic following the expert knowledge. Several methods using a Design software based on expert systems are shown on Fig. 3.1 under the classification "Stochastic optimizer". Stochastic algorithms are based on the generations of some solutions. All these algorithms differ one from another by the choice of the new generation of possible solutions. The most known algorithms are the genetic algorithms. They explore the motor design variable space by means of the mechanisms of reproduction, crossover and mutation, with the aim of producing the best motor design. A global description of the use of a genetic algorithm applied to motor design is presented by [32], which points out that such a method requires a high number of iterations.

3.1.4 Design Methodology Choice

The design method used in the thesis is based on optimization technics, i.e. indirect methods. Compared to methods based on procedural approach, optimization methods offer the possibility to explore the problem space more efficiently although they are sometimes more time consuming. Expert systems are less straightforward to develop and they are dependent on the motor type. Therefore, optimization deterministic methods seem to be more adapted for motor design. Moreover, they offer possibilities which are nowadays not enough exploited in the electromagnetic problems. Optimization methods use either numerical or analytical methods.

Analytical methods are preferred since they are less time consuming than numerical methods. The analytical models are developed in Chapter 4 for the magnetic models and in Chapter 5 for the thermal models.

As presented on Fig. 3.1, there are many optimization algorithms for the chosen method (optimization technics with analytical models). An overview of these algorithms is given in [30]. In motor design, it is interesting to have the possibility to perform optimizations under constraints. Therefore, the chosen optimizer for this thesis is a determinist constrained optimizer with a Sequential Quadratic Programming (SQP) algorithm. SQP is based on the computation of the gradient and the Hessian matrix. The choice of this algorithm permits to use the program Pro@design [33] which offers several advantages compared to others, like matlab or excel. Indeed, Pro@design permits among others to solve implicit functions and to resolve integrals. Moreover, the generation of the gradient and the Hessian matrix is made automatically and should not be calculated by the programmer. Furthermore, the analysis of results is straightforward.

To summarize, the method chosen to design motors is an indirect method. It is based on a constraint deterministic optimizer with a sequential quadratic program using analytical models.

3.2 Introduction to Motor Design

The goal of motor design is to find the best motor fulfilling the specifications for a given application. To find the best solution, a comparison method must be introduced into the design process. These two aspects, motor design and comparison method are the key points leading to the final choice. The comparison method introduces the concept of figures of merit (or merit factors), which are criteria allowing an assistance to motor comparison. This concept is discussed in Section 3.6.

A general approach to design motors by an indirect method is presented on Fig. 3.2. The main stages, described in the following sections, are:

1. definition of the motor specifications and the design objectives;
2. enquiry of the various possibilities satisfying the motor specifications: m technology possibilities (i.e. synchronous motor, induction motor, direct or indirect drive, long or short stator, etc.);
3. first choice, based on the application constraints, between the m possibilities regarding the application, i.e. reduction of the number of possibilities to $n \leq m$;
4. development of the models (magnetical, thermal, mechanical, etc.) in relation to the design objectives. These validated models are developed a part from the motor design process;
5. design of the n motor variants. Constraints and data validation, if necessary an iterative process is applied to change the constraints;
6. study of the sensibility of the parameters around the solution, choice of the optimal solution;
7. comparison of the n motor designs;
8. final motor choice with the use of figures of merit;
9. design validation with a prototype or with FEM program;
10. final solution.

The first two steps are straightforward and are the basis of all design processes. They are introduced together in Section 3.3. This stage permits to select the m possibilities which satisfy the objectives and the specifications. The third point introduces the concept of figures of merit. This aspect is discussed in details in Section 3.6. This first comparison reduces the number of selected machines to $n \leq m$ and it is generally imposed by the application. After this choice, motor designs can be performed following the fourth and fifth step, i.e. with the chosen design method introduced in Section 3.1.4.

After these steps, the n motor designs must be compared between each other in order to find the best solution for the application. This aspect is discussed in Section 3.6. At last, the final design is obtained and it is validated by the FEM.

For this thesis, three models constitute the *global model* which is used by the optimization software. They are mechanical, thermal and magnetic models. The building of a motor model is shown on Fig. 3.3[34]. The first step is to define the specifications of the motor and its constraints. They can be either geometrical (motor dimensions, etc.), magnetical (Maximum flux density, remanent flux density, etc.) electrical (maximum voltage supply, etc.), costs or manufacturing constraints. Materials are also

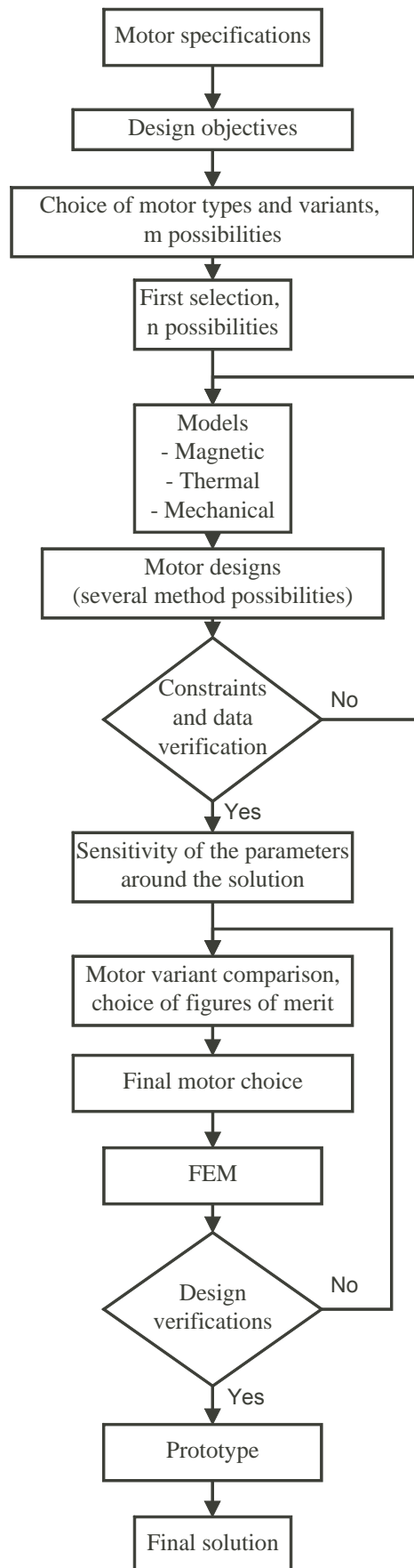


Figure 3.2: Flow chart representing a general approach for motor design.

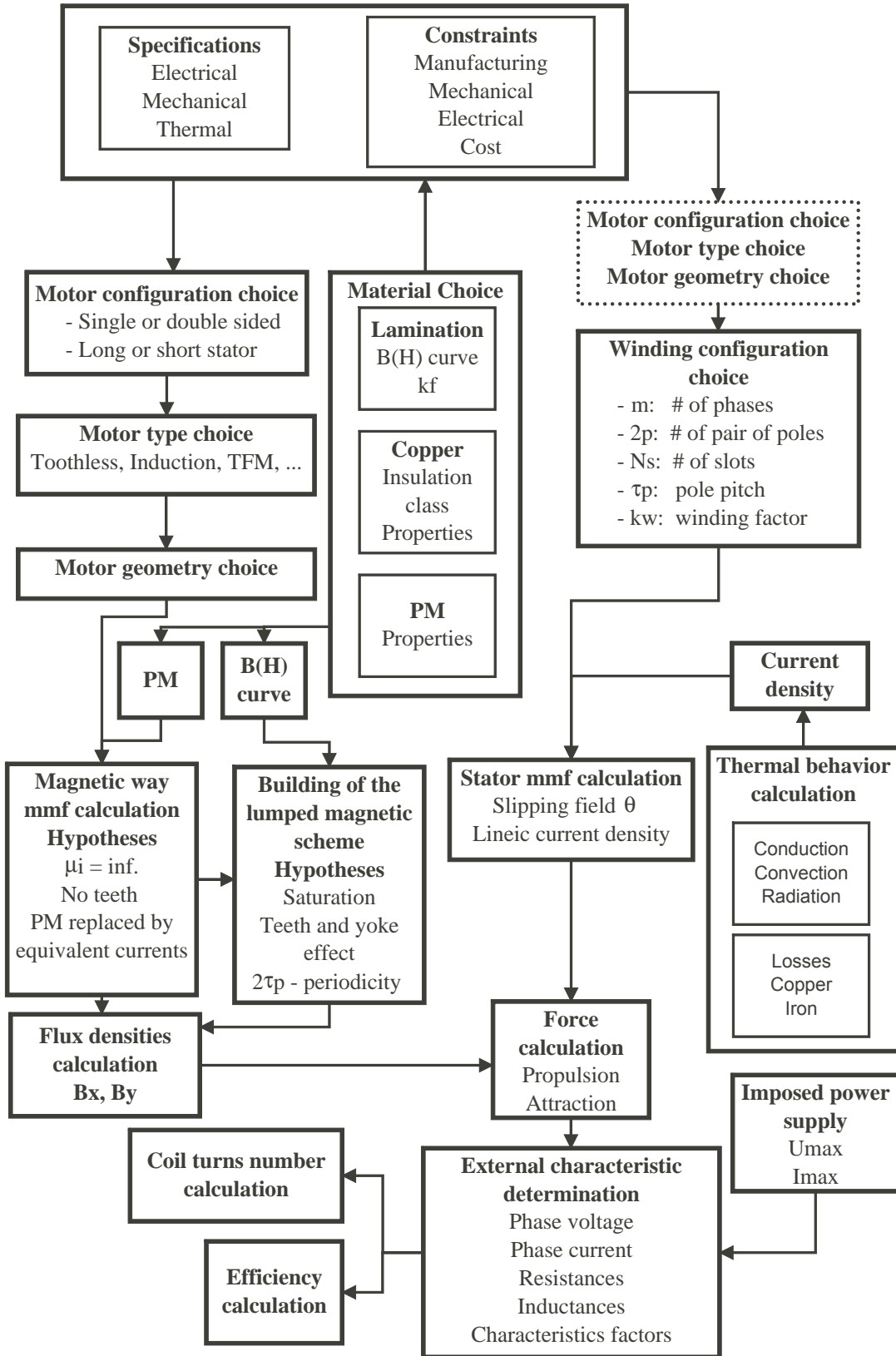


Figure 3.3: Schematic of the methodology to build a motor model.

determined in order to fix several properties and to set new constraints, as for example the maximum flux density in the teeth. From these constraints and specifications, a motor type is chosen depending on the application. Then, the geometry of the motor and its winding can be parameterized.

Thereafter, by taking into account the PM and the lamination properties, the magnetic way mmf is calculated. The effect of the saturation can be taken into account or not depending on the motor type. Simultaneously, the stator mmf is calculated. The current density is limited by a thermal model. By combining both mmf, the propulsion and the attractive forces are calculated. Thereafter, several characteristics can be determined such as the resistances, the inductances, the efficiency, etc. The number of turns per coil N is not a parameter of a pre-design process, as it is presented in Section 4.7.1. Indeed, the number of turns per coil can always be adjusted without changing the motor geometry.

Moreover, if the constraints and the specifications are not well known at the beginning of the project, an iterative process is compulsory.

3.3 Specifications and Objectives

Specifications and objectives to reach in design are very important and should be clearly defined before the beginning of the study. Indeed, they permit to define a solution catalog for the realization of the linear movement.

These two aspects, specifications and objectives, give an orientation for the model development. For example, if the motor is not often used, the thermal model will be different than for a motor which is continuously supplied. In other words, specifications and objectives generate the constraints of the problem and the choice of the assumptions.

Generally, motor designers produce a design which must satisfy several criteria at the same time. These performance objectives can sometimes conflict between them and most existing motor designs are based on mono objective optimization. The multi-objective design can be performed after the optimization process by the use of Pareto-optimization technics as it is presented in Section 3.5.

3.4 Variant Possibilities and First Choice due to the Application

Once the catalog of solutions is defined in relation with the specifications and objectives, a first choice of the most adapted motors must be made since all topologies and variants cannot be studied in details. Chapter 1 gives an overview of the various topologies and motor types constituting the catalog of solutions.

The first choice of the motor is principally related to the application and it reduces the catalog solution to n possibilities. This first choice is generally based on experience, advantages and drawbacks specific to different motor types.

3.5 Introduction to Optimization Problems

This section introduces the basis of an optimization problem. The problem is first mathematically introduced and then an optimization methodology is proposed in which the constraints of the model and various objective functions are discussed.

The optimization algorithms are very useful to avoid the iteration process inherent to a motor design using a deterministic approach.

3.5.1 Mathematical Definition of an Optimization Problem and Various Algorithms

To converge quickly to an optimum design close to the final motor design, an analytical optimization is used as introduced in Section 3.1.4. Nowadays, pseudo optimization with FEM programs are also often used to design motors. Unfortunately, they have the drawback to be time consuming. Moreover, in order to correctly use FEM, an advanced knowledge in motor design is required or an existing design should be used as a starting point.

An optimization problem (P) is defined by the set of equations [35]:

$$(P) \begin{cases} \min f(x) & \forall x \in R^n \\ g_i(x) \leq 0 & \forall i \in \{1, \dots, p\} \\ h_i(x) = 0 & \forall j \in \{1, \dots, g\} \\ x_k \min \leq x_k \leq x_k \max & \forall k \in \{1, \dots, n\} \end{cases} \quad (3.1)$$

$f(x)$ is the objective function, x is a vector containing the n parameters of the analytical model, $g_i(x)$ and $h_i(x)$ are the inequality and equality constraints of the problem, $x_k \min$ and $x_k \max$ are the boundary constraints. The optimization problem can either be constraint or not.

Generally, the optimization algorithms are conceived to converge to the minimum of the objective function $f(x)$. Therefore, if the objective function must be maximized, a new objective function can be defined in either of two ways:

$$f_{\min}(x) \begin{cases} -f(x) & \text{a)} \\ \frac{1}{f(x)} & \text{b)} \end{cases} \quad (3.2)$$

The solution a) is privileged and can be used without particular precautions in motor design. The solution b) can generate end precision problems in the case of very high numbers.

Pro@design treats mono objective functions and gives the nearest minimum solution of the x_k initial values of the problem definition, i.e. it gives the local minimum and not the global minimum. To avoid this problem and to find the global minimum, several optimizations are made by varying the initial conditions. This aspect is automatically generated by the optimization software Pro@design.

Furthermore, the version of Pro@design used for this thesis does not consider a set of integer numbers for the x_k parameters. Therefore, the winding must be defined separately.

3.5.2 Optimization Methodology

Optimization softwares can be used to optimize a new design or to improve the performance of an existing design. The approach for these two problems is the same and it is presented schematically on Fig. 3.4. The outputs of an optimization problem are the geometry parameters and the electrical quantities. The first step is to define the global analytical model of the problem. In the case of motor designs, the global model is composed of specific models as a magnetic model, a thermal model, a mechanical model and a cost model. Depending on the goal of the optimization, some of these specific models can be omitted to build the global analytical model, e.g. for a space project the price can be omitted and therefore the specific economical model is not introduced in the global model. These specific models are introduced in Chapters 4 and 5.

The resolution of an optimization problem can be separated in several steps:

1. definition of the optimization target(s);
2. definition of constraints due to optimization objectives;
3. definition of the motor parameters, i.e. definitions of the most important variables for the motor design;

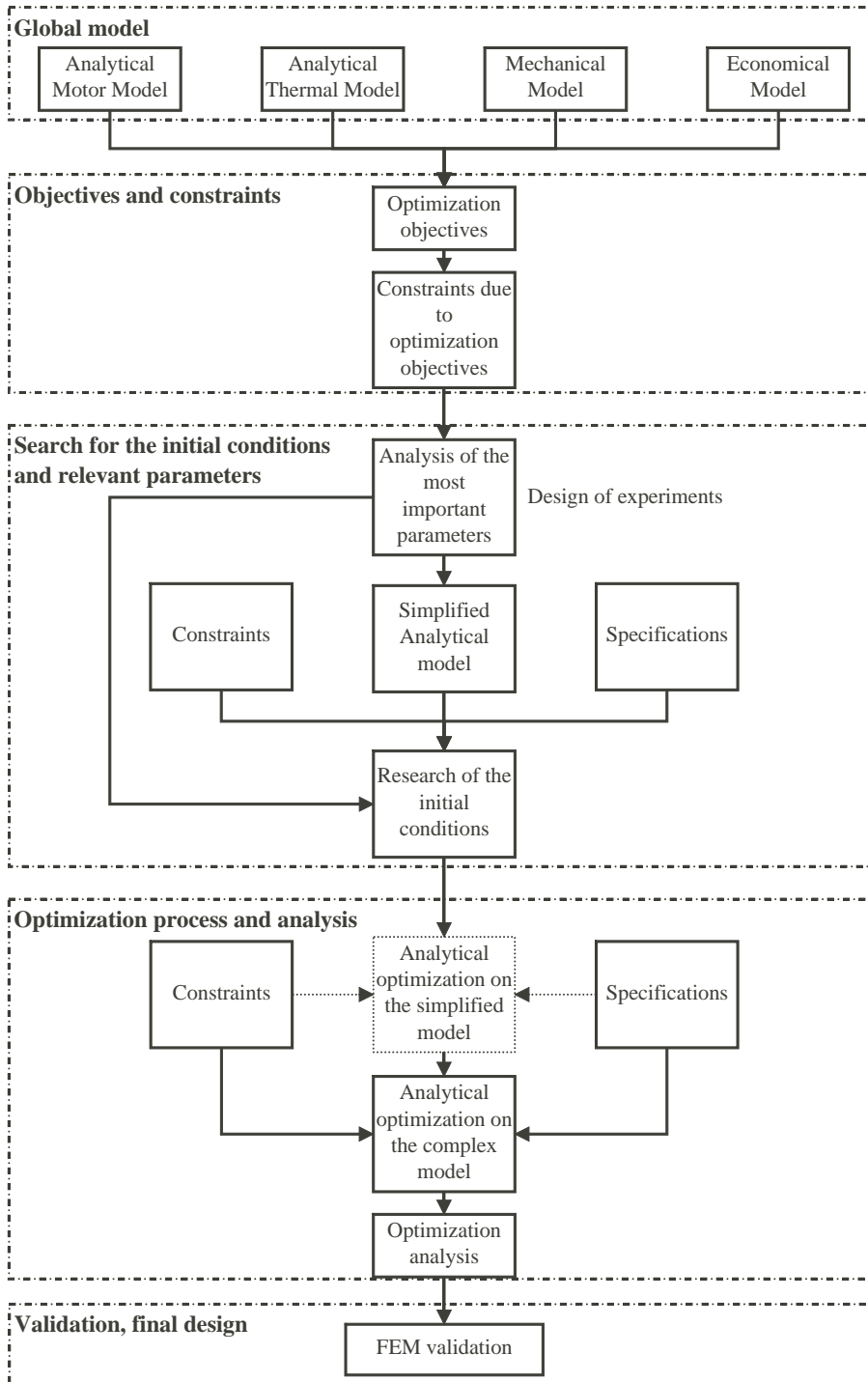


Figure 3.4: Schematic of an optimization process.

4. research of the initial conditions for the optimization algorithm;
5. first optimization with a simplified analytical model;
6. optimization with an accurate analytical model;
7. optimization analysis;
8. design choice;
9. FEM control and definition of the final motor parameters.

The relevant points of the proposed optimization process are discussed more in details in the following subsections.

3.5.2.1 Optimization Constraints

The optimization constraints arise from three distinct aspects: constraints due to the validity domain of analytical models, geometrical and electrical constraints specific to the motor type and constraints due to optimization objectives. These last constraint are used to realized a pseudo multi objective optimization.

Some constraints give the validity domain for each model (magnetical, thermal, mechanical, etc.) and they are imposed by the analytical models. These constraints are useful in order to keep the global analytical model as precise as possible. They are the bounds of the problem and are called the *bound constraints*.

The constraints due to the motor geometry or to electrical reasons can be inequality or equality expressions. For example, the air gap in a motor is often limited to a minimum value for guidance reasons or tolerance reasons, becoming therefore an equality constraint. Some other geometrical constraints, as for example the slot opening, the wire diameter, etc. , are introduced as inequality constraints. These constraints are named the *constructive constraints*.

The last constraints are due to the optimization objective [36]. Since the used program is mono objective, it is sometimes interesting to constraint some other parameters in order to obtain an optimization result which fulfills the specifications. These are the *objective constraints*. In some cases, several parameters are regrouped to form the objective function. Therefore, the objective constraints could be suppressed.

3.5.2.2 Choice of the Optimization Parameters

The choice of the optimization parameters is very important and not always straightforward. This choice is very useful in order to reduce the complexity of the problem and to permit a better understanding of the optimization result. Indeed, if too many parameters are used, the result cannot be efficiently analyzed and therefore the tendency would be to adopt the optimization result without analysis of the other parameters. Moreover, too many parameters risk to increase the number of local minima and therefore it increases the possibility to converge to a local optimum not corresponding to the best one. Even if this drawback can be avoided by changing the initial conditions of the problem, it is however recommended to limit as possible the number of parameters. As an example, in Section 4.7.1, the number of turns per coil N can be chosen arbitrary and adapted once the design is optimized.

The choice of the most important parameters can be made using the method called *design of experiments*, which calculates the effect of the parameters and their interactions on the objective function. This method can be time consuming and is not very useful if the problem is well-known. In motor design, the most important parameters can be deduced from the experience. A non exhaustive list of the most relevant parameters in the case of a toothed motor are:

- the magnet properties and its height;
- the pole pitch;
- the slot and tooth dimensions;
- the winding configuration (number of slots per pole);
- the yoke height;
- the convection coefficient;
- the working rating point (Force, speed, etc.);
- the supply and control strategy.

3.5.2.3 Determination of the Initial Conditions

Due to local minima, the definition of the initial conditions of the problem is critical. Depending on the optimization program, the initial conditions must be in the problem domain, i.e. they must produce a solution where the motor parameters are located between the bound and the constructive constraints. The software Pro@design offers the possibility to begin the optimization even if the initial conditions lead to a solution situated outside the bound constraints.

Initial conditions can be obtained either with a short analysis of a simplified model or from an existing design in the case of the optimization of a realized motor.

3.5.2.4 Optimization and Objective Function

As presented on Fig. 3.4 the optimization can be performed in two stages. The first optimization on a simplified global model allows to find the geometry sensibility on the performances and to have therefore a better overview of the problem. This simplified global model allows the possibility to easily analyze the optimization result and gives the first interesting directions to follow in order to find the optimum. This step, more or less useful depending on the complexity of the problem, permits also to determine the initial conditions of the second step. The second optimization is performed with a more complex model and the initial conditions are close to the optimum avoiding therefore as far as possible local minima.

The choice of the objective function depends of course on the optimization objectives and is realized for the motor working point. Since the used program is mono objective, a tendency is to combine several parameters to form the objective function. Such an approach must be used with care. The use of a sum of several quantities, as proposed by [37], can lead to inappropriate results if the summed quantities are not of the same order of magnitude. To avoid this problem, it is recommended to normalize the quantities [38]. For example, if the efficiency and the cost must be combined to form an objective function, the formulation would be equal to:

$$F_{obj} = \frac{Cost_{ref}}{Cost} + \frac{\eta}{\eta_{ref}} k_{weight}. \quad (3.3)$$

k_{weight} is a weighting factor.

To avoid these problems of quantity combinations it is preferred to have a simple objective function and to limit the objective constraints. For the previous example, the better way would be to define the objective function as equal to the cost and to constraint the efficiency to a minimum value, permitting therefore to easier analyze the result cost.

This last approach is used in this thesis since it is more robust than the other methods. If the motor has several distinct working points, several optimizations for each point must be made and the final motor design will be a compromise between these optimizations by favoring the one corresponding to the nominal working point of the motor. Another approach proposed in [39] consists to duplicate all the parameters by the number of working points. This approach is very useful for motor design with several working points. For example, if a given motor must work at two different speeds, the function efficiency can be doubled in order to constraint a minimum efficiency for the two working points.

3.5.2.5 Optimization Analysis

It is interesting to optimize the same motor under several constraints and several objective functions. Such an approach is needed since the final motor design is always a compromise between several quantities, as for example mass and efficiency. Therefore, mono objective program can produce some results which can be analyzed as the results of a multi objective program. Therefore, Pareto curves are used to analyze the optimization results.

The definition given by [40] is the following:

"Pareto-optimization technic is set forth for solving the multi objective optimization problem in a parametric fashion resulting in a set of optimal solution from which an appropriate compromise design can be chosen, based on the preference of the designer. A feasible solution is Pareto-optimal if there exists no other feasible solution that yields an improvement in any of the component design objectives without causing a decrease in at least one other criterion".

The principle to obtain a Pareto-curve can be summarized in four steps for a bicriterial optimization:

1. choice of the two main objectives (two objective functions, f_1 and f_2);
2. separated optimizations of the two objective functions, defining the limits of the Pareto-curve;
3. research of the Pareto-curve by several additional optimizations;
4. compromised choice of the final solution.

The step three can be achieved in two ways. The first one is to use an objective function similar to (3.3) by including a weighting factor which for the presented example becomes:

$$F_{obj} = k_{weight} \frac{Price_{ref}}{Price} + (1 - k_{weight}) \frac{\eta}{\eta_{ref}}. \quad (3.4)$$

The weighting factor k_{weight} varies from 0 to 1. The second approach is to chose one of the two objective functions and to constraint the second in order to obtain the Pareto-curve. Such a curve is given on Fig. 3.5, for an example case where the efficiency must be maximized (f_1) and the weight minimized (f_2).

At last, the final solution is chosen from the Pareto-curve.

3.5.2.6 FEM Validation

Once the optimized solution is defined, the motor is validated by the FEM program. If the analytical solution and the FEM model are not in agreement, an iterative process is introduced to correct the model. When the analytical optimization is consistent with the FEM results and when all the n motor types are optimized, the design can proceed to the next step which is the motor comparison.

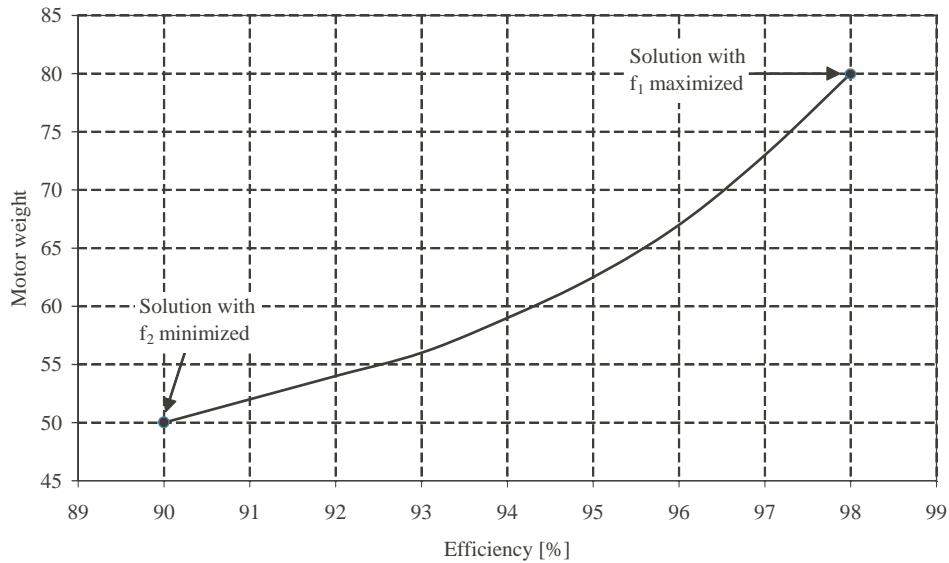


Figure 3.5: Pareto-curve for the optimization of two criteria: the motor weight and the efficiency.

3.6 Comparison Methodology

Once the first steps of the motor design methodology have been performed (Fig. 3.2), the selection of the most suitable motor for the application can be made. This stage is crucial and must be performed with care. Flow chart presented on Fig. 3.6 gives the steps needed to perform a good comparison and therefore a judicious motor choice. This figure introduces the notion of figures of merit which is the basis of the comparison approach. The motor choice can be performed in several stages (two in the case of the Fig. 3.2) as it is explained in Section 3.6.3. Before this step, the conditions required to perform a relevant motor comparison are introduced in Section 3.6.1 and the concept of *figures of merit* is discussed in Section 3.6.2.

3.6.1 Conditions for a Relevant Motor Comparison

Several conditions need to be fulfilled in order to perform a relevant comparison:

1. the constraints on the motor main parameters must be the same;
2. the hypothesis taken for one motor must have the same consequences for the other. It means that to perform a relevant comparison, the precision of the various motor models must be of the same order;
3. motors must have the same objective function to be compared.

These three points allow to obtain a relevant comparison. If one of these points is not respected and the obtained results are close, the comparison must be made with care.

3.6.2 List of Main Figures of Merit

The factors (or figures) of merit represent a way of comparison for the choice of the motor for an application. They can take into account electrical, magnetical, mechanical or also financial aspects. These

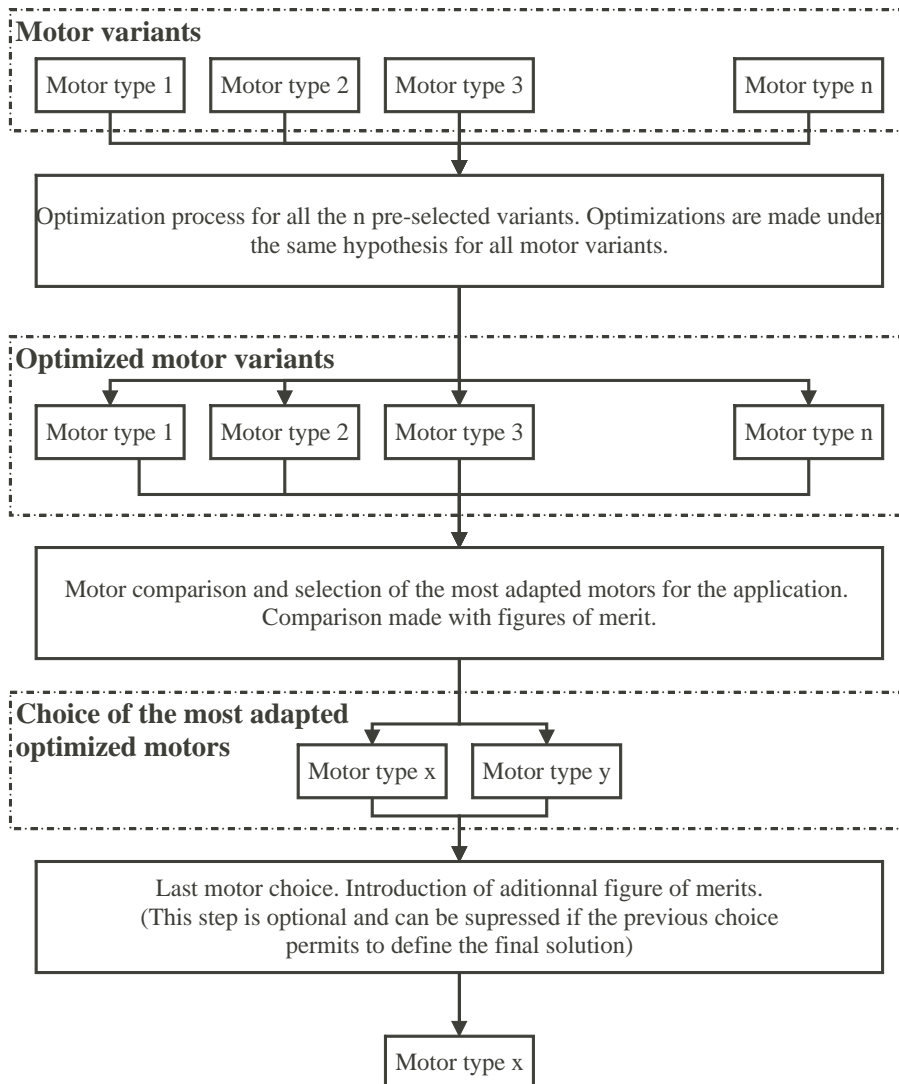


Figure 3.6: Flow chart of the comparison process between the n preselected variants from Fig. 3.2.

factors can be given either with quantifiable values (weight, power per weight, etc.) or by appreciation values (complexity of maintenance, robustness of the solution, etc.).

An inexhaustive list of factors for the motor choice is presented in the following subsections [41]. They are divided in two groups. The first one is related to the motor and the second one is more adapted to mechanical aspects. This list of figures of merit is only introduced to give an idea of the possible factors. They are not all used for a comparison approach and several other can be added.

3.6.2.1 Motor Figures of Merit

These factors can be for example:

- massic propulsion force;
- surfacic propulsion force;
- magnetic field density in the air gap;

- cogging force divided by the propulsion force;
- efficiency multiplied by power-factor;
- motor constant (propulsion force divided by the square root of copper losses), etc.

These factors are often combined factors of several motor quantities. The first three factors are straightforward. The cogging force divided by the propulsion force gives an idea of the perturbation level introduced by the cogging force. The last factor, motor constant, gives an idea of the motor efficiency since it represents the propulsion force divided by the square root of copper losses or the square root of copper and the iron losses. This factor is unfortunately not linear since it depends on the saturation of the motor as well as its heating.

3.6.2.2 Guidance Figures of Merit

These factors can be for example:

- robustness;
- complexity of maintenance;
- maintenance cycle;
- installation complexity;
- life cycle of guidance;
- mean time between failures;
- cost of the guidance system, etc.

All these figures of merit are appreciation factors and have therefore only sense for a comparison approach. They are directly in relation with other quantifiable values such as e.g. the attractive force.

3.6.3 Motor Comparison

The chosen approach to compare motors consists to build a comparative table regrouping the most relevant figures of merit and results for the studied application. A straightforward comparison of the motor variants based on the selected figures of merit, often allows the elimination of several motor types. If this first comparison does not allow to keep only one motor type, other figures of merit can be added to make the final choice between the remaining motors. If the final choice is not straightforward, the figure of merits can be level-headed as it is proposed by [42]. The use of level-headedness factor should permit an automatization of the motor choice by comparison. However due to compromises which must be made, it is suggested to perform the comparison avoiding an automatic process.

3.7 Conclusions

The method chosen to design motors in this thesis is an indirect method based on a constraint deterministic optimizer using analytical models. The optimization process uses a sequential quadratic program and the chosen software permitting such an approach is Pro@design. The design method requires a global model which regroups, in this thesis, a mechanical model, a thermal model and a magnetic model. An optimization based on analytical models offer the advantage to be less time consuming than a numerical optimization.

The introduction of Pareto-curve is useful in some cases where the specifications are not clearly defined or if they are introduced so that a compromise between several values has to be made. On the contrary, if the specifications and the objectives are clearly defined such an approach is not need.

The proposed design methodology will be applied on the case studied in Chapter 7 and will define the best optimized motor for the lift application. This innovative method based on comparison of optimized motors differs from the conventional methods based on determinist approach which is usually applied in motor design.

The presented approach to design motors was introduced in a general way. Therefore, it is also valid for rotative motors and can be applied when another optimization program is used.

Chapter 4

Linear Motor Models

4.1 Introduction

Nowadays, a lot of publications are related to motor design with FEM programs, which implies in most cases a determinist approach. Although recent FEM softwares include optimization algorithms, they have the drawback to be slow and not straightforward to use. Therefore, an analytical optimization is a good approach to rapidly pre-design motors. In order to apply analytical optimizations, several motor models are introduced in this chapter.

First, the magnetic models are discussed (Sections 4.2 to 4.6). These models are useful to analytically calculate the motor parameters such as the force, the efficiency, the induced voltage, etc. The mmf of each magnetic ways (MaW) type are separately analyzed. The notion of equivalent point current to modelize the PM are used.

Then, the motor supply is presented in Section 4.7.3. This model is important in order to make the link between the motor and its supply.

Finally, the motor material costs are discussed in the last part of the chapter in order to give an order of magnitude of the material cost.

The analytical modelling is done with two goals: low and high accuracy level. The former is performed in order to determine the properties of the motor type, its main advantages and drawbacks. This approach is used when a rapid optimization of the motor is desired or to determine the initial conditions for an optimization using the high accuracy and more complex model. The difference between these two analytical models and their applications has been presented with more details in Chapter 3.

As mentioned, each model is validated by comparison with FEM simulations.

4.2 Magnetic Way Models, mmf Calculation

The excitation of all presented MaW is produced by PM and they are modelled applying the same approach. It consists in substituting the parallelepiped magnets by equivalent point currents or by equivalent current densities, as it was presented in Section 2.4.1.

Therefore, to model PM the flux density distribution in the air produced by a point current or by a current density must be known. These aspects will be studied in Sections 4.2.1 and 4.2.2 and are used to build the analytical models of the magnetic ways. Three different configurations to determine the flux density produced by a point current are studied:

1. a point current in the air;
2. a point current placed above an ideal infinite iron plate;

3. a point current between two ideal infinite iron plates.

The flux distribution and the potential vector due to a point current in the air are calculated using (2.9) and the Maxwell's law (2.11) under the following assumptions:

- iron parts have an infinite relative permeability ($\mu_{rir} = \infty$);
- plates have an infinite length and width;
- magnets have a relative permeability equal to 1 ($\mu_{rpm} = 1$).

4.2.1 Flux Distribution in the Air Produced by a Point Current

The presented geometries are two-dimensional.

Configuration Without Iron Parts

For this case the flux distribution in the air is directly obtained from the Maxwell's equation (2.11). The coordinate system is in this case defined as shown on Fig. 4.1.

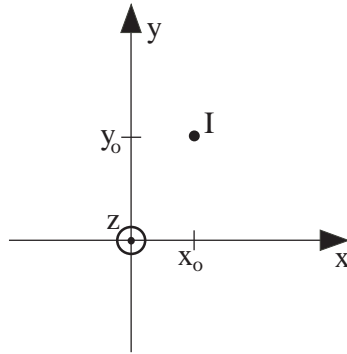


Figure 4.1: Conductor placed in the air at the position (x_0, y_0) with the current flow I .

The flux density at the point (x, y) is given by:

$$\underline{B}_I(x, y) = \frac{\mu_0 \cdot I}{2\pi} \cdot \frac{-j \cdot (y - y_0) + i \cdot (x - x_0)}{(x - x_0)^2 + (y - y_0)^2}. \quad (4.1)$$

The vector potential is calculated using (2.9) and therefore is equal to [43]:

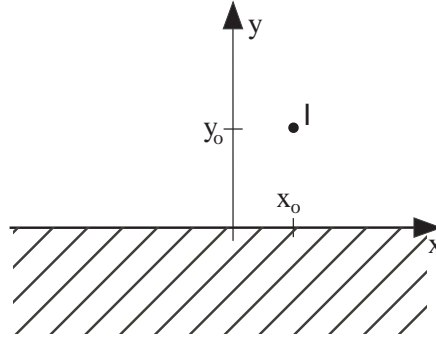
$$A_I(x, y) = -\frac{\mu_0 \cdot I}{2\pi} \ln \left(\sqrt{(x - x_0)^2 + (y - y_0)^2} \right). \quad (4.2)$$

Configuration With an Iron Plate

For a conductor above an ideal iron plate (Fig. 4.2), the flux density distribution and the potential vector can be calculated using (4.1) and (4.2) and applying the image theory [44].

The two components of the flux density distribution for the x-component and for the y-component are given by:

$$B_{x \text{ } I_{1pl}}(x, y) = \frac{\mu_0 \cdot I}{2\pi} \left[\frac{-y + y_0}{(x - x_0)^2 + (y - y_0)^2} + \frac{-y - y_0}{(x - x_0)^2 + (y + y_0)^2} \right], \quad (4.3)$$

Figure 4.2: Conductor above an infinite plate with the current flow I at the position (x_0, y_0) .

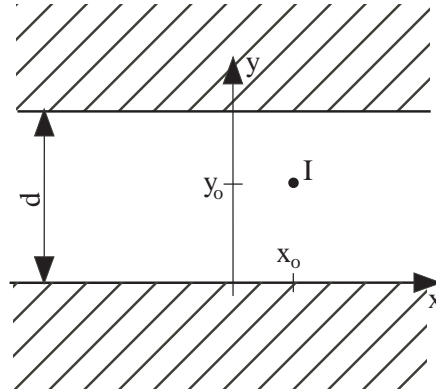
$$B_{y I_{1p}}(x, y) = \frac{\mu_0 \cdot I}{2\pi} \left[\frac{x - x_0}{(x - x_0)^2 + (y - y_0)^2} + \frac{x - x_0}{(x - x_0)^2 + (y + y_0)^2} \right]. \quad (4.4)$$

The complex form of these equations is given in [45]. For the vector potential, the equation is:

$$A_{(x,y)} = -\frac{\mu_0 \cdot I}{2\pi} \left[\ln \left(\sqrt{(x - x_0)^2 + (y - y_0)^2} \right) + \ln \left(\sqrt{(x + x_0)^2 + (y + y_0)^2} \right) \right]. \quad (4.5)$$

Configuration Between two Iron Plates

This configuration is described on Fig.4.3.

Figure 4.3: Conductor with the current flow I in the position (x_0, y_0) between two infinite plates separated by a distance d .

Applying the image theory is more complex in this case because each image produces another image in the opposite plate, resulting in a complex sum of current contributions [44]. In this topology, the results for the two components of the flux density are:

$$B_{x I_{2p}}(x, y) = \frac{\mu_0 \cdot I}{4 \cdot d} \left[\frac{\sin \frac{\pi \cdot (y - y_0)}{d}}{\cosh \frac{\pi \cdot (x - x_0)}{d} - \cos \frac{\pi \cdot (y - y_0)}{d}} + \frac{\sin \frac{\pi \cdot (y + y_0)}{d}}{\cosh \frac{\pi \cdot (x - x_0)}{d} - \cos \frac{\pi \cdot (y + y_0)}{d}} \right], \quad (4.6)$$

$$B_{y I_{2p}}(x, y) = -\frac{\mu_0 \cdot I}{4 \cdot d} \left[\frac{\sinh \frac{\pi \cdot (x - x_0)}{d}}{\cosh \frac{\pi \cdot (x - x_0)}{d} - \cos \frac{\pi \cdot (y - y_0)}{d}} + \frac{\sinh \frac{\pi \cdot (x - x_0)}{d}}{\cosh \frac{\pi \cdot (x - x_0)}{d} - \cos \frac{\pi \cdot (y + y_0)}{d}} \right]. \quad (4.7)$$

and for the potential vector:

$$A_{I_{2p}}(x, y) = \frac{\mu_0 \cdot I}{4\pi} \left[\ln \left(\cosh \frac{\pi(x-x_0)}{d} - \cos \frac{\pi(y-y_0)}{d} \right) + \ln \left(\cosh \frac{\pi(x-x_0)}{d} - \cos \frac{\pi(y+y_0)}{d} \right) \right]. \quad (4.8)$$

4.2.2 Flux Density in the Air Produced by a Lineic Current

If several conductors with a current I are placed one beside the other in an ironless configuration, (4.1) can be integrated either in the x-direction or in the y-direction in order to find the flux density in the air produced by a lineic current density J_s , as presented on Fig. 4.4 for the two configurations.

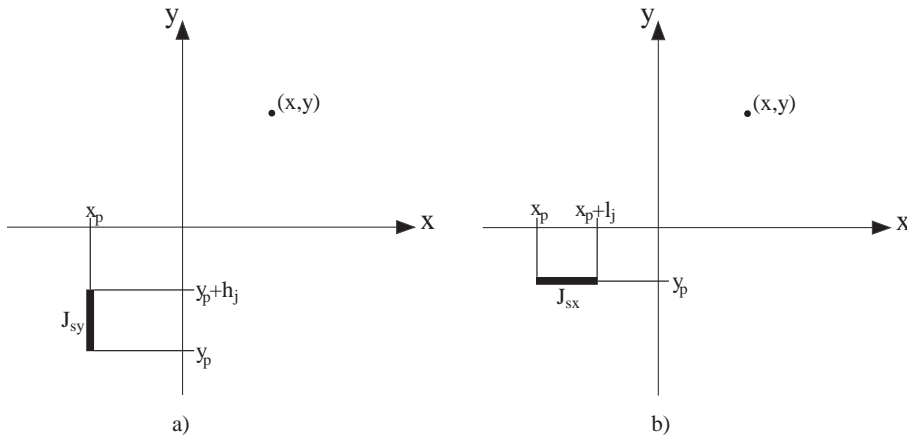


Figure 4.4: Lineic current density in the air, distributed along a height h_j (a) and along a length l_j (b).

If the lineic current density, distributed along the height h_j is parallel to the y-axis, the flux density at the point (x, y) in the air becomes for the x and y-directions:

$$B_x J_{sy}(x, y, x_p, y_p) = \frac{\mu_0 \cdot J_{sy}}{4\pi} \ln \left(\frac{(x-x_p)^2 + (y-y_p-h_j)^2}{(x-x_p)^2 + (y-y_p)^2} \right), \quad (4.9)$$

$$B_y J_{sy}(x, y, x_p, y_p) = -\frac{\mu_0 \cdot J_{sy}}{2\pi} \left(\arctan \left(\frac{y-y_p-h_j}{x-x_p} \right) - \arctan \left(\frac{y-y_p}{x-x_p} \right) \right). \quad (4.10)$$

Similarly, if the lineic current density is parallel to the x-axis, and has a length l_j the equations become:

$$B_x J_{sx}(x, y, x_p, y_p) = \frac{\mu_0 \cdot J_{sx}}{2\pi} \left(\arctan \left(\frac{x-x_p-l_j}{y-y_p} \right) - \arctan \left(\frac{x-x_p}{y-y_p} \right) \right), \quad (4.11)$$

$$B_y J_{sx}(x, y, x_p, y_p) = -\frac{\mu_0 \cdot J_{sx}}{4\pi} \ln \left(\frac{(y-y_p)^2 + (x-x_p-l_j)^2}{(y-y_p)^2 + (x-x_p)^2} \right). \quad (4.12)$$

When it is possible, the preference is given to lineic currents rather than a sum of point currents.

4.2.3 Single Sided Magnetic Way with Mounted PM

The magnetic way (MaW) shown on Fig. 4.6 is the simplest one to modelize. Therefore, it will be studied more in details in order to explain several characteristics of magnetic ways. As the iron parts are supposed ideal, the superposition principle is applicable for all MaW modelling.

The flux density produced by a magnet above a plate, Fig. 4.5, is modelled using (4.9) for the x-component and (4.10) for the y-component, respectively. These formulas are more adapted to modelize a magnet compared to a sum of several point currents and has the advantages to be faster and to have a better accuracy, since the flux density is not dependent on the number of point currents. The approach to modelize a magnet above a plate is defined by two steps. The first one is to replace the magnet by two current densities, as presented in Section 2.4.1. The second step is to apply the image theory and to remove the iron plate. These two steps are represented on Fig. 4.5. The approach is only presented for the y-component of the flux density which is mostly used to produce a force. The x-component can be obtained by a straightforward analogy.

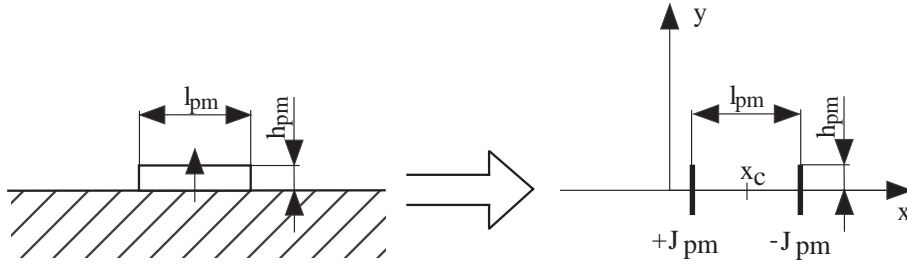


Figure 4.5: Modelling approach of a magnet placed above an ideal iron plate.

Therefore, using (4.10) with the following substitutions;

$y_p = -h_{pm}$, $h_j = 2h_{pm}$ due to the image theory, $x_p = x_c - l_{pm}/2$ and $J_s = J_{pm} = B_r/\mu_0$ for left side of the magnet and $x_p = x_c + l_{pm}/2$ and $J_s = -J_{pm} = -B_r/\mu_0$ for the right side of the magnet, the y-component of the flux density for one magnet is equal to:

$$B_{y1pm}(x, y, x_c) = \frac{\mu_0 \cdot J_{pm}}{2\pi} \left(\operatorname{atan} \left(\frac{y + h_{pm}}{x - x_c - \frac{l_{pm}}{2}} \right) - \operatorname{atan} \left(\frac{y - h_{pm}}{x - x_c - \frac{l_{pm}}{2}} \right) + \right. \quad (4.13)$$

$$\left. + \operatorname{atan} \left(\frac{y - h_{pm}}{x - x_c + \frac{l_{pm}}{2}} \right) - \operatorname{atan} \left(\frac{y + h_{pm}}{x - x_c + \frac{l_{pm}}{2}} \right) \right).$$

Once the model of a magnet is obtained, the MaW model is straightforward to obtain. It consists to substitute x_c by $x_c \pm k \cdot \tau_p$ in (4.13) and to alternate the magnetization direction of the magnets. For example, the y-component of the flux density for a magnetic way with 6 PM (Fig. 4.6) is equal to:

$$B_{y6pm}(x, y) = \sum_{i=0}^5 (-1)^{i+1} B_{y1pm}(x, y, x_i) \text{ with } x_i = -2.5\tau_p + i \cdot \tau_p. \quad (4.14)$$

The analytical model of the flux density in both directions produced by the 6PM MaW is compared to a FEM program. The obtained results are shown on Fig. 4.7 for the y-component and on Fig. 4.8 for the x-component of the flux density. This FEM analysis is performed under the same conditions as the analytical model, i.e. assuming an ideal infinite iron plate under the magnets. As shown, the analytical model (circles) is in good agreement with the FEM for an ideal MaW model (cross). The analytical results are also compared to a *real* MaW, i.e. the magnetic way length is no more infinite and the saturation in the yoke is taken into account. In the presented example, the length of the magnetic way is equal to six times the pole pitch. The comparison given on Fig. 4.7 shows that above the four magnets in the middle of the MaW, there is no significant difference between the analytical model and the FEM. An insignificant difference in amplitudes is due to the saturation in the yoke.

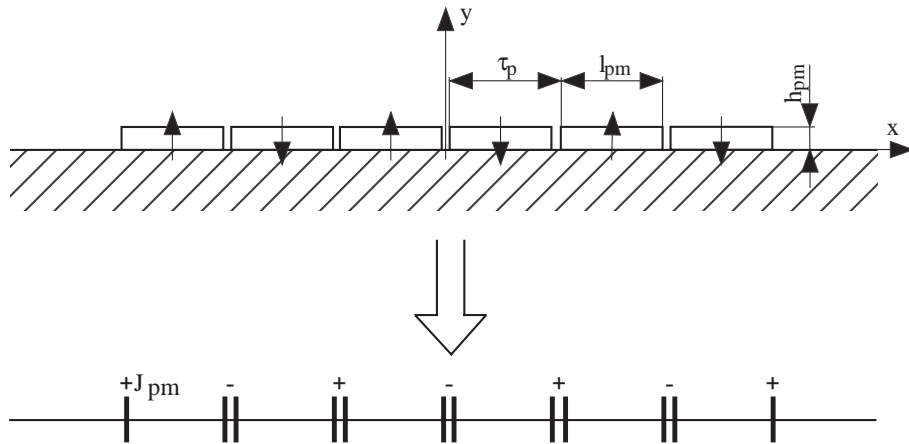


Figure 4.6: Six PM magnetic way model.

For motors with a long stroke, i.e. with a high number of PM, it is recommended to model only a part of the MaW, typically six PM, and to shift the function of the flux density above the two middle PM in order to obtain the flux density along the whole MaW.

Generally, the motor should not travel above the last magnets of each end, in order to not disturb the propulsion force due to the end effect. Nevertheless, if some constraints on the motor volume are very restrictive, the motor must be able to work above the last magnets of each end. With the presented analytical model (4.14), the end effects can be taken into account with a good accuracy, which is an advantage compared to conventional approach using Fourier series. Furthermore, additional comparisons were performed for different parameters of the MaW, validating the presented analytical model.

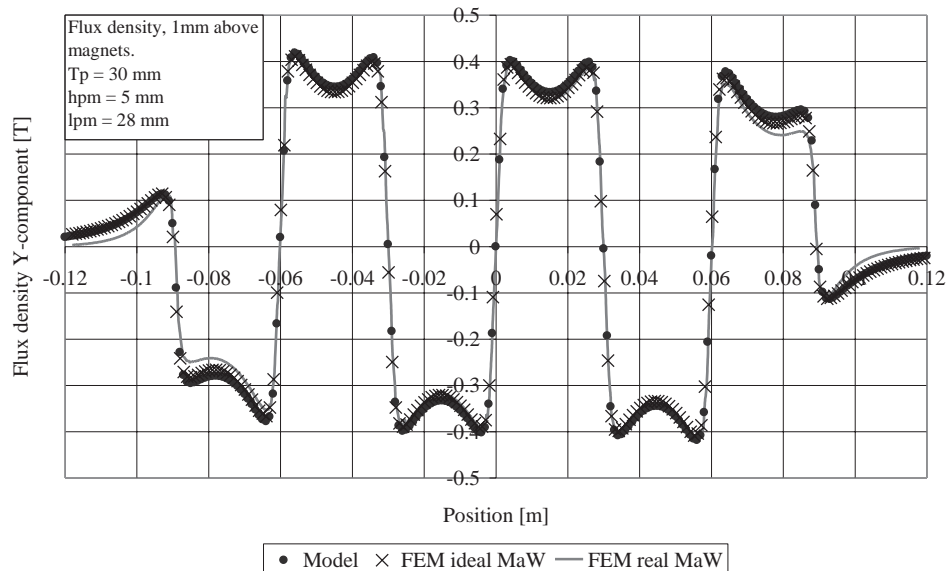


Figure 4.7: y-component of the flux density 1 mm above a 6 PM magnetic way. Comparison between the analytical model (full circles) and FEM simulation; ideal MaW (crosses), real MaW (full line).

To avoid the use of the sum in (4.14) each time when the flux density in the coordinate (x,y) must be calculated, the flux density can be developed in Fourier series. The goal is to replace the useful part

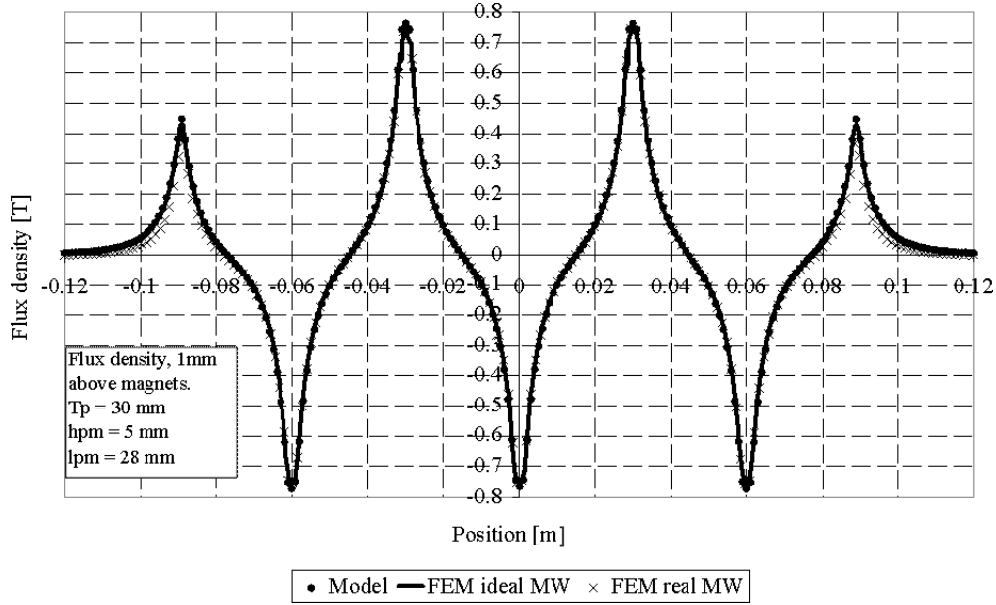


Figure 4.8: x-component of the flux density 1 mm above a 6 PM magnetic way. Comparison between the analytical model (full circles) and an ideal MaW FEM simulation (line).

of the MaW by a Fourier series of a well known function. Three wave forms for the flux densities are analyzed in order to find the best approximation; a square form, a pulsed form and a trapeze form (see Appendix A). A good approximation is obtained using the fundamental of a pulsed form function, as presented on Fig. 4.9. The amplitude \hat{B}_y for the pulsed function is equal to:

$$\hat{B}_y = \frac{(A_{(x,y)} - A_{(x+\tau_p,y)}) \cdot w_{pm}}{l_{pm}}, \quad (4.15)$$

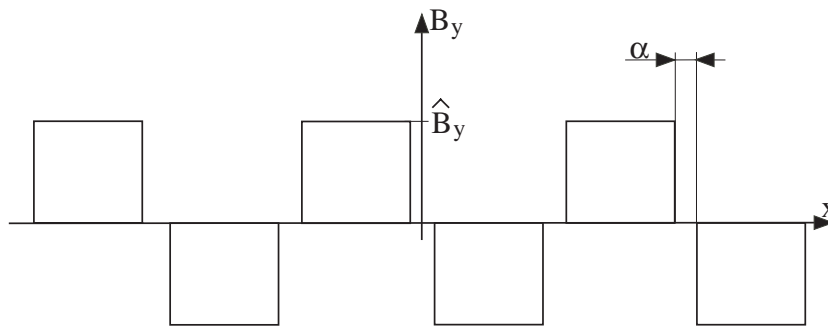


Figure 4.9: Flux density approximation of a MaW using a constant amplitude in the air. α is defined by (4.16)

The angle α in (A.6) corresponds, in edeg, to the distance between two consecutive magnets and is given by:

$$\alpha = \frac{\tau_p - l_{pm}}{2} \cdot \frac{\pi}{\tau_p}. \quad (4.16)$$

Then, the pulsed form can be decomposed with a Fourier serie and its first harmonic can be used in order to design the motor. The comparison between the analytical model (4.14) decomposed in a Fourier

serie, the approximation by a pulsed form and a FEM simulation called real MaW is given in tables 4.1, 4.2 and 4.3 for different configurations . For all presented results, the magnet height is $h_{pm} = 5$ mm, the distance between two consecutive magnets is $\tau_p - l_{pm} = 2$ mm and the pole pitch varies in relation to the studied cases as given in the table caption.

Table 4.1: Harmonics comparison, $\tau_p = 30$ mm, 1mm above the magnet surface.

Harmonic order	Analytical model	Real MaW	Approximative function
1	0.452	0.435	0.456
3	0.173	0.168	0.146
5	0.0793	0.0776	0.08
7	0.0395	0.0388	0.048
9	0.0196	0.0195	0.03

Table 4.2: Harmonics comparison, $\tau_p = 30$ mm, 5mm above the magnet surface.

Harmonic order	Analytical model	Real MaW	Approximative function
1	0.297	0.284	0.27
3	0.048	0.046	0.086
5	0.0093	0.0089	0.0478
7	0.0017	0.0013	0.029

Table 4.3: Harmonics comparison, $\tau_p = 15$ mm, 1mm above the magnet surface.

Harmonic order	Analytical model	Real MaW	Approximative function
1	0.54	0.52	0.513
3	0.11	0.108	0.141
5	0.0265	0.0253	0.052

Consequently, two models for the single magnetic way with mounted PM are given. The first model is very precise and consists to model the magnet with point currents(4.13). This approach requires a high number of calculations to define the flux density in a point (x,y) situated above the magnet surface. Therefore, it is time consuming and increases the complexity during an optimization. To avoid this problem, while maintaining a good approximation, a second model based on Fourier series has been developed. The amplitude of the flux density to decompose in series is given using the flux flowing through a magnet. This faster solution will be privileged for a motor pre-design since in this approach the calculation time is more significant than the accuracy.

The problem of under-harmonics caused by the MaW ends and specific to linear motors can also be analyzed with the proposed models. Indeed, the amplitude resulting of a decomposition in a Fourier series of the y-component of the flux density obtained for a 6PMs MaW (decomposition of the flux density given on Fig. 4.7) is shown on Fig. 4.10. The fundamental of the useful part of the MaW is equivalent to the harmonic 4. The under-harmonics have a relatively low level compared to the fundamentals especially for a high number of magnets. Therefore, they can be neglected.

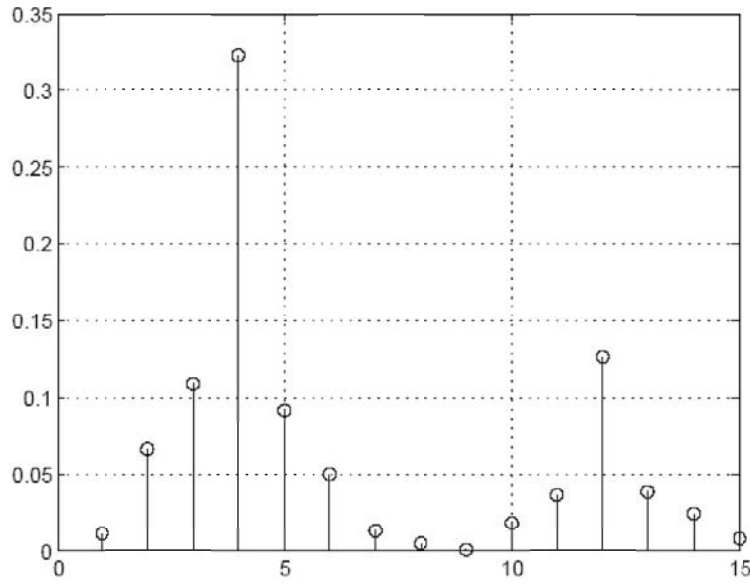


Figure 4.10: Harmonic analysis of the flux density of a 6PM magnetic way. $\nu = 4$ corresponds to the fundamental of the useful part of the MaW.

4.2.4 Single Sided Magnetic Way with Opposite Yoke

Compared to the previous example of the magnetic way, this structure has a yoke in front of the magnets (Fig. 4.11).

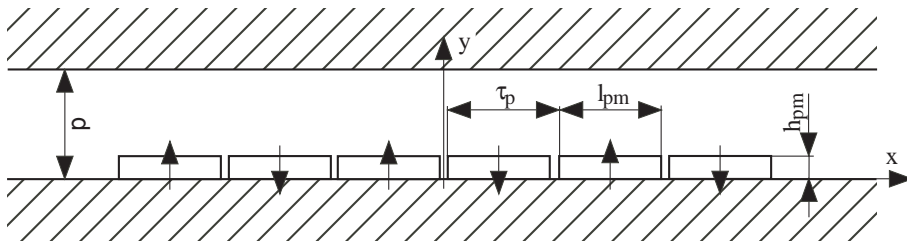


Figure 4.11: 6 PM magnetic way with an infinite opposite yoke.

In this model, the magnet cannot be replaced by a current density because of the complexity to integrate (4.6) and (4.7). Therefore, the magnets must be replaced by a sum of point sources, as shown on Fig. 4.12.

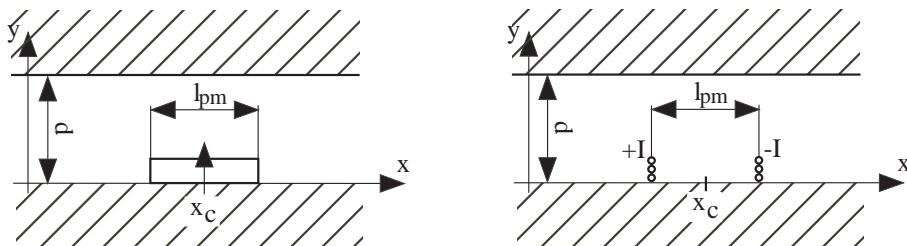


Figure 4.12: Model of a magnet situated between two infinite ideal iron plates, with a number of point currents $N_y = 3$.

Using (4.6) and (4.7), with the current I equal to:

$$I = \frac{B_r}{\mu_0} \cdot \frac{h_{pm}}{N_y}, \quad (4.17)$$

the components of flux density created by a magnet are determined as follows:

$$B_{x \ 1pm \ 2p(x,y,x_c,pos)} = \sum_{i=0}^{N_y-1} \left(B_{x \ I \ 2p} \left(x, y, x_c - l_{pm}, \frac{h_{pm} + 2h_{pm} \cdot i}{2N_y} + pos \cdot (d - h_{pm}) \right) - B_{x \ I \ 2p} \left(x, y, x_c + l_{pm}, \frac{h_{pm} + 2h_{pm} \cdot i}{2N_y} + pos \cdot (d - h_{pm}) \right) \right), \quad (4.18)$$

$$B_{y \ 1pm \ 2p(x,y,x_c,pos)} = \sum_{i=0}^{N_y-1} \left(B_{y \ I \ 2p} \left(x, y, x_c - l_{pm}, \frac{h_{pm} + 2h_{pm} \cdot i}{2N_y} + pos \cdot (d - h_{pm}) \right) - B_{y \ I \ 2p} \left(x, y, x_c + l_{pm}, \frac{h_{pm} + 2h_{pm} \cdot i}{2N_y} + pos \cdot (d - h_{pm}) \right) \right), \quad (4.19)$$

with pos being equal to 0 if the magnet is stuck on the lower plate and equal to 1 if the magnet is stuck on the upper plate.

Simulations with several PM heights and pole pitches have been made to define an ideal number of point currents permitting a good evaluation of the flux density and a low calculation time. As a result, a number of $N_{pc} = h_{pm}/3 \cdot 10^{-3}$ is adopted as being a good compromise.

By analogy to (4.14), the analytical model of a magnetic way with a number of magnets N_{pm} is given by:

$$B_{x \ N_{pm}}(x, y) = \sum_{i=0}^{N_{pm}} (-1)^{i+1} B_{x \ 1pm \ 2p}(x, y, x_i, 0), \quad (4.20)$$

$$B_{y \ N_{pm}}(x, y) = \sum_{i=0}^{N_{pm}} (-1)^{i+1} B_{y \ 1pm \ 2p}(x, y, x_i, 0), \quad (4.21)$$

$$\text{with } x_i = -\frac{N_{pm} - 1}{2} \tau_p + i \cdot \tau_p. \quad (4.22)$$

The comparison with a FEM program showing the good accuracy of the model is presented on Fig. 4.13.

In order to reduce the calculation time, two approaches are presented. The first one is to model the flux density using Fourier transformations of a function presented in Appendix A. As for the single magnetic way, the Fourier transformation of the pulsed form is better adapted to model the MaW. The amplitude is calculated using (4.15).

The second approach is to use directly the pulsed form, Fig. 4.9, to model the y component of the flux density and to determine the amplitude \hat{A} by applying the Ampere's law (2.19):

$$\hat{B}_y = \frac{B_r \cdot h_{pm}}{d \cdot \mu_{r \ pm} - h_{pm} (\mu_{r \ pm} - 1)}, \quad (4.23)$$

B_r and $\mu_{r \ pm}$ are the PM characteristics.

This approach is only valid when the flux leakage path length is shorter than two times the linkage flux path length (Fig. 4.14). Therefore, the following inequation must be satisfied:

$$d \leq \frac{\pi}{2} \left(\epsilon \cdot l_{pm} + \frac{\tau_p - l_{pm}}{2} \right) + h_{pm}. \quad (4.24)$$

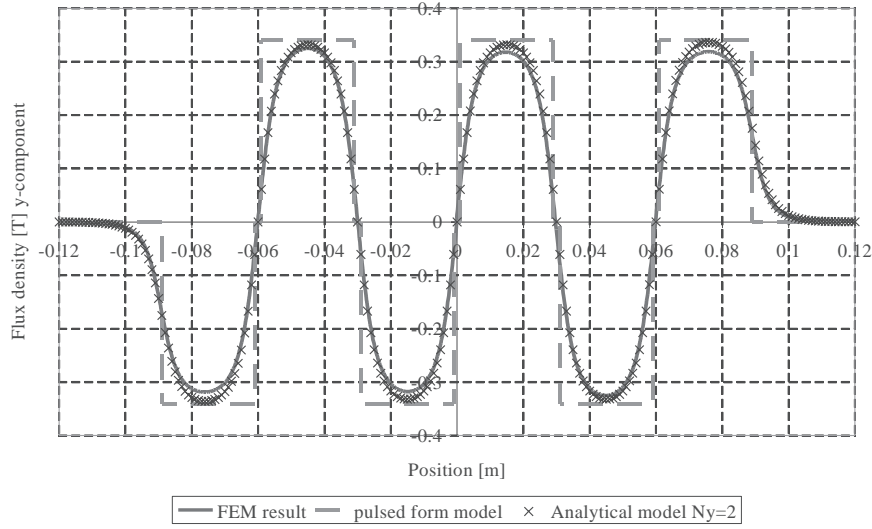


Figure 4.13: Comparison of the flux density in the middle of the air gap $(d-h_{pm})/2$ ($d = 14 \cdot 10^{-3}$, $h_{pm} = 4 \cdot 10^{-3}$ and $\tau_p = 30 \cdot 10^{-3}$).

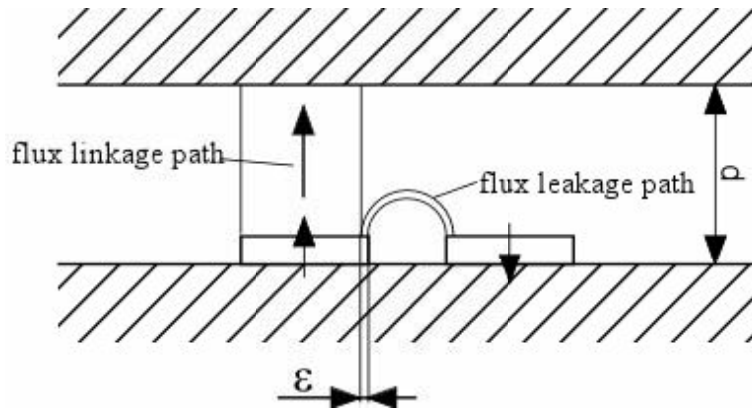


Figure 4.14: Leakage between two consecutive magnets.

Furthermore, by assuming $\mu_{r\ pm} = 1$ and by introducing a leakage factor σ_f taking into account the flux coupling between two consecutive PMs, the following expression is obtained:

$$\hat{B}_y = B_r \cdot \frac{1}{\frac{d-h_{pm}}{h_{pm}} + \sigma_f} \quad (4.25)$$

σ_f is given for several air gap heights in [11]. It varies from 1 to about 1.08 for an air gap height from 0.2 to 3 mm, respectively.

Three different analysis are presented to valid the models. The two first cases are done with a magnet height of $h_{pm} = 5$ mm, and an air gap of $d = 10$ mm, whereas the last case is with a magnet height $h_{pm} = 2$ mm and an air gap of $d = 5$ mm. The distance between two consecutive magnets is $\tau_p - l_{pm} = 2$ mm with a pole pitch varying following the cases as given in the table captions. These comparisons are made using Fourier series. For this reason the approximation with a constant amplitude of the flux density along the magnet length cannot be compared using this approach.

Table 4.4: Harmonics comparison 1mm above the magnet surface, $\tau_p = 30$ mm and $d = 10$ mm.

Harmonic order	Analytical model	Real MaW	Approximative function
1	0.483	0.469	0.487
3	0.163	0.164	0.155
5	0.074	0.078	0.085
7	0.0344	0.0395	0.052
9	0.0152	0.0198	0.032

Table 4.5: Harmonics comparison 5mm above the magnet surface, $\tau_p = 30$ mm and $d = 10$ mm.

Harmonic order	Analytical model	Real MaW	Approximative function
1	0.372	0.362	0.337
3	0.0475	0.0485	0.107
5	0.0083	0.0097	0.058

Table 4.6: Harmonics comparison 2.5mm above the magnet surface, $\tau_p = 20$ mm and $d = 5$ mm.

Harmonic order	Analytical model	Real MaW	Approximative function
1	0.398	0.386	0.377
3	0.064	0.065	0.113
5	0.0133	0.015	0.054

As for the single sided magnetic way, the Fourier transformation is a good solution to build a simple and precise model.

The yoke height is calculated with the Ampere's law (2.19) and the flux conservation (2.11) by assuming that the magnet mmf is much higher than the coil mmf. Therefore, the result to calculate the height of the yoke is calculated as:

$$h_{yoke} = \frac{B_r \cdot l_{pm} \cdot h_{pm}}{B_{yoke} (\mu_{r\ pm} (d - h_{pm}) + h_{pm})}. \quad (4.26)$$

B_{yoke} is the flux density in the yoke. This value must be chosen in order not to over saturate the yoke. Typically, the value is situated in the knee of the iron saturation curve.

For a motor pre-design, the relation (4.23) is privileged for its simple implementation. For a more precise design, the relation (4.22) gives better results.

4.2.5 Double Sided Magnetic Ways

The results obtained with the single sided MaW with opposite yoke can be used to investigate a double sided magnetic way (Fig.1.4). Therefore, magnets are modelled by a sum of N_y point currents distributed along the magnet height h_{pm} , as presented on Fig. 4.15.

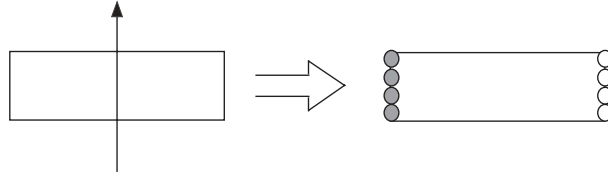


Figure 4.15: Distance between two consecutive point source to model the magnet.

The flux densities for a double sided magnetic way are equal to:

$$B_{x N_{pm}}(x, y) = \sum_{i=0}^{N_{pm}} B_{x1pm\ 2p}(x, y, x_i, 0) + \sum_{i=0}^{N_{pm}} B_{x1pm\ 2p}(x, y, x_i, 1) \quad (4.27)$$

$$B_{y N_{pm}}(x, y) = \sum_{i=0}^{N_{pm}} B_{y1pm\ 2p}(x, y, x_i, 0) + \sum_{i=0}^{N_{pm}} B_{y1pm\ 2p}(x, y, x_i, 1) \quad (4.28)$$

The height of the yoke is calculated with a lumped magnetic scheme and is equal to:

$$h_{yoke} = \frac{2 \cdot B_r \cdot l_{pm} \cdot h_{pm}}{B_{yoke} (\mu_{r\ pm} (d - 2h_{pm}) + 2h_{pm})}. \quad (4.29)$$

The difference between the analytical model of the flux density in the y-direction and the FEM program is represented on Fig. 4.16 with a distance between the two plates $d = 10$ mm, a magnets height of $h_{pm} = 4$ mm and a pole pitch $\tau_p = 30$ mm.

As for the previous magnetic way, the y-component of the flux density can be modelled by a pulsed form (Fig. 4.9) with an amplitude equal to:

$$\hat{B}_y = \frac{2 \cdot B_r \cdot h_{pm}}{d \cdot \mu_{r\ pm} - 2 \cdot h_{pm} (\mu_{r\ pm} - 1)}. \quad (4.30)$$

4.2.6 Halbach Array

Halbach array (HA) has the particularity to enhance the flux on one side (strong side) and to weaken the flux on the other side (weak side). In contrast with others MaW, Halbach array does not need a yoke to close the flux path between two magnets. This implies a reduction of the MaW weight [46]. Halbach array can also be either double sided or single sided (Fig. 1.4). The former is used with no ferromagnetic material and coils often travel between the two magnet arrays. Therefore (4.9), (4.10), (4.11) and (4.12) can be used to define the flux density in the air produced by a lineic current. The later, can be used with a toothless or a toothed motor. In these cases, the theory of images must be used.

Here, only the model of a single sided MaW in the air is given (Fig. 4.17), in order to give the methodology to model a HA. The approach consists to replace all the magnets by their equivalent current density, parallel to their magnetization direction.

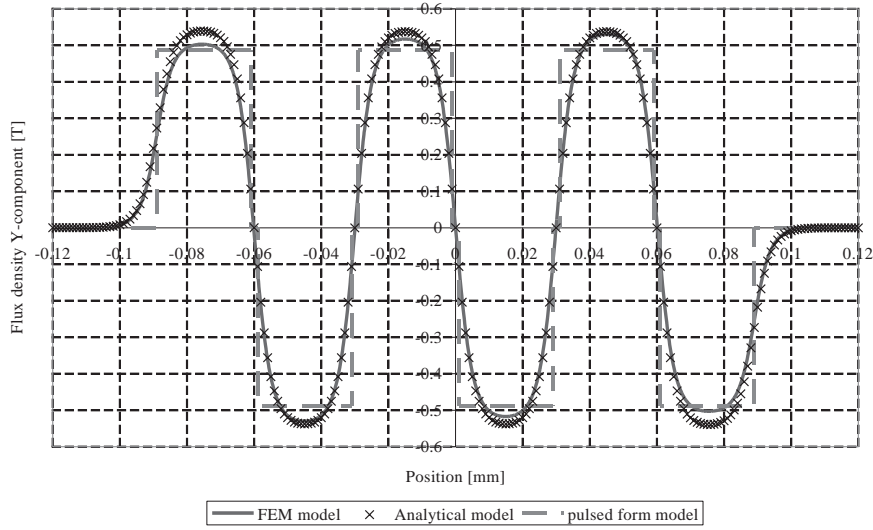


Figure 4.16: Comparison of the flux density on the air gap at the distance $d/2$.

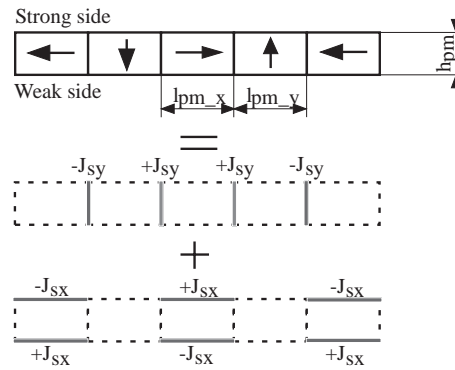


Figure 4.17: Methodology to model a 5 PM Halbach array.

Therefore, the analytical model for the x-component and the y-component of the flux density of a HA with five PM are given by:

$$\begin{aligned}
 B_{x \text{ HA}} = & -B_x J_s M_y(x, y, -l_{pm_y} - 0.5 \cdot l_{pm_x}, 0) + B_x J_s M_y(x, y, -0.5 \cdot l_{pm_x}, 0) + B_x J_s M_y(x, y, +0.5 \cdot l_{pm_x}, 0) \\
 & - B_x J_s M_y(x, y, +l_{pm_y} + 0.5 \cdot l_{pm_x}, 0) + B_x J_s M_x(x, y, -l_{pm_y} - 1.5 \cdot l_{pm_x}, 0) - B_x J_s M_x(x, y, -0.5 \cdot l_{pm_x}, 0) \\
 & + B_x J_s M_x(x, y, 0.5 \cdot l_{pm_x} + l_{pm_y}, 0) - B_x J_s M_x(x, y, -l_{pm_y} - 1.5 \cdot l_{pm_x}, h_{pm}) + B_x J_s M_x(x, y, -0.5 \cdot l_{pm_x}, h_{pm}) \\
 & - B_x J_s M_x(x, y, 0.5 \cdot l_{pm_x} + l_{pm_y}, h_{pm}),
 \end{aligned} \quad (4.31)$$

$$\begin{aligned}
 B_{y \text{ HA}} = & -B_y J_s M_y(x, y, -l_{pm_y} - 0.5 \cdot l_{pm_x}, 0) + B_y J_s M_y(x, y, -0.5 \cdot l_{pm_x}, 0) + B_y J_s M_y(x, y, +0.5 \cdot l_{pm_x}, 0) \\
 & - B_y J_s M_y(x, y, +l_{pm_y} + 0.5 \cdot l_{pm_x}, 0) + B_y J_s M_x(x, y, -l_{pm_y} - 1.5 \cdot l_{pm_x}, 0) - B_y J_s M_x(x, y, -0.5 \cdot l_{pm_x}, 0) \\
 & + B_y J_s M_x(x, y, 0.5 \cdot l_{pm_x} + l_{pm_y}, 0) - B_y J_s M_x(x, y, -l_{pm_y} - 1.5 \cdot l_{pm_x}, h_{pm}) + B_y J_s M_x(x, y, -0.5 \cdot l_{pm_x}, h_{pm}) \\
 & - B_y J_s M_x(x, y, 0.5 \cdot l_{pm_x} + l_{pm_y}, h_{pm}).
 \end{aligned} \quad (4.32)$$

The flux density distribution obtained with a FEM program is given on Fig. 4.18.

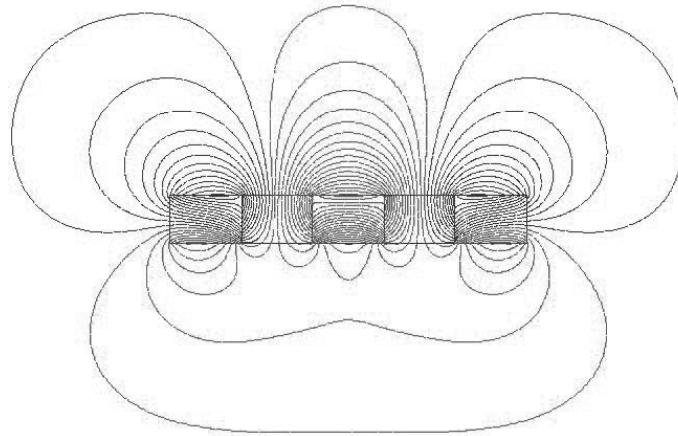


Figure 4.18: Flux distribution for a 5 PM Halbach array.

The comparison between the analytical model and the FEM program is shown on Fig. 4.19 for the strong side and on Fig. 4.20 for the weak side. The comparisons are made in a distance of 1 mm above magnets.

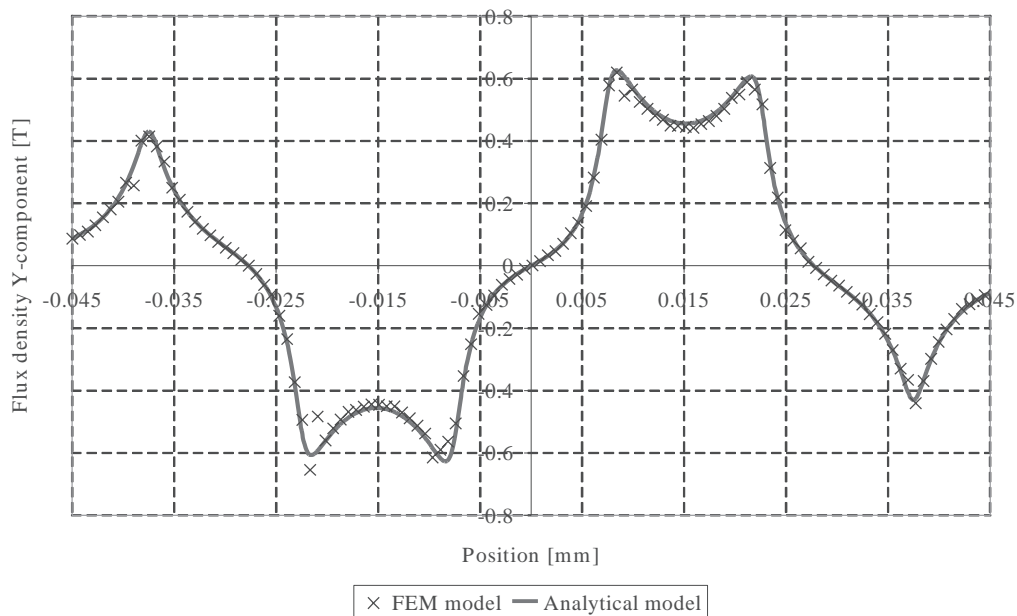


Figure 4.19: Flux density (1mm above PM) comparison between the analytical model and the FEM program for the strong side of a HA ($h_{pm} = 8 \cdot 10^{-3}$, $l_{pmx} = l_{pmy} = 15 \cdot 10^{-3}$).

These figures show that the agreement between both methods is very good.

Depending on both magnet lengths l_{pmx} and l_{pmy} , the form of the flux density can vary from a sine form to a square form. Therefore, in order to keep a rather good precision, it is decided not to develop a simplify model based on Fourier transformation.

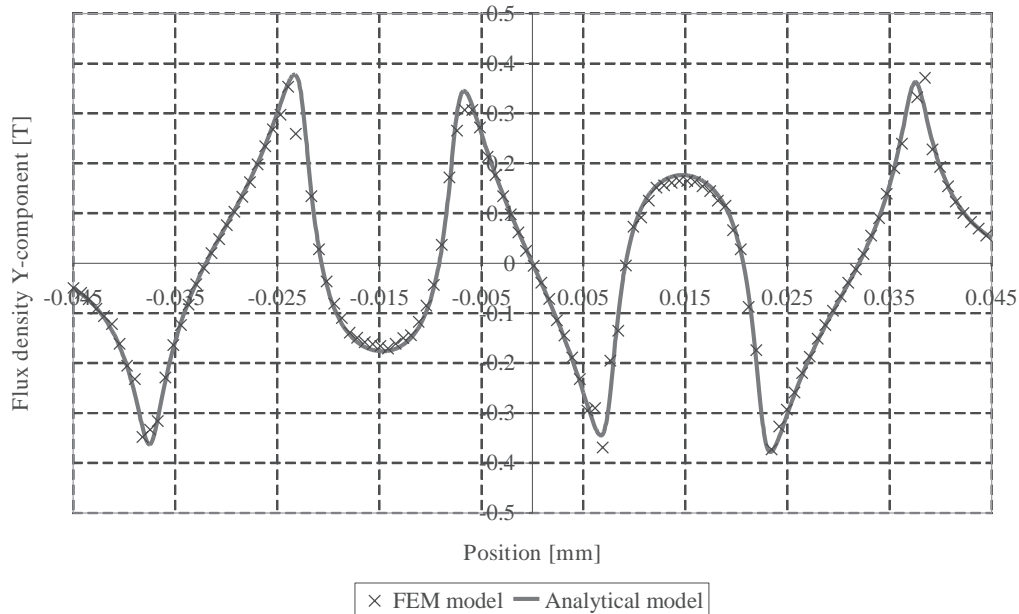


Figure 4.20: Flux density (1mm under PM) comparison between the analytical model and the FEM program for the weak side of a HA ($h_{pm} = 8 \cdot 10^{-3}$, $l_{pmx} = l_{pmy} = 15 \cdot 10^{-3}$).

4.2.7 Conclusion

In general, two analytical models are proposed to modelize a MaW. The first one, based on the sum of point currents, is a very accurate one, but complex. In order to perform a much efficient optimization in term of calculation time, an alternative model is generally proposed. It consists in using the Fourier transformation or in modelling the flux density with a simple form such as pulsed or square form (as introduce in Appendix A. This last simplification gives only good results with a double sided MaW or with a single sided MaW with opposite yoke.

To summarize this section, all the formulas used to model a MaW are listed in Table 4.7 for the accurate model and the simplified model(s).

Table 4.7: Equations used to model the MaW.

	B_y Accurate model	B_y Simplified (Fourier)	B_y Simplified (Pulsed form)	B_x Accurate model
Single sided MaW with mounted PM	(1.13),(1.14)	(1.13),(1.14) (A.6)	—	(1.9),(1.14)
Single sided MaW with opposite yoke	(1.19),(1.21)	(1.15),(1.16) (A.6)	(1.23) (A.6)	(1.18),(1.20)
Double sided MaW	(1.19),(1.27)	(1.15),(1.16) (A.6)	(1.29) (A.6)	(1.18),(1.26)
Halbach array	(1.29)	—	—	(1.28)

4.3 Winding Configurations and Models

There are not numerous scientific papers related to motor windings and more particularly to linear motor winding; therefore, the goal of this chapter is to give a method as general as possible to define windings [47, 48, 49].

4.3.1 Winding Factors

Each winding is characterized by its winding factor ${}^{\nu}k_w$. It consists of three relative coefficients: the pitch factor ${}^{\nu}k_s$, the distribution factor of the coils ${}^{\nu}k_z$ and the skewing factor ${}^{\nu}k_{sk}$. A fourth factor is introduced in the thesis, the distribution factor of the turns ${}^{\nu}k_{zc}$, which is used in some particular cases (toothless and ironless motors). It can be added or included in the distribution factor of the coils k_z . All these factors depend on the harmonic number ν related to the pole pitch. Geometrical parameters of a coil, useful to define the winding, are given on Fig. 4.21. Other characteristics defining a coil are: its height h_{coil} which does not influence the active surface, the number of turns per coil N , the diameter of the wire d_{cu} and the copper filling factor k_{cu} .

For all motor designs, it is assumed that the straight part of the coil is equal to the magnet width w_{pm} .

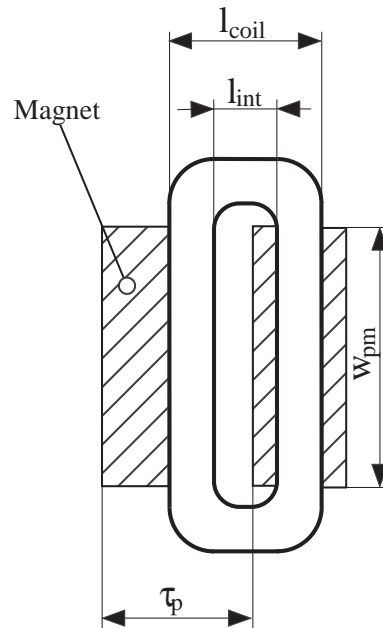


Figure 4.21: Coil sizes: l_{coil} is the length of the coil, l_{int} is the length of the intern turn and w_{pm} is the active part width of the coil.

These winding factors are related to the flux produced by the PM and crossing the winding. They are obtained by comparison with a coil having a coil opening equal to one pole pitch.

The first step is to find the emf for one conductor travelling at the speed v above a sinusoidal flux density distribution. The emf will be also sinusoidal and it is equal to:

$${}^{\nu}emf_{cond} = {}^{\nu} B \cdot w_{pm} \cdot v. \quad (4.33)$$

ν is the harmonic number of the Fourier series of the flux density B .

Thereafter, the emf of two conductors connected in series and separated by a pole pitch can be calculated as:

$${}^{\nu}emf_{turn} = 2 \cdot {}^{\nu}emf_{cond} \quad (4.34)$$

since each conductor is in front of the same flux density amplitude. Now, if the two conductors are separated by a coil opening s smaller than one pole pitch (Fig. 4.22), the induced voltage in (4.34) must be corrected by the pitch factor ${}^{\nu}k_s$ equal to:

$${}^{\nu}k_s = \left| \sin \left(\nu \frac{s}{\tau_p} \frac{\pi}{2} \right) \right|, \quad (4.35)$$

with s the distance, taken in the middle of a slot, separating the forward conductor of the return conductor. Although, all the turns of a coil have not the same length, the assumption that the two conductors of a turn are separated by a distance s can be made, since all turns are connected in series.

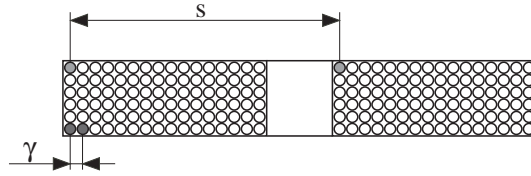


Figure 4.22: Shifted value γ between two consecutive turns with a coil opening s .

$$s = \begin{cases} \frac{l_{coil}}{2} + \frac{l_{int}}{2} & : \text{ for a toothless motor} \\ \tau_n & : \text{ for a toothed motor} \end{cases} \quad (4.36)$$

Furthermore, if the coil is composed of several turns as illustrated on Fig. 4.22, two consecutive turns are separated by a shift value γ . This value produces a shift difference between the induced voltages generated in the wires. The distribution factor of the turns ${}^{\nu}k_{zc}$ permits, in particular cases, to take into account this phase difference. This factor depends on the harmonic number ν and it is equal to:

$${}^{\nu}k_{zc} = \frac{\sin \left(\frac{\nu N_x \gamma \cdot \pi}{2\tau_p} \right)}{N_x \sin \left(\frac{\nu \gamma \cdot \pi}{2\tau_p} \right)}. \quad (4.37)$$

N_x is the number of wires in the x-direction ($N_x = 16$ for the case presented on Fig. 4.22).

In some cases, a same phase has several coils separated by a length γ_c as shown on Fig. 4.23.

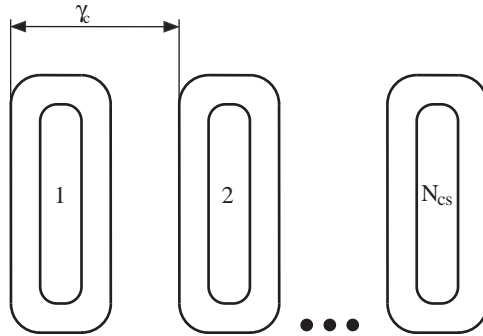


Figure 4.23: Phase difference γ_c between N_{cs} coils of the same phase in serie.

If γ_c is not a multiple of τ_p , a phase difference appears between these coils. Therefore, the induced voltage of the coils belonging to the same phase can only be vectorially summed. The distribution factor of the coils ${}^\nu k_z$ allows to consider this aspect. This factor is, by analogy to (4.38), equal to [50]:

$${}^\nu k_z = \frac{\sin\left(\frac{\nu N_{cs} \gamma_c}{2}\right)}{N_{cs} \sin\left(\frac{\nu \gamma_c}{2}\right)}. \quad (4.38)$$

N_{cs} is the number of coils in series and ν an odd number.

The cogging force can be minimized in some applications by skewing either the PM or the stator teeth by an angle α , as shown on Fig. 4.24. As a result, the flux linkage and hence the back emf are altered. The skewing factor ${}^\nu k_{sk}$ takes this effect into account [51]. It is given by:

$${}^\nu k_{sk} = \frac{\sin\left(\frac{\nu \cdot \alpha}{2}\right)}{\frac{\nu \cdot \alpha}{2}}. \quad (4.39)$$

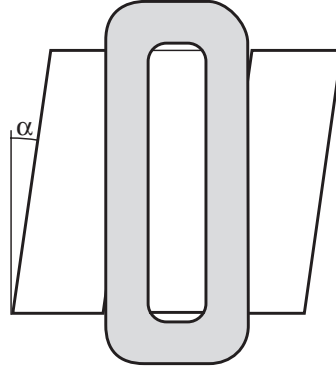


Figure 4.24: MaW skewed by an angle α .

Therefore, by introducing (4.35), (4.37), (4.38) and (4.39) into (4.34) the induced voltage of a coil becomes:

$${}^\nu emf_{coil} = \sum_N {}^\nu emf_{turn} \cdot {}^\nu k_s \cdot {}^\nu k_{zc} \cdot {}^\nu k_z \cdot {}^\nu k_{sk} = \sum_N {}^\nu emf_{turn} \cdot {}^\nu k_w. \quad (4.40)$$

The emf is proportional to the winding factor ${}^\nu k_w$. Its maximum value is equal to one and it is only reached in some particular cases as explained in the following chapters.

4.3.2 Winding Possibilities

Windings are divided in two groups: concentrated windings and distributed windings. To classify them, the number of slots N_s per pole per phase q is introduced:

$$q = \frac{N_s}{m \cdot N_p}. \quad (4.41)$$

In this approach, only three phase windings ($m = 3$) are analyzed which implies a number of slots multiple of 3. Furthermore, linear motors can have an odd number of N_p poles, contrary to rotative motors where the number of poles must be even ($2p$).

These two constraints, $N_s = k \cdot m$ and N_p integer, are the two entrances of a table which defines all the winding possibilities. The table of all feasible configurations can be obtained by following several steps, as it is presented in this section.

If the condition:

$$\frac{N_s}{m \cdot \text{GCD}(N_s, N_p)} = k, \quad k \text{ integer}, \quad (4.42)$$

is satisfied, where GCD is the highest common divisor, a m phases winding can be built for this combination of N_p and N_s . The number of slots is defined by analogy to a rotative motor.

This first step permits to build a table containing all the possible windings. For example, Table 4.8 gives all possibilities for $N_p \leq 4$ and $k \leq 4$.

Table 4.8: Three phases winding possibilities, generated in relation with (4.42).

$N_p \backslash N_s$	3	6	9	12	...
1	✓	✓	✓	✓	...
2	✓	✓	✓	✓	...
3	×	×	✓	×	...
4	✓	✓	✓	✓	...
⋮	⋮	⋮	⋮	⋮	...

Before going further on, the geometry of a toothed motor is introduced. The supply part is composed of a stack of magnetic laminations with a number of slots N_s and number of teeth N_t , generally equal to:

$$N_t = N_s \pm 1. \quad (4.43)$$

The dimensions of the supply part are given on Fig. 4.25.

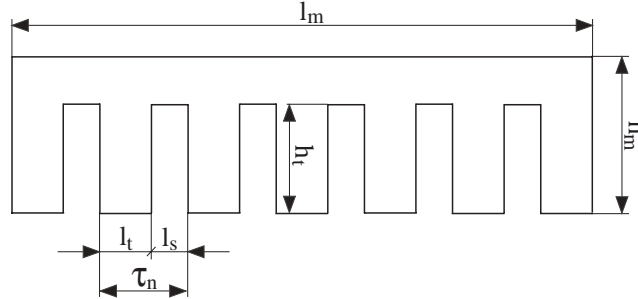


Figure 4.25: Geometrical parameters of the supply part.

As mentioned previously, q permits to classify windings in two groups. To define its minimum value several assumptions are made. It is supposed that the tooth length and the slot length are equal and that the tooth length is smaller than the pole pitch. Therefore, the minimum number of slots per pole per phase must be higher than:

$$q > \frac{1}{2 \cdot m} \quad (4.44)$$

implying:

$$N_s > N_p/2. \quad (4.45)$$

This approach of finding all the combinations of N_p and N_s suitable for a three phase winding is summarized in a schematic scheme shown on Fig.4.26.

Thereafter, winding configurations are separated in two groups [52]:

1. concentrated, i.e. non-overlapping, windings;

2. distributed, i.e. overlapping, windings.

Motors with a concentrated winding have $q \leq 0.5$, implying a distance between two consecutive teeth equal or higher than 120 electrical degree (edeg). Nevertheless, a winding with a $q > 0.5$ can also be mounted with concentrated coils, but the winding factor 1k_w will not be higher than 0.866, generating a low force density.

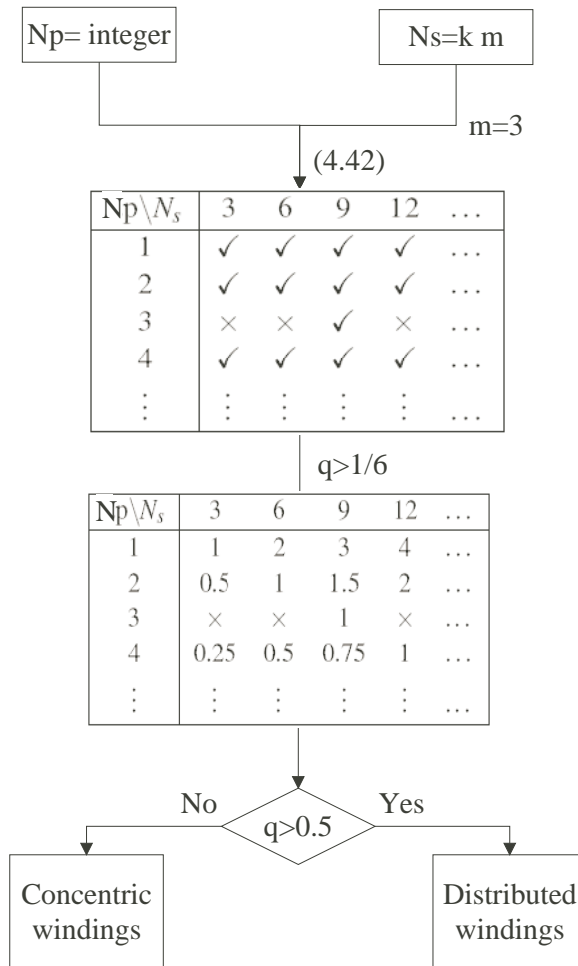


Figure 4.26: Schematic of all the combinations of N_s and N_p occurring to a feasible three phase winding.

These two winding possibilities, concentrated and distributed, are presented in more details in the following sections.

The number of slots and poles has also an impact on the cogging force [53] as presented in Section 4.3.3 and on the copper losses, Section 4.3.4.

4.3.2.1 Concentrated Windings

To maximize the efficiency of the motor and to reduce the copper losses, it is advantageous to have short end-windings. Therefore, non-overlapping windings are often used when possible ($q \leq 0.5$). Concentrated windings in linear motors is a good solution since no additional teeth are needed to perform a symmetric winding, as it is sometimes the case for distributed windings (see Section 4.3.2.2). To define a winding, the number of layers is important since for the same number of slots and poles, different

windings are feasible. For a single-layer concentrated winding (Fig. 4.27), only alternate teeth carry a coil (one coil per slot) and for a double-layer concentrated winding (Fig. 4.28) all teeth are surrounded with a coil (two coils per slot).

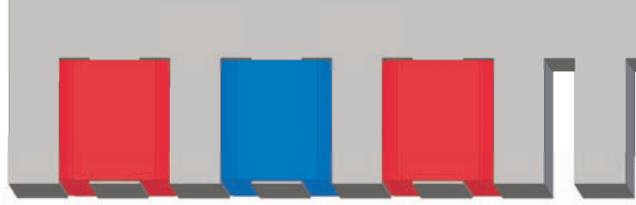


Figure 4.27: Single-layer concentrated winding.

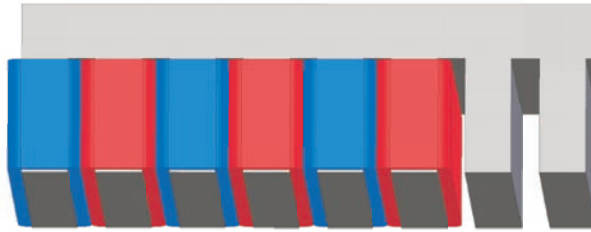


Figure 4.28: Double-layer concentrated winding.

To characterize these windings, winding factors are calculated. The pitch factor (4.35) is straightforward to evaluate if all tooth lengths are the same since the coil opening s is equal to:

$$s = \frac{N_p}{N_s} \cdot \tau_p = \tau_n \quad (4.46)$$

During a pre design process, s can always be assumed equal to τ_n . The distribution factor k_{zc} (4.37) can be taken into account depending on the coil length.

For the calculation of the distribution factor, the two cases (single layer and double layer) are analyzed separately.

Single-layer concentrated winding

The single layer concentrated winding imposes an even number of slots. For a three phase single layer concentrated winding the number of coils per phase N_{cp} is equal to:

$$N_{cp} = \frac{N_s}{2 \cdot 3}. \quad (4.47)$$

The first winding configuration consists to place N_{cp} adjacent coils, on alternate teeth. Coils of the other phases are shifted by a multiple ($\neq 3$) of 60 edeg. This winding configuration does not always lead to the better solution since it does not take into account a possible symmetry of the winding, i.e. the number of motor sectors (As introduced in Section 1.4). Therefore, to find the number of coils of the same phase to mount in series N_{cs} , the number of motor sectors which is equivalent to the number of symmetries in a rotative motor, must be found and it is equal to:

$$N_{sym} = GCD(N_{cp}, N_p). \quad (4.48)$$

Thereafter, the number of coils of the same phase mounted consecutively N_{cs} is:

$$N_{cs} = \frac{N_s}{2 \cdot 3 \cdot N_{sym}}. \quad (4.49)$$

This permits to estimate the distribution factor k_z . These N_{cs} coils must not be mounted in parallels, since a current circulation would appear between them. Therefore, the distribution factor for a given number of slots and poles can be calculated as follows:

$${}^\nu k_z = \frac{\sin\left(\frac{\nu \cdot N_{cs} \alpha_d}{2}\right)}{N_{cs} \sin\left(\frac{\nu \cdot \alpha_d}{2}\right)}, \quad (4.50)$$

with α_d the tooth pitch in electrical radian given by:

$$\alpha_d = 2 \frac{N_p \cdot \pi}{N_s}. \quad (4.51)$$

For different combinations of slot and pole numbers, Tables C.1 and C.2 in Appendix C give the winding factors for the first and the third harmonic.

Double-layer concentrated winding

In this configuration, the number of slots can be an odd number, implying more possibilities. The same approach as for a single layer can be followed. The number of coils per phase N_{cp} is, for this configuration, equal to:

$$N_{cp} = \frac{N_s}{3}. \quad (4.52)$$

Substituting (4.52) in (4.48), the number of motor sectors, equal by analogy to the number of symmetries N_{sym} , can be found. Therefore, N_{cs} becomes:

$$N_{cs} = \frac{N_s}{3 \cdot N_{sym}} \quad (4.53)$$

and the distribution factor is obtained using (4.50) with

$$\alpha_d = \frac{N_p \cdot \pi}{N_s} \pm k \cdot \pi, \quad k = 0, 1, \quad (4.54)$$

located between $-\pi/3$ and $\pi/3$. Tables C.3 and C.4 in Appendix give the winding factors for the first and the third harmonic, for various combinations of slots and poles.

4.3.2.2 Distributed Windings

These windings, characterized by a number of poles per slot and per phase q higher than 0.5 are used for large motors. For linear motors, these windings lead sometimes to an asymmetric distribution of the coils. This phenomenon is illustrated on Fig. 4.29 [13] for which some slots are not totally filled with copper.

In linear motors, the distributed winding is not often used and therefore only the winding construction principle and calculation are introduced. Therefore, motors with such a winding are not analyzed in the thesis.

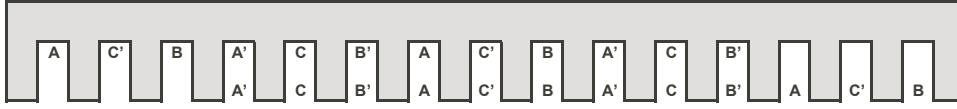


Figure 4.29: Full pitch distributed winding, $m = 3$, $q = 1$ and $N_p = 5$ [13].

Distributed windings can have q integer or fractional. These two cases are discussed separately.

q integer number

The distribution factor of the turns ${}^\nu k_z$ can be defined in relation with q , since q is the number of coils in series under one pole pitch. The other coils of the same phase are shifted by a value which is a multiple of τ_p . Therefore, ${}^\nu k_z$ is calculated as:

$${}^\nu k_z = \frac{\sin\left(\frac{\nu\pi}{2m}\right)}{q \sin\left(\frac{\nu\pi}{2mq}\right)}. \quad (4.55)$$

As for concentrated winding, slots with one and two layers are analyzed to determine the pitch factor ${}^\nu k_s$. Windings with one layer can only be obtained with N_s even and a shortening of the coil length is not possible. On the other hand, for a two layer winding a shortening is possible. The distance between two consecutive slots τ_n is equal to:

$$\tau_n = \frac{N_p \cdot \tau_p}{N_s}. \quad (4.56)$$

The number of possibilities to make a shortening are higher with a high value of q . The coil shortening cs , in number of slots, will fix the length of s as follows:

$$s = \begin{cases} \tau_p & : \text{single layer winding} \\ \tau_p - cs \cdot \tau_n & : \text{double layer winding} \end{cases}. \quad (4.57)$$

Therefore, the pitch factor is calculated using (4.35) and (4.57).

The shortening is also used to reduce the impact of parasitic harmonics on the induced voltage. To eliminate the harmonic ν the following relation is used [50]:

$$s = \frac{\nu - 1}{\nu} \tau_p. \quad (4.58)$$

Hence, s cannot take all values, this equation must be coupled with (4.57) which is possible only under the following condition:

$$\frac{1}{\nu} \cdot \frac{N_s}{N_p} = \text{Integer} \quad (4.59)$$

If this relation is not fulfilled the harmonic ν cannot be **totally** suppressed.

q fractional number

The use of q fractional was introduced to reduce the harmonics on the induced voltage. To evaluate the pitch factor, the same approach as for q integer is used. This factor depends also on the coil shortening.

On the other hand, the distribution factor is calculated as follows [54]:

$${}^{\nu}k_z = \frac{\sin\left(\frac{\nu\pi}{2m}\right)}{\gamma \cdot \sin\left(\frac{\nu\pi}{2m\gamma}\right)}. \quad (4.60)$$

With γ the numerator of the fraction $q = \gamma/\beta$. Furthermore, γ and β must not have a same common divisor.

4.3.3 Impact on the Cogging Force

For toothed motors the choice of N_p and N_s has a direct impact on the cogging force. The number of cogging periods for one pole translation is given by a fractional part of the least common multiple (LCM) of the pole and slot number

$$k_{cogg} = \frac{LCM(N_p, N_s)}{N_p}. \quad (4.61)$$

k_{cogg} is introduced to denote the goodness of slot and pole number combination from the point of view of cogging force. There is no direct relation between k_{cogg} and the amplitude of the cogging force although it has been found that the smaller the factor k_{cogg} the larger will be the cogging force [55]. Table 4.9 gives k_{cogg} for several combinations of teeth and poles. The bold values on the diagonal of the table separate distributed and concentrated windings.

Table 4.9: k_{cogg} for several combinations of teeth and poles, it corresponds to the number of periods of the cogging force per pole.

$N_p \backslash N_s$	3	6	9	12	15	18	21	24	...
2	3	3	9	3	15	9	21	12	...
3			3			6			...
4	3	3	9	3	15	9	21	6	...
5	3	6	9	12	3	18	21	24	...
6			3			3			...
7		6	9	12	15	18	3	24	...
8		3	9	3	15	9	21	3	...
9									...
10		3	9	6	3	9	21	12	...
11		6	9	12	15	18	21	24	...
12			3			3			...
13			9	12	15	18	21	24	...
14			9	6	15	9	3	12	...
15			3			6			...
16			9	3	15	9	21	3	...
⋮	⋮	⋮	⋮	⋮	⋮	⋮	⋮	⋮	...

In addition to the tooth ripple component of cogging force, linear motors exhibit a significant cogging force amplitude owing to the finite length of the stator, of which is not the case in rotative machines. The impact of these end effects are not taken into account in this analysis. This part of the cogging force has one period per pole and introduces therefore a low cogging harmonic to the cogging force harmonic created by the interaction of the tooth and the magnets.

The minimization of the cogging force due to the end effect is discussed in Section 4.4.5. For values higher than $k_{cogg} = 6$ the main part of the cogging force is due to the end effect and for a redesign the impact of the cogging force due to the interaction of the tooth and the magnets can be neglected.

4.3.4 Impact on the Copper Losses

The volume of copper and therefore the Joule losses depend on the winding type. They are equal to:

$$P_{cu} = \int_{V_{cu}} \rho \cdot J^2 dV = \rho \cdot J^2 \cdot V_{cu}. \quad (4.62)$$

To compare the copper losses produced by two motor windings, a figure of merit F_{cu} is introduced. By assuming that the motors to compare have the same MaW dimensions (i.e. same pole pitch and same PM dimensions), the same force per active surface. Moreover, if F_{cu} is related to a pole pitch, in order not to be influenced by the motor length, this factor is equal to:

$$F_{cu} = \frac{N_s k_w^2 \cdot k_{cu} \cdot S_{slot}}{N_p l_{mean}}. \quad (4.63)$$

S_{slot} is the slot area, N_s is the number of slots and l_{mean} is the average wire length for one turn. It is equal to:

$$l_{mean} = 2 \cdot w_{pm} + 2 \cdot l_{int} + 2(l_{coil} - l_{int}). \quad (4.64)$$

The filling factor depends on the winding configuration. Typical values used in the thesis are given in Table 4.10.

Table 4.10: Filling factors depending on the winding type.

	k_{cu}
Concentrated winding (1 layer)	0.6
Concentrated winding (2 layers)	0.55
Distributed winding	0.35÷(0.7)

The filling factors are higher for the concentrated windings than for the distributed. For this winding, the filling factor can vary from 0.35 to 0.7 following the motor power. For a distributed winding a filling factor close to 0.35 is more adapted in regard to the studied motor. The higher filling factor for concentrated winding is due to the possibility to manufacture the coils outside the motor for concentrated windings. Nowadays, the tendency is to press the coils into the slots in order to reach a high winding factor [56].

The slot length is a multiple of k , $k < 1$, of the tooth pitch τ_n given by (4.56). Furthermore, by assuming a same slot height for all motors the slot area becomes proportional to:

$$S_{slot} \sim k \cdot \tau_n = \frac{k \cdot \tau_p \cdot N_p}{N_s}. \quad (4.65)$$

By introducing (4.65) into (4.63) the figure of merit for the copper losses becomes equal to

$$F_{cu} = \frac{k_w^2 \cdot k_{cu}}{l_{mean}}. \quad (4.66)$$

A high factor means few losses. In this relation, the importance of the winding factor is shown since copper losses are proportional to the winding factor square. Figure 4.30 shows as an example a copper

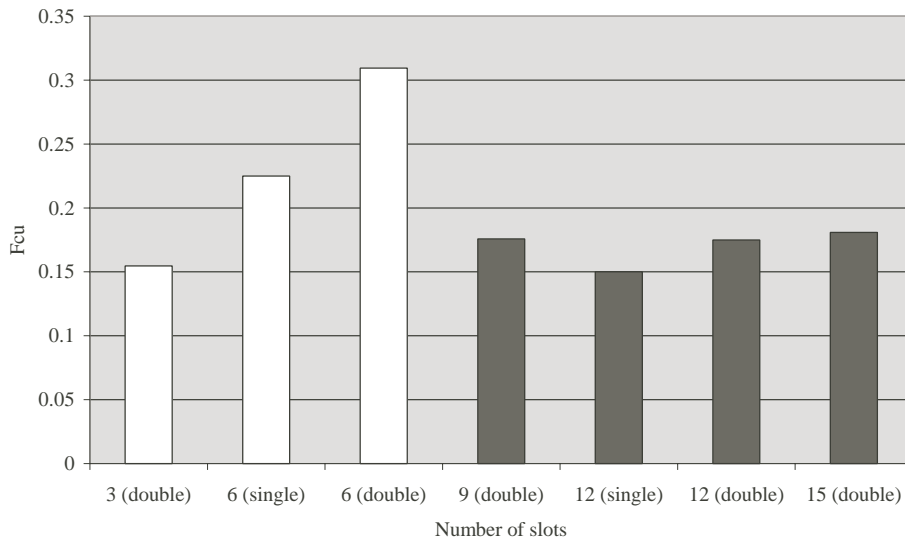


Figure 4.30: Copper losses figures of merit for $N_p = 4$. Distributed windings are presented with dark plain bars, white plain bars are for concentrated windings.

losses comparison between different number of slots for a given number of poles $N_p = 4$. The tooth length is assumed equal to the half tooth pitch and the PM width is the same for all cases. The winding factors for distributed windings are assumed equal to 0.35.

This factor will have an influence on the choice of the number of slots. Nevertheless it is advised to compare the windings with the same technology, concentrated or distributed.

4.3.5 Impact on the Attractive Force Distribution

The attractive force due to the motor winding has more importance in rotative motors than in linear motors. However, this impact is introduced in order to present a complete approach about windings. The winding creates an AC component of the attractive force, while the PMs create a DC component of the attractive force.

In rotative motors, the DC attractive forces produced by each magnet are compensated by symmetry. Therefore, if the motor is not supplied and the rotor is centered, no forces acts on it. This is a non resting position. However, if the coils of a same phase are not uniformly distributed along the circumference, unbalanced radial forces and magnetic noise appear when the motor is supplied [57]. Consequently, this effect is less pronounced for higher number of symmetries (better with even symmetries). The number of symmetries is obtained using (4.48). For example, a motor with a number of slots $N_s=27$ and a number of poles $N_p=26$ has no symmetries ($N_{sym}=1$), implying that all coils of the same phase are distributed along one third of the air gap circumference. This results in a high unbalanced radial force when the motor is supplied.

The unbalanced radial forces introduced for rotative motors becomes pulsed attractive forces in linear motors. These pulsed forces, due to the motor supply, are less disturbing for the guidance system since linear motors have a high attractive force due to the PMs. In the case of a double sided motor, where the resulting attractive force is compensated, these pulsed forces can disturb the system if the motor is not centered.

These AC component of the attractive force due to a supplied winding can produce vibration or audible noise.

4.3.6 Winding Constraints Leading to Winding Choice

The first constraint for windings has been introduced in Section 4.3.2 and it fixes a lower value of $q < 1/2m$. The new constraints are illustrated in Fig. 4.31 which is the extension of the Fig. 4.26.

The second constraint depends on the fundamental of the winding factor 1k_w . A low winding factor means, for a given propulsion force, high power losses (4.66). Therefore, this value is limited to a minimum value $^1k_w \text{ limit}$, generally equal to 0.866. Hence, all combinations of slot number and poles with a winding factor:

$$^1k_w < ^1k_w \text{ limit} \quad (4.67)$$

are eliminated. The levels of the harmonic distortion can also be limited. This value is defined as:

$$THD = \frac{\sqrt{\sum_{\nu=2}^{\infty} (\nu k_w)^2}}{^1k_w} \quad (4.68)$$

A third limitation, which is due to the motor specifications, is applied on the number of poles N_p . Indeed, to reduce the iron losses, the frequency supply part is bounded with a maximum value f_{max} . Therefore, for a specified maximum speed v_{max} for the mover, a minimum pole pitch length is given as being equal to:

$$\tau_p \text{ min} = \frac{v_{max}}{2 \cdot f_{max}} \quad (4.69)$$

Thereafter, if the motor length cannot be longer than a maximum value $l_{m \text{ max}}$ or shorter than a minimum value $l_{m \text{ min}}$, the range of the number of poles N_p is defined by¹:

$$\text{floor}^* \left(\frac{l_{m \text{ min}}}{\tau_p \text{ max}} \right) \leq N_p \leq \text{ceil}^{**} \left(\frac{l_{m \text{ max}}}{\tau_p \text{ min}} \right) \quad (4.70)$$

4.3.7 Winding Choice - Discussion

The first choice in motor design concerning motor winding is often the number of poles N_p which is fixed in regards with the supply frequency (4.70) and the propulsion force. Once a range of N_p is defined, the various possibilities for the number of slots is given using the condition (4.42). Afterward, the combinations of N_s and N_p for which a low winding factor occurs, are eliminated (4.67). These three first steps lead to a limited winding possibilities.

The next step is to choose a winding type: concentrated non overlapping winding or distributed overlapping winding. This choice is imposed either by manufacturing reasons or by geometrical reasons, but also by the aid of merit factors introduced in Sections 4.3.3 to 4.3.5.

A winding type can be chosen regarding geometrical constraints. This approach can be used as a systematic analysis. For motors with a low number of poles compared to the motor length it is more interesting to use a distributed winding in order to have a better distribution of the conductors along the supply part. On the contrary, for small motors with a high number of poles N_p , a distributed winding will need a lot of slots which can result in a small tooth pitch and therefore to increase manufacturing complexity.

Therefore, the choice of a winding can be summarized by the following points:

1. range possibilities for the number of poles;
2. choice of the possibilities for the number of slots according to the tooth pitch/height;

¹* rounds the elements between brackets to the nearest integers towards minus infinity. ^{**} rounds the elements between brackets to the nearest integers towards infinity.

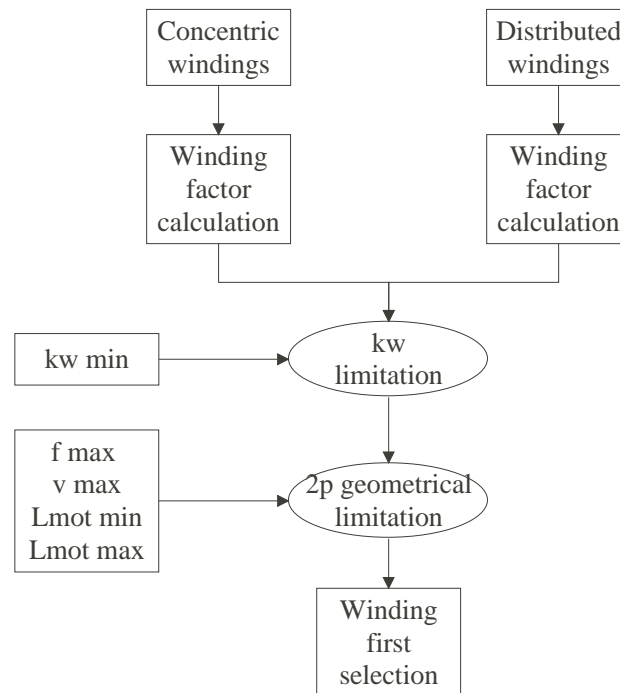


Figure 4.31: Constraints for the choice of winding.

3. application of the winding factor constraint (typically $^1k_w > 0.866$);
4. choice of the winding type: concentrated or distributed.
5. comparative study based on the cogging force, the copper losses, iron losses;
6. final choice of N_p and N_s .

Furthermore, concentrated windings have the particularity to produce a mmf with more harmonics in the air gap. These harmonics will produce additional iron losses. This aspect is discussed in the Section 4.5 for toothed motors.

4.4 Toothless Linear Motor

The analytical model of a toothless linear motor depends on the motor type and especially on the MaW type. Several motor structures are introduced as examples on Fig. 4.32. Once the motor topology defined, the suitable MaW model is applied (Section 4.2). Thereafter, electrical characteristics, i.e. the winding (Section 4.4.1) and the supply command (Section 4.4.4) must be chosen. The motor model is then build by regrouping the analytical models of these four parts. Finally, other constraints are added to the motor model in order to take into account external influences, as for instance a thermal model or some mechanical constraints, leading to a multi physical model.

Several assumptions are made for the analytical models:

1. the relative permeability of the iron parts are considered as infinite;
2. the relative permeability of PM is equal to 1;
3. the considered iron plates which maintain the PM of the MaW are infinite;

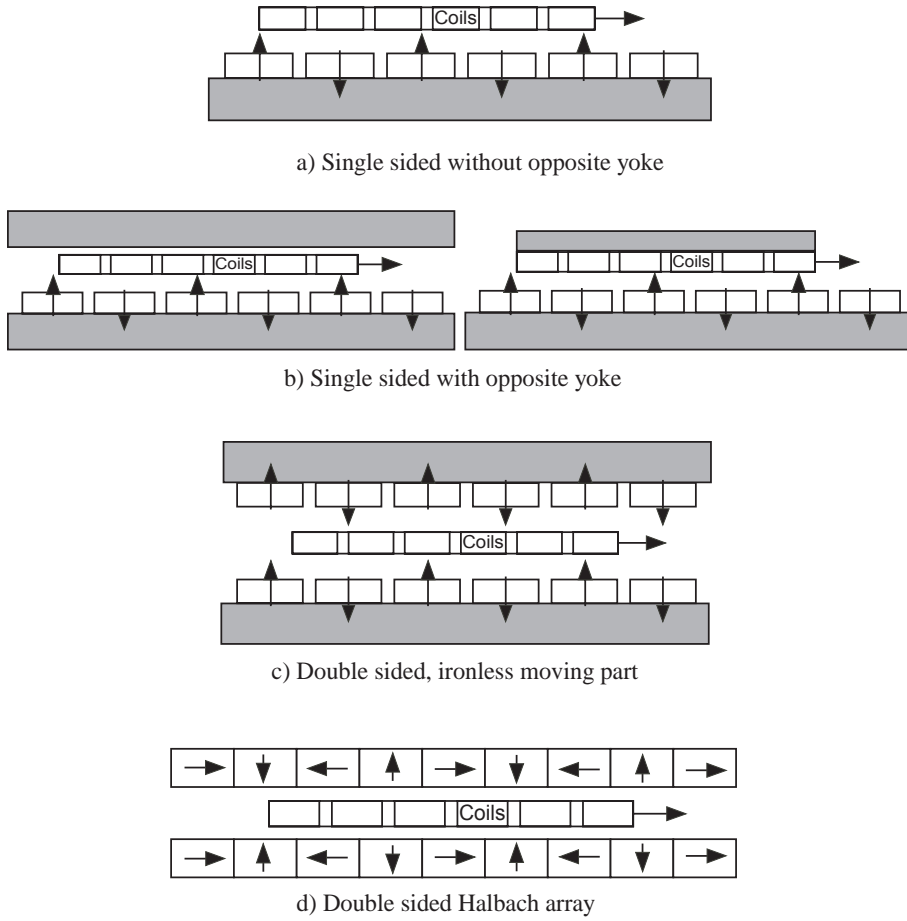


Figure 4.32: Several toothless motor topologies.

- forces due to the end windings are neglected, i.e. only the copper part of a coil above a magnet produces a force.

The magnetic models are not dependent on the motor topology ShS or LS. The difference between these two topologies occurs in calculation of motor efficiency, motor thermal behavior, cost estimation, etc. , but not in the magnetic models.

4.4.1 Winding Possibilities

Only concentric windings are studied in this thesis since they are the most widespread in the industry. This comes from the possibility to perform the coils outside the motor making them therefore easy to manufacture. Nevertheless, the presented methodology to design toothless motors is also valid for other windings such as Gramme's or distributed overlapping windings in the air gap. Windings of toothless motors are assumed to be double layers. These motors do not have skewed PM and therefore the skewed factor νk_{sk} is equal to 1. Since the coil length l_{coil} can be higher than one pole pitch, the distribution factor of the turns νk_{zc} is taken into account. The only factor which is not dependent on the number of coils per turns and the inner length of the coil is the distribution factor k_z given in Table 4.11 for different combinations of coils number (equivalent to the number of slots, since the winding is considered as a double layer) and pole number.

Table 4.11: Fundamental distribution factor 1k_z for toothless motors.

$N_p \backslash N_{coil}$	3	6	9	12
1				
2	1			
3				
4	1	1		
5	1	0.966		
6			1	
7		0.966	0.844	
8		1	0.960	1
9				
10		1	0.960	0.966
11		0.966	0.844	0.958
12			1	
13				0.958
14				0.966

As shown in table, there is only three winding configurations with a distributed factor equal to 1. These windings, studied more in detail in this section, consist of three juxtaposed coils, which form a motor segment (Section 1.4). These three winding configurations in relation to the coil length l_{coil} are:

1. $N_{coil} = 3, N_p = 2 : \frac{\tau_p}{3}(60 \text{ edeg}) < l_{coil} \leq \frac{2\tau_p}{3}(120 \text{ edeg})$;
2. $N_{coil} = 3, N_p = 4 : \frac{2\tau_p}{3}(120 \text{ edeg}) < l_{coil} \leq \frac{4\tau_p}{3}(240 \text{ edeg})$;
3. $N_{coil} = 3, N_p = 5 : \frac{4\tau_p}{3}(240 \text{ edeg}) < l_{coil} \leq \frac{5\tau_p}{3}(300 \text{ edeg})$.

The configurations show that the coil opening varies between 60 edeg and 300 edeg. In general, the coil opening can vary between 0 and 360 edeg. The other solutions are not studied since they are less interesting. Indeed, a coil length higher than 360 edeg is not a good solution because a part of the force produced by the coil is cancelled by itself. For a coil length varying between 300 edeg and 360 edeg some areas without wires appear between two consecutive coils in order to keep a multiple of 120 edeg between two phases. This produces a lower force per surface unit. On the contrary, a coil length smaller than $\tau_p/3$ generates very low force and therefore is not taken into consideration (low winding factor).

To avoid areas without wires, toothless motors are often designed with a coil length equal to or near the upper value of the three possible ranges, i.e. a coil opening of 120 edeg, 240 edeg or 300 edeg.

The three winding configurations with their wound direction and their phases succession are presented on Fig. 4.33.

Other interesting windings with several juxtaposed coils of the same phase are introduced in Section 4.4.5.

The pitch factor (4.35) is calculated with a coil opening s equal to:

$$s = \frac{l_{coil}}{2} + \frac{l_{int}}{2}. \quad (4.71)$$

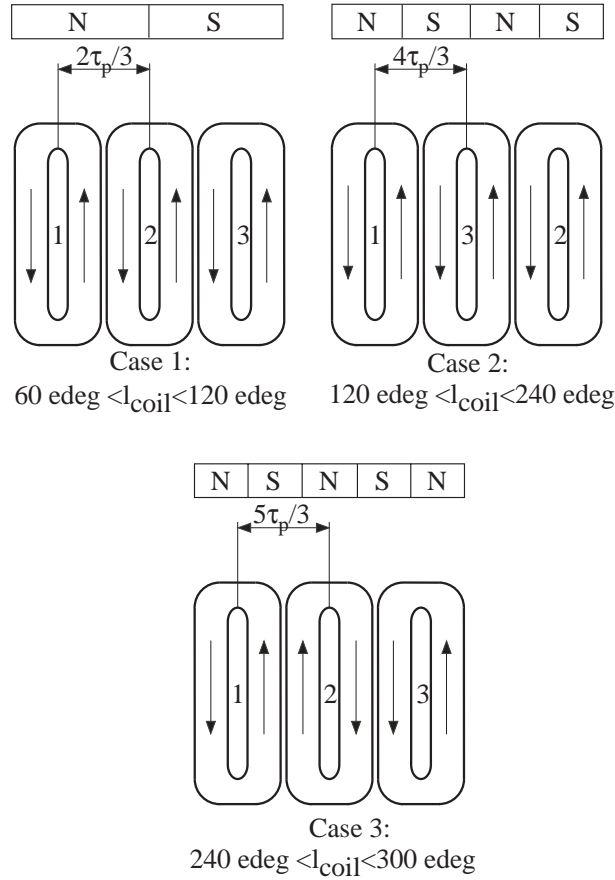


Figure 4.33: Three possibilities for toothless motors with concentric windings.

4.4.2 Model for the Induced Voltage Calculation

The induced voltage or emf is calculated using (2.16), which gives for a moving coil:

$$emf(x_c) = \sum_{i=1}^N v \cdot w_{pm} \cdot B(i, x_i, y_i). \quad (4.72)$$

Here, v is the speed of the coil, x_c is the position of the coil, N is the number of turns per coil and $B(i, x_i, y_i)$ is the flux density shown by the conductor i , situated in the position (x_i, y_i) . The flux density is given by the expressions developed in Section 4.2 which depend on the chosen MaW. In order to calculate the emf for a coil travelling at the speed v in a magnetic field, the flux density shown by each conductor must be calculated either by an approximate formula or by the accurate model of the MaW. By varying x_c for a distance equal to one pole pitch, the waveform of the induced voltage and its amplitude are determined. Generally, the number of turns per coil is not known during an optimization process and in order to be able to find the form of the induced voltage, a fictive number of turns per coil $N_f = N_x \cdot N_y$ is chosen arbitrary, in respect with a proportionality between the x-side (N_x) and the y-side (N_y) of the coil. With N_f , a fictive induced voltage emf_f is determined. Once the design is finalized and the real number of turns per coil is defined, the real induced voltage can be calculated as follows:

$$emf = emf_f \cdot \frac{N}{N_f}. \quad (4.73)$$

Alternative method, which is faster but less accurate consists to decompose the flux density produced by the magnetic way in Fourier series and to use winding factors. As presented in Section 4.3, the winding factor varies in relation with the harmonic number ν of the Fourier series. Therefore, the induced voltage is equal to:

$${}^{\nu}emf_{coil} = \sum_N {}^{\nu}emf_{turn} \cdot {}^{\nu}k_{zc} \cdot {}^{\nu}k_s. \tag{4.74}$$

This approach permits to simplify the model.

Comparison with FEM program for the two presented methods are given on Fig. 4.34. The corresponding coil dimensions are given in Table 4.12.

Table 4.12: Coil dimensions for comparison with the FEM.

Coil dimensions	MaW dimensions
$l_{coil} = 40 \cdot 10^{-3}$	Single sided MaW
$l_{int} = 4 \cdot 10^{-3}$	with opposite yoke
$h_{coil} = 8 \cdot 10^{-3}$	$\tau_p = 30 \cdot 10^{-3}$
$w_{pm} = 1$	$h_{pm} = 4 \cdot 10^{-3}$
$N_x = 18$	$l_{pm} = 28 \cdot 10^{-3}$
$N_y = 8$	$d = 14 \cdot 10^{-3}$

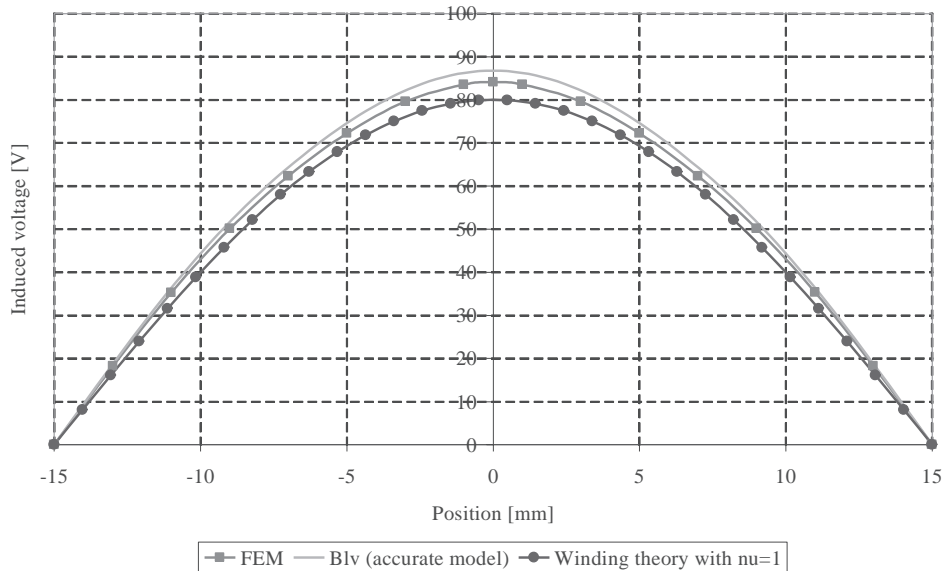


Figure 4.34: Comparison of calculated induced voltage between two methods and FEM analysis. Blv is related to (4.72).

The distribution factor ${}^{\nu}k_{zc}$ depends on the number of turns per coil contrary to the pitch factor ${}^{\nu}k_s$ which can be analyzed for the three winding configurations of the Fig. 4.33. Therefore, values ranges of the pitch factor for the first harmonic are given in Table 4.13 assuming the maximum length coil for each case and by varying the length l_{int} . Therefore, the coil opening s varies between $l_{coil\ max}/2$ and $l_{coil\ max}$. The analysis of the other harmonics is not presented since they change considerably with the coil opening s . This table shows that winding case with a coil length of 240 edeg is less dependent on l_{int} than other winding.

Table 4.13: Pitch factor range for the first harmonic of the induced voltage for the three presented windings

		Winding cases		
		$l_{coil\ max}$	$l_{coil\ max}$	$l_{coil\ max}$
		120 edeg	240 edeg	300 edeg
νk_s	$\nu = 1$	0.5 - 0.866	0.866 - 1	0.5 - 1

With this approach, it can be demonstrated that winding with a maximum coil length l_{coil} smaller than 60 edeg is not a good solution since the pitch factor varies between 0.258 and 0.5. A low value of the pitch factor means a low induced voltage, i.e. a low propulsion force. Therefore, for a given propulsion force a motor with a low winding factor needs a higher current density, which consequently increases the Joule losses.

4.4.3 Model for Inductances and Mutuals Determination

The magnetic flux passing through an area can be calculated by a line integral of the vector potential A along the boundary area c (2.12). In a two dimensional configuration [45], the flux passing through a coil is calculated as:

$$\phi = w_{pm} \cdot (A_1 - A_2), \quad (4.75)$$

where w_{pm} is the coil (magnet) width and A_1, A_2 are the potential vectors at the two points delimiting the coil, due to a current I flowing in it. This equation is valid if the cross section of the wire can be neglected. The inductance is found by dividing (4.75) by the current I . If the coil has a non-negligible section, the superposition principle can be applied (the iron is assumed ideal) to determine its inductance. It can be calculated from the average vector potential over each winding section, as:

$$L = w_{pm} \left[\frac{\sum_i A_i}{NI} - \frac{\sum_j A_j}{NI} \right], \quad (4.76)$$

A_i and A_j are the potential vectors resulting of all the other conductors of the coil (Fig. 4.35).

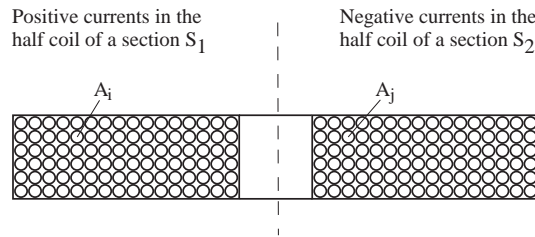


Figure 4.35: Definition for the calculation of the inductance.

A good approximation to calculate the inductance is to model the coil by a turn with its conductors placed in the middle of each areas S_1 and S_2 . Therefore, the inductance can be calculated as follows:

$$L = \frac{N^2}{I} w_{pm} \cdot (A_1 - A_2). \quad (4.77)$$

This equation can be also used to calculate the mutual inductances M_{ij} between the phase i and the phase j .

4.4.4 Force Determination

For toothless motor, the Laplace's equation (2.26) is used to calculate the forces produced by a supplied coil in a magnetic field. The propulsion force produced by one supplied coil is given by:

$$F_{x\ coil}(x_{coil}, i) = \int_{y_c=0}^{h_{coil}} \int_{x_c=x_{coil}-\frac{l_{coil}}{2}}^{x_{coil}+\frac{l_{coil}}{2}} B_y(x_c, y_c) \cdot I_i(x_c) \cdot dx_c dy_c. \quad (4.78)$$

Here, $I_i(x_c)$ is the current supply of the coil i situated in the position x_c (Fig. 4.36).

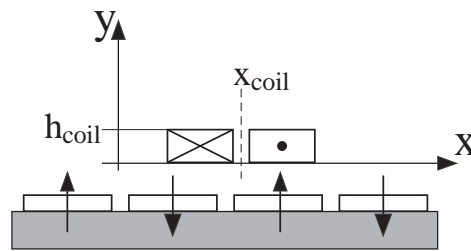


Figure 4.36: Coil position above a single sided magnetic way.

By varying x_{coil} from 0 to τ_p , the force shape and its peak value can be found. For a three phase motor with three coils, the total force can be calculated by shifting the coils in x direction as follows:

$$F_{x\ tot}(x) = \sum_{i=1}^3 F_{x\ coil} \left(x_{coil} + (i-1) \frac{2\tau_p}{3}, i \right). \quad (4.79)$$

This permits to determine the shape and the peak force of a toothless motor, depending on the current form (sinus, square or other) and the motor position x_{coil} . To achieve this result, the current according to the position must be given. The force generated by the coil in the-y direction (attractive or repulsive force) can be found by replacing the flux density $B_y(x_c, y_c)$ with the flux density in the x-direction $B_x(x_c, y_c)$.

For a first motor pre-design, the fundamental of Fourier series are used to reduce the complexity of the model. The goal is to approximate the current and the flux density by a Fourier series, as presented in Section 4.2 and to use them in (4.79). Two same harmonic orders of the current and the flux density produce a constant force independent of the coil position x_{coil} . In contrary, two different harmonic orders of the current and the flux density create a sinus pulsative force with a harmonic order equal to the difference of their harmonic number. This pulsative force has a mean value equal to zero. The total force is equal to the sum of all contributions. To perform a pre-design, the study of the fundamental is often enough. Therefore, as the force is independent of the position x of the motor, it can be determined in a particular position x , as for instance the position where the current in one phase reaches its peak value².

Another solution to calculate the force is based on the power $emf \cdot i$ produced by a supplied coil. This solution is not introduced here.

Figures 4.37 and 4.38 show the accuracy of the model for the propulsion force and the attractive force, respectively. These geometrical dimensions of the motor are the same as in Section 4.4.2. The courant waveform is assumed constant during 120 edeg with a current density equal to 2A/mm².

²The maximum force produced by a coil supplied with the peak current \hat{I} , occurs when the center of the coil is positioned at the middle distance between to consecutive magnets consisting of a MaW.

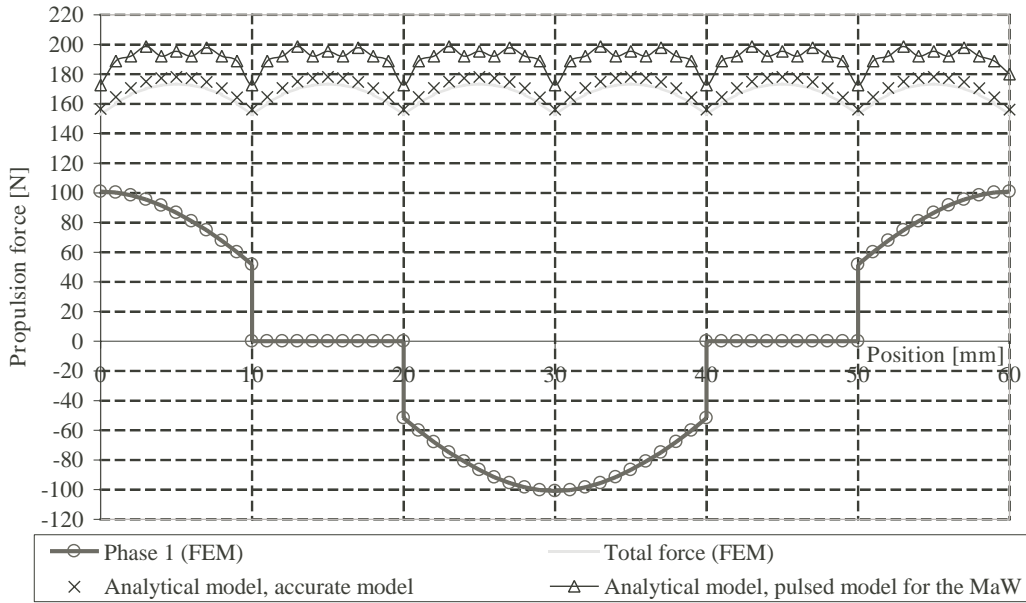


Figure 4.37: Propulsion force comparison between FEM and two analytical models (Using equivalent currents or a pulsed function to model the flux density).

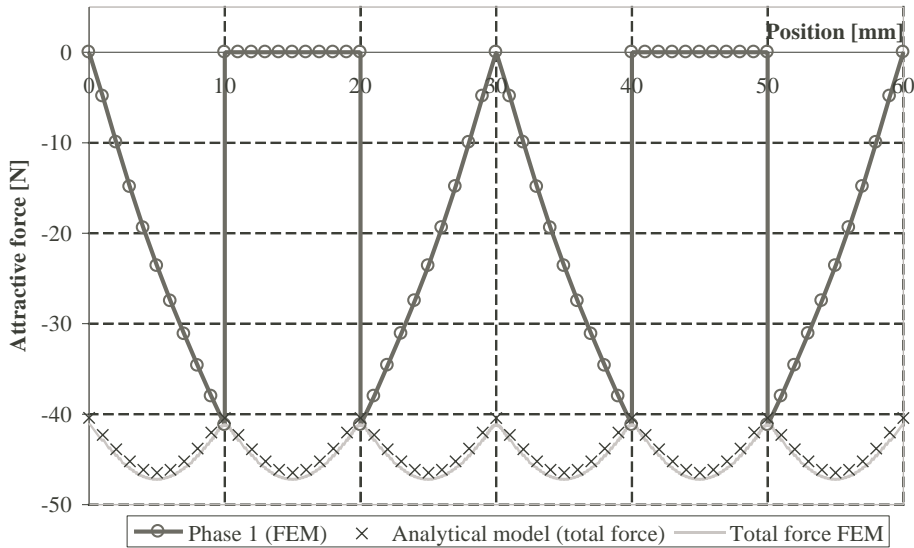


Figure 4.38: Attractive force as a function of the position. Comparison between FEM and the analytical model using equivalent current to model the flux density.

These graphs show the difference of accuracy between the two analytical models. When the flux density is modelled by a pulsed function, the total force calculation has a more pulsed form due to discontinuities of the flux density. Nevertheless, this model gives a sufficient precision for a motor pre-design.

4.4.5 Special Cases

In most cases, toothless motors do not have an attractive force and a cogging force when they are not supplied. Nevertheless, some configurations presented on Fig. 4.39 have these particularities.

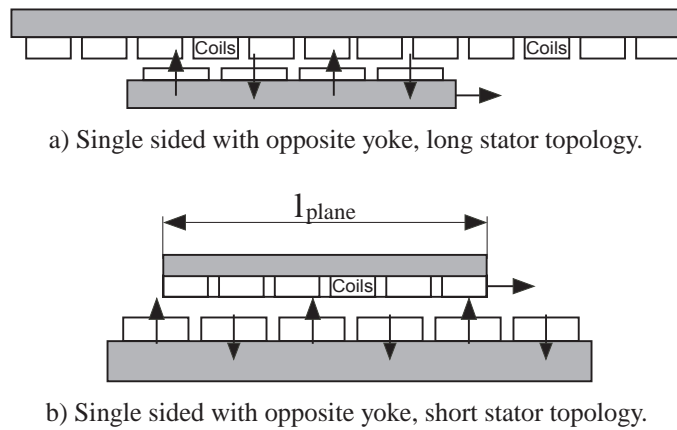


Figure 4.39: Toothless motor topologies which have an attractive force and a cogging force.

The cogging force cannot be suppressed, but it can be minimized in a first approach by choosing a length of the plate l_{plate} equal to:

$$l_{plate} = \left(k + \frac{1}{2}\right) \tau_p, \quad k = 1, 2, \dots \quad (4.80)$$

This length must recover of course all coils. The possibility to have an oblique shape at each plate end reduces also the cogging force [58]. This effect is difficult to model and therefore it is not taken into account in a pre-design model. Hence, the analysis of this effect can be performed with a FEM programm once the pre-design is done.

To evaluate these forces, a modulation function $w(x)$ must be superposed to the flux density expression defined for a single MaW with opposite yoke. This modulation function represents the relative permeability seen by the MaW and is given in Appendix D. For a good approximation, a square function can be used to find the attractive force but a better accuracy is obtained using the cos-exp function D.

These forces are calculated using (2.28) and (2.29) by substituting H_x and H_y with $w_x \cdot H_x$ and $w_y \cdot H_y$. A comparison between FEM simulation and the analytical model using a square modulation function is presented on Fig. 4.40. The length of the plate is equal to $l_{plate} = 0.045$. The graph shows a good accuracy of the analytical model compared to FEM.

To reduce the cogging force produced by the finite length of the yoke, [59] proposes to analyze the cogging force waveform developed at one end of the yoke and to optimize its axial length so that an opposing cogging force waveform is developed at the other end. Therefore, it is possible to obtain nearly zero resultant force. Unfortunately, this approach requires FEM simulations and the results are not really better than using (4.80).

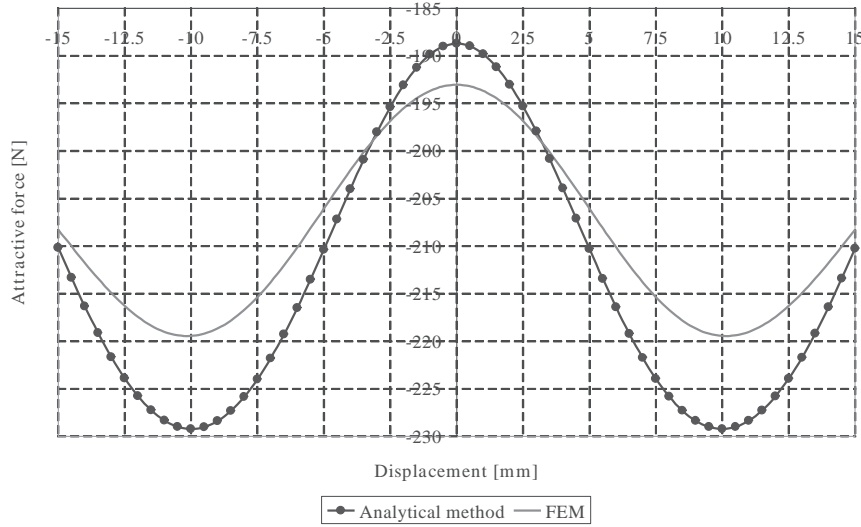


Figure 4.40: Attractive force in the case of a toothless motor, comparison between analytical and FEM models ($\tau_p = 0.02$, $h_{pm} = 0.002$ and $\delta = 0.01$).

4.5 Toothed Synchronous Motor With Permanent Magnets

The supply part can be mounted with three different MaW. The first is a MaW with mounted PM and in this case the model of a single MaW with opposite yoke must be used. The second is a MaW with inserted magnets and the last is a Halbach array.

As for the toothless motor, forces due to the end windings are neglected and therefore the motor width is equal to the magnet width w_{pm} .

The steps to model a toothed motor are presented in this chapter for a ShS motor with mounted PM magnetic way.

4.5.1 Winding Choice and Motor Geometry

This motor type has more winding configurations than linear toothless motors and the choice of the winding is based on the methodology introduced in Section 4.3. The winding chosen to illustrate the model is a two layers winding with $N_p = 8$ and $N_s = 9$. This winding consists of three consecutive coils per phase as illustrated on Fig.4.41. In a rotative machine such a winding will produce an unbalanced attractive force on the rotor.



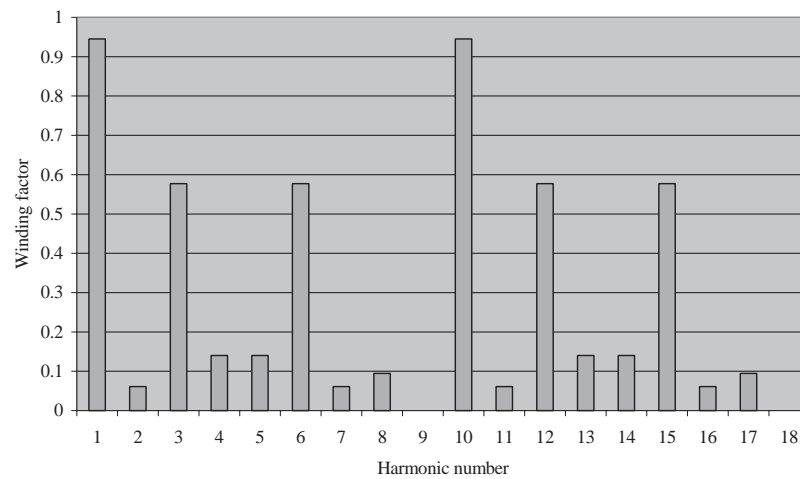
Figure 4.41: Winding configuration of a $N_p = 8$ and $N_s = 9$ linear machine.

As shown, this motor does not have additional teeth at each motor end. This aspect will be further discussed in Section 4.5.7.2. The winding factors, corresponding to integer harmonics, are listed in Table 4.14.

For the upper harmonics ($\nu > 9$), winding factors can be obtained by analogy since the harmonic spectrum is periodic with a factor 9 (since $N_s = 9$), as shown on Fig. 4.42.

Table 4.14: Winding factors for a linear motor with $N_p = 8$ and $N_s = 9$.

harmonic ν	winding factor νk_w
1	0.945
2	0.061
3	0.577
4	0.140
5	0.140
6	0.577
7	0.061
8	0.945
9	0

Figure 4.42: Winding factor for integer harmonics for a linear machine with $N_p = 8$ and $N_s = 9$.

Moreover, the mmf produced by a concentrated winding is not only composed of integer harmonics but also of sub and fractional harmonics. For example, the subharmonic $\nu=1/2$ have a corresponding winding factor equal to $^{1/2}k_w=0.14$. The mmf in the air gap due to the PMs of the MaW is only composed of odd harmonics. Therefore, only the odd harmonics created by the winding produce a propulsion force. The other harmonics produce only iron losses in the iron parts.

The geometrical parameters and the electrical properties of the studied motor are given in Table 4.15 and the sizes are related to Fig. 4.43.

4.5.2 Propulsion Force Determination

The propulsion force is obtained from the Maxwell's stress tensor (2.27) [60], which is equal to:

$$dF_t = B_n \cdot H_t \cdot dS, \quad (4.81)$$

where B_n is the normal component of the flux density created by the magnets and H_t is the tangential magnetic field produced by the motor supply.

B_n is obtained using either (4.23) or (4.22). To use 4.81, the air gap must be increased to take into account the slot effect. Indeed, the flux density in the air gap decreases under each slot opening due

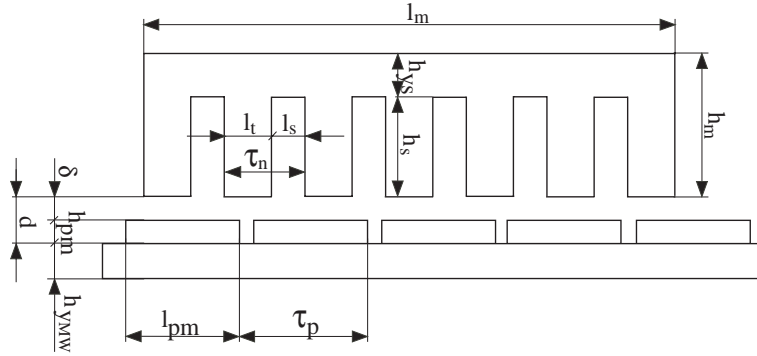


Figure 4.43: Geometrical parameters of a toothed motor.

Table 4.15: Geometry parameters and the electrical properties of the studied motor.

Geometry parameters	values	[mm]
Pole pitch	τ_p	30
Tooth pitch	τ_n	26.66
Magnet height	h_{pm}	5
Magnet length	l_{pm}	28
Magnet width	w_{pm}	100
Tooth length	l_t	12.66
Slot height	h_s	25
Yoke height	h_y	12
Air gap	δ	1
Electrical, magnetic properties		values
Filling factor	k_{cu}	0.6
mmf peak per coil	$N\hat{I}$	1000
PM remanent magnetic flux	B_r	1.23
PM relative permeability	$\mu_{r\ pm}$	1.05

to the increase of reluctance. The change in the mean magnetic flux density caused by slot openings corresponds to a fictitious increase of the air gap. The relation between fictitious air gap δ' and physical air gap d is expressed with the Carter's factor $k_c > 1$.

4.5.2.1 Carter Factor

The Carter factor is defined by a conform representation of an infinitely deep slot with an infinite ideal slot pitch τ_n . This factor is equal to [61]:

$$k_c = \frac{\tau_n}{\tau_n - \gamma \cdot d_1}, \quad (4.82)$$

d_1 is the air gap for the Carter factor calculation and γ is given by:

$$\gamma = \frac{4}{\pi} \left\{ \frac{l_s}{2d_1} \operatorname{atan} \left(\frac{l_s}{2d_1} \right) - \ln \left(\sqrt{1 + \left(\frac{l_s}{2d_1} \right)^2} \right) \right\}, \quad (4.83)$$

γ is a factor in relation to the ratio l_s/d_1 . For $l_s/d_1 > 1$, γ is approximated by:

$$\gamma = \frac{\left(\frac{l_s}{d_1}\right)^2}{5 + \frac{l_s}{d_1}}. \quad (4.84)$$

Depending on the authors, the Carter factor can be estimated for the mechanical air gap $d_1 = \delta$ [62], for the magnetic air gap $d_1 = \delta + h_{pm}$ [63] or for an air gap d_1 equal to:

$$d_1 = \frac{h_{pm}}{2} + \delta. \quad (4.85)$$

(4.85) can be used under the assumption that the flux lines are parallel to the magnetization of the PM under its mid-height. It means that the flux lines under the half of the magnet are not influenced by the slots as shown on Fig. 4.44. Thereafter, the Carter factor allows to estimate an intermediate value of the air gap d_{int} equal to:

$$d_{int} = k_c \cdot d_1. \quad (4.86)$$

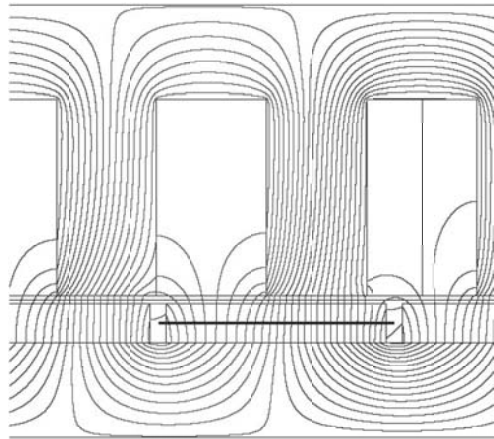


Figure 4.44: Flux lines distribution due to the magnets.

The various relations for the calculation of the fictitious air gap are related in Table 4.16.

Table 4.16: Various strategies for the fictitious air gap calculation applying the Carter factor.

	Air gap for Carter factor calculation d_1	Carter's factor k_c	Intermediary air gap d_{int}	Fictitious air gap δ'
A) mechanical air gap	δ	1.6	$k_c \cdot d_1$	$d_{int} + h_{pm} = 6.6 \cdot 10^{-3}$
B) magnetical air gap	d	1.21	$k_c \cdot d$	$d_{int} = 7.2 \cdot 10^{-3}$
C) combined air gap 1	$\delta + h_{pm}/2$	1.31	$k_c \cdot d_1$	$d_{int} + h_{pm}/2 = 7.1 \cdot 10^{-3}$
D) combined air gap 2	$\delta + h_{pm}/2$	1.31	$k_c \cdot d$	$d_{int} = 7.9 \cdot 10^{-3}$

All the presented methods to increase the air gap are studied in parallel in order to make a choice on the strategy to adopt. Moreover, the Carter's factor does not take into account the saturation in the iron parts, which also affects the induction in the air gap. Therefore a saturation factor is introduced to take into account the magnetic potential in the iron parts.

4.5.2.2 Saturation Factor

The saturation effect can be taken into account with a saturation factor k_{sat} which increases the air gap, like the Carter's factor. Therefore, if the saturation is taken into account the fictitious air gap becomes equal to:

$$\delta'' = k_{sat}\delta', \quad (4.87)$$

with:

$$k_{sat} = 1 + \sum_i \frac{l_i \cdot S_{pm}}{\mu_{r_i} \cdot S_i \cdot d \cdot k_f}. \quad (4.88)$$

i is related to the iron parts constituting the lumped magnetic scheme and k_f is the stacking factor. For the studied motor, the most saturated part is situated in the end tooth at the position shown on Fig. 4.45. As in this position the lumped scheme is symmetric, only one half can be studied. Therefore, for this

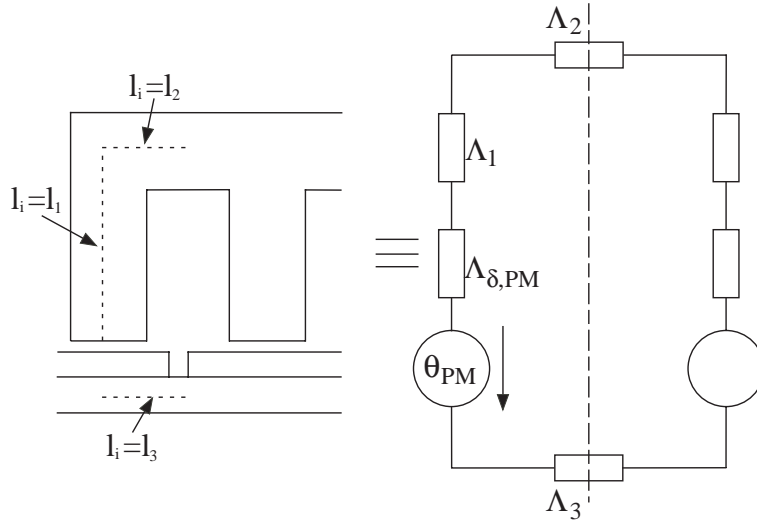


Figure 4.45: Saturation at the motor end (worst case) and lumped equivalent magnetic scheme.

configuration (always valid for concentrated windings since the tooth pitch varies between 120 edeg and 360 edeg) and by solving (4.88), the saturation coefficient is equal to $k_{sat} = 1.055$. This coefficient is estimated for the worst case, i.e. no flux leakage. To take into account the flux leakage between two magnets, an additional lumped scheme is needed and the impact can be transmitted to the surface of the PM by decreasing it in relation with the flux leakage.

The total fictitious air gaps for the four cases are calculated and presented in Table 4.17.

Table 4.17: Fictitious air gap determination for the calculation of the normal component of the flux density.

	Fictitious air gap $\delta'' [mm]$
A) mechanical air gap	7.0
B) magnetical air gap	7.6
C) combined air gap 1	7.5
D) combined air gap 2	8.3

It is important to design the teeth and the yoke in the position presented on Fig. 4.45. Indeed, if the motor is not symmetric as a rotative motor the flux is not necessarily divided in two to circulate in the yoke. This is illustrated on Fig. 4.46.

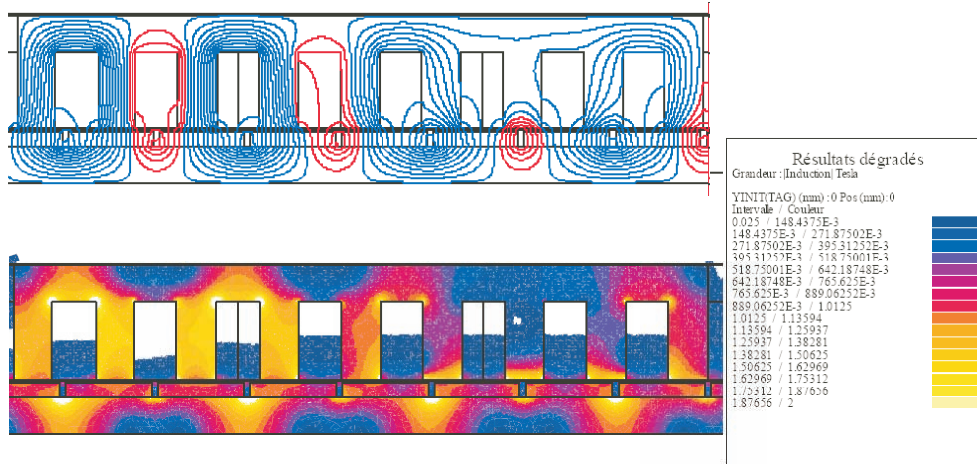


Figure 4.46: Flux distribution in the yoke due to the PMs.

4.5.2.3 Calculation of the Propulsion Force

The normal flux densities in the air gap must be calculated with the fictitious air gaps given in Table 4.17. If the flux density in the air gap is approximated by a pulsed form, the amplitude of the pulsed form, the amplitude of the first harmonic of the flux density ${}^1\hat{B}_n$ and its rms value 1B_n are given in Table 4.18.

Table 4.18: Normal flux densities for various fictitious air gaps.

	\hat{B}_n pulsed fct	${}^1\hat{B}_n$	1B_n
Case A	0.868	1.10	0.78
Case B	0.796	1.00	0.71
Case C	0.813	1.03	0.73
Case D	0.731	0.93	0.65

The magnetic field must be now determined in order to calculate the propulsion force. It can be estimated with the magnetic scalar potential Θ in the air gap as:

$$\mathbf{H} = -\nabla\Theta, \quad (4.89)$$

and hence the tangential magnetic field H_t is:

$$H_t = -\frac{d\Theta}{dy}. \quad (4.90)$$

The magnetic scalar potential produced by the winding is defined as:

$${}^\nu\hat{\Theta} = \frac{\sqrt{2}}{\nu \cdot \pi} m \frac{N_{cp} \cdot NI {}^\nu k_w}{N_p/2}. \quad (4.91)$$

Since Fourier's series are used, the distribution of the magnetic scalar potential is sinusoidal along the air gap and the tangential magnetic field (sometimes called current lineic density) becomes:

$$\nu \hat{H}_t = \frac{\pi \nu}{\tau_p} \hat{\Theta}. \quad (4.92)$$

Finally, the propulsion force is given by:

$$F = \sum_{\nu, k} w_{pm} \int_0^{N_p \cdot \tau_p} \nu \hat{H}_t \sin\left(\frac{\nu \pi}{\tau_p} x\right) \cdot k \hat{B}_n \sin\left(\frac{k \pi}{\tau_p} x - \phi\right) \cdot dx \quad (4.93)$$

This equation takes into account the current waveform (sinusoidal current supply, 120° current supply, etc...), by decomposing it in a Fourier's series. For $\nu = k$, the propulsion force is constant and for all values $\nu \neq k$, the propulsion force is pulsed with a period equal to $|\nu - k|$ and with an average value of zero. For a motor pre-design, only the propulsion force produced by the fundamental is calculated and therefore for $\phi = 0$, corresponding to a maximum efficiency if iron losses are not considered, (4.93) becomes:

$$F = \frac{w_{pm} \cdot N_p \cdot \tau_p}{2} \hat{H}_t \cdot \hat{B}_n, \quad (4.94)$$

The use of these formulae to determine the propulsion force is not dependent on the number of layers, i.e. the winding distribution. The method which takes into account this effect consists to replace the winding by a lineic current in the air gap and to calculate the propulsion force by applying the Laplace force. The lineic current density in the air gap is calculated following [64]. First, the magnetic scalar potential created by the winding is calculated. It is assumed that the magnetic field H_δ has the wave form presented on Fig. 4.47 for the three coils of the phase 1.

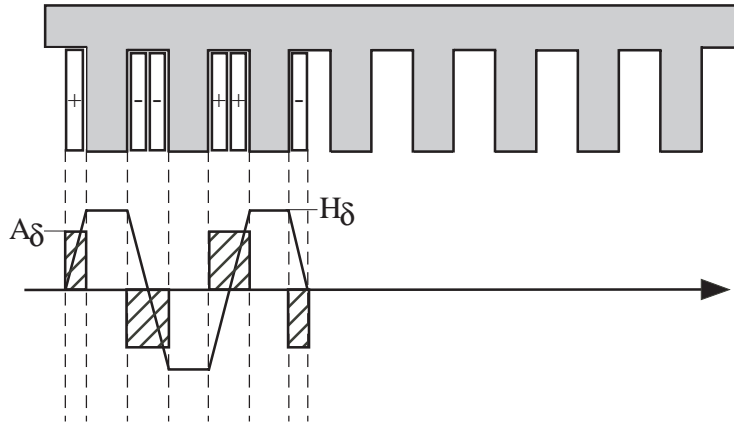


Figure 4.47: Lineic current density calculation for the three coils of the phase 1.

The amplitude of the magnetic field is equal to:

$$\theta_\delta = H_\delta \cdot \delta' = \frac{1}{2} \frac{k w \cdot N I}{k_{sat}}, \quad (4.95)$$

and the lineic current becomes equal to:

$$A_\delta = \frac{d}{dx} \theta_\delta \quad (4.96)$$

Then the propulsion force can be calculated with the Laplace' force.

As comparison, with a peak current of 1A, the propulsion force obtained with a FEM program is equal to 817N by taking into account the iron saturation and 837N if the iron parts are supposed ideal. The propulsion forces obtained with the analytical models are given in Table 4.19.

Table 4.19: Propulsion forces obtained with analytical models.

	Maxwell (4.94) [N]	Laplace (4.96) [N]
Case A	934	1050
Case B	857	963
Case C	874	980
Case D	787	885

This comparison permits to eliminate case A (Application of Carter's factor on the mechanical air gap) and case C (Application of Carter's factor on a combined air gap) since they result in a higher propulsion force than the FEM results. The cases B and D are both accurate enough, but the case D is privileged since it gives a smaller propulsion force than FEM. The higher propulsion force than FEM in the case B can be explained by the fact that the Carter's factor does not take into account the leakage flux in the air gap. Indeed, with the Carter factor, it is assumed that all the flux lines go from the stator to the rotor. Therefore, it can be assumed that the case D takes into account leakage flux in the air gap since it has a higher air gap than the case B.

The difference occurring between Maxwell method and Laplace method results from the calculation of the flux density: Maxwell method uses the first harmonic of the flux density whereas the Laplace method assumes a constant flux density in the air gap. This difference explains why using the Laplace method a higher propulsion force is obtained than using the Maxwell method. To design the motors, the Maxwell method is applied.

4.5.3 Attractive Force at No Load

For the attractive force, the Maxwell equation (2.28) is used and the tangential component of the flux density is considered as negligible compared to its normal component. Therefore, the mean value of the attractive force is equal to:

$$F_{att} = \frac{1}{2\mu_0} w_{pm} \int_0^{N_p \cdot \tau_p} B_y^2(x, y) \cdot dx. \quad (4.97)$$

If the normal flux density produced by the magnets is decomposed in a Fourier series, the form is:

$${}^\nu F_{att} = \frac{1}{2\mu_0} w_{pm} \int_0^{N_p \cdot \tau_p} {}^\nu B_y^2(x, y) \cdot dx. \quad (4.98)$$

The magnetic flux density is evaluated in no-load and in the position $y = \delta''$, i.e. along the teeth surface. The use of the equivalent current to model the magnetic way is not a good approach to determine the attractive force. Indeed, the integral of (4.97) would be very difficult to integrate and time consuming if this aspect is introduced as a result in an optimization process. Therefore, simplified formulae to model the normal component of the flux density in the air gap are more suitable. If the flux density is modelled by a pulsed form, the integral is straightforward to solve.

The calculated attractive force is not dependent on the position, although it is the case in a practical realization. However, the model gives a good approximation on the mean attractive force as presented in Table 4.20 where all the attractive forces for each air gap model are presented.

Table 4.20: Attractive force comparison between FEM and analytical model.

	FEM [N]	Analytical model [N]
Case A	5570	6710
Case B	5570	5650
Case C	5570	5880
Case D	5570	4770

It is shown that the privileged case to calculate the propulsion force (Case D) leads to underestimate the attractive force. Therefore, a special attention must be made when the guidance system of the motor is designed.

Another important value is the attractive force appearing under one tooth. This force has an amplitude variation which can produce vibration and audible noise. To estimate this value, the attractive force is calculated only under one tooth pitch in several x -positions. In this case, only the model using equivalent currents to model the MaW has sense and the effect of the slot on the flux density is taken into account by a permeance function as proposed by [65]. The attractive force on one tooth is presented on Fig. 4.48.

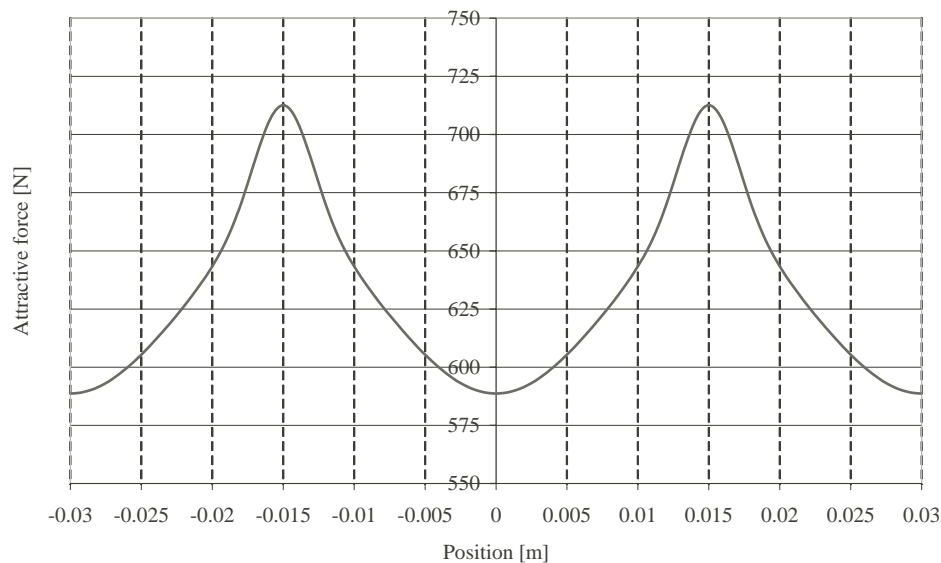


Figure 4.48: Attractive force under one tooth.

4.5.4 Iron Part Model and Design

The propulsion and attractive force calculation is presented in a determinist approach, i.e. the motor geometry is defined. In an optimization process, the stator and the MaW dimensions must be variable and therefore a lumped magnetic scheme is introduced to parameterize the motor geometry. In order to not increase the complexity of the model several assumptions are made:

1. only the worst case at no-load is analyzed;

2. all the flux flowing through the magnet is closed through the stator in the next magnet, i.e. all the flux flowing into a magnet is the same than in the MaW yoke. It is not divided in two, like in rotative machines due to the end effect;
3. there is no slot flux leakage;
4. the flux lines are modelled with arcs and lines;

The model is the one presented on Fig. 4.45, which is the worst case. In contrast to rotative motors, all the flux through the magnet can flow in the same direction in the magnetic way yoke. Therefore, at no-load, the magnetic flux is equal to:

$$\phi = H_c \cdot h_{pm} \cdot \Lambda_{eq} \quad (4.99)$$

Λ_{eq} is the equivalent permeance of the half-lumped magnetic scheme and is equal to:

$$\Lambda_{eq} = \left(\frac{1}{\Lambda_1} + \frac{1}{\Lambda_2} + \frac{1}{\Lambda_3} \right)^{-1} \quad (4.100)$$

Thereafter, by giving an admissible range values of the flux density in all iron parts, the geometrical dimensions can be defined. The solving of this non linear system, due to the BH curve (Appendix B), is made by an implicit function.

The results for the flux density in the iron parts with the given motor dimensions are presented in Table 4.21. For comparison, the flux density obtained with a FEM program is shown on Fig. 4.49

Table 4.21: Absolute values of the flux density in the various iron parts for the developed example.

	FEM	Analytical
Flux density in the tooth Case A	1.65	1.98
Flux density in the tooth Case B	1.65	1.86
Flux density in the tooth Case C	1.65	1.88
Flux density in the tooth Case D	1.65	1.71
Flux density in the yoke Case A	1.75	2.1
Flux density in the yoke Case B	1.75	1.96
Flux density in the yoke Case C	1.75	1.98
Flux density in the yoke Case D	1.75	1.8

Moreover, to avoid a demagnetization of the magnet, the mmf of the coil must be limited compared to the mmf of the PM. Therefore, a demagnetization coefficient k_{dem} is introduced and limited to:

$$k_{dem} = \frac{\theta_{pm}}{\theta_{coil}} = \frac{H_0 \cdot h_{pm}}{NI} \geq 2. \quad (4.101)$$

This approach is valid for a motor pre-design even if the coil mmf is not taken into account for the calculation of the flux densities in the iron parts. For the same motor, the flux density in the teeth can be higher if the coil mmf is taken into account, leading to more saturation in the iron part. Indeed, following the current waveform supply and the motor position, the coil mmf can enhance or weaken the flux flowing in the tooth due to the magnets, as presented on Fig. 4.50. This figure presents only one tooth sinusoidal supplied travelling above two magnets.

The worst case is obtained when the tooth edge is aligned on the PM edge. At this position the coil mmf is equal to 719 At for the presented motor. This coil mmf can be added to the PM mmf, in order to perform a control on the tooth saturation. If this approach is applied to the case D, the flux density in the tooth will increase to 2 T. Nevertheless, this aspect can be omitted during a pre-design optimization.

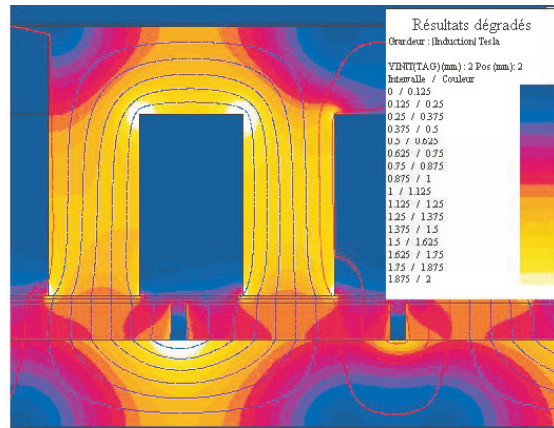


Figure 4.49: Induction distribution in the tooth at no load (worst case).

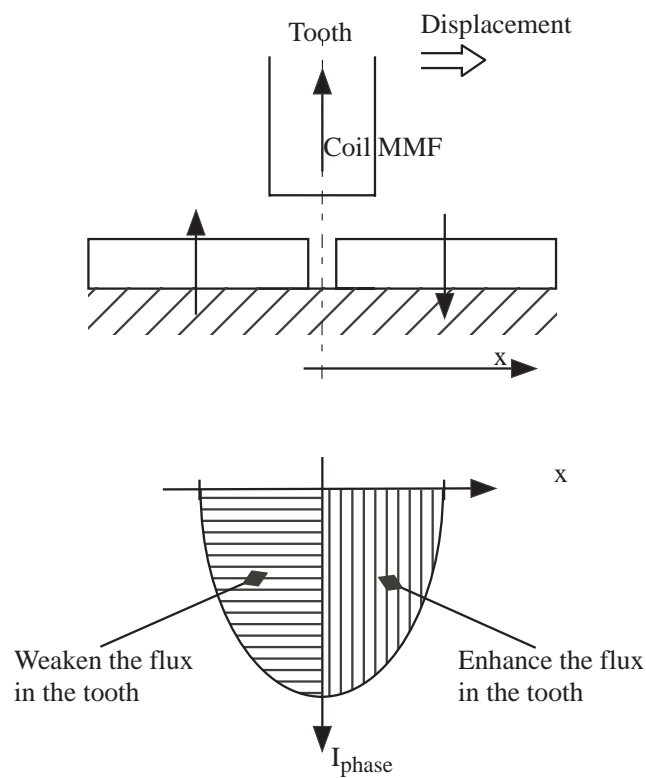


Figure 4.50: Influence of the coil mmf on the tooth saturation.

4.5.5 Induced Voltage Model

There are two possibilities to calculate the induced voltage. The easiest way is to calculate it using the propulsion force. The propulsion force given in Section 4.5.2 is equal to:

$$F = \frac{3 \cdot emf_{rms} I_{rms}}{v} \quad (4.102)$$

Therefore, the rms value of the first harmonic of the emf is equal to:

$${}^1 emf_{rms} = \frac{{}^1 F v}{3 \cdot I_{rms}} \quad (4.103)$$

For the presented motor with a number of turns per coil equal to $N = 500$, the rms value of the current is equal to 1.414 A. These values are chosen to permit a comparison between the analytical models and FEM. The peak values of the induced voltage obtained by this way are presented in Table 4.22.

Table 4.22: Induced voltage peak value comparison between FEM and analytical models.

		model (4.103)	model (4.104)
emf [V]	Case D	295	263
		262	263

Another possibility is to evaluate the induced voltage using the winding factors presented in Section 4.3. The induced voltage is therefore equal to [64]:

$${}^1 \hat{emf} = 2N_{cp} \cdot N \cdot v \cdot {}^1 k_w \cdot w_{pm} \cdot {}^1 \hat{B}_n \quad (4.104)$$

As presented in Table 4.22 the analytical models give similar results. Therefore both formulations can be used. In this approach, only the first harmonic of the induced voltage is used. The other harmonics can be taken into account without difficulty. However, in a predesign process, the harmonic rangs higher than 1 can be neglected.

4.5.6 Self Inductance and Mutual Inductance Determination

For the inductance calculation, the assumption that all self inductances are equal is made. The same assumption for mutual inductances is admitted and they are all equal to L_m [34].

The total magnetic flux seen by the phase 1, with $i_1 + i_2 + i_3 = 0$, is equal to:

$$\Psi_1 = L_{11} \frac{di_1}{dt} + L_{12} \frac{di_2}{dt} + L_{13} \frac{di_3}{dt} = (L_{11} - L_m) \frac{di_1}{dt}, \quad (4.105)$$

with L_{11} the self inductance which is composed of the main inductance L_{1h} and the leakage inductance $L_{1\sigma}$ as:

$$L_{11} = L_{1\sigma} + L_{1h}. \quad (4.106)$$

From (4.105) and (4.106) the cyclic inductance L_s is introduced as:

$$L_s = L_{1h} + L_{1\sigma} - L_m. \quad (4.107)$$

This inductance is used to model the behavior of one phase as explained in Section 4.7.1.

The main inductance L_{1h} is equal to:

$$L_{1h} = \frac{4 \cdot \mu_0}{\pi^2} \cdot \frac{\tau_p \cdot w_{pm}}{(N_p/2) \cdot \delta'} (N_{tot} \cdot {}^1 kw)^2, \quad (4.108)$$

where N_{tot} is the number of turns in series per phase, i.e the number of turns per coil multiplied by the number of coils per phase. The demonstration of this result is given in [64]. The leakage inductance is composed of the the slot leakage inductance and the end-winding leakage inductance. [26] gives several formulae for the slot leakage depending on the slot form.

Furthermore, for a three-phase motor the relation between the main inductance and the mutual inductance is given as:

$$\frac{L_m}{L_{1h}} = -\frac{1}{2}. \quad (4.109)$$

for their fundamentals [22].

The inductance can also be obtained using a lumped magnetic scheme.

Table 4.23 compares the self inductances obtained using the different methods.

Table 4.23: Comparison between self inductance obtained by several methods (N=500).

	FEM	Analytical (4.108)	Lumped magnetic scheme
Self inductance L_{11} [mH]	71	97.5	87.5

This table shows that the given formula can be used to estimate the order of magnitude of the inductance. The result with the lumped magnetic scheme is obtained with the following assumptions:

1. the iron is ideal;
2. there is no flux leakage;
3. there is no fringe effect.

If the iron saturation is taken into account, the self inductance will decrease approaching the FEM value. For a motor pre-design, the proposed formula (4.108) is adopted.

4.5.7 Special Cases

4.5.7.1 Tooth Crown

In such a motor, the tooth can have an end tooth crown in order to reduce the cogging force and to have a better flux linking between the coil and the magnet. Such a tooth is presented on Fig. 4.51, where the tooth length l_s is increased to l_{st} .

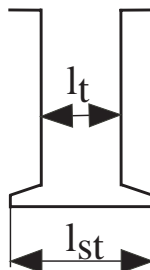


Figure 4.51: Tooth crown geometrical quantities.

In a linear motor the tooth crown has the following impacts on the motor design:

1. in most cases, increase of the attractive force;

2. reduction of the stator mmf due to the decrease of the copper filling factor k_{cu} ;
3. difficult winding manufacturing.

The two last points are straightforward and are therefore not discussed here. For the presented case, if the tooth is increased as:

$$l_{st} = 1.6 \cdot l_t, \quad (4.110)$$

the Carter coefficient would be equal to $k_c = 1.061$ producing an increase of about 25% of the flux density produced by the magnets. This would result in an increase of 56% of the attractive force which implies more constraints for the motor guidance.

With such a tooth geometry the copper filling factor will decrease. For such a motor a value of 0.4 is adopted. For the same slot area, the mmf would decrease by 27%. Therefore, the propulsion force would decrease, taking into account the increase of the flux density and the decrease of the stator mmf, by 9%.

In conclusion, the tooth crown in linear motor with concentrated winding does not bring as much advantages as for rotative motors since the attractive force is not compensated. The tooth crown is also used in order to reduce the cogging force. As presented in Section 4.3.3 in order to have a low cogging force it is privileged to chose a number of poles and teeth leading to a high least common multiple factor than to try to reduce the cogging force by adding tooth crowns. For a motor with high losses in the PM, the tooth crown can be useful to reduce the magnetic flux density seen by the PMs.

4.5.7.2 Additional Teeth at the Motor End

As presented on Fig.4.47, the studied motor has no additional teeth at each motor end. The cogging force due to the teeth is not so relevant if the number of poles and teeth are correctly chosen (compensation effect). However, a cogging force with a period equal to τ_p , due to the first and the last teeth edges appears. In order to eliminate as much as possible this parasitic force, the PMs can be skewed or additional teeth end can be added on both sides. These additional teeth do not increase significantly the propulsion force. However, depending on their design they can increase or decrease the effect of reluctance force. The analysis of the cogging force due to the tooth end is very difficult to perform with an analytical method [45] and therefore FEM are used to show their impact on the cogging force. To illustrate this phenomena, several tooth end lengths and slot lengths (Fig. 4.52) are analyzed. The first analysis consist to fix $l_2 = l_s$ and to vary l_1 and the second approach consist to fix $l_2 = l_s/2$ and to vary l_1 . The results are shown on Fig. 4.53 and Fig. 4.54 for $l_2 = l_s$ and $l_2 = l_s/2$, respectively.

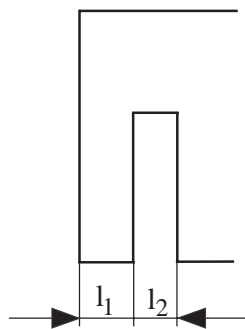


Figure 4.52: Tooth end quantities.

The cogging forces for these cases are compared to the cogging force for a motor without additional tooth end (denoted normal on figures). Generally, an additional tooth end increases the resulting cogging force since it introduces a non linearity in the tooth distribution. This effect is more important in the case

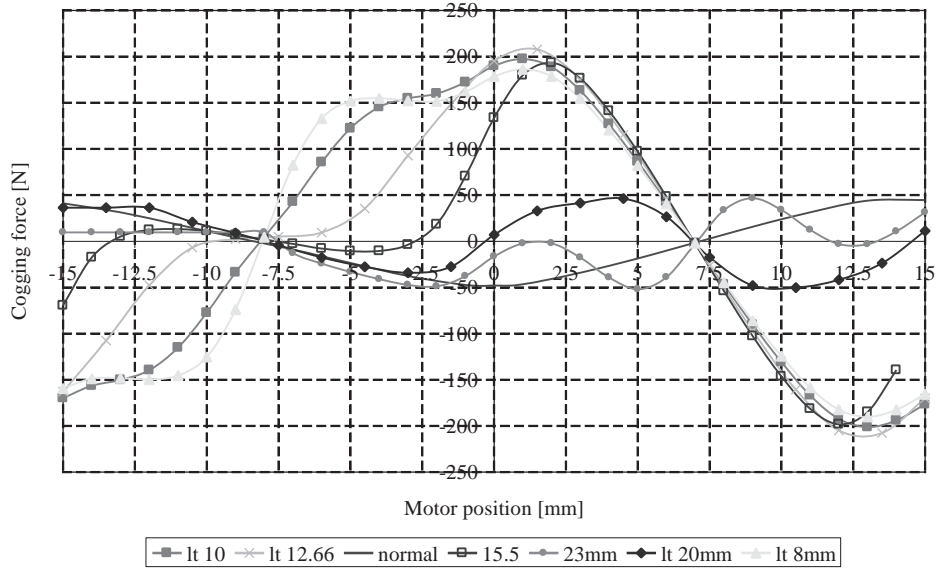


Figure 4.53: Cogging force with $l_2 = l_s$ and with l_1 variable.

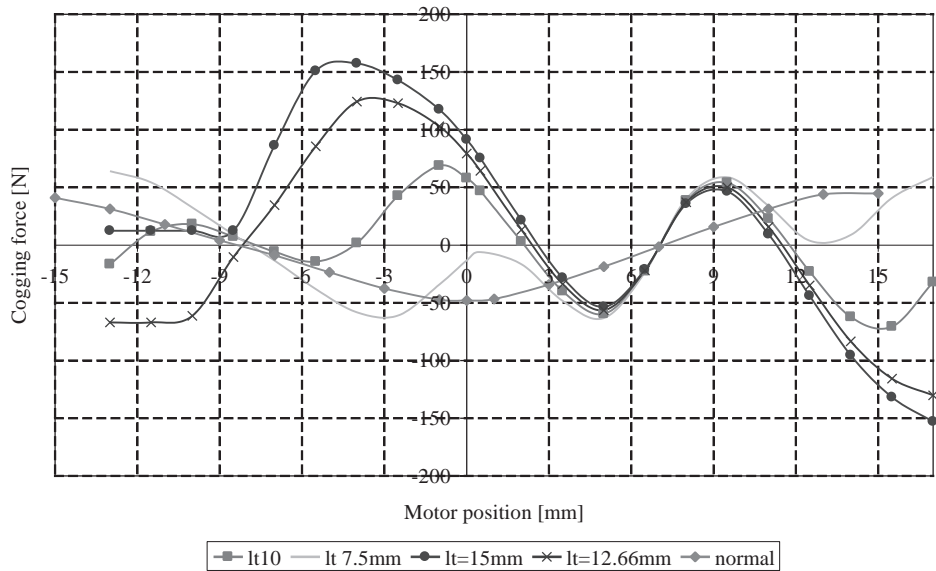


Figure 4.54: Cogging force with $l_2 = l_s/2$ and with l_1 variable.

with $l_2 = l_s$ since the cogging force due to this tooth end is summed with the cogging generated by one motor tooth. This effect is maximal when the tooth end has the same sizes as the motor tooth. Therefore if a tooth end is added, it is advised to chose it with another size than a motor tooth ($l_1 \neq l_t$ and $l_2 \neq l_s$). An efficient way to reduce the cogging force due to the end effect was patented by [66] and consist to realize a slopping end. This slopping end is not straightforward to design and requires FEM. Indeed, a poor design can result in an increase of the cogging force compared to the case without additional tooth.

If the solution with a sloping end cannot be used, the better way to reduce as much as possible the cogging force is to chose a number of teeth and slots with a high k_{cogg} (4.61) and to skew the PM as proposed in Section 4.3.1.

4.6 Transverse Flux Linear Motor

4.6.1 Introduction

The main advantage of Transverse Flux Linear Motors (TFM) is the difference between the magnetic direction of the permanent magnets and the air gap flux path direction that allows to produce a high flux density in the air gap and therefore a high propulsion force density. Due to their topologies these motors are generally phase independent.

Several TFM are proposed in the literature and [67] gives their categorization. The motor studied here is a PM excitation TFM with a passive track. This motor has been designed by the "Institut für Elektrische Maschinen RWTH Aachen, Germany" [68] and a prototype has been realized by collaboration between Schindler SA and ETEL SA. It is shown on Fig. 4.56.

This motor is composed of two motors mounted on the same way and supplied independently. Each motor has two phases and the two independent motors are shifted by 45 edeg. Figure 4.55 and Table 4.24 give more information about the coil distribution. The coils of a same phase are connected in series.

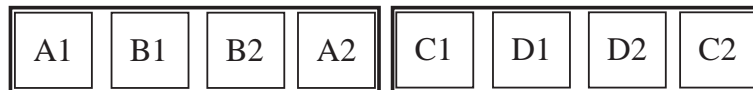


Figure 4.55: Four phases TFM composed by eight motor modules.

Table 4.24: TFM coil distribution of the eight motor modules.

Coil	Coil distribution [edeg]
A1	0
A2	360
B1	90
B2	270
C1	135
C2	135
D1	225
D2	45

The motor is a short stator motor. The moving part consists of coils and PMs. One motor module is presented on Fig. 4.57 (face view) and Fig. 4.58 (bottom view).



Figure 4.56: Four phases TFM prototype composed by eight motor modules.

The passive track, shown on Fig. 4.59, is made with toothed laminations and is segmented each two teeth in order to avoid eddy currents in the track.

The moving part takes place in the middle of the track as presented on Fig. 4.60

This motor uses two stacks of iron and PM to produce the excitation. The stator winding goes above the way in order to close the linkage flux. It uses four modulated air gaps, two per stack, to produce the propulsion force. As a disadvantage two extra air gaps (Fig. 4.60) are introduced in order to be able to create the coupling flux between both stator winding and rotor teeth. This solution brings additional disadvantages: all the mechanical parts fixing the part must be electrically isolated in order to avoid leakage flux in the different iron parts. Furthermore, the guidance system is very complex and noisy. Moreover, this motor has a high cogging ripple and reluctance force. Nevertheless, it has the advantages to have a very simple winding and a good thermal dissipation.

Construction details and geometrical parameters of the motor are given in Appendix E.

The motor model is based on a lumped magnetic scheme.

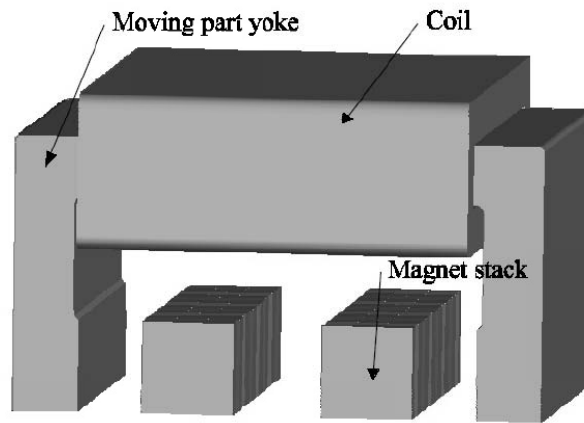


Figure 4.57: One motor module of the studied TFM, front view.

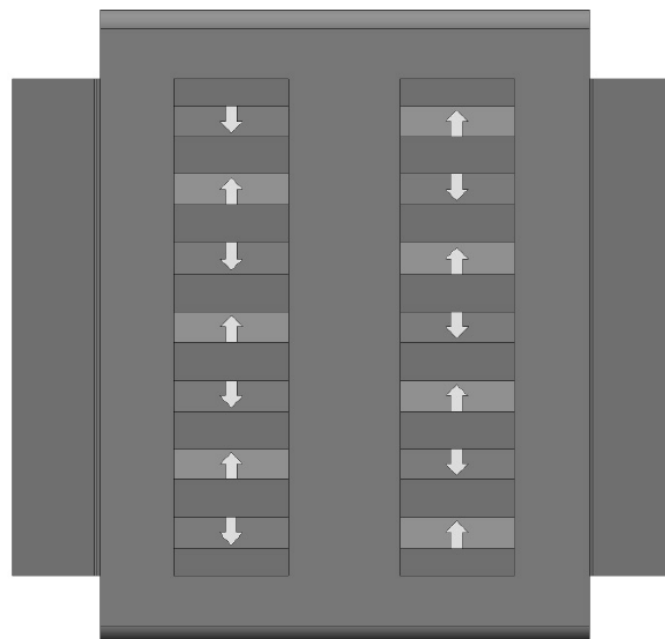


Figure 4.58: One motor module of the studied TFM, bottom view.

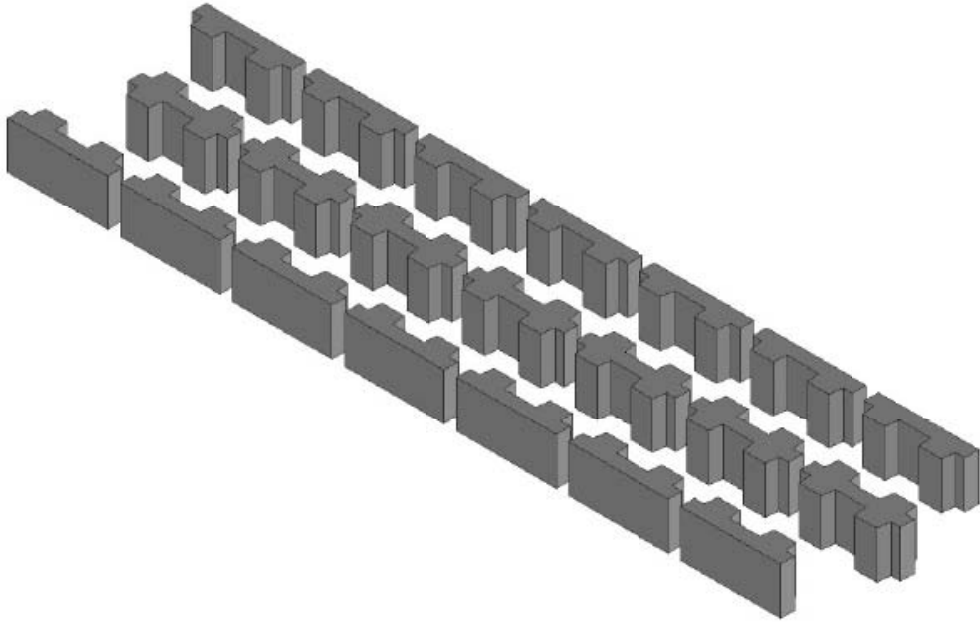


Figure 4.59: Passive track of the studied TFM.

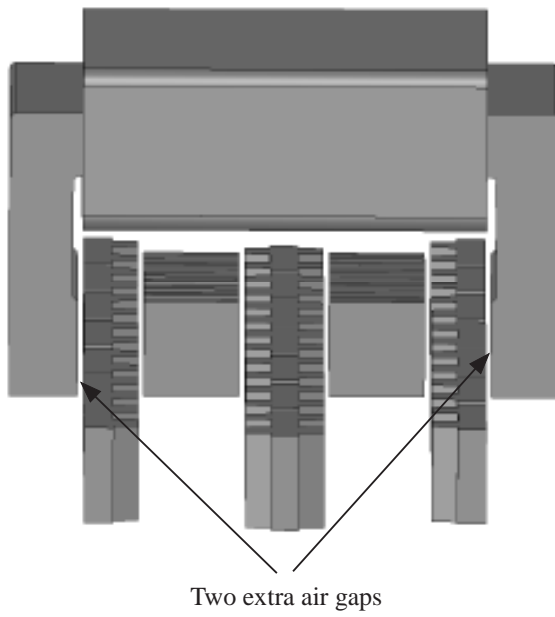


Figure 4.60: One module in the track.

The results obtained with the proposed lumped magnetic scheme given in Appendix E are not enough precise in order to be able to design correctly such a motor in this way. Moreover, the optimization program Pro@design does not allow the use of matrices. Therefore, this motor could not be by a simple way optimized. Hence, it was particularly studied with FEM. The model presented in Appendix E is given in order to present the complete approach.

4.6.2 Motor Performances

The motor performances are presented in Table 4.25.

Table 4.25: TFM performances

		Nominal values	Peak values
Propulsion force	[kN]	3.9	6
Maximum speed	[m/s]	1	1
Motor power	[kW]	3.9	6
Motor phase voltage	[V]	250	250
Phase current (rms)	[A]	12.2	19
Copper losses	[kW]	1	2.4
Efficiency	[%]	79.3	71.4
Voltage constant	$[\hat{V}/\text{m/s}]$	113	113
Force constant	$[\text{N/A}]$	320	320

Due to their structure, TFMs have high cogging and reluctance forces. The former is presented on Fig. 4.61 and the latter on Fig. 4.62 for the peak case ($NI=3200\text{At}$).

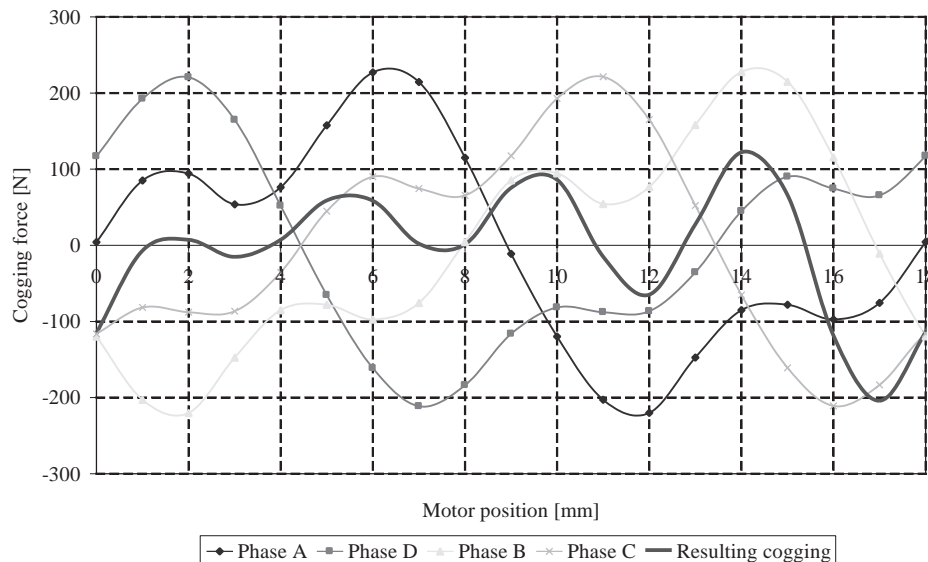


Figure 4.61: Cogging force for the TFM ($\tau_p = 18\text{mm}$). The cogging force corresponding to one phase is given for two modules.

The resulting cogging force is not very high compared to the nominal propulsion force. Nevertheless, when the motor produces a low propulsion force, the cogging force can disturb significantly the

propulsion force. This effect may be observed when the motor works at low speed at no-load. It creates vibration and audible noise.

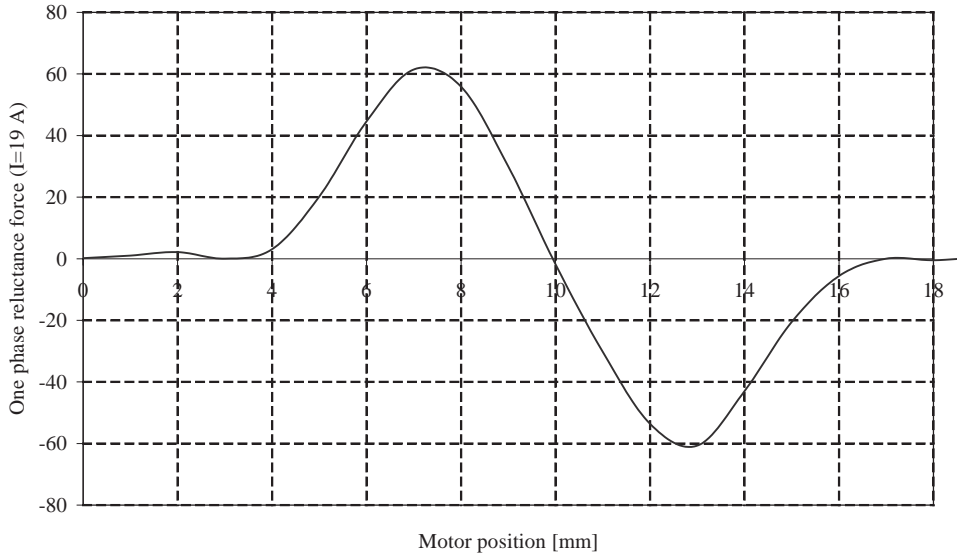


Figure 4.62: Reluctance force for a supplied phase ($I=19A$, $\tau_p=18mm$).

The reluctance force (created by the coils only) is not as important as the cogging force but it increases the ripple effect noticed at low speed and at no-load.

Therefore, if the static characteristic of the propulsion force for one module is given as a function of the motor position and for different coil mmf, some distortion will appear for low value of the coil mmf. Such an analysis is presented on Fig. 4.63.

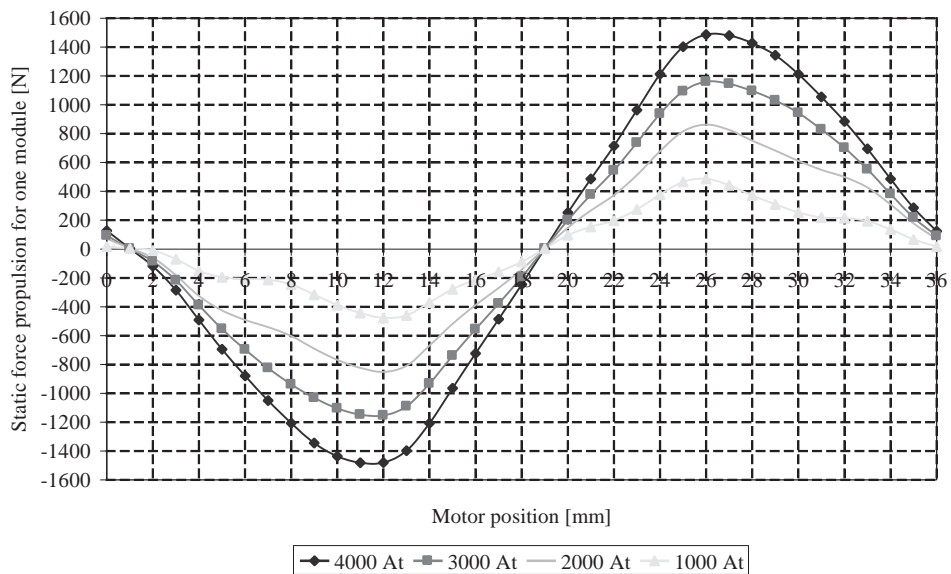


Figure 4.63: Static characteristic of the propulsion force for one module for different coil mmf.

The case corresponding to a coil mmf of 2000 At is the nominal case. The propulsion force is not close to a sine, leading to a non constant force for the motor along its displacement. As Fig. 4.64 shows it, the induced voltage is close to a sine and therefore, the distortion on the propulsion force can be compensated by imposing no sinusoidal currents. This solution has been applied on the prototype.

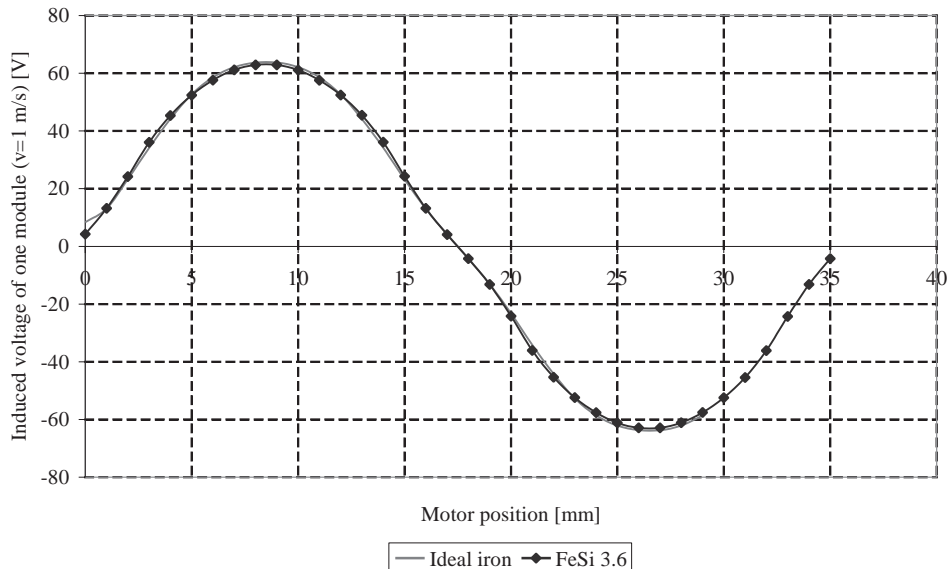


Figure 4.64: Induced voltage for one motor module.

The presented simulation shows clearly the problem linked to TFM motors: the cogging ripple. Moreover, the presented prototype has not an adapted guidance system. This causes frequent motor breakdowns. The obtained experiments are not presented since they are not precise enough and interesting for this thesis.

4.6.3 Conclusions and Discussions

This prototype motor was not really successful and therefore no additional effort was devoted to its modelization. Furthermore, the choice to not develop a precise analytical model was especially due to the studied application, for which it does not represent a convenient solution. This aspect will be discussed in details in Chapter 7.

Due to its structure, TFM requires iron laminations for both, the moving part and the reactive part. This implies manufacturing problems more particularly for the stack assembling. Another problem is the guidance system which is not precise enough and rigid.

Neglecting mechanical problems, TFM could be an interesting solution for a lift system with a short stator and counterweigh, since both, PMs and coils, are moving.

4.7 Motor Power Supply

The objective is not to have an accurate model of the converter but to define the behavior of the machine and more particularly its power factor.

This model permits to define the number of turns per coil N , the copper wire diameter, which are not optimization parameters, as it is discussed in Section 4.7.1.

The difference between LS supply and ShS supply will be also discussed in this Section.

4.7.1 Motor Electrical Model

The electrical model of a motor is presented by its phasor diagram. This diagram consists on the phase resistance, the cyclic inductance and the emf per phase. The model of one phase is presented on Fig. 4.65.

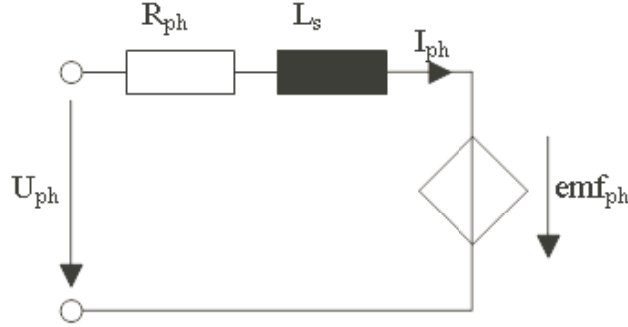


Figure 4.65: One phase electrical model of a motor.

In general, this circuit is analyzed for the first harmonic but can be extended to other harmonics.

Two main approaches to supply a motor are often used: voltage supply or current supply [22].

For a current supply, which will be the case in the application presented in Chapter 7, it is interesting to fix the current in phase with the induced voltage. For this command strategy, the maximum force is reached. The corresponding phasor diagram is presented on Fig. 4.66.

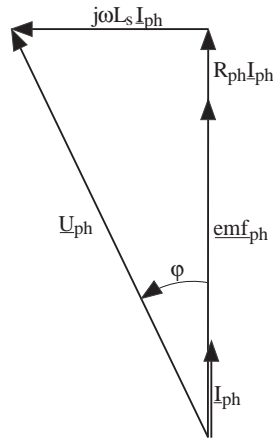


Figure 4.66: Phasor diagram for the maximum propulsion force.

The power factor $\cos(\phi)$ and the voltage phase U_{ph} is calculated as:

$$\cos(\phi) = \frac{emf_{ph} + R_{ph} \cdot I_{ph}}{U_{ph}} \quad (4.111)$$

$$U_{ph} = \sqrt{(emf_{ph} + R_{ph} \cdot I_{ph})^2 + (\omega L_s I_{ph})^2} \quad (4.112)$$

This voltage is limited by the DC voltage source of the converter U_{DC} . To impose a current control, the lines to lines motor voltage must always be smaller than the DC voltage source.

All the quantities constituting the phasor diagram (U_{ph} , $R_{ph}I_{ph}$, $j\omega L_s I_{ph}$ and emf_{ph}) are proportional to the number of turns per coil N . Therefore, for an imposed voltage source U_{ph} , N is adapted to a new number of turns per coil Nn in order to keep emf_{ph} smaller than U_{ph} . Then, the new values of the phase resistance Rn_{ph} and the phase inductance Ln_{ph} become:

$$Rn_{ph} = R_{ph} \frac{Nn^2}{N^2} \quad (4.113)$$

$$Ln_{ph} = L_{ph} \frac{Nn^2}{N^2} \quad (4.114)$$

This shows that the number of turns per coil can be chosen at the end of an optimization process.

4.7.2 Differences Between ShS Supply and LS Supply

The two topologies LS and ShS are presented on Fig 4.67 and on Fig. 4.68, respectively.

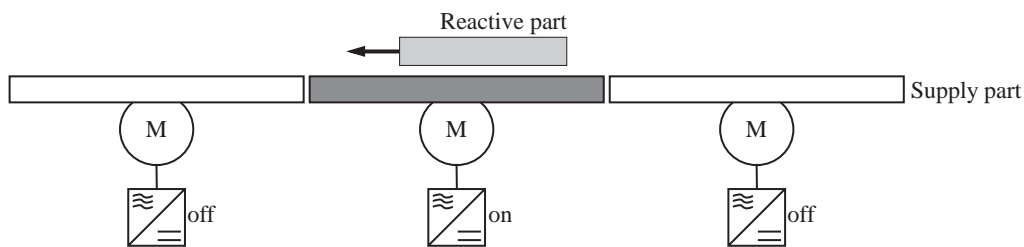


Figure 4.67: LS motor configuration.

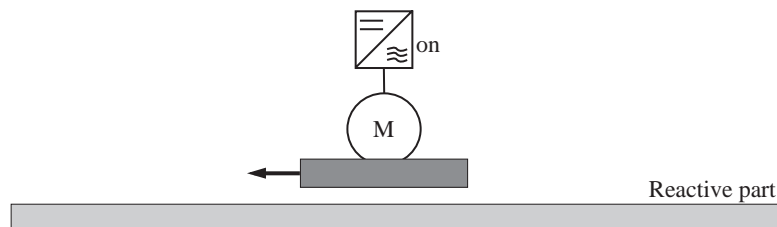


Figure 4.68: ShS motor configuration.

The main differences between these two configurations are the efficiency, the motor electrical connection and the investment costs.

A ShS motor has a better efficiency than a LS motor. Indeed, as the motor is longer than the mover and it is supplied by segments, the copper losses will be higher than in a ShS configuration. Therefore, the copper losses are introduced in [W/m] for a LS motor. Moreover, the current density for LS motor is generally increased compared to ShS motor, since the motor duty cycle is less than 1.

As introduced in Chapter 1.4, the linear motor can be made of several motor sectors, which can be electrically connected either in parallel or in series for a ShS motor. This is allowed because each motor sector has, at each time, the same induced phase voltage. On the contrary, the motor sectors can only be mounted in series for a LS motor. If this constraint is not respected, the motor will overheat. Moreover, for LS motors, supply parts situated under the way have to be switched on as the mobile progresses, the different parts of the stator being commanded by its own converter. As it is introduced in the studied case in Chapter 7, other problems must be taken into account, such as the moving mass leading to an increase of the motor power, the energy transmission, the motor duty cycle, etc.

4.7.3 Motor Working Domain

The motor can operate only in a constraint domain of the propulsion force-speed diagram, as presented on Fig. 4.69. This figure corresponds to a continuous duty cycle operation. This domain can be increased for an intermittent duty cycle.

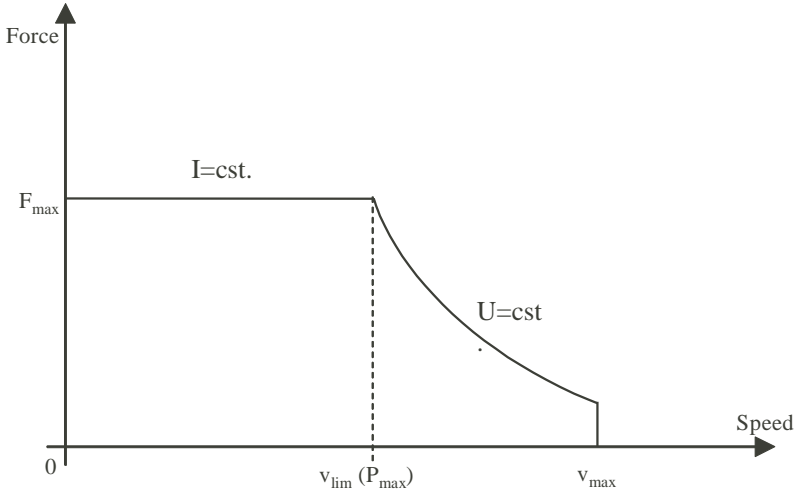


Figure 4.69: Motor general working domain for a continuous duty cycle.

In the case of a current regulation and with the current in phase with the emf, the maximum force is set by the maximum rated temperature of the motor. This force can be given until a speed equal to v_{lim} which corresponds to the maximum power given by the motor converter. Then the domain is delimited by a non linear curve where the rms voltage is imposed and constant. The equation of this curve is equal to [22]:

$$F(v) = 3 \frac{emf}{v \sqrt{R^2 + \omega^2 L_s^2}} (U \cos(\phi_s - \epsilon) - emf \cos(\phi_s)). \quad (4.115)$$

R and L_s are the resistance and the cyclic inductance per phase respectively, ϵ is the phase difference between the supply voltage and the induced voltage, ϕ_s is the phase difference between the supply voltage and the phase angle of the supply part.

The speed can be limited or not, depending on the motor specifications: to limit the iron losses, to avoid a demagnetization of the magnets, or for mechanical reasons.

4.8 Motor Cost Estimation

In a design approach the only liable price is the material cost. The assembly costs and the manufacturing costs are strongly dependent on the design itself and can consequently not be estimated as long as the design is not clearly defined. However, in the following sections several material costs are given. These prices per kilogram are based on industrial experiences. For the winding costs, another approach is presented.

As motor costs are very difficult to determine since they are dependent on the quantities, the volumes, etc., this analysis is only presented in order to show a tendency. Nevertheless this cost analysis will permit to compare two same motors technologies in terms of material costs.

4.8.1 Material Cost

The material cost is estimated through its mass as follows:

$$MC_i = C_{m_i} \cdot m_i \quad (4.116)$$

m_i is the mass of the material i consisting the motor and C_{m_i} is its cost per kilogram.

4.8.2 Winding Cost

The winding cost is estimated as follows:

$$Cost_{wind} = MC_{copper} + N \cdot \Omega_{wind}^{-1} \cdot Work_{costs}, \quad (4.117)$$

where MC_{copper} is the copper cost, N is the number of turns per coil, Ω_{wind} is the angular rotation of the machine used to wound the coil and $Work_{costs}$ are the working costs. Ω_{wind} depends on the wire diameter and the coil width.

4.9 Motor Mechanical Model

Linear motors are mainly used to perform a translational movement of a load. Therefore, the dynamic behavior of the movement is governed by the Newton's second law of motion

$$\sum \mathbf{F} = m\mathbf{a}. \quad (4.118)$$

Two simple cases of a translational motion horizontal and vertical are introduced. These cases are used in Chapter 7.

4.9.1 Horizontal Motion

In a horizontal motion, the gravity does not affect the force needed to perform the motion and therefore (4.118) becomes:

$$\mathbf{F}_m = (m_m + m_{load}) \mathbf{a} - \mathbf{F}_{res} - \mathbf{F}_{load} \quad (4.119)$$

F_m is the force produced by the motor, m_m and m_{load} are the moving masses of the motor and the load, a is the acceleration, F_{res} is a resistive force due to the guidance system and F_{load} is a perturbation force as presented on Fig. 4.70.

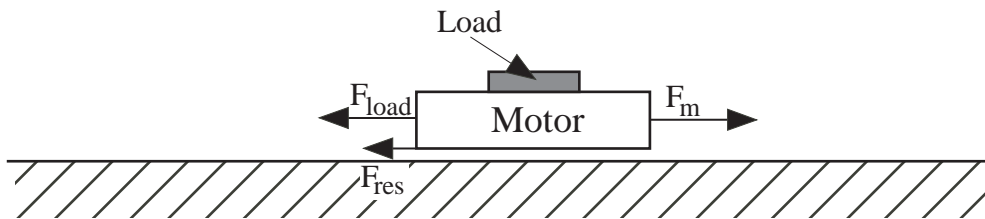


Figure 4.70: Forces acting on a motor during a horizontal movement.

4.9.2 Vertical Motion

For a vertical motion the gravity is introduced. Therefore, (4.119) becomes:

$$\mathbf{F}_m = (m_m + m_{load})(\mathbf{a} + \mathbf{g}) - \mathbf{F}_{res} - \mathbf{F}_{load} \quad (4.120)$$

a is in a vector form since the sign of a changes if the motor goes down or up. If the load weight and the motor weight are not compensated by an external concept, the motor must produce a force during a vertical displacement at constant speed.

4.9.3 Low Energy Displacement Profile

The problem of energy becomes very important in some applications. Therefore, it is interesting to define a displacement having the minimum energy consumption. The displacement is a parabola speed profile and can be approximated by a trapezoidal speed profile as presented on Fig. 4.71.

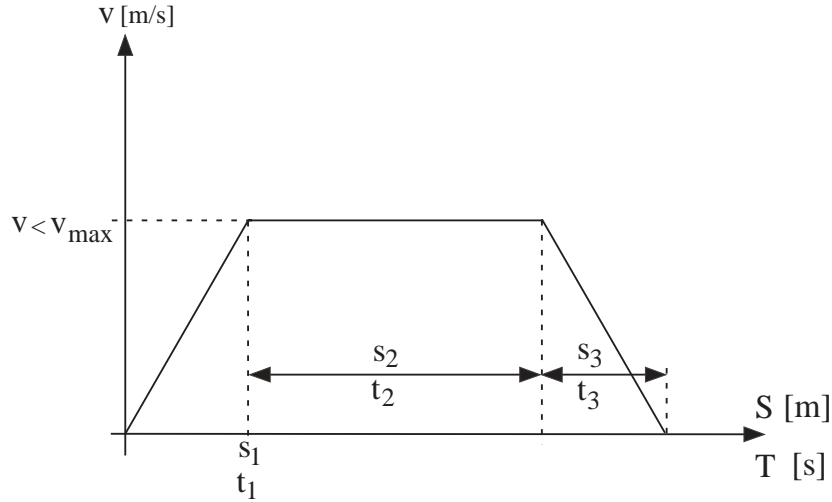


Figure 4.71: Typical displacement

This displacement of a length S_t , performed during the time T , is defined by three phases. The first is an acceleration period characterized by a constant force during a time t_1 . The second period is a displacement at constant speed v and the last phase is a deceleration period. If only the Joule losses are considered and if the mechanical losses are assumed constant (not dependant on the speed) the total energy losses are [69]:

$$W_j = 3 \cdot RI_1^2 \cdot t_1 + 3 \cdot RI_2^2 \cdot t_2 + 3 \cdot RI_3^2 \cdot t_3 \quad (4.121)$$

where R is the phase resistance and I_i are the rms currents. As the goal is to find the minimum energy losses, (4.121) must be derived with respect to the time and set equal to zero. The obtained result shows that the times t_1 , t_2 and t_3 are equal to a third of the total travelling time T . Thereafter, the acceleration a , the speed v and the distances travelled during each period can be found:

$$a_1 = -a_3 = \frac{9S_t}{2T^2}, \quad (4.122)$$

$$v = \frac{3S_t}{2T}, \quad (4.123)$$

$$s_{t1} = s_{t3} = \frac{S_t}{4}. \quad (4.124)$$

These relations are only valid if the joules losses are taken into account and if the mechanical losses are considered independent of the speed.

If the mechanical dissipation is proportional to the speed, the mechanical energy losses must be added to (4.121) and thereafter the global losses must be derived with respect to the time and set to zero. The mechanical losses are given by:

$$W_{mec} = \frac{C_v \cdot S^2}{(T - t_1)^2} \left(T - \frac{7t_1}{3} \right) \quad (4.125)$$

C_v is coefficient given the brake force in relation with the speed.

The solution of the derivative of the total energy losses cannot be analytically solved and some numerical methods can be used in order to find the solution [70].

4.10 Conclusions

Several models have been introduced in this chapter. Concerning the electromechanical part, the MaW are precisely modeled using the point current or the approximative function based on lumped magnetic schemes. For a pre-design motor, the approximative functions are enough precise and are not time consuming. For a final optimization design the precise model is advised. A global method for the choice of a winding is introduced and is valid for both rotative and linear motors. This analysis on winding introduces a distribution factor of the coil which can be used for length coils in the case of ironless motors. Nevertheless, the winding study could be completed by taken into account the iron losses due to the sub and fractional harmonics produced by the winding mmf.

Regarding the toothless and ironless motors, the given models are very accurate and are based on the Laplace's force. These models can be used to calculate the attractive and propulsion forces for all current waveforms. However, a special attention must be made to the yoke length of a toothless motor in order to limit as much as possible the cogging force generated by the plate ends.

For the toothed motor, different possibilities of using the Carter factor have been analyzed. The choice to apply it on a distance composed by the mechanical air gap and the half magnet height leads to accurate models. The end effects and the cogging forces are more important than for toothless motor. Therefore, it is advised to analyze this effect using the FEM

For the studied TFM, the model is not enough precise in order to design a correctly a motor. Compared to other models, TFM model is based on a lumped magnetic scheme. It was decided not to proceed with the optimization of this model since the prototype has shown that this motor was not adapted for the studied application. to solve the matrices and therefore, it becomes very difficult to introduce a lumped magnetic scheme in the program. The development of a more accurate model of this motor can constitute an interesting future work.

Chapter 5

Thermal Model of a Motor

5.1 Introduction

A good thermal model of a motor is as important as a magnetic motor model since it determines the admissible current density for the nominal working point. Heat transfer is the principal restrictive effect on the motor power. Therefore, the thermal behavior must be taken into account in all motor designs. To achieve a good thermal transfer, it is important to have a good motor cooling and also a good thermal exchange with the external surroundings.

The problem of heat transfer is very complex and regroups three phenomena: the conduction, the convection and the radiation. The basis theory of heat transfer is introduced in Section 5.2. Section 5.3 deals with heating sources.

In some cases, the motor duty cycle D_c , which is defined as the ratio between the ON-time of the motor and the sum of the ON and OFF times of the motor, can influence its thermal behavior. This aspect is discussed in Section 5.4.

Section 5.5 deals with experiments realized in order to validate the empirical formulas introduced in this chapter. Finally, the last section discusses the main aspects in developing the thermal model of a motor.

5.2 Theory of Thermal Transfers

5.2.1 Conduction

The thermal conduction is a transport of energy in a medium due to a temperature gradient. It is given by the Fourier's law [71, 72]. Figure 5.1 shows the thermal conduction in a cylindrical bar thermally isolated along its surface. The heat flux q through a material is given by:

$$q = k \cdot S \cdot \frac{\Delta T}{\Delta x} + c \cdot \rho_m \cdot V \cdot \frac{\partial T}{\partial t}, \quad (5.1)$$

k is the thermal conductivity of the material, ρ_m is its density, c is its specific heat, S is its surface, V is its volume and T is its temperature.

In a motor pre-design, the transient behavior can be omitted and therefore only the steady state is analyzed. This corresponds to the worst case in term of thermal constraints. Hence, (5.1) can be simplified by introducing a thermal conduction resistance R_{th} , in order to build a thermal lumped network, as:

$$q = k \cdot S \cdot \frac{\Delta T}{\Delta x} = \frac{T_2 - T_1}{R_{th}}, \quad (5.2)$$

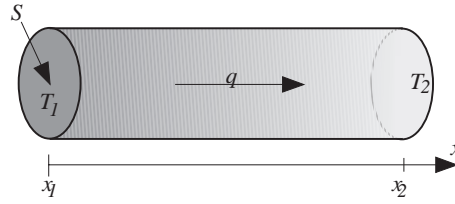


Figure 5.1: Conduction phenomena caused by a temperature gradient $\Delta T = T_2 - T_1$.

with:

$$R_{th} = \frac{x_2 - x_1}{k \cdot S}. \quad (5.3)$$

The factor k depends on the material and significant values for electrical motors are given in Table 5.1. To model the conduction, temperature dependence of the thermal conductivity is not taken into account and the values at 20°C are admitted for all materials.

Table 5.1: Thermal conductivity for several materials used in electrical motors.

Composition	k at 20 °C [W/mK]
Air	0.026
Copper	386
PM (NdFeB)	9
Steel	46
Winding insulation	0.9

For heterogenous materials it is not straightforward to calculate the conduction. This is the case for coils (copper or aluminium and insulation) and laminated stacks (iron and insulation).

For the coils, an approach to calculate the conductivity is given in [72], which proposes to join all the conductors in the center of the slot and to distribute the volume of the insulation around the copper volume. An alternative approach gives an equivalent conductivity for a slot as a function of the copper wire diameter and the distance between their centers [73]. Therefore, an equivalent thermal resistivity of 0.9 W/mK for a coil is adopted [74] and it is assumed that this value is not dependent of the coil and wire dimensions.

For laminated yokes, two materials are in parallel with the thermal flux direction. The general form of the equivalent conductivity is:

$$k_e = \sum_i V_i \cdot k_i, \quad (5.4)$$

V_i is the volume of the material i . For a laminated yoke (5.4) becomes:

$$k_e = k_f \cdot k_{ir} + (1 - k_f) k_{ins}, \quad (5.5)$$

k_f is the stacking factor (or lamination factor) which can be assumed equal to 0.95.

5.2.2 Radiation

Radiation is the energy emitted by matter of an emissivity ϵ at the temperature T_S to an open space. This heat transmission is given by the Stefan-Boltzmann's relation:

$$q_i = \sigma_{sb} \cdot \epsilon \cdot (T_S^4 - T_\infty^4) = h_r \cdot (T_S - T_\infty), \quad (5.6)$$

h_r is the radiation heat transfer coefficient given by:

$$h_r = \sigma_{sb} \cdot \epsilon \cdot (T_S^3 + T_\infty \cdot T_S^2 + T_\infty^2 \cdot T_S + T_\infty^3). \quad (5.7)$$

T_∞ is the room temperature, ϵ is the emissivity depending on the radiation surface and it is related to the black body. The value of the Stefan-Boltzmann constant is equal to $\sigma_{sb} = 5.67 \cdot 10^{-8}$.

For a black body, ϵ is equal to 1 and for the motor laminations this factor can be adopted equal to 0.95. Therefore, the radiation heat transfer coefficient h_r varies from 6 to 7 for a surface temperature in the range between 40°C and 70°C and a room temperature of 20°C.

Equation (5.6) defines a radiation thermal resistance equal to:

$$R_{th} = \frac{1}{h_r \cdot S}, \quad (5.8)$$

S is the surface of radiation.

5.2.3 Convection

Convection is a process of heat transfer between a solid and a fluid, which creates an air flow due to the density variation of the fluid caused by its temperature gradient. The free convection is only caused by density difference coming from the temperature gradient in the fluid. If the flow is created by external means (fans, winds, ...) the convection is called forced convection. Both convection processes can be described by the same equation:

$$q = \bar{h}_c S (T_S - T_\infty), \quad (5.9)$$

\bar{h}_c is the mean convection heat transfer coefficient. It changes in relation with the convection type. S and T_S are the surface in contact with the air and its temperature, respectively. This equation permits to define a convection resistance:

$$R_{th} = \frac{1}{\bar{h}_c \cdot S}. \quad (5.10)$$

The calculation of the mean convection heat transfer coefficient \bar{h}_c is based on empirical adimensional numbers depending on the convection type [71].

The convection mode imposes the theory and more particularly the adimensional number to use, for solving the problem. Indeed, the mean convection heat transfer coefficient \bar{h}_c depends on the Prandtl Pr and the Rayleigh Ra numbers for the free convection and on the Reynolds Re and Prandtl Pr numbers for the forced convection. These numbers define for both cases the Nusselt number Nu , which gives the mean convection heat transfer coefficient \bar{h}_c for a plate of a length l :

$$\bar{h}_c = \frac{\overline{Nu} \cdot k}{l}, \quad (5.11)$$

k is the thermal conductivity of the air and it depends on its temperature [71]. In this thesis, it is assumed that the temperature is uniformly distributed on the surface which participate to the convection heat transfer and that the air flow conditions are the same for the whole surface.

5.2.3.1 Free Convection

Two cases are analyzed for the free convection: a hot vertical and a hot horizontal plate, both with a finite length l , as shown on Fig.5.2.

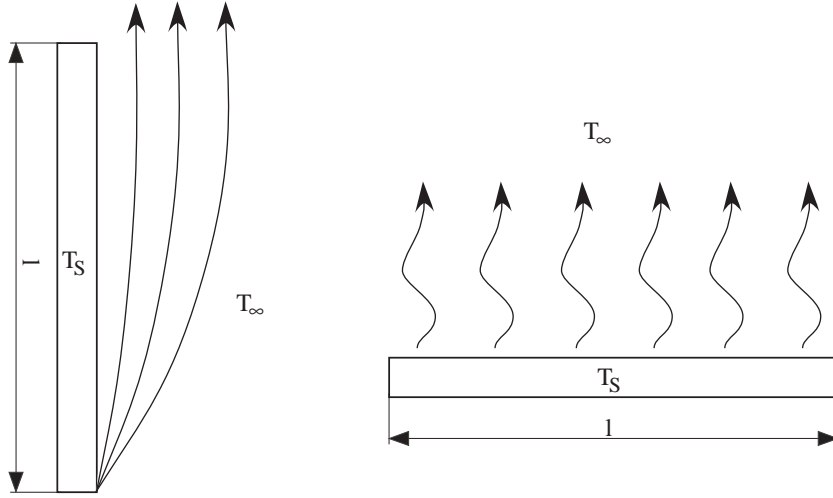


Figure 5.2: Vertical plane and horizontal plane for the study of the free convection.

In a free convection process the Rayleigh number determines the flow nature [71]. A Rayleigh number $Ra \leq 10^9$ indicates a laminar flow while upper values imply a turbulent flow. The Rayleigh number is defined as:

$$Ra_l = \frac{g \cdot \beta (T_S - T_\infty) l^3}{\nu \alpha}. \quad (5.12)$$

Here, ν is the kinematic viscosity, α is the thermal diffusivity, g is the gravity acceleration and β is the volumetric thermal expansion equal to:

$$\beta = \frac{2}{T_S + T_\infty} = \frac{1}{T_f}, \quad (5.13)$$

with T_f the film temperature.

α and ν are temperature depending. These quantities are assumed to be linear in a standard temperature range, i.e. for temperatures varying between -20°C and 180°C ¹. Therefore, α is approximated as follows:

$$\alpha = 2.25 \cdot 10^{-5} + 1.58 \cdot 10^{-7} \cdot (T_f - 300) \quad (5.14)$$

and ν is approximated by:

$$\nu = 1.59 \cdot 10^{-5} + 1.052 \cdot 10^{-7} \cdot (T_f - 300). \quad (5.15)$$

For a **vertical plate** of a length l , the Nusselt number is calculated as:

$$\overline{Nu}_l = 0.59 \cdot Ra_l^{1/4} \quad (5.16)$$

for a laminar flow (which is usually the case in linear motors). The convection heat transfer coefficient \overline{h}_c can be determined using (5.11).

For a **horizontal plate**, the Nusselt number is as follows:

$$\overline{Nu}_l = 0.54 \cdot Ra_l^{1/4} \text{ for } 10^4 \lesssim Ra_l \lesssim 10^7, \quad (5.17)$$

$$\overline{Nu}_l = 0.15 \cdot Ra_l^{1/3} \text{ for } 10^7 \lesssim Ra_l \lesssim 10^{11}. \quad (5.18)$$

¹The precision of this approximation is less than 8%.

5.2.3.2 Forced Convection

In a forced convection case, the Rayleigh number is replaced by the Reynolds number Re in order to differentiate the laminar from the turbulent flow. If this dimensionless number is over the critical Reynolds number $5 \cdot 10^5$, the flow is assumed as turbulent. Reynolds number is dependent on the plate length and is equal to:

$$Re_l = \frac{v_\infty \cdot l}{\nu}, \quad (5.19)$$

where v_∞ is the external flow velocity. For a forced convection the properties of the gases must be evaluated for the temperature T_f , called the film temperature:

$$T_f = \frac{T_S + T_\infty}{2}. \quad (5.20)$$

The interesting case is a finite horizontal plate of a length l with an external flow of a speed v_∞ and at temperature T_∞ blowing above it. For a laminar flow, the Nusselt number is equal to:

$$\overline{Nu}_l = 0.6654 \cdot Re_l^{1/2} \cdot Pr^{1/3} \quad (Re_l \lesssim 10^5), \quad (5.21)$$

with:

$$Pr(T_f) = \frac{\nu(T_f)}{\alpha(T_f)} \quad (5.22)$$

For a turbulent flow an approach to calculate the Nusselt number is given in [71] and it is equal to:

$$\overline{Nu}_l = 0.037 \cdot Re_l^{4/5} \cdot Pr^{1/3}. \quad (5.23)$$

Thereafter, the convection heat transfer coefficient can be deduced from (5.11) and an equivalent thermal resistance can be calculated.

5.3 Heating Sources

The heating sources in motors are Joule losses and iron losses which regroup the hysteresis losses and the eddy current losses.

5.3.1 Joule Losses

Due to the electrical resistivity of the conductor, Joule losses are temperature dependent. Without taking into account the skin effect, Joule losses are equal to:

$$P_{cu}(T) = m \cdot R_{ph}(T) \cdot I_{ph}^2 = \rho_{cu} \cdot V_{cu} \cdot J^2 \cdot (1 + \alpha_c \cdot \Delta T). \quad (5.24)$$

Here, m is the number of motor phases, R_{ph} is the phase resistance, I_{ph} is the rms current in one phase, V_{cu} is the total copper volume of the motor, α_c is the temperature coefficient (0.004 for the copper), ρ_{cu} is the copper resistivity and J is the current density.

5.3.2 Iron Losses

Iron losses are the sum of hysteresis losses and eddy current losses [72].

Hysteresis losses are due to the non-linearity between the flux density B and the magnetic field H in a material, which is caused by a delay to magnetize or demagnetize the material. When the flux density in the material varies between two values, B_{min} and B_{max} , losses are proportional to the hysteresis surface and to the frequency of the flux density f . Moreover, since the energy in a material is proportional to the product of the flux density and the magnetic field, hysteresis losses are proportional to the square of the flux density \hat{B} if the hysteresis cycle is symmetric as on Fig. 5.3 [22]. To reduce these losses, the use of ferromagnetic material with a thin hysteresis cycle (FeNI or FeSI) is recommended. Hysteresis losses are given by:

$$P_h = C_h \cdot f \cdot \hat{B}^2 \cdot m, \quad (5.25)$$

C_h is the coefficient of the hysteresis losses and m is the mass of the material excited by the flux density.

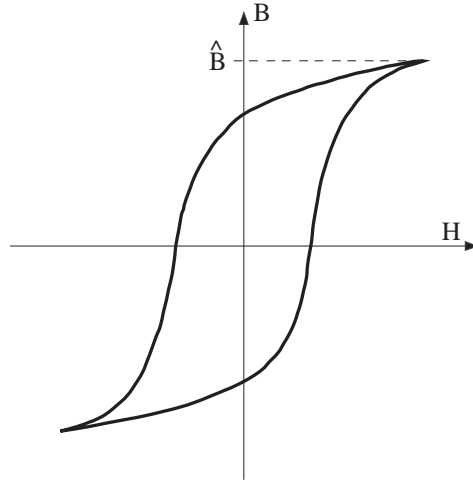


Figure 5.3: Hysteresis cycle.

Eddy currents in a material are generated by an alternative flux density. Eddy currents are proportional to the square of the flux density and the frequency square [75]. To reduce Eddy currents, the electrical resistivity must be increased. Therefore, magnetic circuits are splitted up to several lamination of a thickness e . Eddy currents are equal to:

$$P_w = C_w \cdot f^2 \cdot \hat{B}^2 \cdot e^2 \cdot m. \quad (5.26)$$

In practical cases, for a given thickness of lamination and a given quality, iron losses including the two effects are the sum of (5.25) and (5.26):

$$P_{Fe} = f \cdot \hat{B}^2 \cdot m \cdot [C_h + C_w \cdot f \cdot e^2] \quad (5.27)$$

This expression is simplified as follows:

$$P_{Fe} = C_p \left(\frac{f}{50} \right)^k \left(\frac{\hat{B}}{1} \right)^2 m. \quad (5.28)$$

The values k and C_p are generally given by the manufacturer or they can be deduced from experimental measurements, [74] gives some coefficients. Due to a high polarization created by magnets, iron

losses are neglected for the toothless motor. For other motors iron losses must be taken into account in the stator part as well as in the reactive part. Iron losses in the stator are mainly due to the pulsating field produced by the magnets. Furthermore, additional iron losses in the stator are due to the magnetic flux produced by the coil supply. Additional losses produced by a PWM command are not taken into account. For the reactive part, iron losses are due to magnetic flux produced by the coil and by the magnetic flux pulsation produced by the variation of magnetic tooth permeance.

A good approximation of the losses are obtained using only the fundamental of the Fourier series of the magnetic flux density.

5.3.3 Magnet Losses

The resistivity of sintered NdFeB magnets is rather low ($\rho_{PM} \cong 100 \cdot 10^{-6} \Omega/m$). Therefore, the Eddy current losses in conductive PM due to magnetic fields produced by the stator slots and the coil mmf cannot be neglected. These losses are generated by the harmonics frequency of the magnetic flux. For a PM (Fig. 5.4) the current density J_y flowing in the magnet is deduced from (2.10) and it is equal to [76]:

$$J_y(x) = \frac{x}{\rho_{pm}} \cdot \frac{dB}{dt} \quad (5.29)$$

If it is assumed that the induced currents in the PM do not perturb the flux density in the air gap, that the flux density is perpendicular to the magnet surface and is no position dependent and that the end effects of the magnet are neglected, the current density has therefore only a component in the y-direction.

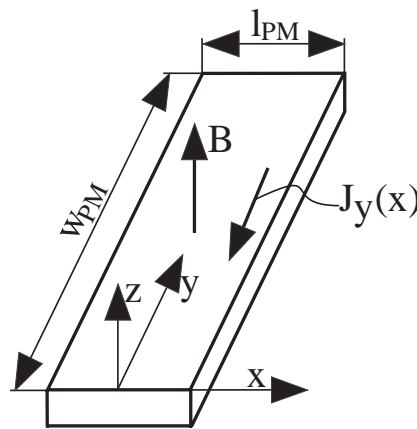


Figure 5.4: Magnet losses produced by a pulsed magnetic flux density B .

As the flux density is assumed uniform, the magnet losses are equal to

$$P_{pm}(t) = \rho_{PM} \int J_y^2(x) \cdot dV_{pm} = \rho_{pm} \cdot h_{pm} \cdot w_{pm} \int_{-l_{pm}}^{l_{pm}} J_y^2(x) \cdot dx \quad (5.30)$$

$$P_{pm} = \frac{w_{pm} \cdot h_{pm} \cdot l_{pm}^3}{12\rho_{pm}} \cdot \frac{1}{T} \int_0^T \left(\frac{dB}{dt} \right)^2 dt \quad (5.31)$$

ρ_{PM} is the resistivity of the PM.

The assumption that the flux density seen by the PM is only time dependent leads to over estimate the Eddy current losses in the PM. The flux density, presented on Fig. 5.6, seen by the magnet and due to

a tooth travelling along the axis x above the magnet (Fig. 5.5) can be modelled by a travelling wave as:

$$B_{pm}(x, t) = \bar{B} + \hat{B} \cdot \sin\left(\frac{\pi \cdot x}{\tau_n/2} - \omega_{pm} \cdot t\right), \quad (5.32)$$

ω_{pm} is the frequency pulsation seen by the magnet. This value is equal to:

$$\omega_{pm} = 2\pi \frac{v}{\tau_n}. \quad (5.33)$$

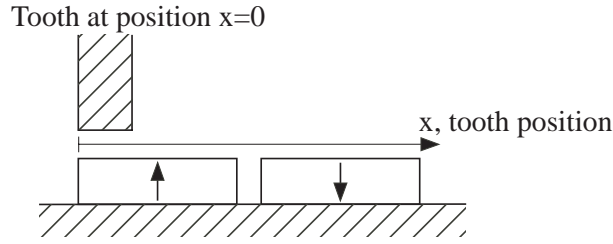


Figure 5.5: Tooth travelling along the axis x above the magnet.

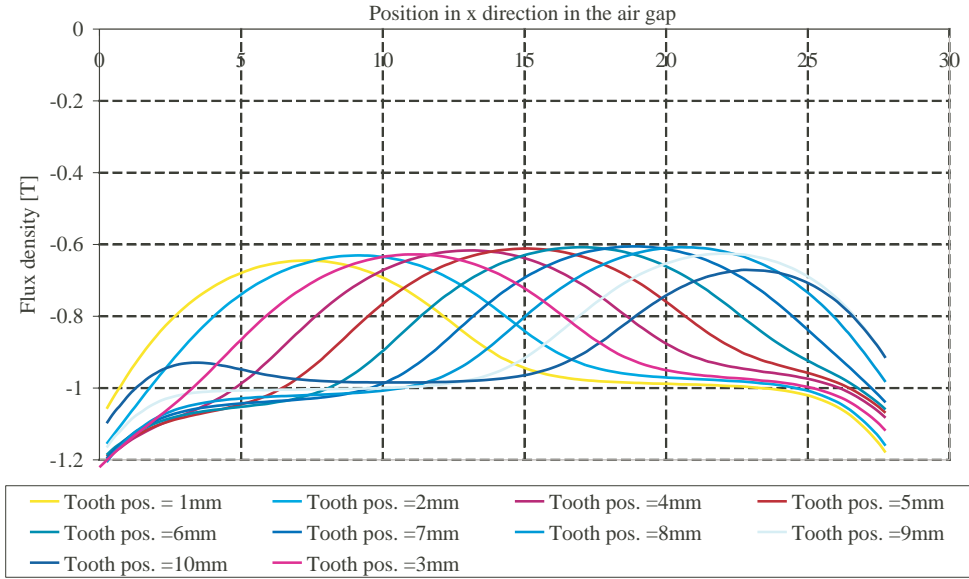


Figure 5.6: Flux density waveform above the magnet for several stator positions, tooth-slot interaction on the flux density.

Therefore, the flux variation in the PM is equal to:

$$emf_{pm} = -\frac{d\phi}{dt} = -\frac{d}{dt} \int \int_{S_{pm}} B_{pm}(x, t) \cdot dS, \quad (5.34)$$

S_{pm} is the PM surface. Thereafter, the Eddy current losses into the PM can be evaluated as

$$P_{pm} = \frac{emf_{pm}^2}{R_{pm}}, \quad (5.35)$$

with R_{pm} the PM resistance equal to

$$R_{pm} = \rho_{pm} \cdot \frac{2w_{pm}}{h_{pm} \cdot l_{pm}/2} \quad (5.36)$$

Therefore, using (5.34) and (5.32) into (5.35), the magnet losses at no load into one magnet are equal to

$$P_{pm} = \frac{\left(\frac{2 \cdot w_{pm} \cdot \omega_{pm} \cdot \hat{B} \cdot \tau_n \cdot \pi}{2\sqrt{2}} \cdot \sin\left(\frac{l_{pm} \cdot \pi}{\tau_n}\right) \right)^2}{R_{pm}} \quad (5.37)$$

5.4 Impact of the Motor Duty Cycle on the Motor Design

The duty cycle of the motor is defined as follows:

$$D_c = \frac{t_{on}}{t_{on} + t_{off}}, \quad (5.38)$$

t_{on} and t_{off} are the ON-time duration and the OFF-time duration of the motor, respectively. In most cases, the motor duty cycle D_c is less than 1 and the maximum allowed current density of the motor can be increased compared to a motor with $D_c=1$. Therefore, the motor volume can be reduced.

First, the thermal constant of the motor is estimated using (5.1):

$$\tau = R_{th} \cdot c \cdot \rho_m \cdot V_{cu}, \quad (5.39)$$

for which only the thermal capacitance c of the copper and the free convection are considered. This corresponds to the worst case. Depending on the thermal constant τ , two cases appear:

1. the thermal constant is smaller or close to the ON time. Then, the transient behavior must be studied in order to find the maximum reached temperature which defines the current density limit;
2. the thermal constant is much higher than the ON time. Therefore, the difference between the temperatures when the motor is supplied and when it is switch off is low. The average temperature is considered in order to fix the maximum current density.

During the ON time, the coil temperature increases as:

$$T(t) = T_{max} \cdot (1 - e^{-t/\tau}) + T_0 \cdot e^{-t/\tau} \quad (5.40)$$

During the OFF time, the coil temperature decreases following:

$$T(t) = T_0 \cdot e^{-t/\tau} - T_\infty \cdot (e^{-t/\tau} - 1). \quad (5.41)$$

T_0 is the initial coil temperature at the beginning of transient mode (ON or OFF), T_{max} is the temperature reached for $t = \infty$ and T_∞ is the ambient temperature.

In the first case, the thermal behavior must be analyzed using (5.40) and (5.41). T_{max} is delimited by the motor specifications and fixes the limit current density.

For the second case, the motor is first analyzed for a duty cycle of $D_c = 1$ permitting to consider only the stable state. This fixes the maximum current density $J_{D_c=1}$ and therefore the maximum losses for a given T_{max} . Thereafter, by keeping the same mean losses, the new current density depending on the duty cycle is defined as:

$$J_D = \frac{J_{D_c=1}}{\sqrt{D_c}} \quad (5.42)$$

if the saturation of the iron is neglected. Consequently, for a given propulsion force, the active width w_{pm} can be decreased.

In such an approach, the current density must be also bounded in order not to demagnetize the PM, i.e. the stator mmf must be smaller than the PM mmf ($\theta_{coil}/\theta_{PM} < k_{dem}$).

5.5 Experiments

In order to validate the empirical formulae, two measurements have been realized. They consist in measuring the convection and radiation of an iron plate heated by electrical resistances and of a geometry similar to a toothless motor.

5.5.1 Heated Iron Plate

5.5.1.1 Set-up

The heated iron plate used in measurements is presented on Fig. 5.7. Resistances to heat the plate are located in slots and a thermal conductive paste guarantees a good thermal transfer between the plate and the resistances (Fig. 5.8).

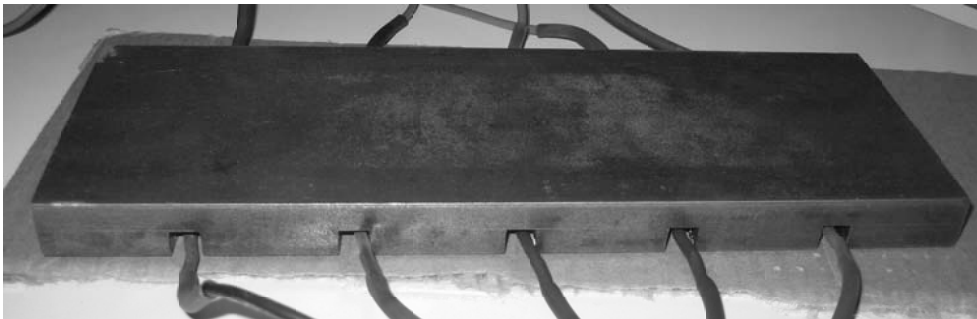


Figure 5.7: Convection and radiation evaluation of an iron plate, experiment measurements.

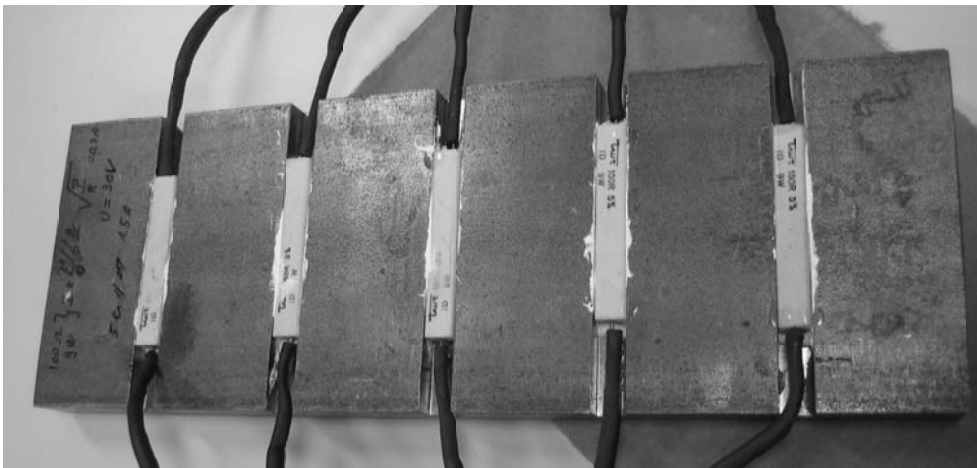


Figure 5.8: Resistance network to heat the iron plate.

During the measurements, the plate is placed on a paperboard in order to isolate its bottom face. Furthermore, the emissivity of the plate is assumed to be 0.95. Plate sizes are:

- Plate length: 230 mm
- Plate width: 80 mm
- Plate height: 15 mm

To realize good measurements, the thermal steady state must be reached and the temperature must be uniformly distributed on the surface (for the plate, three points of measurements).

5.5.1.2 Results: Free Convection

Table 5.2 gives results of measurements and calculations for two different electrical powers. The radiation and convection heat transfer coefficients can be summed to form a coefficient \bar{h}_{cr} , as given in Table 5.2.

Table 5.2: Results of the measurements of the horizontal plate.

Electrical power W	Plate temperature °C	Room temperature °C	Convection + Radiation \bar{h}_{cr}	
			Theory W/°K/m ²	Experiments W/°K/m ²
17	60	24	12.4	14
21.5	78.5	23	13.7	14.6

The theoretical coefficient h_{cr} is calculated by applying the theory given in Sections 5.2.2 and 5.2.3 to all the surfaces of the plate, except the one in contact with the paperboard. Therefore, \bar{h}_{cr} is equal to:

$$\bar{h}_{cr} = \frac{P}{(T_S - T_\infty) \cdot S} \quad (5.43)$$

P is the electrical power needed to heat the plate and S is the total surface area in contact with the ambient air.

There is a discrepancy between theory and experiment. This comes probably from the assumption that no heat transfer is performed between the plane and the paperboard. As the theory gives a lower combined coefficient \bar{h}_{cr} than the measurements, this permits to accept the theoretical values and to apply them to motor design.

For this example, the theoretical convection and radiation coefficients as well as the combined coefficient \bar{h}_{cr} as a function of the plate temperature are given on Fig. 5.9.

Furthermore, additional measurements have also been performed with a vertical plate. These measurements are less in accordance with the theory (5.16) since a difference up to 18% appears between the theory and the measurements. In practice the plate dissipate more heat than predicted by theory. Therefore, if the motor is designed in accordance with the theory, the current density will be constraint to a value of about 8% less than the motor can admit. This difference gives a security margin.

5.5.1.3 Forced Convection

To measure the forced convection, the plate was introduced into a small wind tunnel. A grate in the input and output of the wind tunnel make the airflow laminar. The velocity and the temperature of the air were measured with an anemometer with integrated thermometer.

During measurements, the pressure in the tunnel is assumed equal to the atmospheric pressure. This assumption results in neglecting the dependence of the kinetic viscosity in the pressure. Indeed, the kinetic viscosity varies with pressure through its dependance on density.

The obtained results are summarized in Table 5.3. They are completed by the relation of \bar{h}_{cr*} given by [74] which is equal to:

$$\bar{h}_{cr*} = 12 + 6 \cdot v^{0.8} \quad (5.44)$$

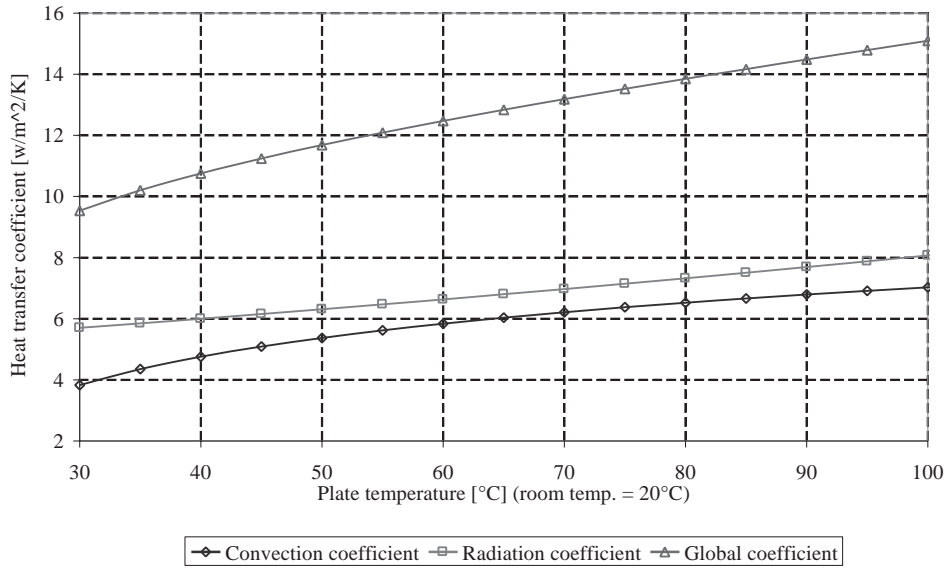


Figure 5.9: Convection, radiation and combined coefficients as functions of plate temperature (room temperature = 20°C).

Table 5.3: Results of the measurements of the horizontal plate in the wind tunnel.

power W	air velocity m/s	Measurements			Theory		
		plate temp. °C	room temp. °C	h_{cr} W/°K/m ²	plate temp. °C	h_{cr} W/°K/m ²	h_{cr}^* W/°K/m ²
23.3	2	40.5	14	31.7	56.5	19.75	22.4
42.7	2	61	14	32.8	90.7	20.1	22.4
42.7	2.9	56.5	13.8	36.2	76.1	24.8	26.1
42.8	3.2	56	14.2	37	73	26.3	27.2
42.7	4.1	49	14.5	44.7	64.8	30.6	30.5

This relation is an approximative function where the coefficient 12 represent the convection and radiation without a forced air. It is interesting to denote that both the formulae (5.23) and (5.44) are very similar, as shown in Table 5.3.

The results are not in accordance with the theory since a difference of about 50% is obtained. Several other formulae such (5.23) were used in order to obtain a better correlation with the practical measurements, but the obtained results were less accurate. As h_{cr} is proportional to the power, the difference could be explained partially taking into account the thermal transfer to the bottom of the plate. Nevertheless, these power losses must be small since the plate is thermally insulated. The difference comes certainly from the end effect of the plate, where some small whirlwind are generated.

To conclude, the proposed formula (5.23) is not appropriate for a pre design process where dimension constraints are very restrictive. In this case, a corrective factor should be introduced with care. If the weight or the motor volume is not constraining, (5.23) can be applied, as consequence to underdesign the current density.

5.5.2 Fictive Toothless Motor

5.5.2.1 Set-up

The fictive toothless motor consists of three coils in series supplied by a DC source. An aluminium plate recovers the coils and the air gap between the coils and the plate can be adjusted. Figure 5.10 shows the analyzed configuration. The emissivity of the aluminium plate is assumed equal to 0.82 and the plate sizes are the following:

- plate length: 230 mm
- plate width: 80 mm
- plate height: 15 mm

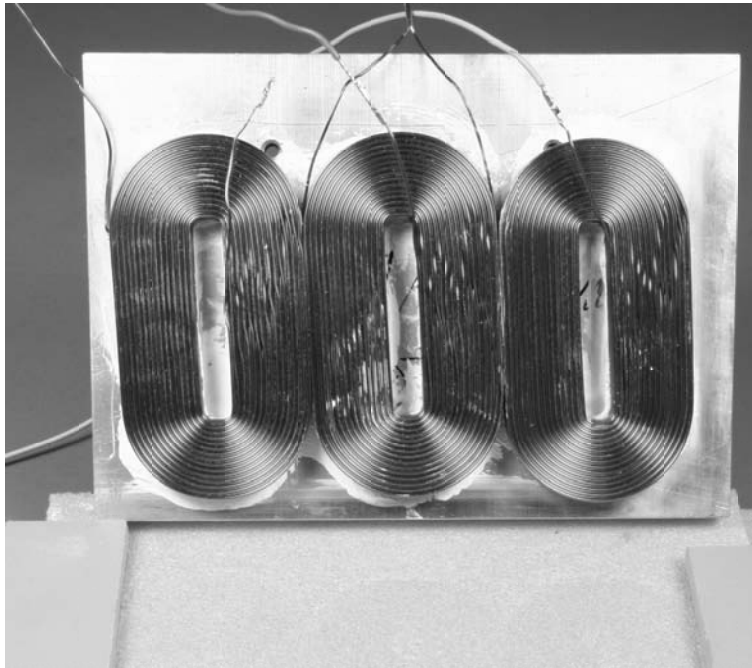


Figure 5.10: Convection and radiation evaluation of a fictive toothless motor, experiment.

As for the previous analysis, coils are thermally isolated on their bottom faces and it is assumed that no thermal transfer occurs in this direction.

5.5.2.2 Results: Free Convection, horizontal

During this experiment, the temperatures of the coils and the plate are measured for several air gaps. Table 5.4 shows the results for the steady state.

To compare these measurements with the theory, a simple lumped thermal model is built and it is presented on Fig. 5.11. $R_{th\ coil}$ is the conduction thermal resistance of the coil, $R_{th\ air\ gap}$ is the thermal resistance of the air gap and $R_{th\ conv+rad}$ is the thermal resistance modelling the convection and the radiation of the aluminium plate. The thermal resistance of the air gap is split in two thermal resistances. The first thermal resistance $R_{th\ air\ gap\ 1}$ modelizes the heat transfer in direction of the room temperature. The second $R_{th\ air\ gap\ 2}$ modelizes the thermal transfer between the coils and the plate. The conductivity

Table 5.4: Results of the thermal measurements of the fictive toothless motor.

Electrical power W	Air gap mm	Temperature		
		Coils °C	Plate °C	Room °C
5.3	1.5	62	50	22.5
9	1.5	84.5	63	22.5
5.4	2.9	69	47	24
8.2	2.9	91	59	23
10.2	0	76.5	76	23

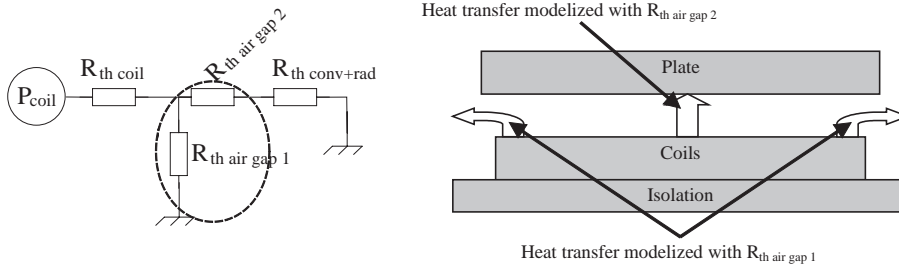


Figure 5.11: Theoretical consideration for convection and radiation evaluation of a fictive toothless motor.

thermal resistance of the plate is near zero and therefore it is not taken into account. The main difficulty is to model the thermal transfer into the air gap. The first step is to assume that all the power produced by the coils flows through the plate. Therefore, $R_{th\ air\ gap\ 1}$ is assumed equal to infinity. The coil thermal resistance is calculated using (5.3) and the thermal resistance of the plate is estimated using (5.8) and (5.10).

For the air gap it was first assumed that the heat transfer is made by conduction but this assumption leads to inaccurate results. Therefore, the heat flow in the air gap is modelled by a rectangular cavity. Globe and Dropkin proposed an empirical formula for the horizontal cavity heated from below [71]. This relation is equal to:

$$\overline{Nu}_L = \frac{\bar{h}_c \cdot L}{k} = 0.069 \cdot Ra^{1/3} Pr^{0.074}. \quad (5.45)$$

This model gives the results shown in Table 5.5.

Table 5.5: Model results of the thermal behavior of the fictive toothless motor with the air gap modelled by a rectangular cavity.

Electrical power W	Air gap mm	Exp. temperature			Model temperature		
		Coils °C	Plate °C	Room °C	Coils °C	Plate °C	Room °C
5.3	1.5	62	50	22.5	59.1	49.2	22.5
9	1.5	84.5	63	22.5	81.2	64.7	22.5
5.4	2.9	69	47	24	62.1	47	24
8.2	2.9	76.5	76	23	77.3	62	23

The comparison with the measurements validates the theory for the convection and radiation thermal resistance of the plane. For an air gap of 1.5 mm, the model is in good agreement with the measurements

and permits to conclude that for small air gaps, the use of the rectangular cavity is a good approach. For higher air gaps this model does not provide accurate results. A model of an air gap in rotative motors has been developed in [73] where it is proposed to fix the Nusselt number at the value of $Nu = 2$ in the air gap. This value is given for low speed rotation and can be therefore adopted for linear motors at standstill (critical case). The obtained results are in agreement with the theory, as shown in Table 5.6.

Table 5.6: Model results of the thermal behavior of the fictive toothless with $Nu = 2$ in the air gap.

Electrical power W	Air gap mm	Temperature		
		Coils meas. °C	Coils model °C	Room °C
5.3	1.5	62	66.6	22.5
9	1.5	84.5	93.7	22.5
5.4	2.9	69	70	24
8.2	2.9	91	89.1	23

Therefore, the use of $Nu = 2$ seems to be a good approach. As the theory gives higher temperatures of the coils than the measurements, it implies a more restricting limitation on the maximum allowed current density.

This model can be used in all cases. However, for a better accuracy in cases with small air gaps, the air gaps can be modelled with a rectangular cavity.

5.5.2.3 Results: Free Convection, vertical

To model the air gap, several relations proposed by [71] were tested as well as the modelization of the air gap by a parallel plate channel as well as by a rectangular cavity. The best correlation with the measurement has been obtained using:

$$\overline{Nu}_L = 0.42 \cdot Ra_L^{1/4} Pr^{0.012} \cdot \left(\frac{l_m}{\delta}\right)^{-0.3}, \quad (5.46)$$

which gives the Nusselt number for a rectangular cavity with a large ratio l_m/δ , where δ corresponds to the air gap height and l_m is the pseudo motor length. This relation gives a Nusselt number near 2, as it was proposed in Section 5.5.2.2.

A good agreement with the measurements is obtained as presented in Table 5.7

Table 5.7: Comparison between the measurements and model results of the thermal behavior with $Nu=2$ in the air gap.

Electrical power W	Air gap mm	Temperature measurements			Temperature calculation	
		coils °C	plate °C	room °C	coils °C	plate °C
9.2	2.5	85	52	19	93	64
5.6	2.5	59	43	19	67	48

5.5.2.4 Results: Forced Convection

The main difficulty is to model the air gap, i.e. the two thermal resistances modelling the air gap (Fig. 5.11). Indeed, in this case, the thermal resistance $R_{th\ air\ gap\ 1}$ can not be assumed equal to infinity, since the ambient air flows in the air gap.

Several models were tested in order to estimate as precisely as possible the temperature of the coils and the plate. They are summarized as follows:

1. the air gap is modelled with a rectangular cavity and $R_{th\ air\ gap\ 1}$ is assumed infinite;
2. the thermal resistance $R_{th\ air\ gap\ 2}$ is assumed zero and $R_{th\ air\ gap\ 1}$ is modelled using a relation for a laminar flow in tubes [71];
3. the thermal resistance $R_{th\ air\ gap\ 2}$ is estimated by taking into account only the radiation and $R_{th\ air\ gap\ 1}$ is modelled using a relation for a laminar flow in tubes;
4. the thermal resistance $R_{th\ air\ gap\ 2}$ is estimated by assuming $Nu = 2$ and $R_{th\ air\ gap\ 1}$ is modelled using a relation for a laminar flow in tubes.

The simplest approach (the first model) gives inaccurate temperature values: the coil temperature are about two times and the plate temperature up to four times higher than those obtained in measurements. Therefore, the thermal resistance $R_{th\ air\ gap\ 1}$ must be taken into account, as it is done in the second model. It is obtained using the relation given in [71], which gives the Nusselt number in relation to the flow tube dimension, i.e. for the presented case in relation with the air gap and the pseudo motor width. In this case the given Nusselt number is $Nu_{tube} = 5$. Therefore, the thermal resistance $R_{th\ air\ gap\ 1}$ is equal to:

$$R_{th\ air\ gap\ 1} = \frac{D_h}{Nu_{tube} \cdot k \cdot w_m \cdot l_m} \quad (5.47)$$

D_h is the hydraulic diameter and it is given by:

$$D_h = \frac{4 \cdot S_c}{P}, \quad (5.48)$$

S_c and P are the flow cross-sectional area and the wetted perimeter, respectively. This second model leads also to non accurate results which permits to conclude that the thermal resistance $R_{th\ air\ gap\ 2}$ can not be assumed as zero.

For the two last models both thermal resistances $R_{th\ air\ gap\ 1}$ and $R_{th\ air\ gap\ 2}$ are taken into account. Three possibilities to model the air gap were analyzed, as shown on Fig. 5.12.

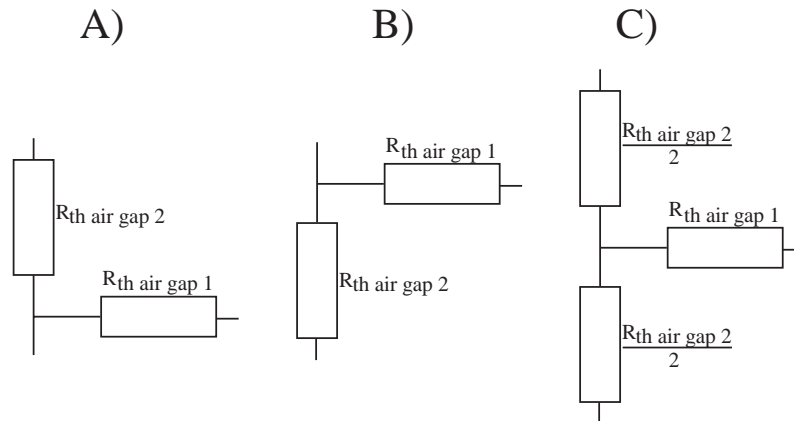


Figure 5.12: Three possibilities to model the air gap.

The best results are obtained by modelling the air gap with the lumped thermal resistance (C) and to assume $Nu = 2$ for the heat transfer between the coils and the plate. The results are given in Table 5.8.

Table 5.8: Comparison between the measurements and the theoretical values for the pseudo ironless motor in the wind tunnel and comparison with the presented model.

Measurements						Theory		
power W	air gap mm	air speed m/s	temperature			temperature		
			coil °C	plate °C	room °C	coil °C	plate °C	h_{cr} W/°K/m ²
10.61	1.5	2	55	33	13	51.1	22.7	21.2
10.8	1.5	3.1	50	28	12.2	50.5	21	27.7
19.6	1.5	3.1	70	36.5	12.5	81	28.4	27.7
30.3	1.5	3.2	92	49	12.5	116	36.6	28.3
10.3	3	2	62	21	12.5	67.6	25.2	21.1
18.3	3	3.2	91	24	12.6	107	32.2	28.3
27.2	3	3.2	122	27	12.6	150	41.9	28.3

This model gives acceptable results, even if it is not so accurate then those presented in the previous sections. This comes from the difficulty to model the air gap. Indeed, the proposed model of the thermal resistance $R_{th\ air\ gap\ 2}$ does not take into account the variation of the air gap.

Therefore, to build a more accurate model, it is recommended to perform several experiments on a structure having geometrical dimensions close to those given by motor design and to fit the experiment results with, for example, a polynomial model.

5.6 Motor Thermal Model

The purpose of a thermal model is to fix the maximum current density in the coil in order to not exceed the material allowed temperature. The temperature range of each material is given by the insulation class. The motor is generally built for a specified insulation class (A, B, F, H, etc). Therefore, a thermal model is essential for motor design.

To develop a thermal model several assumptions are made:

1. the heat transfer is only carried out to the room air;
2. there is no air flow in the air gap ($R_{th\ air\ gap\ 1} = \infty$) since it is a restrictive case;
3. the thermal conductivity of the iron parts (PM, yokes, ...) is assumed ideal ($R_{th} = 0$);
4. external additional coolings are taken into account by empirical coefficients;
5. for toothless motors, the only considered losses are Joule losses.

A methodology to build a motor thermal model is illustrated on Fig. 5.13, where the dashed boxes are the input parameters of the model and boxes with thick solid lines are the outputs. The first step is to define all the losses in the motor. Then the equivalent thermal resistances are calculated by assuming a forced convection heat transfer coefficient for the moving part. The convection is therefore calculated for an air flow equal to the motor speed. Once the thermal resistances and the losses are determined, a motor thermal model is developed. Thereafter, the maximum current density is found. Furthermore, if the motor has an external cooling, the maximum current density can be increased by a cooling factor given in Table 5.9. These factors are determined by industrial experiences (ETEL SA). With the increase of the current density, the magnet width can be decreased.

For toothless motors and the TFM motor, the thermal models are trivial. Therefore, only a thermal model for toothed motors is presented here as an example.

Table 5.9: Cooling factors permitting to increase the current density.

	No cooling	Air cooling under pressure	Water cooling under pressure
Cooling factor	1	1.6	2.5

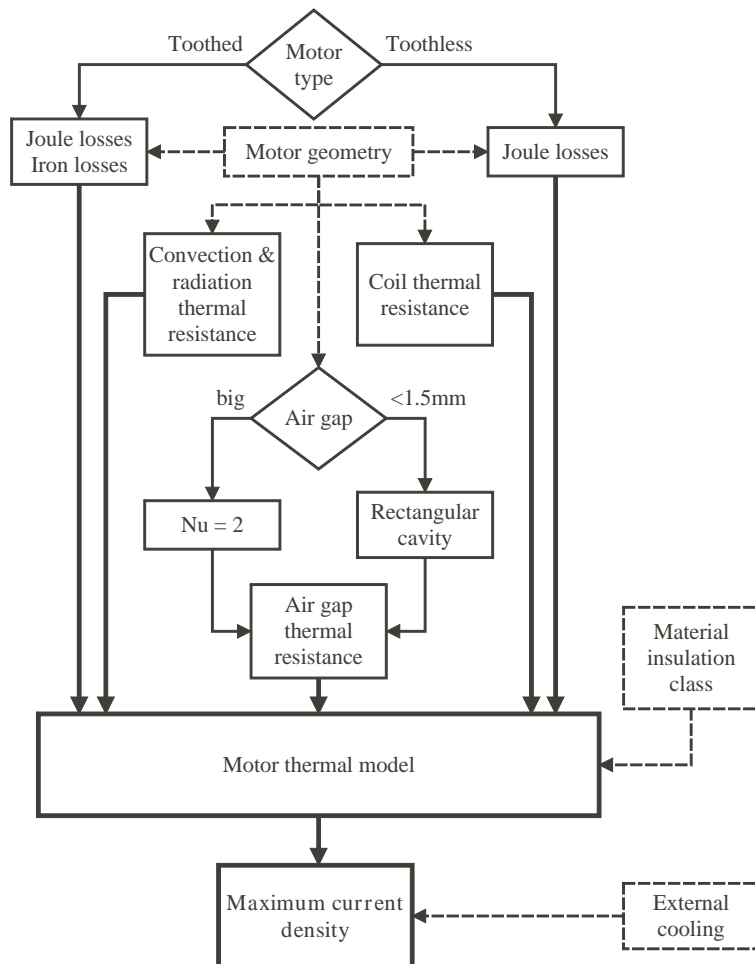


Figure 5.13: Schematic of the thermal model development.

5.6.1 Example: Thermal Model of a Short Stator Toothed Motor

The thermal model of the motor studied in Section 4.5 is developed.

First, the conditions for the motor thermal model are chosen. Indeed, the thermal model changes following the work conditions (motor at standstill, LS or ShS with a constant speed, etc.). For the example, it is assumed that the supply part moves with a speed of 1 m/s and therefore the motor surface exchanges its heat by radiation and forced convection.

The approach consists to evaluate the mean losses of each part and to build a lumped thermal model.

Figure 5.14 shows the heating sources produced by the toothed motor. They consist on the iron losses in the yokes (MaW and supply part) and the teeth, on the Eddy currents in the PM and the Joule losses in the winding. The goal is to regroup all the mean losses of the same nature and of the same level. Therefore, the copper losses represent only one heating source. The same approach is taken for the iron losses. The lumped thermal model is shown on Fig. 5.15.

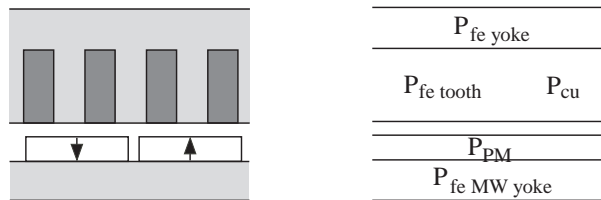


Figure 5.14: Heating sources of a toothed motor.

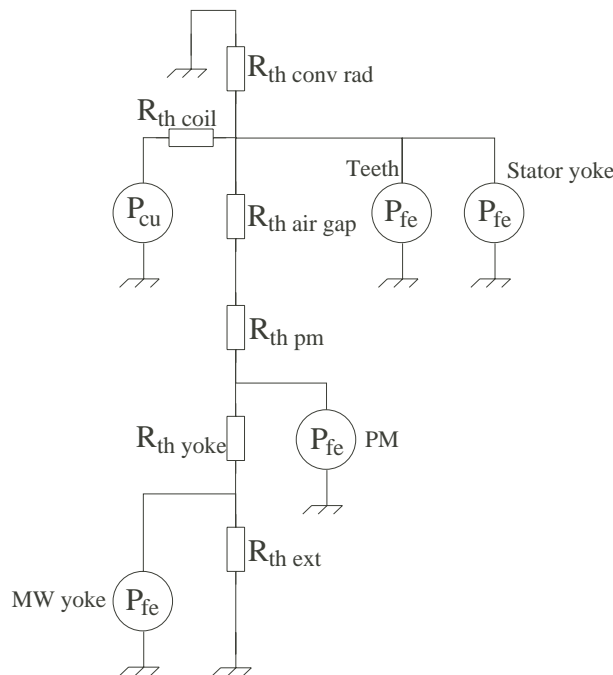


Figure 5.15: Global thermal model of a toothed motor.

The global thermal model shows, for a better understanding, the thermal conduction resistances. Such a model is very straightforward to build and it is in most cases enough precise.

If the conduction thermal resistance of PM and of the yoke are neglected and it is assumed no heat transfer in the MaW direction ($R_{thext} = \infty$), the scheme can be simplified as shown on Fig. 5.16. In

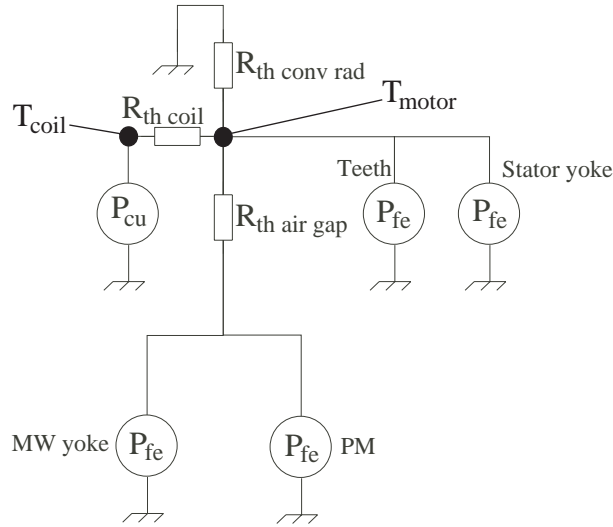


Figure 5.16: Simplified thermal model of a toothed motor.

this example, it is assumed that the motor has a long stroke and therefore the losses in the MaW (PM and yoke) do not influence the thermal behavior of the moving part. These heating sources can also be suppressed on Fig. 5.16. Therefore, the temperature of the MaW can be assumed equal to the room temperature.

All the iron losses P_{fe} are calculated for each iron parts (MaW yoke, teeth and stator yoke) following (5.28). The peak value of the flux density in each part can be estimated using a lumped magnetic scheme. For the studied motor, Table 4.21 gives the peak value of the flux density in the teeth and in the yoke supply part, in no-load. Therefore, if the stator is built with a standard laminated iron (N800-50HA), the following iron losses, at no-load, are obtained:

$$P_{feTeeth} = 1.1 \left(\frac{v/(2 \cdot \tau_p)}{50} \right)^{1.6} \left(\frac{\hat{B}}{1} \right)^2 (N_t \cdot w_{pm} \cdot h_t \cdot l_t \cdot \rho_{ir}) = 0.18 \text{ [W]}, \quad (5.49)$$

$$P_{feStatoryoke} = 1.1 \left(\frac{v/(2 \cdot \tau_p)}{50} \right)^{1.6} \left(\frac{\hat{B}}{1} \right)^2 (w_{pm} \cdot h_{ys} \cdot l_m \cdot \rho_{ir}) = 0.1 \text{ [W]}. \quad (5.50)$$

The Joule losses are estimated using (5.24) and are equal to

$$P_{cu} = 170 \cdot (1 + \alpha_c \cdot \Delta T) \text{ [W]}. \quad (5.51)$$

In the PM, only the losses due to the slots are taken into account since it is assumed that the PM mmf is much higher than the stator mmf and that Eddy currents in the PM do not affect the flux density in the air gap. This assumption is not valid for transient supply where the coil mmf could be close to the PM mmf. Using (5.37) the Joule losses in the magnets are found to be 7W. Although this losses do not influence the motor thermal behavior, they are useful to evaluate the motor efficiency. The yoke of the MaW is made of a standard steel (S430FU) and the losses in the Maw yoke are calculated using (5.28).

The convection and radiation resistance $R_{th \text{ conv rad}}$ is estimated with (5.3) and (5.8). The surface S includes all the surfaces in contact with the air, i.e. the five faces surrounding the coils except the active surface. The conductive resistance of the the coil $R_{th \text{ coil}}$ is calculated using (5.4). For the air gap model, the rectangular cavity model can be used since the air gap is small enough ($<1.5\text{mm}$).

Therefore, the motor temperature is evaluated as

$$T_{motor} = \sum P \cdot R_{th\ conv\ rad} + T_{\infty}, \quad (5.52)$$

the temperature of the coil is

$$T_{coil} = P_{cu} \cdot R_{th\ coil} + T_{motor}. \quad (5.53)$$

By solving this thermal lumped scheme, the coil and plate temperatures can be found. Table 5.10 shows these temperatures for a case without to take into account the temperature coefficient α_c in (5.24) and for the normal case whit $\alpha_c = 0.004$. This comparison indicates clearly the importance of this factor and demonstrates also that the motor can not work under these specifications with a duty cycle equal to 1.

Table 5.10: Coil and plate temperatures obtained by solving the thermal model.

	$\alpha_c = 0$	$\alpha_c = 0.004$
Coil temperature	205	325
Plate temperature	191	295

Figure 5.17 shows the coil temperature in relation with the motor duty cycle D . Therefore, if the coil temperature is limited to 120°C , the maximum duty cycle is about $D = 0.32$.

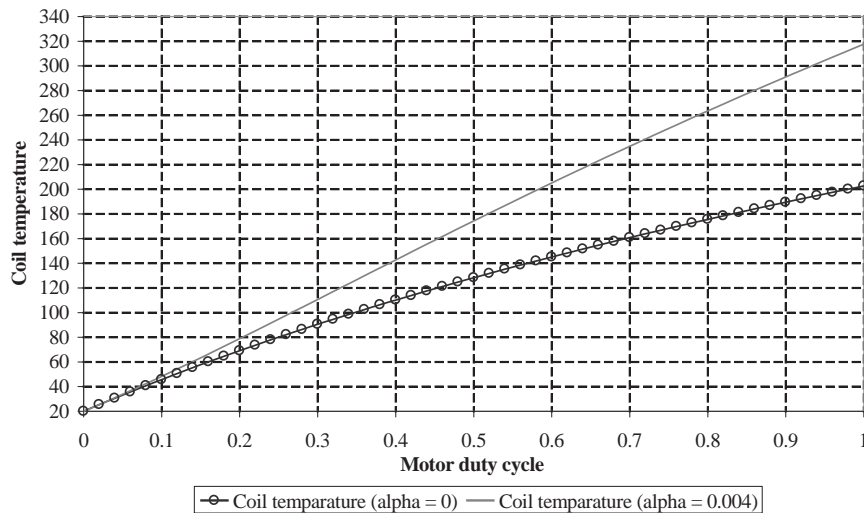


Figure 5.17: Temperature evolution in relation to the motor duty cycle.

5.6.2 Influence of the Thermal Model on the Magnetic Model

As mentioned, the thermal model limits the current density and therefore the motor power. This direct impact is an important constraint for the motor.

Indirect consequences must also be related to the magnetic model of the motor. The first one is the increase of the electrical resistance with the temperature given by (5.24). The second one is the decrease of the remanent flux density of the PM with the temperature increase. This is summarized in Table 2.1, which gives the properties of the PMs. This phenomena can be irreversible in some cases. These two

aspects have as consequence to decrease the propulsion force for a fixed current density. Nevertheless, this aspect can be omitted (or the temperature for the coil and the PM is fixed) in a motor pre-design and can be taken into account if a more precise motor model is required or when the temperature range varies significantly.

5.7 Conclusions

Thermal models are very difficult to develop since the air movement due to the heating is not straightforward to model. Nevertheless, the proposed empirical formulae give a good accuracy for phenomena at standstill. As shown in Section 5.5, these formulae are less accurate with forced cooling. However, the forced convection or a motor travelling at constant speed can be modelled with the proposed formulae.

In a motor thermal model, a great difference appears between ShS and LS since for the same application the duty cycle is not the same. It means a different thermal behavior.

For the heating sources, the difficulty to have a good approximation of the iron losses comes from the fact that the coefficient C_p and the frequency reference are not always given by the manufacturer. These factors can be obtained by experiments.

The proposition to model the thermal behavior of the air gap by a rectangular cavity offers good results. This new aspect can also be used when a forced air flows into the air gap.

Generally, the presented models are accurate enough to define the maximum current density. However, practical measurements remain the best approach to verify the thermal model and to valid it.

Chapter 6

Motor Design Analysis and Comparison

6.1 Introduction

In this chapter several motor concepts and Magnetic ways are discussed and compared. The sensitivity of the optimized result to relevant parameters is shown in order to discuss the advantages and drawbacks of several motor topologies.

In Section 6.2, different magnetic ways are compared and some sensitivity analysis are presented. Section 6.3 deals with toothless motor, for which several topologies and windings are compared. In Section 6.4, the toothed motors are discussed. Finally, in Section 6.5 toothless and toothed motors are compared.

The comparison methodology is based on the Section 3.6.3. To realize a good comparison the models must have the same precision and the design process for the compared motors must be also the same.

6.2 Magnetic Ways, Air Gap MMF

The MaW introduced in Section 4.2 allows to compare their mmf. This comparison aspect is very interesting and it is, in most cases, only roughly studied. Therefore, this section will define the advantages and drawbacks of each MaW. The different analysis will show the relation between the flux density in the air gap and the PM volume which has an important impact on the material cost. Therefore, the proposed comparison analysis are interesting in order to limit the PM volume.

The studied MaW introduced in Section 4.2 are divided in three groups:

- single magnetic ways without opposite iron part;
- single magnetic ways with opposite iron part and small air gap;
- magnetic ways with high air gaps for toothless motors.

For these comparisons, iron parts are considered ideal $\mu_{r\ ir} = \infty$ and the PM relative permeability is assumed equal to $\mu_{r\ pm} = 1$.

6.2.1 Single Magnetic Ways without Opposite Iron Part

Two different single MaW without opposite iron part are studied; the single sided MaW with mounted PM and the single sided Halbach array (Fig. 1.4). These ways are used with an ironless winding.

The first comparison criterion is the mean value of the flux density on one pole pitch. The results with several magnet heights and pole pitches are analyzed, as shown on Fig. 6.1. For this comparison and for

a given pole pitch, the magnet volume between the two MaW is the same. Therefore, the magnet height differs slightly between the single MaW with mounted PM (Fig. 4.11) and the single HA (Fig. 4.18), as:

$$h_{pm\ HA} = \frac{h_{pm\ single\ MaW} \cdot l_{pm\ single\ MaW}}{\tau_p}. \quad (6.1)$$

Figure 6.1 shows that the mean value of the flux density (\bar{B}) of a HA depends strongly on the pole pitch. It is mainly due to magnet length $l_{pm\ x}$ (Fig. 4.17) which have a magnetization parallel to the movement. Indeed, $l_{pm\ x}$ increase the flux line length in the air gap compared to a single sided MaW with mounted PM. Therefore, single HA are more adapted for small pole pitches.

Furthermore, for a single sided MaW with mounted PM, Fig. 6.1 shows the non linear dependance of \bar{B} as a function of the magnet height. This observation introduces the variation sensitivity of \bar{B} to the magnet height and therefore the difficulty to find an optimum by taking into account the PM cost and the motor performances. This problem of sensitivity is the key point of the optimum result analysis. For a single sided MaW, the mean value of the flux density as a function of the pole pitch and the magnet height is given on Fig. 6.2.

Another relevant comparison is made on the flux density wave form, as shown on Fig. 6.3. This explains the tendency to have a higher \bar{B} with HA than with single sided MaW, for high h_{pm} . This figure shows the flux density concentration above the y-magnetized magnet of the single HA. For this figure, the length of $l_{pm\ x}$ and $l_{pm\ y}$ are equal to the half pole pitch.

The HA can be designed in order to have a flux density waveform close to a sine. As examples, the waveforms of the flux density for several cases are shown on Fig. 6.4. Their respective Fourier transformations are given on Fig. 6.5.

Figure 6.5 shows a slightly higher magnetic flux fundamental value for the single HA with a ratio $l_{pm\ x}/\tau_p < 0.5$ than for a single sided MaW.

To conclude, single sided HA are less adapted for large pole pitches than single sided MaW with mounted PM. Moreover, for a high PM volume, HA have a better flux density (distribution and peak value) in the air gap than single sided MaW with mounted PM. HA are also very difficult to assemble and tolerance problems can appear. Therefore, single sided HA are not a good solution to realize single sided MaW for common applications. However, they can be interesting for specific applications. For example, in an application requiring a LS motor, it could be advantageous to use a single sided HA since it is lighter than a single sided MaW with mounted PM (HA has no yoke), meaning a higher acceleration [77].

6.2.2 Single Magnetic Ways with Opposite Iron Part with Small Air gap

This group of MaW with a small air gap ($\delta/\tau_p \leq 0.1$) are used with toothed supply parts (Fig.4.25). The case with a high air gap, which groups the MaW for toothless motors, is discussed in the following section. All the presented results are defined at the middle of the mechanical air gap $\delta/2$ and all the comparisons between MaW topologies are made for the same magnet volume. In this Section, a MaW with inserted magnets is introduced beside the single sided MaW with mounted PM and the HA single sided. The MaW with inserted magnets is modelled with a lumped magnetic scheme. The geometrical quantities of this MaW are presented on Fig. 6.6.

This model is not so accurate compared to the other MaW models since the analytical results for the flux density are up to 15% higher than those obtained with a FEM. This difference comes from the flux leakage which is not straightforward to model. Nevertheless, this MaW is introduced in order to show its advantages and drawbacks. However due to the model accuracy, it cannot be directly compared with the two others.

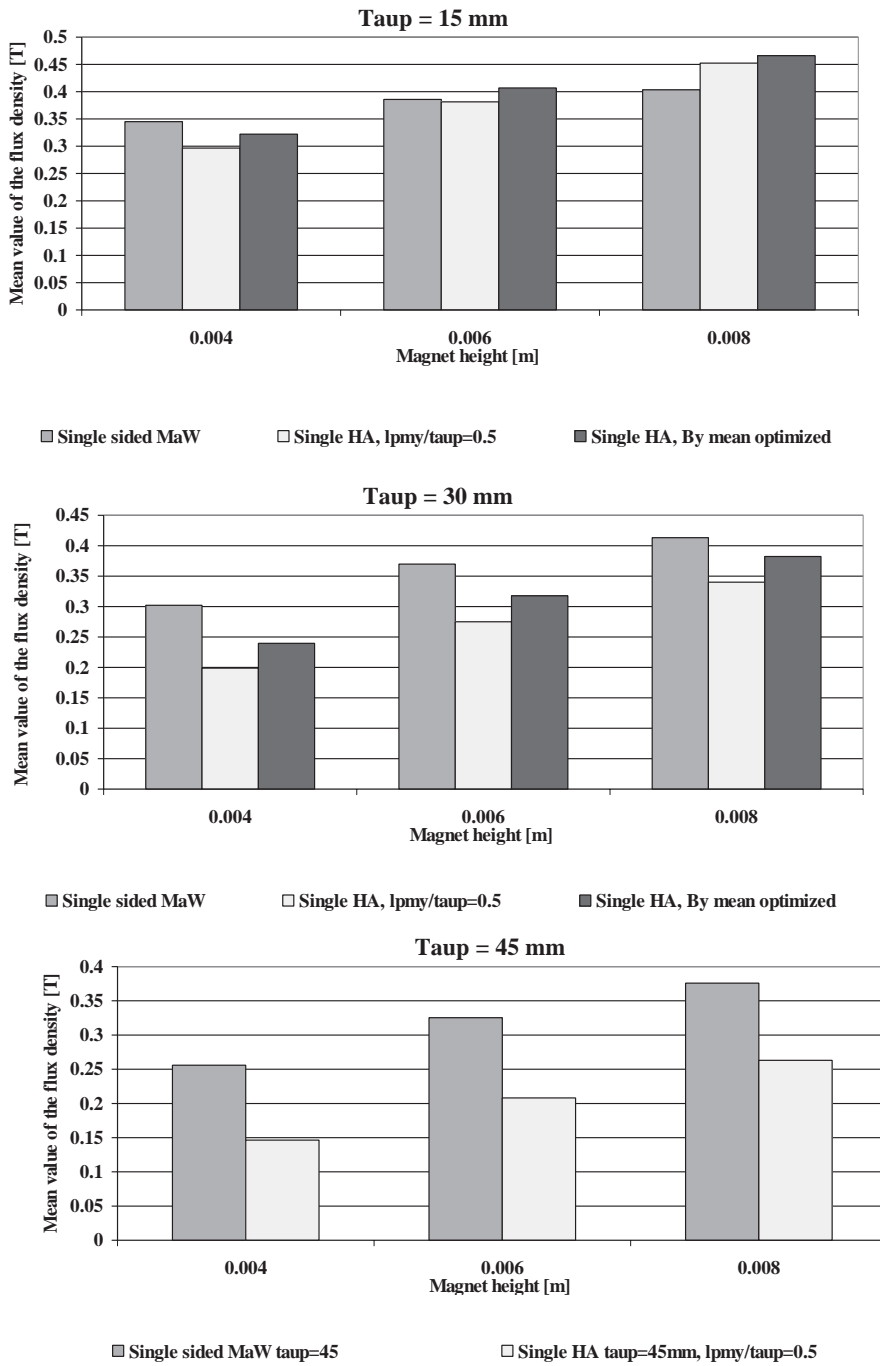


Figure 6.1: Mean value comparison of the flux density at 1 mm above the magnet height.

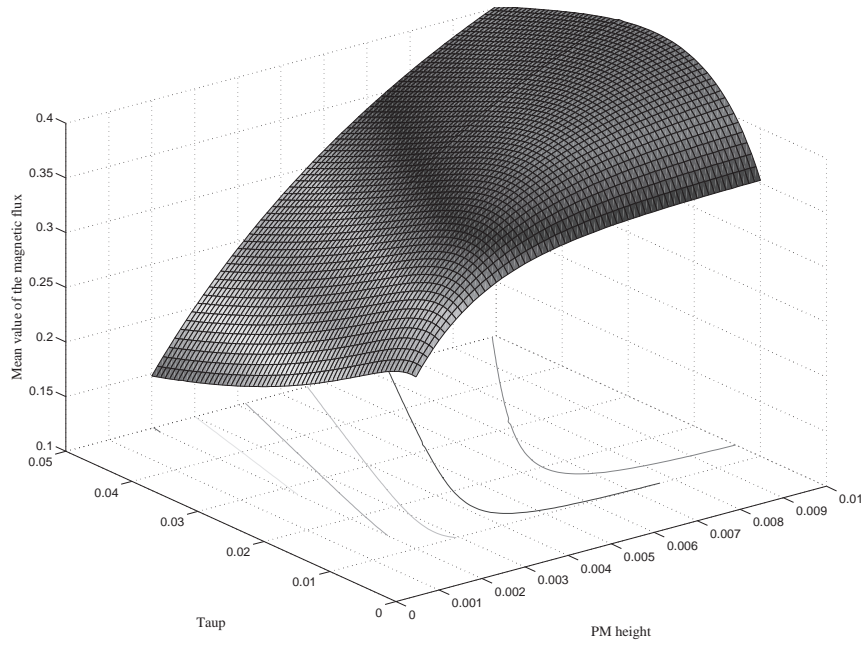


Figure 6.2: Mean value of the flux density for a single sided MaW (1mm above magnet surface), $\tau_p = 15$ mm.

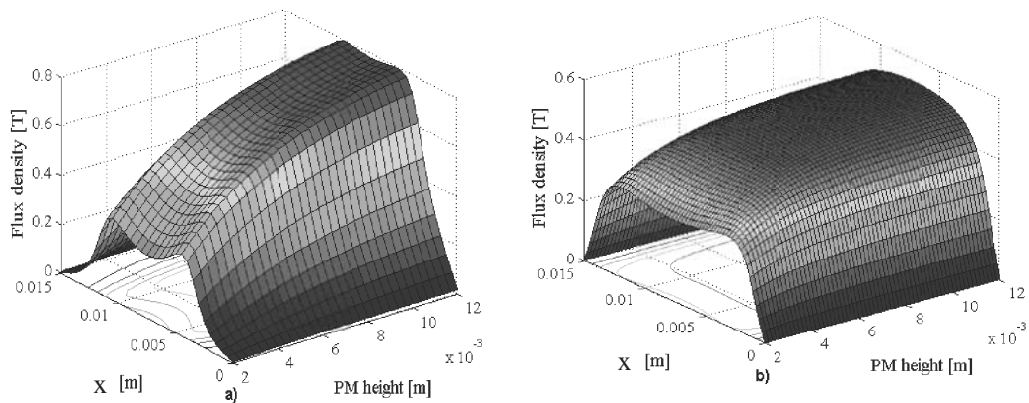


Figure 6.3: Flux density waveform comparison between single sided MaW (a) and single HA (b), 1mm above magnet surface.

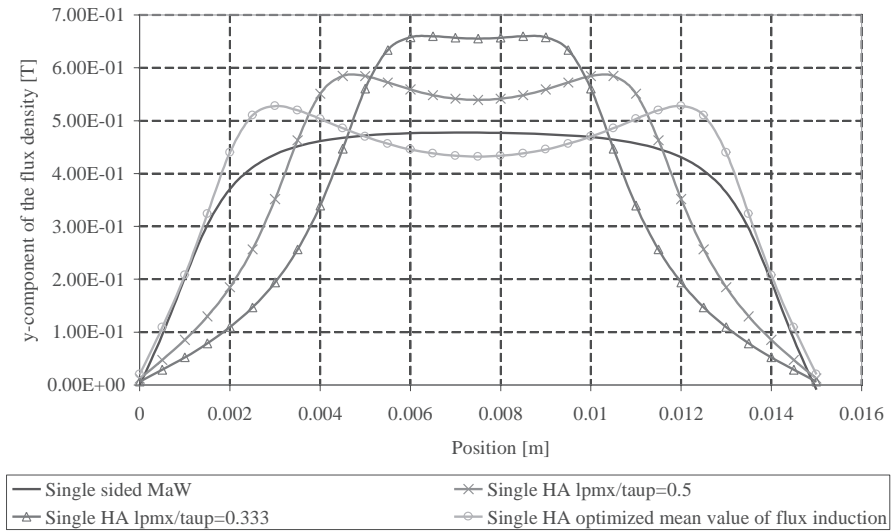


Figure 6.4: Flux density waveform comparison between the single sided MaW with mounted PM ($h_{pm} = 6$ mm) and the single sided HA ($h_{pm} = 5.2$ mm), 1mm above magnet surface.

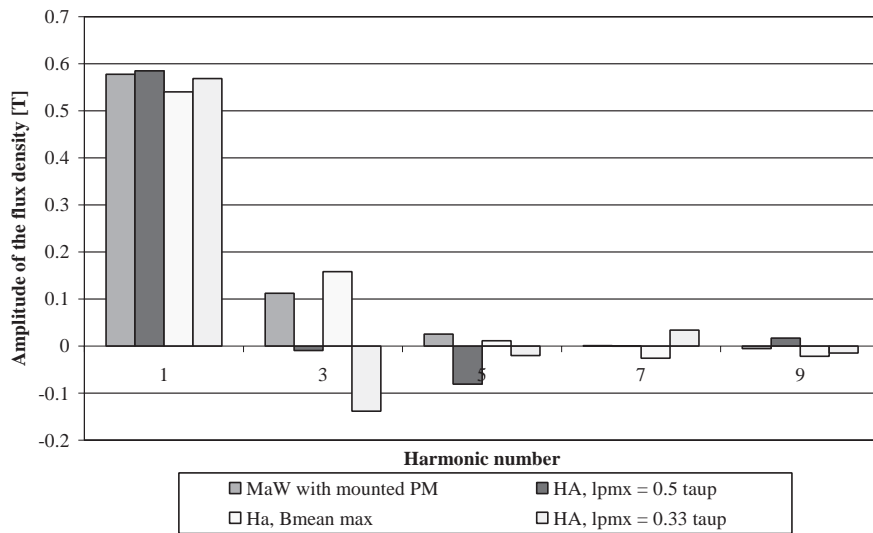


Figure 6.5: Fourier analysis comparison between the single sided MaW with mounted PM ($h_{pm} = 6$ mm) and the single sided HA ($h_{pm} = 5.2$ mm), 1mm above magnet surface.

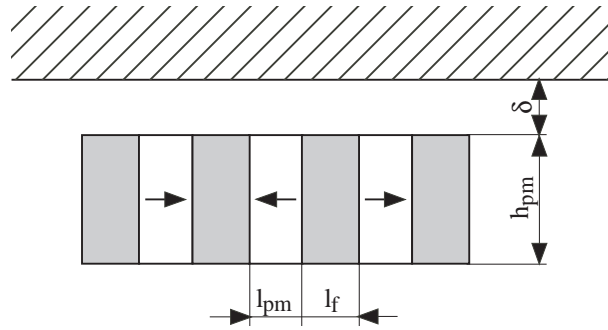


Figure 6.6: Geometrical quantities for the MaW with inserted magnets.

The study of \bar{B} above one pole pitch does not differ compared to the case without opposite iron, as presented on Fig. 6.1. Therefore, in this configuration with opposite iron part, HA are also more adapted for rather small pole pitches τ_p . The flux density waveform for $h_{pm} = 6$ mm, $\delta = 2$ mm and τ_p varying from 0.01 to 0.05 mm is presented on Fig. 6.7. It shows that this MaW is not adapted for high pole pitches. Indeed, for a high pole pitch the magnetic flux has a weak flux density above the x-magnetized PM. These PM has the tendency to decrease the performance of HA for high pole pitches. On the contrary, for small pole pitches the magnetic flux in the air gap becomes close to a sine.

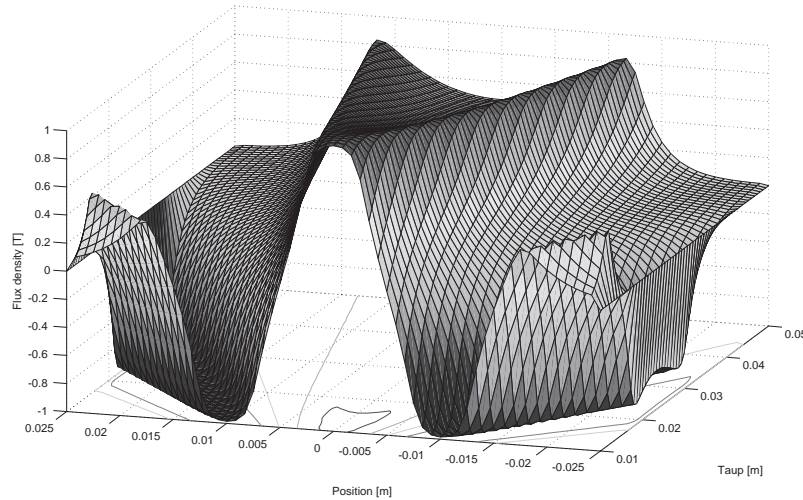


Figure 6.7: Flux density waveform as a function of the pole pitch for an HA ($h_{pm} = 6$ mm, $\delta = 2$ mm, $l_{pm} x / \tau_p = 0.5$).

In a determinist design approach (Section 3.1.1) the choice of the magnet height in regards to the mechanical air gap is difficult to make since it is a compromise between the MaW cost, the propulsion force density (proportional to the flux density created by the PM in the air gap) and the attractive force (proportional to the flux density square created by the PM in the air gap). Figure 6.8 shows the mean value of the flux density and the attractive force (related to a magnet height of 5mm) as a function of the magnet height. Using the proposed design methodology, the choice of the magnet height in regard to the air gap height is a result of the optimization process depending on the objective function and the constraints.

As for the single MaW without opposite yokes, the flux density waveform varies with $l_{pm} x / \tau_p$

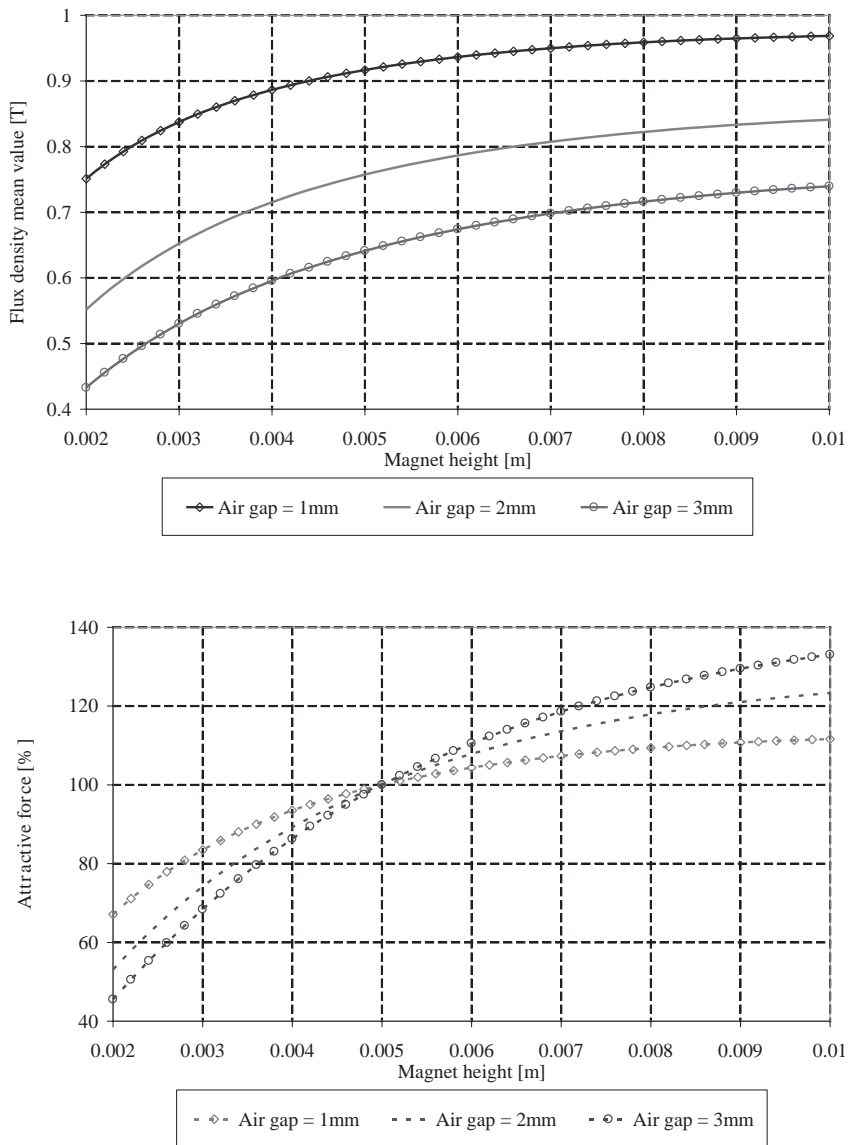


Figure 6.8: Flux density mean value over one pole (solid lines) for several air gaps as a function of the magnet height ($\tau_p = 30mm$) and attractive force (dashed lines) relative to the case with a magnet height of 5mm.

(Fig. 4.18). Figure 6.9 shows the flux density waveform of a HA as a function of this ratio ($h_{pm} = 6\text{mm}$, $\delta = 2\text{mm}$, $\tau_p = 20\text{mm}$). This waveform is in some cases close to a sine. For comparison, the magnetic flux for a single MaW with mounted PM is presented on Fig. 6.10. Moreover, in order to achieve the same performances, the magnet volume must be increased in the case of a HA.

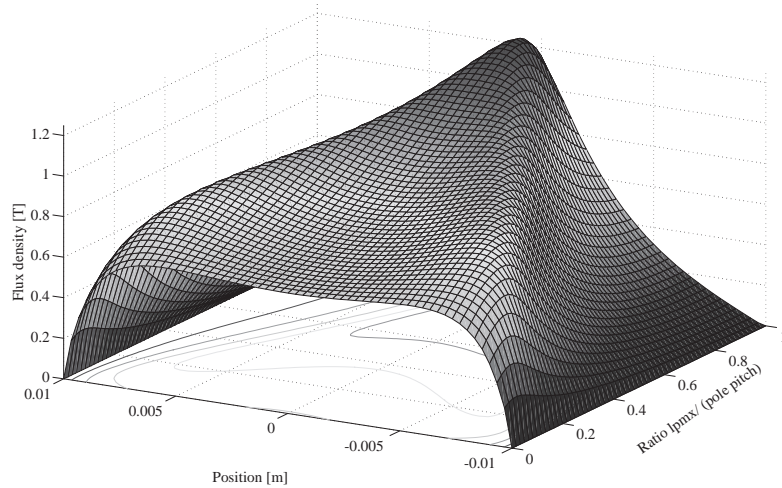


Figure 6.9: Flux density in the air gap as a function of the x-magnetized magnet length for a single sided HA MaW with opposite yoke ($h_{pm} = 6\text{ mm}$, $\delta = 2\text{ mm}$, $\tau_p = 20\text{ mm}$).

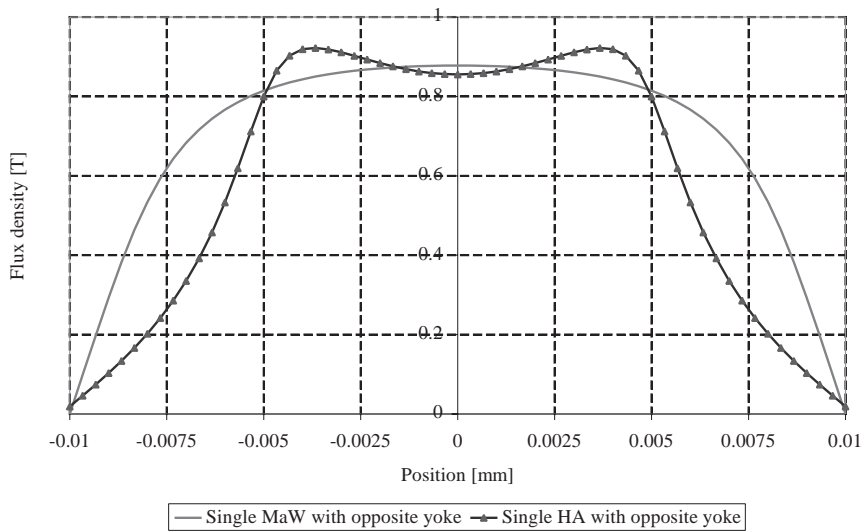


Figure 6.10: Flux density in the air gap for the single MaW with opposite yoke ($h_{pm} = 6\text{ mm}$, $\delta = 2\text{ mm}$, $\tau_p = 20\text{ mm}$) and the single HA with opposite yoke ($h_{pm} = 5.4\text{ mm}$, $\delta = 2\text{ mm}$, $\tau_p = 20\text{ mm}$).

For the same magnet geometry, MaW with inserted magnets has a higher flux density in the air gap compared to the MaW with mounted magnets. Figure 6.11 shows the variation of the flux density in the air gap and its mean value ($\delta = 2\text{ mm}$ and $\tau_p = 20\text{ mm}$). The computation required for this model is more time consuming than for the other MaW models. This comes from the saturation in the iron parts.

Nevertheless, the computation time is still acceptable.

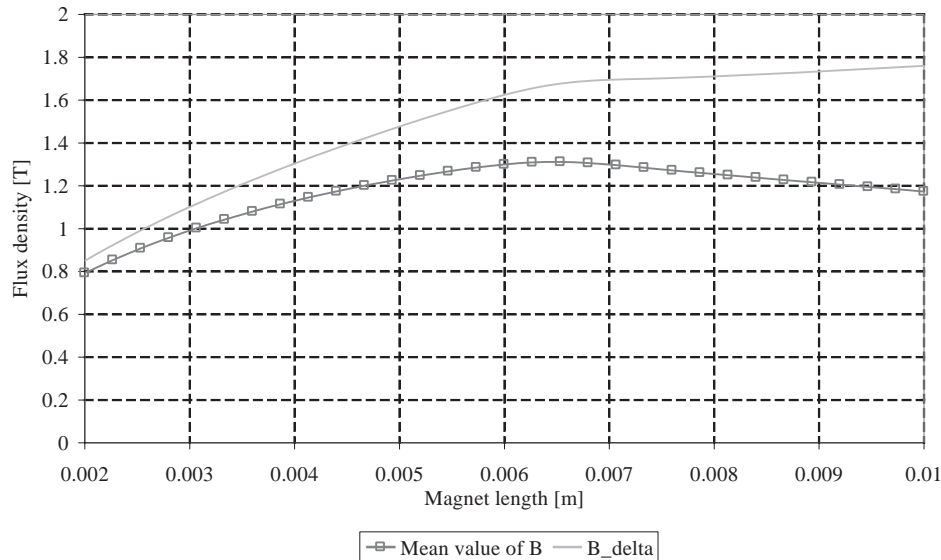


Figure 6.11: Peak value of the flux density in the air gap (solid line) and its mean value (squares) for a MaW with insert magnets as a function of magnet length ($\tau_p = 20$ mm, $h_{pm} = 18$ mm).

The MaW with inserted PMs generates a high flux density in the air gap. The drawback is that it produces a reluctance and a cogging force when it is used with a toothed motor. Moreover, as the HA, MaW with inserted PM are difficult to manufacture and to assemble.

6.2.3 Magnetic Ways for Ironless Motors

These magnetic ways, usually double sided, are :

- double sided MaW with mounted PM Fig. 1.4 c);
- double sided Halbach array Fig. 1.4 e);
- single sided MaW with opposite iron plate Fig. 1.4 b).

They are characterized by a large air gap in order to introduce the coils into it. For the comparison, the air gaps vary between 4 and 15 mm for $\tau_p = 30$ mm.

In the two last sections, it was noted that HA are not adapted for high pole pitches since the mean value of the flux density is, for a same magnet volume, smaller than for the other MaW. Therefore, double HA are not studied for high pole pitches.

Compared to the double sided MaW with mounted PM, the single sided MaW with opposite iron plate leads always, for a same magnet volume, to a smaller flux density, as presented on Fig. 6.12. This is mainly due to higher leakage flux. However, the variant with the single sided MaW with opposite iron plate can be chosen for geometry reasons.

As shown on Fig. 6.13, double sided Halbach array has, for a high volume of magnet, a better mean value of the flux density than the double sided MaW with mounted PM. Therefore, if the cost is not a restricting factor, HA becomes a good solution to achieve a high magnetic flux density in the air gap.

Another relevant comparison is the variation sensitivity of \bar{B} with the air gap. As shown on Fig. 6.14, \bar{B} for HA array is less sensible to the air gap height.

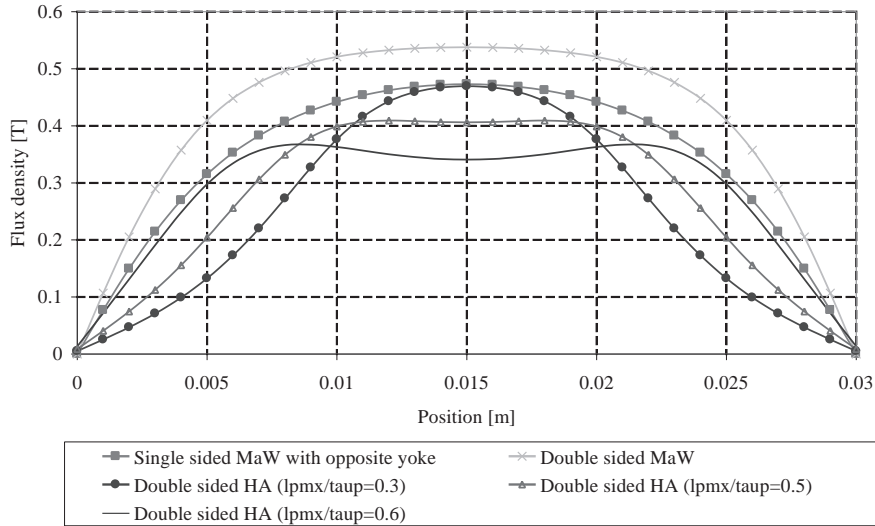


Figure 6.12: Waveform comparison between MaW with a high air gap and the same magnet volume ($\tau_p = 30$ mm, $h_{pm} = 4$ mm (double sided), $\delta = 10$ mm).

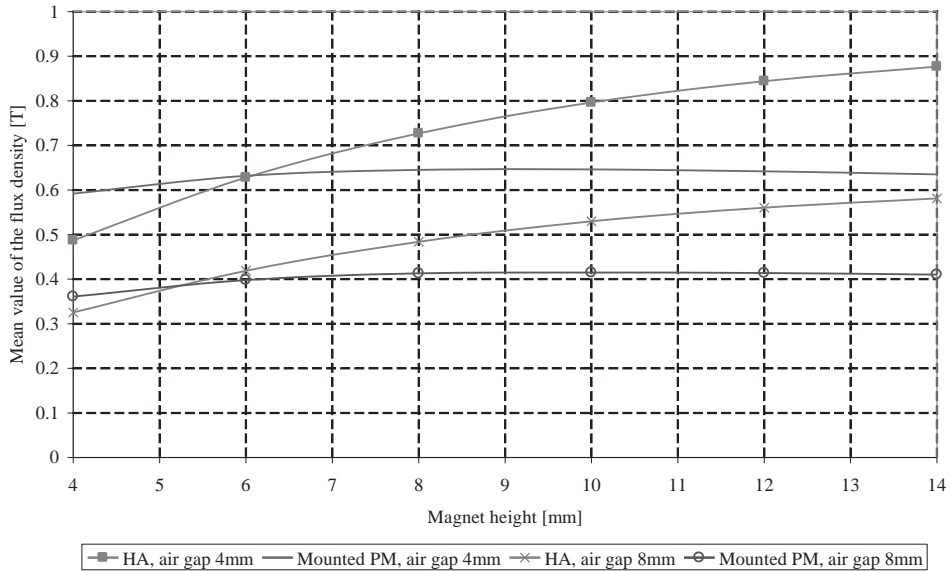


Figure 6.13: Comparison of the flux density mean value between double sided Halbach array and a double sided MaW with mounted PM, $\tau_p = 15$ mm.

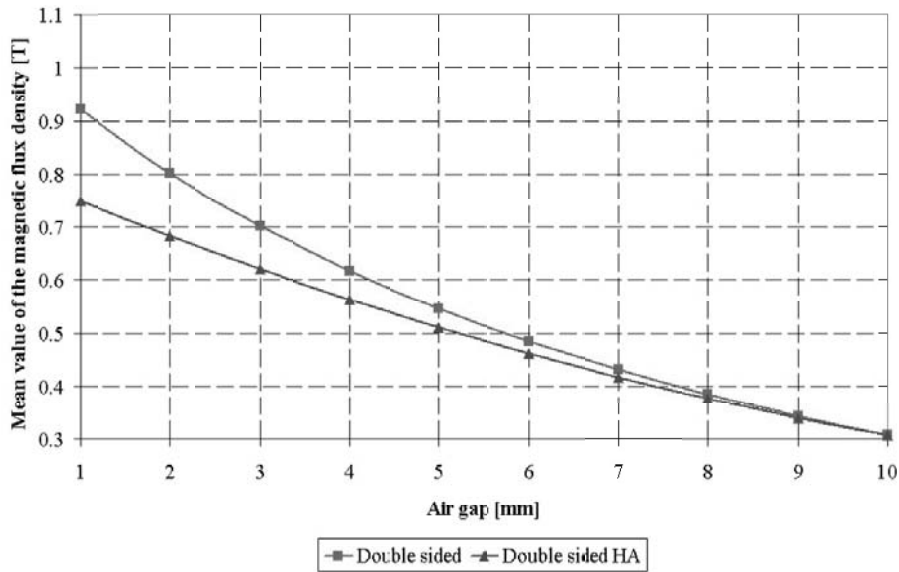


Figure 6.14: Comparison of the sensitivity of the air gap on the magnetic flux density mean value \bar{B} ($\tau_p = 15$ mm, $h_{pm} = 5$ mm).

6.2.4 Magnetic Ways Comparison: Conclusions

The studied MaW are all composed of magnets, although the excitation can also be produced by DC coils and teeth. This last solution was not studied in this thesis since it is only an adapted solution for motors requiring a high power. More information about this aspect can be found in [11].

The studied Halbach array is the simplest variant and it can be composed of more than two magnets per pole as presented on Fig. 6.15. Such a MaW has the advantage to produce a sinusoidal waveform in the air gap, which can be in some peculiar cases an advantage. On the other hand, it is very difficult to manufacture.



Figure 6.15: Halbach array with three magnets per pole.

Generally, HA needs a higher PM volume magnets to reach the same magnetic flux in the air gap. On the other hand they have the advantages to not have iron parts and therefore no iron losses. Moreover, the possibility to have a more sinusoidal magnetic flux distribution in the air gap could be an advantage for specific applications requiring a constant propulsion force. Furthermore, HA are more adapted for rather small pole pitches for two main reasons. First, due to their structure they have a higher y-component of the flux density than MaW with mounted PM. Second, with a high pole pitch, the x-magnetized PM becomes difficult to magnetize due to its length.

The solutions with mounted PM are the most adapted MaW for linear motors. They are easier to manufacture and to assemble than HA or MaW with inserted PMs. Moreover, these MaW are more dependant on the manufacturing precision. Regarding magnet issues, HA needs more PM volume to achieve good performances than MaW with mounted PM. Consequently for these two main reasons (volume of magnets (cost) and difficulty to industrialize) HA magnetic ways are not widespread in linear motor technologies.

The solution with inserted PMs are more adapted for tubular motors. A particular attention must be made on the cogging force that is generated by this MaW, since it can disturb the propulsion force.

6.3 Toothless and Ironless Motors

The goal of this section is to compare the toothless motors and to characterize each topology in order to define their working domain. These motors are characterized by high dynamic performances (acceleration and speed), no cogging and reluctance forces, no relevant iron losses and in the most cases no attractive force. High acceleration means high propulsion force and therefore reducing the moving mass becomes a priority. To have a light mover, a good solution is to move the coils without yoke (ironless solution) or to move the magnetic way. Four motors without yoke (Ironless) and one motor with yoke (Toothless) are compared, as presented on Fig. 6.16. Ironless motors are mainly dedicated to high acceleration whereas toothless motor is more adapted for a higher propulsion force .

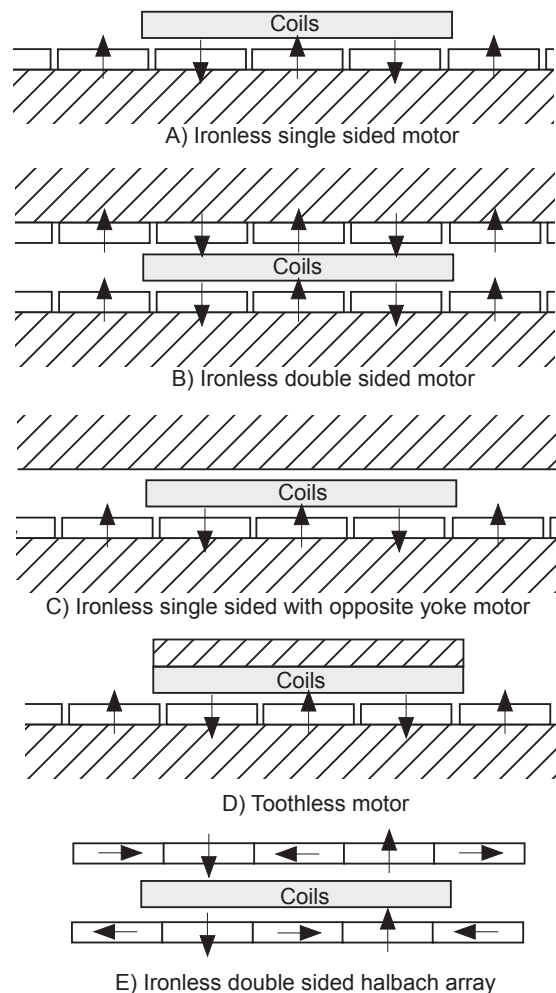


Figure 6.16: Toothless and ironless motor variants.

The thermal models are about the same (if the iron thermal conductivity is assumed as ideal) for the motors A) and D) and for the motors B), C) and E). The following assumptions are made for the thermal model:

- the conductance thermal resistances of the magnets and the iron parts are neglected;
- the air gap(s) are modelled with a rectangular cavity with $Nu = 2$;
- the heat transfer is made in both directions (up and down) of the coil;
- when heat transfer is made through an air gap to a yoke or PM (double sided Halbach array), the convection and radiation surface is considered as twice the coil surface (i.e. the motor has a stroke equal or higher than two times the motor length);
- the motor is considered at standstill ($v=0$) with a duty cycle $D_c=1$;
- only the steady state is modelled;
- the copper losses and the remanent induction of the PM are temperature dependent.

These thermal models are very restrictive and do not take into account the speed of the motor which can be assumed as a forced convection. The analysis of the MaW allows to establish a ranking of the proposed motors in terms of maximum propulsion force. Indeed, for a same magnet volume and a same mover the motor A) will produce the smaller propulsion force whereas the motor B) will develop the higher propulsion force.

Three windings types are considered as presented on Fig 4.33. They are three-coil concentrated windings. The coil opening is either 120 edeg, 240 edeg or 300 edeg. These windings are compared and by analogy the advantages or drawbacks of other windings (Table 4.11) are deduced. All the presented results are made for a motor with three coils. Therefore, to compare the propulsion forces, the force density is preferred.

To perform a good comparison between the motors, the constraints must be the same. They are listed in Table 6.1.

Table 6.1: Chosen motor constraints for a relevant comparison

B_r	Remanent induction of PM	1.23 T
d_{cu}	Copper diameter	0.2-1.6 mm
k_{cu}	Copper filling factor	0.6
h_{coil}, h_{pm}	Coil and PM height	2-10 mm
l_{int}	Inner coil length	4 mm
w_{pm}	PM width (Active width)	<150 mm
δ	Air gap	1 mm
τ_p	Pole pitch	<50 mm
T_{coil}	Coil temperature	<120°C
T_{pm}	PM temperature	<60°C
T_∞	Room temperature	20°C

6.3.1 Ironless Single Sided Motor

This motor is the less powerful of all toothless motors since it has no opposite yoke to close efficiently the magnetic flux. Nevertheless, this motor does not require a lot of space and the guidance system is easy to realize. It is studied with two different MaW: with mounted PM and with HA.

6.3.1.1 Ironless Single Sided Motor with Mounted PM

The maximal propulsion forces for several pole pitches and the three winding types are found by optimization under the constraints introduced in Table 6.1. These maximum forces are presented in Table 6.2.

Table 6.2: Maximum forces for ironless motor with a single sided MaW with mounted PM. Several pole pitch lengths.

			coil opening [edeg]		
			120	240	300
50 [mm]	F_{max}	[N]	44.1	113	132
	τ_p F_s	[N/m ²]	2967	3822	3540
	k_m	[N/ \sqrt{W}]	8.2	15.8	16.8
	k_w	[-]	0.567	0.927	0.989
	l_{int}	[mm]	4.99	8.74	7.56
30 [mm]	F_{max}	[N]	28.6	74	86.4
	τ_p F_s	[N/m ²]	3180	4092	3852
	k_m	[N/ \sqrt{W}]	6.4	12.6	13.6
	k_w	[-]	0.597	0.944	0.995
	l_{int}	[mm]	4.44	7.11	6.33
15 [mm]	F_{max}	[N]	11	28.5	34
	τ_p F_s	[N/m ²]	2455	3160	3010
	k_m	[N/ \sqrt{W}]	3.2	6.6	7.2
	k_w	[-]	0.669	0.952	0.998
	l_{int}	[mm]	4	4.05	4

For all these cases, the restrictive factor is the temperature of the magnets (60°C). To maximize the propulsion force, the program set the most geometrical parameters (h_{coil} , h_{pm} , l_{coil}) to their maximum values, except for the inner length of the coil l_{int} . This value changes in order to limit the copper losses as related in Table 6.2.

This table shows that a winding with a maximum coil opening of 120 edeg is not a good solution since it has a low force density propulsion F_s and a low motor constant k_m . The low motor constant is due to the poor winding factor k_w (4.63). Coil opening of 120 edeg is only adapted for applications requiring rather small propulsion force in a small volume. If the motor is limited by two poles, a distributed winding would be more adapted.

The winding with the maximum coil opening of 300 edeg has a better motor constant than with a coil opening of 240 edeg. This is due to the pitch factor k_s which is close to one for a coil opening of 300 edeg. On the other hand, a toothless motor with a coil opening of 240 edeg reaches a better force density. This results from the thermal model since the increase of the power losses is more important than the capacity to evacuate the heat.

Moreover, Table 6.2 shows the variation of the force density with the pole pitch. This can be explained with Fig. 6.1. It illustrates that for high h_{pm} , \bar{B} is higher with a pole pitch of 30 mm than for the others. This directly influences the propulsion force. The propulsion force density and the motor constant are given in relation to the pole pitch for the two different coil openings (240 edeg and 300 edeg) on Fig. 6.17.

This graph shows that the two motors are very similar in term of performances. Therefore, without taking into account the application which introduces some additional constraints (acceleration, geometry, volume, cost, etc.), it is not possible to differentiate them and to favorize one winding.

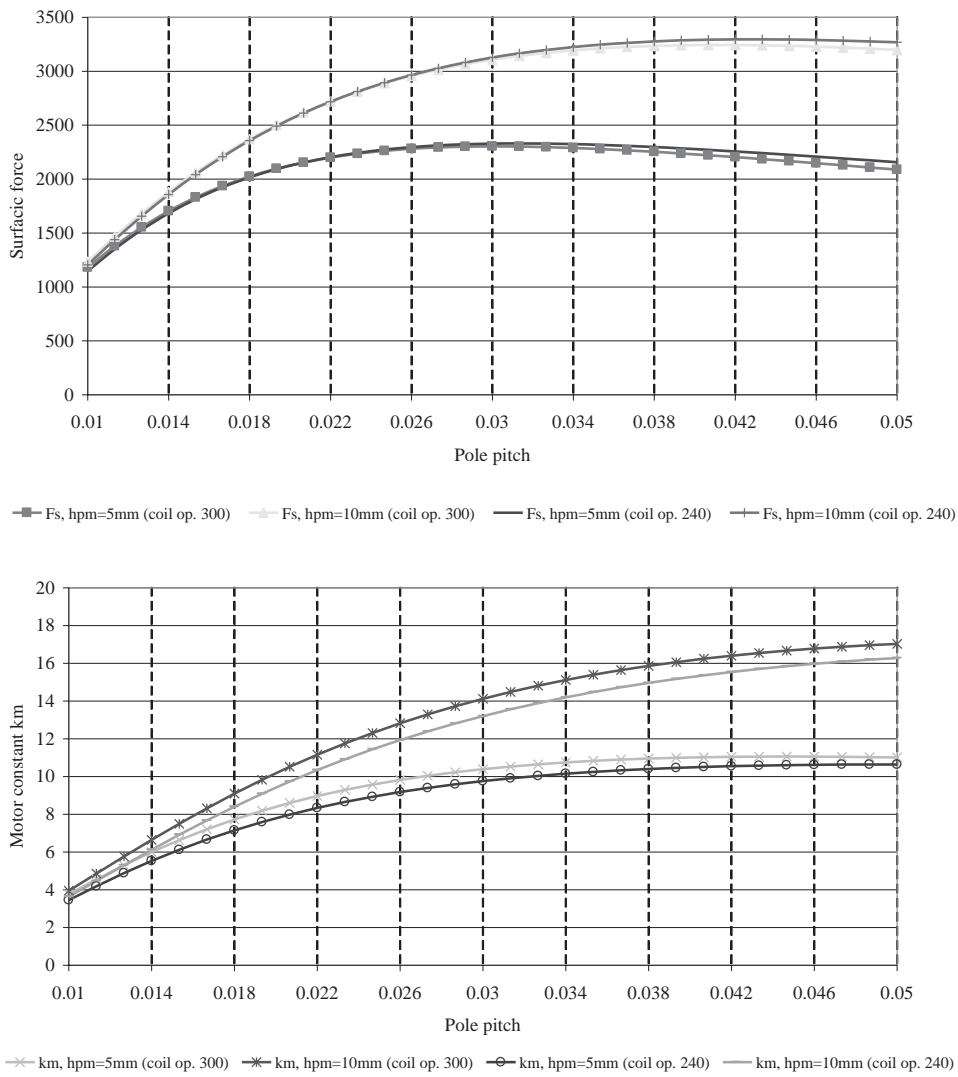


Figure 6.17: Propulsion force density and motor constant for a single sided ironless motor with mounted PM as a function of the pole pitch for the two different coil openings, 240 edeg and 300 edeg.

6.3.1.2 Ironless Single Sided Motor with HA

For this motor only the coil openings of 240 edeg and 300 edeg are studied. The maximum propulsion forces are given in Table 6.3.

Table 6.3: Maximum propulsion forces for ironless motor with single sided HA and several pole pitch lengths.

			coil opening	
			240	300
50 [mm]	F_{max}	[N]	102.5	128.7
	F_s	[N/m ²]	3450	3432
	k_m	[N/ \sqrt{W}]	14.3	16.2
	k_w	[-]	0.967	0.999
30 [mm]	F_{max}	[N]	76.5	95.1
	F_s	[N/m ²]	4250	4230
	k_m	[N/ \sqrt{W}]	13.1	14.9
	k_w	[-]	0.961	0.999
15 [mm]	F_{max}	[N]	36.8	45.4
	F_s	[N/m ²]	4096	4033
	k_m	[N/ \sqrt{W}]	8	9.6
	k_w	[-]	0.951	0.999

This table shows that in comparison with a single sided ironless motor with mounted PM, HA are adapted for rather small pitch factor. Moreover, the two coils openings are very similar and without taking into account an application the choice of the winding cannot easily be made.

6.3.1.3 Ironless Single Sided Motor Comparison

Figure 6.18 shows the maximum surfacic propulsion force and its motor factor for the both studied motors with $h_{pm} = 10$ mm and $h_{pm} = 5$ mm, and for a coil opening of 240 edeg. The magnet volume is the same for both MaW and therefore (6.1) is used.

These graphs illustrate that HA are adapted for small pole pitches and that they require a higher magnet volume to be competitive. The non linearity between the force density and the PM height h_{pm} shows that the magnet height must be also made regarding the magnet cost.

6.3.2 Toothless Motor

Compared to the others, this motor has a heavier moving part due to the yoke, as illustrated on Fig. 4.32. Although a coil opening of 120 edeg seems less interesting in terms of performances, it is taken into account here. To reduce as much as possible the cogging force produced by the plate, its length can be given by (4.80) since the air gap is rather high. The maximum propulsion force is found by optimization for several pole pitches and results are presented in Table 6.4. The restricting factor is again the PM temperature.

The propulsion force per surface unit is higher than for ironless motors with single sided MaW without yoke. This advantage becomes less important as the pole pitch decreases. As the thermal model is this time more restrictive, the coil height vary following the cases. A higher pole pitch allow a better heat dissipation leading to have a higher coil height.

For this motor, the attractive force must also be studied in order to show the dependence of this parameter on the PM and air gap heights. Figure 6.19 shows the attractive force per surface unit for a

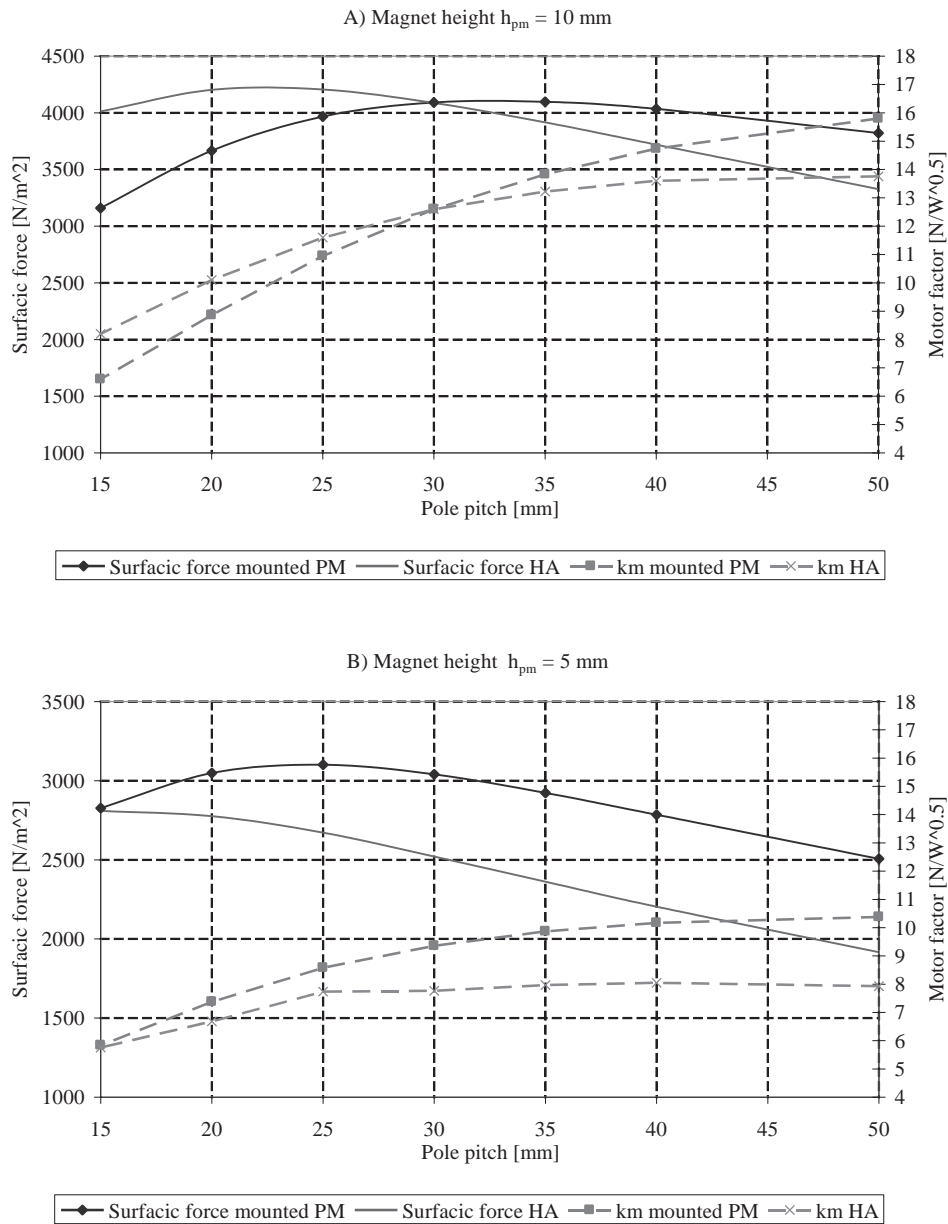


Figure 6.18: Maximum force density and motor constant comparison between both studied motors. A) $h_{pm} = 10$ mm and B) $h_{pm} = 5$ mm.

Table 6.4: Maximum propulsion forces for toothless motor and several pole pitch lengths.

			coil opening [edeg]		
			120	240	300
50 [mm]	F_{max}	[N]	73.2	189.1	221
	F_s	[N/m ²]	4880	6300	5900
	k_m	[N/ \sqrt{W}]	13.6	26.5	28.1
	k_w	[-]	0.585	0.931	0.994
	h_{coil}	[mm]	9	8.4	8.5
	l_{int}	[mm]	6.5	10.3	9.5
30 [mm]	F_{max}	[N]	40.3	106	124.3
	F_s	[N/m ²]	4477	5905	5224
	k_m	[N/ \sqrt{W}]	9.3	18.6	19.8
	k_w	[-]	0.604	0.944	0.996
	h_{coil}	[mm]	6.4	6.0	6.0
	l_{int}	[mm]	4.8	7.2	6.8
15 [mm]	F_{max}	[N]	14.5	39.0	45.4
	F_s	[N/m ²]	3220	4340	4037
	k_m	[N/ \sqrt{W}]	4.5	9.3	9.87
	k_w	[-]	0.669	0.951	0.9985
	h_{coil}	[mm]	3.5	3.2	3.2
	l_{int}	[mm]	4	4	4

toothless motor. It is assumed that this value is not dependent on the pole pitch. The attractive force becomes more sensitive to the air gap height as the PM height increases. Therefore, the attractive force is an important criteria for a toothless motor design.

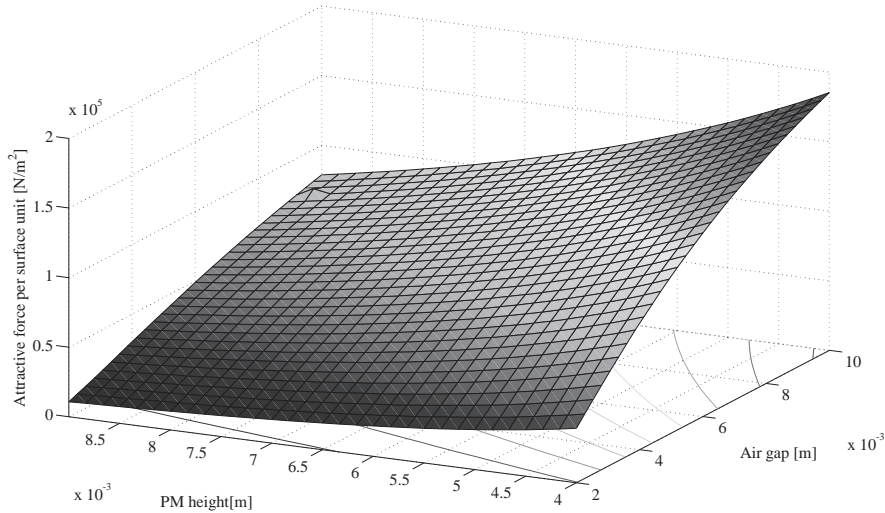


Figure 6.19: Attractive force per surface unit for a toothless motor as a function of the PM and air gap height.

Concerning the winding, no additional conclusions can be made compared to the Section 6.3.1.1.

Sometimes, it is interesting to define the peak force of the motor, i.e. the value which can be reached during a short ON time. An example of the calculation of the peak force is introduced here. This value is limited by two aspects:

- a possible demagnetization of the PM due to the coil mmf;
- the maximum coil temperature.

To determine a peak force F_{peak} , the duration of the motor ON time t_{on} must be first determined. During this time, it is assumed that there is an adiabatic overheating of the coil. Therefore, (5.1) becomes:

$$\frac{\partial \theta_{coil}}{\partial t} = \frac{J_{peak}^2 \cdot \rho_{cu}}{c \cdot \rho_c} = k_{\theta} \cdot J_{peak}^2 \quad (6.2)$$

k_{θ} is the heating factor depending on the temperature through the copper resistivity ρ_{cu} . For a maximum temperature in the coil of 120°C, the heating factor is equal to [78]:

$$k_{\theta} = 6.76 \cdot 10^{-15}. \quad (6.3)$$

Therefore, the thermal limit of the maximum rms current density J_{peak} is given by:

$$J_{peak} = \frac{1}{\sqrt{2}} \sqrt{\frac{T_{coil} - T_{\infty}}{t_{on} \cdot k_{\theta}}} \quad \text{for } k_{dem} \leq 2. \quad (6.4)$$

Moreover, by giving a condition that the mmf of the coil must be smaller than the mmf of the PM, the maximum current density and the peak force can be found. This peak force can only be reached during a limited ON time. If the motor is already on a given temperature, the peak force cannot be obtained during the same ON time.

Figure 6.20 shows the maximum theoretical propulsion forces and their respective current densities as functions of the ON time of the motor. However, this propulsion force can be achieved only if the supply part is designed to tolerate the required power and if the mechanical part is designed to support both the maximum force and the resulting acceleration. The effect of saturation in the beginning of the curve is due to the restriction on the coil mmf ($\theta_{PM}/\theta_{coil} \geq 2$).

For a given application, a mechanical model can be added as presented in Section 4.9 as well as a motor supply model as introduced in Section 4.7.3. In an optimization process, the peak force can be also introduced in order to optimize the motor for both its working point (nominal force and speed) and its peak force. Such an approach is interesting for applications requiring a high acceleration followed by a displacement at constant speed.

6.3.3 Ironless Double Sided Motor

For this motor type, three topologies are compared:

- ironless with a double sided MaW with mounted PM;
- ironless with a double sided HA;
- ironless with a single sided MaW with mounted PM. and opposite yoke

As seen in the previous sections, the winding with a coil opening of 120 edeg is not a good solution in terms of performances. Therefore, this winding is not taken into account here. The maximum forces for several pole pitches are optimized and are given in Tables 6.5, 6.6 and 6.7 for the three topologies. In order to be able to achieve a better comparison between the double sided ironless motor and the single

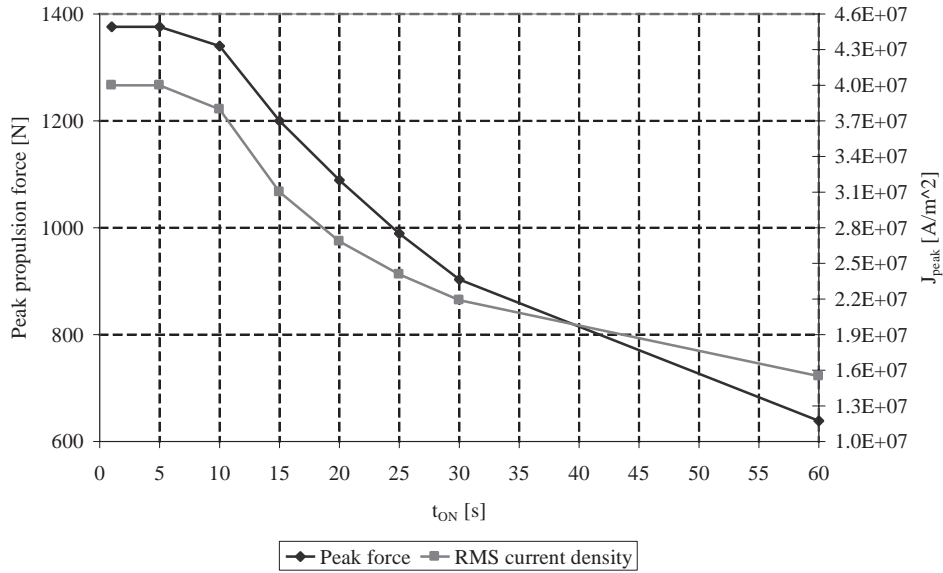


Figure 6.20: Maximum theoretical propulsion force and current density for a toothless motor as a function of the ON time.

Table 6.5: Maximum forces for an ironless motor with a single sided MaW with mounted PM. Results for several pole pitches.

			$h_{pm} \leq 10mm$ coil opening		$h_{pm} \leq 20mm$ coil opening	
			240	300	240	300
50 [mm]	F_{max}	[N]	180.7	213	217.1	257
	τ_p	F_s [N/m^2]	6022	5680	7235	6850
		k_m [N/\sqrt{W}]	25.0	26.5	30	32
		k_w [-]	0.931	0.993	0.891	0.995
30 [mm]	F_{max}	[N]	99.2	117.5	106	126
	τ_p	F_s [N/m^2]	5510	5220	5880	5580
		k_m [N/\sqrt{W}]	17.2	18.4	18.4	19.3
		k_w [-]	0.945	0.996	0.948	0.997
15 [mm]	F_{max}	[N]	34.0	40.8	34.0	40.8
	τ_p	F_s [N/m^2]	3780	3630	3780	3630
		k_m [N/\sqrt{W}]	8.04	8.7	8.04	8.7
		k_w [-]	0.951	0.998	0.951	0.998

Table 6.6: Maximum forces for several pole pitch lengths for an ironless motor with a double sided MaW with mounted PM.

			coil opening	
			240	300
50 [mm]	F_{max}	[N]	264	318
	τ_p F_s	[N/m ²]	8810	8570
	k_m	[N/ \sqrt{W}]	36.6	39.7
	k_w	[-]	0.927	0.98
30 [mm]	F_{max}	[N]	152	187
	τ_p F_s	[N/m ²]	8390	8310
	k_m	[N/ \sqrt{W}]	26.2	29.4
	k_w	[-]	0.944	0.988
15 [mm]	F_{max}	[N]	75	90.8
	τ_p F_s	[N/m ²]	8335	8068
	k_m	[N/ \sqrt{W}]	17.8	19.4
	k_w	[-]	0.951	0.998

sided ironless motor with opposite yoke, the latter is first optimized under the specified constraints and thereafter with a magnet height $h_{pm} \leq 20$ mm. This permits to have the same magnet volume than the other ironless motors.

For the double sided motor with PM the optimization process is rather time consuming due to the point current sum (4.29). To obtain more efficiently the optimized results, a simplified model could be used (4.30). It decreases the optimization time by a factor of 400 and has the tendency to give a higher propulsion force up to about 7%.

For the ironless motor with a double sided HA two optimizations are presented. The first one imposes a ratio $l_{pm\ x}/\tau_p = 0.5$ and the second one is for a non constraint ratio.

Table 6.7: Maximum force for several cases for an ironless motor with a double sided HA .

			$(l_{pm\ x}/\tau_p=0.5)$		$l_{pm\ x}/\tau_p$ free	
			coil opening		coil opening	
			240	300	240	300
50 [mm]	F_{max}	N	213	260	220	261
	τ_p F_s	N/m ²	7174	6943	7407	6964
	k_m	N/ \sqrt{W}	29.5	32.5	30.5	32.6
	k_w	[-]	0.963	1	0.961	1
30 [mm]	F_{max}	N	157	189	161	189
	τ_p F_s	N/m ²	8735	8410	8943	8421
	k_m	N/ \sqrt{W}	27.3	29.7	27.9	29.7
	k_w	[-]	0.958	1	0.956	1
15 [mm]	F_{max}	N	75.7	89.7	76.7	89.8
	τ_p F_s	N/m ²	8413	7976	8461	7960
	k_m	N/ \sqrt{W}	17.9	19.2	18	19.2
	k_w	[-]	0.956	0.998	0.953	0.998

The results of the propulsion force for HA by the analytical models are lower for about 10% compared with FEM. The optimizations of the propulsion force are not significantly different if the ratio

$l_{pm\ x}/\tau_p$ is not constraint. It means that the ratio $l_{pm\ x}/\tau_p = 0.5$ is almost optimal.

As predicted by the comparison of the mean value of the flux density, the double sided HA is less adapted for high pole pitches. Moreover, ironless motor with a single sided MaW with opposite yoke leads to worse results than with a double sided MaW. This is due to the flux leakages which are more important in this case.

The difference between the double sided motor with mounted PM and HA are the same as in Section 6.3.1. Moreover, as presented on Fig. 6.12, the HA has, for the same PM volume, a lower flux density than with mounted PM. Therefore, for the ironless motor with HA the coil height does not reach its upper value in each optimization. For example, with $\tau_p = 15$ mm and a maximum coil opening of 240 edeg, the coil height is equal to $h_{coil} = 6.3$ mm. This permits to reach higher acceleration compared to the case with mounted PM (for the same propulsion force). This could be a great advantage for specific applications.

6.3.4 Toothless Motor Comparison - Conclusion

Concerning the winding, it is demonstrated that a maximum coil opening of 120 edeg is not a good solution, excepted in application requiring a small motor length. Indeed, it has a low winding factor and produces therefore high copper losses. Nevertheless, if a toothless motor must be designed for $N_p = 2$, an overlapped winding would be more adapted.

On the other hand, the performances obtained with the two other windings are very similar and the choice between them will depend on the application. If the parameters of the coils (Fig. 4.21) are considered separately, the following noticing can be made.

l_{int}

- The inner length of the coil is in most cases close to its minimum value (this minimum value is compulsory to wound the coil). In some cases it is interesting to increase this value in order to decrease the copper losses. A small variation will not generate a high decrease of the propulsion force.
- On the other hand, this length has a direct influence on the slot opening s , i.e. on the winding factor k_w and the motor constant k_m . Therefore, as the propulsion force is less sensible to l_{int} , it is sometimes interesting to increase l_{int} in order to increase the motor factor.

l_{coil}

- This value is very important and is normally set to its maximum or close to the coil opening in order to achieve a high propulsion force.
- Moreover, the higher this value is, the higher will be the slot opening. This is still more important with a high w_{pm} . For small w_{pm} (close to the pole pitch), a compromise must be found between the end winding (copper losses) and the coil opening s .

h_{coil}

- This value increases the air gap and therefore the magnet height must be increased in order to achieve a high value of the flux density in the air gap (6.13). Therefore, if the magnet volume is constrained, it is preferred to assemble several motor modules than to increase the coil height.

w_{pm}

- The choice of this quantity is the result of a compromise between the cost of the magnetic way and the motor efficiency. Higher the width is, better will be the efficiency since the joule losses due to the end winding are proportionally less important. On the other hand, it will increase the investment costs as explained in Section 7.6.

Table 4.11 can be completed in order to show the interesting concentrated winding solutions. These solutions are given in bold in the Table 6.8.

Table 6.8: Fundamental distribution factor 1k_z for toothless motors. The interesting winding solutions are given in bold.

$N_p \backslash N_{coil}$	3	6	9	12
1				
2	1			
3				
4	1	1		
5	1	0.966		
6			1	
7		0.966	0.844	
8		1	0.960	1
9				
10		1	0.960	0.966
11		0.966	0.844	0.958
12			1	
13				0.958
14				0.966

The thermal constraints are very restrictive for the toothless motor and the single sided ironless motor, since in a normal use (not at standstill) the coils are directly in contact with the room temperature. Moreover, a forced convection can be assumed when they are travelling. On the other hand, even if the coils are moving, ironless double sided motors cannot transfer efficiently their heat to the environment. For these motors, the proposed thermal models at standstill are then closer to a normal use. For this reason, toothless and ironless motors can not be directly compared. To achieve a good comparison an application is required.

Nevertheless, it can be assumed that ironless motors are more dedicated to high dynamic applications whereas toothless are more adapted for applications requiring high propulsion force. The conclusions made for the MaW comparison are also valid for this motor technology.

In term of losses comparison criterion, it is preferred to work with the motor factor k_m rather than the motor efficiency. Nevertheless, the comparison based on the motor factor or the efficiency can, if not strictly made, lead to inappropriate conclusions. Indeed, the motor with the better efficiency does not produce in all cases the less losses.

Another difficulty, specific to linear motors, is to define the number of motor modules. For a given motor surface active, what is the best compromise, a length or a wide motor? This question can only be answered considering the application.

6.4 Toothed Motors

6.4.1 Winding Choice

For the toothed motors, the first choice to be made is the winding with its number of slots and poles. As the domain of interest are concentrated windings, the number of slots per poles and phases is $q \leq 0.5$ (Section 4.3.2). To illustrate a motor design, the proposed methodology (Section 3) is applied to the application studied in this thesis, i.e. an MMS. The specifications required to choose the winding are given here without going into details. More information about these specifications is given in Chapter 7.

First, the supply frequency is limited to 100Hz. For a maximum speed of the motor $v = 3.5\text{m/s}$, the minimum pole pitch is (4.69):

$$\tau_p \geq 17.5 \text{ mm}. \quad (6.5)$$

For the application, it was chosen to have a pole pitch between $25\text{mm} \leq \tau_p \leq 35 \text{ mm}$ in order to limit as more as possible the iron losses. Furthermore, the motor length is limited for manufacturing and mechanical reasons as:

$$0.45 \leq l_m \leq 0.55. \quad (6.6)$$

Therefore, the number of poles is confined between (4.70):

$$12 \leq N_p \leq 22. \quad (6.7)$$

By introducing a winding factor $^1k_w \geq 0.9$ and by selecting the combinations of N_s and N_p leading to a low cogging force ($k_{cogg} \geq 12$), the interesting combinations of slot and pole numbers are obtained. They are given in Table 6.9. The check mark with an asterisk are windings with both possibilities, one or two layers, while the check marks denote a two layer winding.

Table 6.9: Possible combinations of slot and pole numbers, for the winding factor $^1k_w \geq 0.9$ and a combination leading to a low cogging force.

$N_p \backslash N_s$	12	15	18	21	24
14		✓			
16		✓			
17			✓*		
19			✓*		
20				✓	
22				✓	✓*

The solution with $N_p = 22$ and $N_s = 24$ has the lowest k_{cogg} factor leading to a higher cogging force (4.61).

After this first selection, the number of winding possibilities is equal to 10.

However, all these solutions cannot be studied and an additional selection based on the combinations which have the same number of slots N_s (the same winding) must be made.

For a given motor length l_m , the supply frequency is given by:

$$f = \frac{v}{2 \cdot l_m} (N_p). \quad (6.8)$$

The motor with a higher number of poles have then a higher supply frequency. This corresponds to an increase of the iron losses following (5.28). Therefore, the solutions with $N_p = 19$, $N_s = 18$ and $N_p = 22$, $N_s = 21$ are eliminated.

Finally, this selection based on several criteria leads to six possible windings which are (N_p/N_s) : (14/15), (17/18)*, (20/21), (22/24)*.

6.4.2 Maximum Propulsion Force

The comparison of maximum propulsion forces is made on the chosen winding types. The constraints are given in Table 6.1 and the thermal model at standstill is considered (Section 6.3). In this case, the motor has no iron and PM losses. The additional constraints are given in Table 6.10.

Table 6.10: Additional constraints relative to toothed motors.

B_s, B_y	Tooth and yoke flux density	<1.8 T
h_s	Slot height	<0.1 m
l_m	Motor length	0.45-0.55 m

The maximum propulsion forces for each winding achieved under the given constraints and thermal model are listed in Table 6.11. The restricting factor is again the magnet temperature, fixed at $T_{pm} = 60^\circ C$.

Table 6.11: Maximum propulsion forces for several windings for a toothed synchronous motor.

$(N_p/N_s)_{\# \text{ layers}}$		(14/15) ₂	(17/18) ₁	(17/18) ₂	(20/21) ₂	(22/24) ₁	(22/24) ₂
F_{max}	[N]	3075	3250	3177	3252	3730	3580
F_{att}	[N]	22200	23370	23370	24200	25840	25840
F_s	[N/m ²]	37260	39360	38420	39420	45150	43370
k_{cu}	[-]	0.55	0.6	0.55	0.55	0.6	0.55
k_m	[N/ \sqrt{W}]	220	233	231	238	246	239
k_w	[-]	0.951	0.956	0.953	0.953	0.958	0.949
k_c	[-]	1.248	1.212	1.212	1.187	1.146	1.146

This first comparison shows that toothed motors are more powerful than ironless motors. The propulsion forces for all the windings are almost the same and the program imposes for all cases a magnet height of $h_{pm} = 10$ mm and fixes the slot height to its maximum value. The presented comparison allows to make some interesting conclusions.

In term of propulsion force and for the same number of poles and slots, windings with one layer have a higher maximum force than windings with two layers. This is mainly due to their winding factor k_w and their copper filling factor k_{cu} , which are higher for one layer than for two layers.

As this comparison is made at standstill, there are no iron and PM losses. The only losses are copper losses. For a same number of layers per slot, the motor with the smallest tooth pitch will have, following (4.82), the smallest Carter factor k_c . Smaller the Carter factor, higher is the propulsion force. By sorting windings from the smallest tooth pitch to the highest (for a same motor length), a classification of the propulsion forces is obtained. The increasing order is the following: (22/24), (20/21), (17/18), (14/15). On the contrary, the motors with the higher number of poles will produce higher iron losses. Therefore, this comparison shows that a compromise must be made between iron losses and copper losses. Among these proposed motors and for an application at low speed, the winding (22/24) would be the most adapted, although at high speed the motor with the winding (14/15) would be preferred.

Therefore, the choice of the winding is dependent on the application and its working point(s) (speed, propulsion force, etc.).

To find the compromise between iron losses and copper losses, the motor constant k_m is completed by taking into account the iron losses. The second motor factor k_{m2} is introduced as:

$$k_{m2} = \frac{F}{\sqrt{P_{cu} + P_{iron}}}. \quad (6.9)$$

To show the motor constant variation as a function of the speed, a comparison is presented for the windings (22/24) and (17/18). These winding have both possibilities i.e. 1 and 2 layers per slot and a different pole pitch τ_p for a given motor length. Although the motor is not any more at standstill, the thermal constraints are kept the same, in order to compare the results with those in the previous Sections.

The maximum propulsion forces for the studied windings as a function of the speed are shown on Fig. 6.21. It is interesting to denote the influence of iron losses in the stator on the maximum force propulsion. For $v = 3.5$ m/s, which corresponds to the maximum speed reached by the motor for the presented application, the different windings develop about the same propulsion force. Figure 6.22 shows the motor constant k_{m2} as a function of the motor speed. As it was predicted, the motors with a higher number of poles for a same motor length are more adapted for low speed. Indeed, this figure shows that the solutions (22/24) have a higher motor constant at low speed than the solutions (17/18). At high speed, this tendency is reversed due to the iron losses.

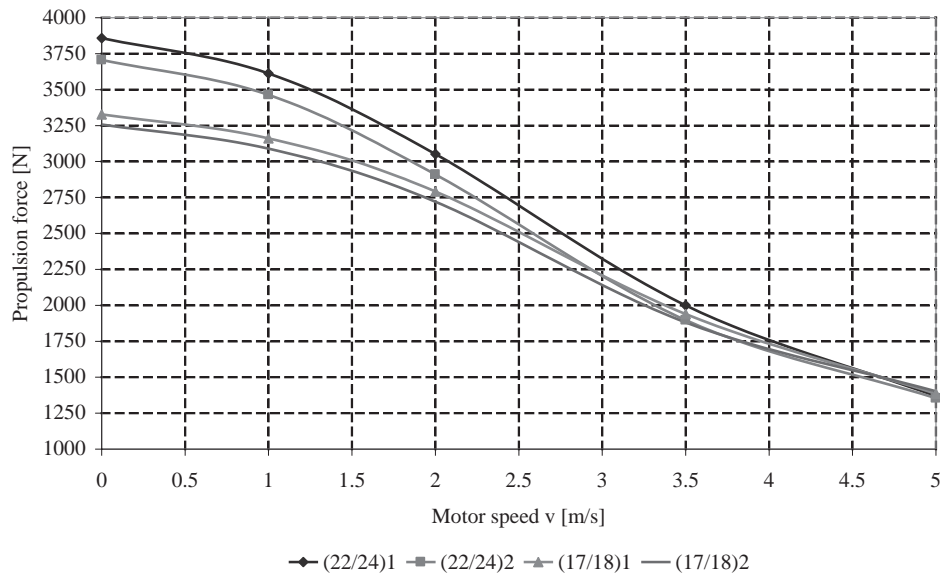


Figure 6.21: Maximum propulsion force under the given constraints (Table 6.1 and Table 6.10) and for a same motor length.

For $v=0$, the maximum force is obtained when the magnet height is equal to its maximum and when the flux density in the tooth is also maximal.

For $v \neq 0$, the iron losses increases with the speed. Therefore, the tendency will be to reduce the flux density in the teeth. As shown on Fig. 6.23 where the iron losses in the supply part are presented as a function of h_{pm} and l_s , the flux density is more sensitive to the magnet height than the tooth length. Therefore, to reduce the iron losses at high speed and to achieve the maximum propulsion force, the tendency is to reduce the magnet height. In this case, a special attention must be made on the ratio between the PM mmf and the coil mmf which becomes close. The case with two layers per slot is less critical than the case with one layer per slot, for which the coil mmf is higher. For this reason, there is an intersection on the Fig. 6.23 between the two curves of the same number of poles and slots, but with a different number of layers.

For the iron losses computation, it was assumed that they are not influenced by the coil mmf. If the coil mmf is close to the PM mmf and if the teeth are slightly saturated, the additional iron losses should be taken into account. This aspect was not modelised in this thesis.

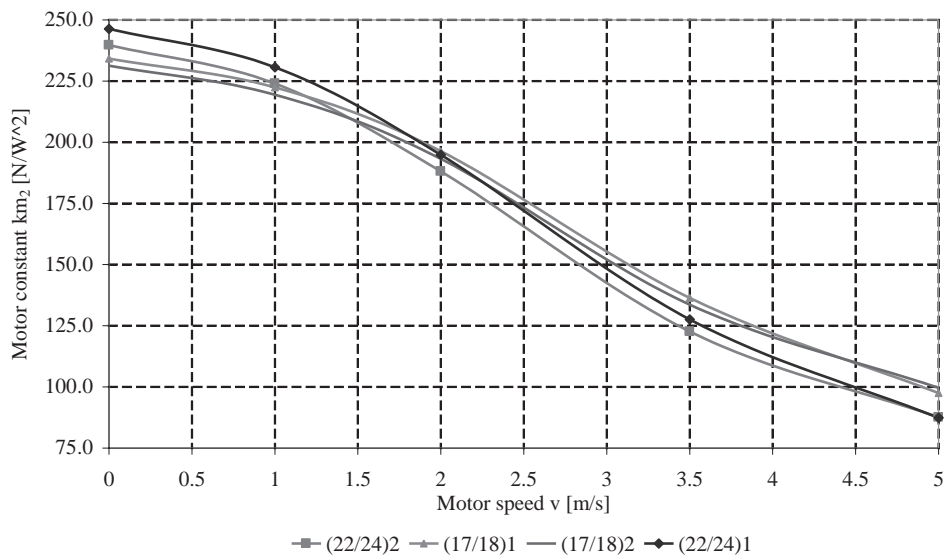


Figure 6.22: Motor factor k_{m2} corresponding to the maximum propulsion force presented on Fig. 6.21.

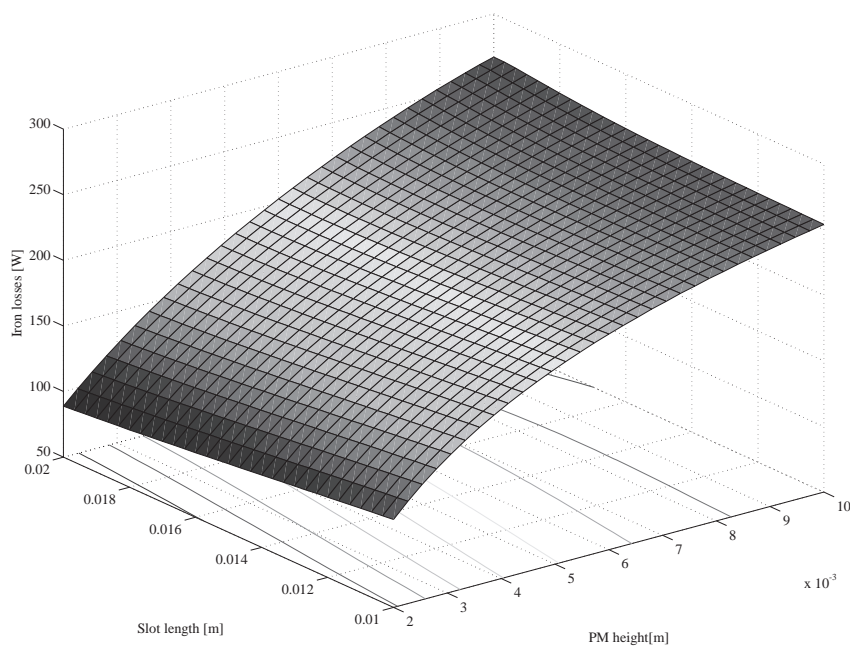


Figure 6.23: Iron losses as a function of the magnet height and the slot length.

The mmf distribution in the air gap due to the coils is not the same for a single layer winding than for a two layers winding. It was noticed that the latter has tendency to produce less iron losses. This is due to a better flux distribution.

Moreover the number of layers influences the cyclic inductance L_s . For a same number of turns per slot, the case with one layer per slot will have a higher L_s than in the case with two layers per slot. This decrease of the cyclic inductance represents an advantage for an application requiring a high dynamic.

This comparison based on the propulsion force and the motor constant does not take into account additional restrictive factors such as the material cost, the mobile mass (which is comparable to the inertia in the case of rotative motors) or other constraints introduced by the application. The following section gives a more detailed analysis of a motor in order to show the influence of several parameters on the motor design.

6.4.3 Motor Design, Parameter Sensitivity.

A winding is chosen to illustrate the parameter sensitivity. It is the $(17/18)_2$. By starting with the design which gives the maximum propulsion force (1881 N) at the nominal speed of 3.5 m/s, several parameters will be changed in order to evaluate their effect on the motor performance.

The first interesting parameter is the magnet height h_{pm} . By keeping the same losses as in the preliminary design, the propulsion force is optimized with several given h_{pm} corresponding to an increase or a decrease in percent of the nominal value $h_{pm} = 4.73$ mm. Figure 6.24 shows the maximum force variation as a function of h_{pm} .

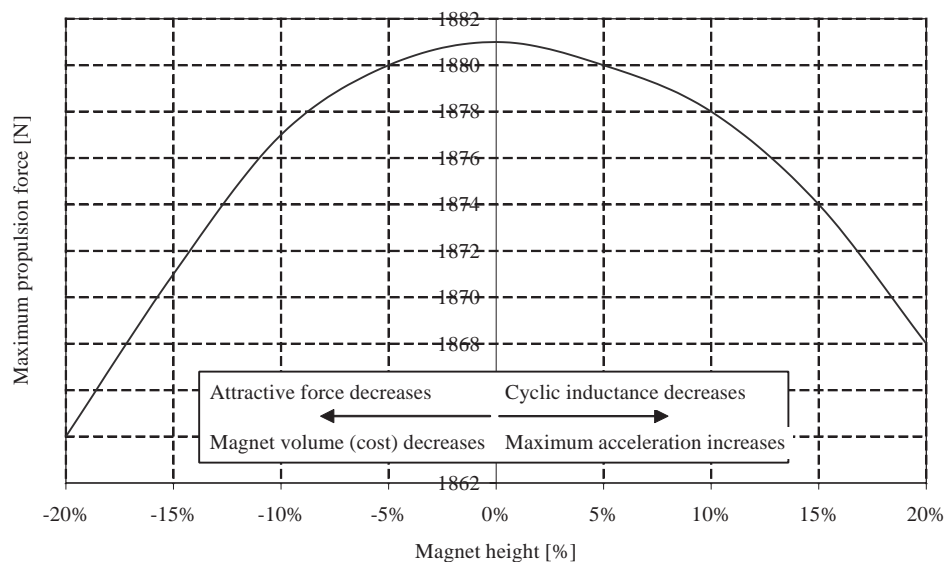


Figure 6.24: Maximum propulsion force for $v=3.5$ [m/s] as a function of the magnet height h_{pm} . The reference is the maximum propulsion force with a magnet height $h_{pm} = 4.73$ mm.

For the given constraints, the variation of the PM height has not a significant impact on the maximum propulsion force. Nevertheless, by decreasing the magnet height, the PM cost and also the attractive force will decrease, which affects roughly the motor material cost. This aspect will be an additional constraint for the presented application. This cost constraint will be introduced by a function which will take into account both the material cost and the exploitation costs. This aspect will be discussed in Chapter 7.

Moreover, this figure shows the duality between an optimized design and the compromise which can be made.

An approximation of the attractive force around the reference point can be estimated as follows:

$$F_{att} = F_{att\ ref} \cdot \left(\frac{\delta + (1 + \varepsilon) \cdot h_{pm\ ref}}{(1 + \varepsilon) \cdot (\delta + h_{pm\ ref})} \right)^2. \quad (6.10)$$

ε is the variation in percent of the magnet height.

Another important parameter is the slot length l_s (or tooth length). Figure 6.25 shows the propulsion force, the saturation factor k_{sat} (4.88) and the respective PM temperature as a function of the slot length l_s . These graphics are very interesting since they show the problem of the validity domain. In this case, when l_s is too long, the flux density in the tooth exceeds B_3 (Annexe B), which is the highest magnetic flux amplitude permitted by the adopted model (only the central part of the BH curve is modelled). Therefore the graph shows that it is compulsory to stay in the limits of the model.

This analysis shows also that by varying the slot length, the maximum propulsion force can be increased. This increases, for a constant current density, the copper losses which causes an increase of the motor temperature. This analysis on the slot length permits to show the necessity to stay in the limits of the problem and to pay special attention on the most limiting factors of the optimization.

Another interesting parameter is the magnet width w_{pm} . The variation of this parameter has, as in the case of a rotative motor, an impact on the motor constant, but also an important influence on the motor material cost in the case of a long stroke. Indeed, for a long stroke and a same active surface, it is preferred to have for material cost reasons, a long rather than a wide motor. This construction aspect is discussed in details in Section 7.6.1. To show the relation between motor width and motor length, three additional designs are considered as presented in Table 6.12. All these designs have the same pole pitches.

Figure 6.26 shows the maximum propulsion force and their motor constant k_{m2} as a function of the motor width, for a slot height of $h_s = 0.05$ m and $h_s = 0.03$ m.

If only the motor width would be changed and the other geometrical quantities and the current density remain unchanged, the propulsion force is proportional to the motor width if the end extremities are neglected. The motor constant k_{m2} decreases less with the decrease of the motor width. From Fig. 6.26 it can be seen that the maximum propulsion force is higher for a small motor width than for a high motor width. This is explained by the fact that the reduction by half of the motor width does not correspond to a decrease by a half of the convection and radiation surfaces since the motor faces contribute also to the heat transfer. As a consequence, the motor losses can be increased by a factor higher than two. This is validated by Fig. 6.26, since for rather small slot height the maximum propulsion force does not increase significantly. On the contrary, the motor constant k_{m2} decreases. Therefore a compromise between the number of motors in series and the motor constant must be made. This compromise will be also influenced by the motor costs. For a long stroke, it will be preferred to build several motors in series whereas for a small stroke, the choice of a wider motor will be advantageous.

Several other compromise designs will be presented in Chapter 7 in relation to the studied application.

6.5 Motor Comparison - Conclusions

With these different optimizations, several conclusions can be made on the studied motor types. In linear motors, the comparison between toothless and toothed motors is not so difficult as for rotative motors [79], since the force density can be directly compared. On the contrary, for rotative motors, the rotor radius must be taken into account in order to compare the motor torque. Therefore, toothed motors are clearly dedicated for high propulsion force whereas ironless motors are more adapted for applications requiring a high acceleration or a high dynamic.

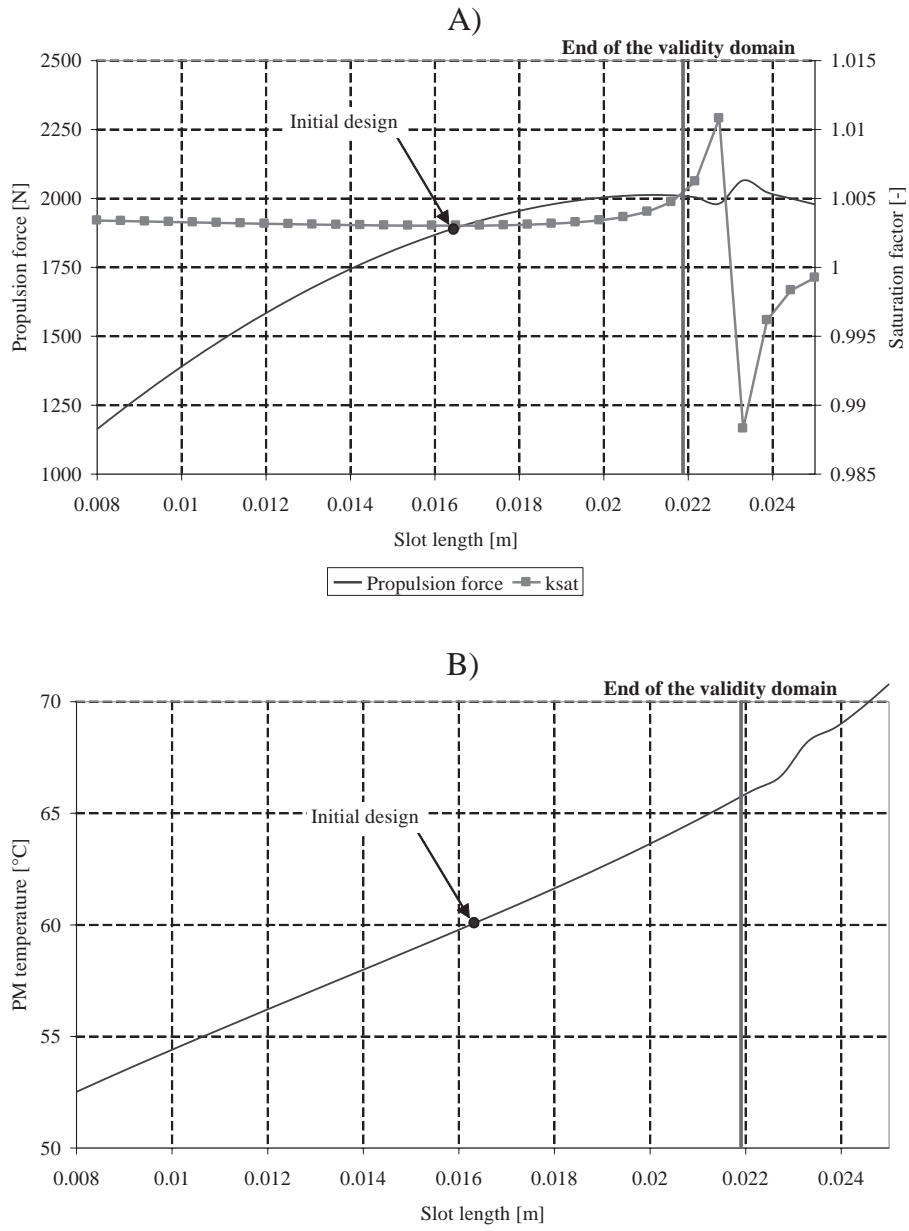


Figure 6.25: Propulsion force and saturation factor (A) and PM temperature (B) with variation of the slot length around the initial design ($F_{max} = 1881 \text{ N}$, $v=3.5 \text{ m/s}$).

Table 6.12: Four motors design with different magnet width and number of poles and slots.

N_p	17	34	51	68
N_p	18	36	54	72
w_{pm} [mm]	150	75	50	37.5

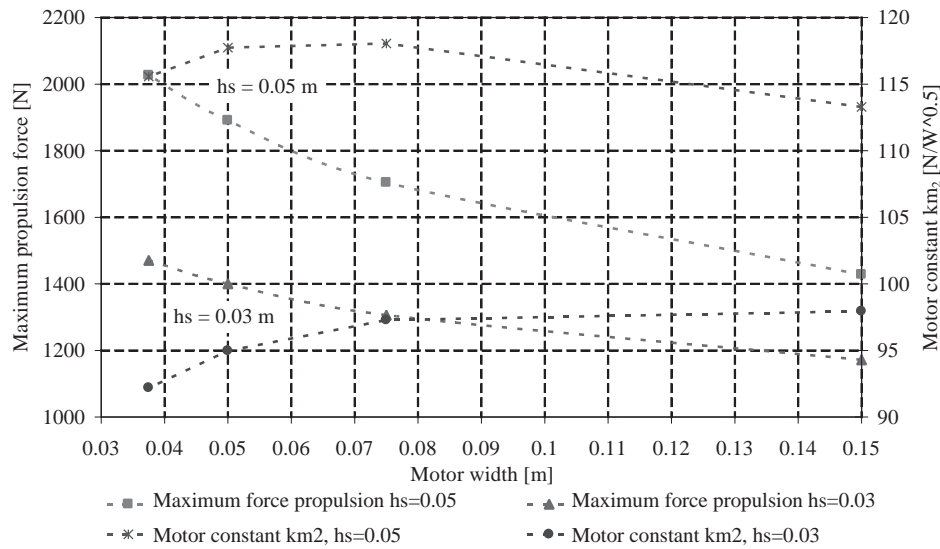


Figure 6.26: Maximum propulsion force and its corresponding motor constant k_{m2} as a function of the motor width, for a slot height of $h_s = 0.05$ m and $h_s = 0.03$ m

If the motors are designed at standstill with comparable thermal models, the force density for toothed motors can arise up to about 4 N/cm^2 . By comparison, ironless motors with a double sided MaW can develop up to about 0.8 N/cm^2 whereas toothless motors can produce up to about 0.6 N/cm^2 .

On the other hand, if the thermal model takes into account the motor speed, the force density for toothed and toothless motors could be increased in a ShS case. For a speed of 3.5 m/s , which is the speed of interest for the studied application, the force density increases up to 5.5 N/cm^2 for the toothed motor and up to 1.2 N/cm^2 for the toothless motor.

Concerning the acceleration, the ironless motor with a double sided MaW permits to achieve high acceleration up to 150 m/s^2 whereas toothed motors allows an acceleration up to 80 m/s^2 .

Therefore, these two key points, acceleration and maximum propulsion force, show clearly the difference between toothed and toothless motors.

Concerning ironless motors, the motor with a double sided MaW reaches the highest acceleration. Concerning the MaW and for high pole pitch (in order of 30 mm or higher) the solution with mounted PM is preferred. On the other hand, for small pole pitches, HA becomes an interesting solution.

Moreover, in an optimization process, it is interesting to analyze the restricting factor(s). For the presented analysis, the temperature was often the most restricting factor. As shown in Chapter 5, thermal models are not so precise as the electromagnetical ones. Therefore, by constraining the problem by non precise quantities, it is compulsory to ensure that the optimized result will be, in the real application, situated in the constrain domain and will therefore not produce a motor overheating. In this thesis, all the presented thermal models lead to higher temperature than the results obtained in experiments. Therefore, no overheating should be possible.

In this chapter, the principal key points of each motor type were shown. More precise comparisons can be made by taking into account the application. For example, such an analysis between ironless motors for a high dynamic application is presented in [77].

Chapter 7

Application - Linear Motor for a Lift

7.1 Introduction

This chapter deals with a linear motor for a lift. This application has been briefly introduced in Section 1.1. The methodology presented in Chapter 3, which defines the sections of this chapter, is used.

In large cities, due to expensive land price, high-rise buildings are built, in which the space dedicated to the elevators is considerable and reduces the rented surfaces. To decrease the size of these "lost" surfaces, a Multi Mobile System (MMS) is proposed. It is a system with several cars travelling up and down in the same shaft, as described in [80, 81]. The traffic optimization during up peak traffic (early in the morning) or down peak traffic (late afternoon) leads to dedicate several shafts with the same car direction, having smaller cabins than conventional solutions. Furthermore, a horizontal transfer of the cars is needed to allow them to change shafts. Such a traffic optimization, adjusted directly to the traffic demand, permits to decrease the needed surface thus increasing the rented surface. This leads to a better financial management of the building and a better service. In the MMS of the future, the individual cabins can move autonomously. This requires a ropeless (without counterweight) elevator system with self-propelled cabins. Therefore, linear drives become a must. It implies high mechanical power and energy consumption. The lack of counterweight has also a direct effect on the required mechanical power: since the maximum admissible acceleration is less than 13 % of the gravity, the major part of the mechanical power is dedicated to compensate the gravity. As a direct consequence, the recovery of the potential energy is extremely important.

Such an MMS differs from the solutions presented in Elevators for Skyscrapers [1] and in High Rise Elevators For the 21st Century [2], but is closer to conveyor technologies, as described in [3].

The main advantages are:

- more rented surfaces;
- reduced average travelling time;
- more travelling capacities in case of building evacuation;
- positive return on investment.

Whereas the main drawbacks are:

- complex electronic and mechanic;
- high power and energy needed;
- high investment cost.

The following aspects are crucial in the MMS:

- the arrangement of the shafts and the organization of the cars in them;
- the drive system needed to realize the autonomous movement of the individual cars;
- the control of the cars based on the customer requirements. The destination call control patented by Schindler can offer important advantages. In this control, starting and destination landing are known before the passenger enters the car. The control also knows the number of passengers having the same destination. With this information the traffic can be controlled more efficiently;
- safety and availability of the entire system;
- cars in lightweight construction and their mechanical rendering;
- power supply and potential energy recuperation.

The main goal of such a MMS is to increase the rental surface by decreasing the space needed by the lifts. An MMS can reduce the lift space up to 75% [82].

More details related to MMS can be found in [4, 83].

7.2 Specifications and Objectives

The traffic management defines the motor specifications [82, 84]. The goal of an MMS regarding time efficiency is to offer at least the same traffic characteristics as a conventional lift. In this example, only the case with small cabins is studied. Two motions of the cabins are considered: the vertical cabin motion in a given shaft and the horizontal motion during the cabin transfer from one shaft to the shaft aside. It is necessary to specify that both movements, the vertical and the horizontal, cannot be realized with the same motor drive. Nevertheless, the possibility to drive the cabin with the same motor has been analyzed [82]. Unfortunately, the solution was mechanically very complicated and the switching duration time (the time needed for one cabin to change shaft) was too long. Therefore, the continuous movement (vertical-horizontal-vertical) is considered and is realized with a sleigh [83].

Table 7.1 gives the MMS specifications. They do not take into account the increase of weight due to the propulsion system. Indeed, this weight differs following the motor type and topology. In a ShS case the converter and a high power system of energy transmission must also be embarked.

The speed of an MMS is reduced compared to a conventional lift (up to 10 m/s). Indeed, the traffic efficiency is not considerably affected by the maximum speed, but it depends on the acceleration, on the waiting time and on the time requested for entering and leaving the cabin.

Traffic simulations (done by ETHZ, [82]) show that the handling capacity is on average 3-4 times and maximum 10 times higher than with the conventional elevators. On the contrary to the actual lifts, the handling capacity will not decrease with the building height. The different studied scenarios and related results have allowed to define the motor specifications, the number of shafts, the cabin size and the number of cabins.

To determine the energy and the cost balances a reference building with the following specifications is considered:

- number of floors: 18+3 (Entrance floors);
- floor height: 4.2 m;
- number of cabins: 16;

Table 7.1: Motor specifications.

			Building over 60m small cabins	
			vertical motion	horizontal motion
System specifications	Rated load	[kg]	630	0
	Car weight ¹	[kg]	450	450
	Levelling accuracy	[mm]	< 1	< 1
	Static cabin distance	[m]	0.4	–
	Dynamic cabin distance	[m]	3	–
	Number of cabins	[Nb/m]	0.06	–
	Supply voltage	[V]	3x460	3x460
	Noise	[dBa]	< 50	< 50
Motor geometry specifications	Motor weight	[kg]	TBD	TBD
	Length	[m]	max. 2	max. 2
	Depth	[m]	the smallest	the smallest
	Width	[m]	max. 1.2	max. 1.2
	Air gap	[mm]	3	3
Motor working specifications	Peak force ¹	[kN]	11.9	0.25
	Peak power ¹	[kW]	41.7	0.15
	Continuous force ¹	[kN]	10.6	–
	Continuous power ¹	[kW]	37.1	–
	Max. motor duty cycle		30%	50%
	Speed	[m/s]	3.5	0.6
	Acceleration	[m/s ²]	1.2	0.5
	Max. acceleration (empty cabin)	[m/s ²]	5.8	0.5
	Motor temperature	[°C]	120	120
	Max room temperature	[°C]	40	40
Cooling		TBD	No	

- number of shafts: 3.

The goal of the project is to define the best motor for the application. It must fulfill the specification and the whole system must be competitive in terms of costs and security compared to a conventional lift.

7.3 Design Methodology

The methodology used to design the motor for the MMS is based on Chapter 3. Here, the key points are recalled in order to have a better understanding of the following sections:

1. all the considered motor topologies and types will be introduced and a first selection related to the application will be made. This selection will be based on the basic characteristics of each motor, i.e. no motor designs will be performed for this step;
2. several additional figures of merit will be introduced and several motor pre-designs will be performed in order to build a comparative table. By using this table, a second motor selection will be made;

3. the choice of the motor topology, ShS or LS and single or double sided, will be made. This choice will be imposed by the application;
4. the pre-selected motors for the chosen topology will be compared in order to choose the best adapted motor type. After this last selection, the final motor will be designed and validated by FEM.

7.4 Linear Motor Type Possibilities for an MMS

All considered motors for this application are presented on Fig. 7.1. They can be asynchronous or synchronous motors. Nine motors and four topologies (short or long stators and double or single sided) are first considered.

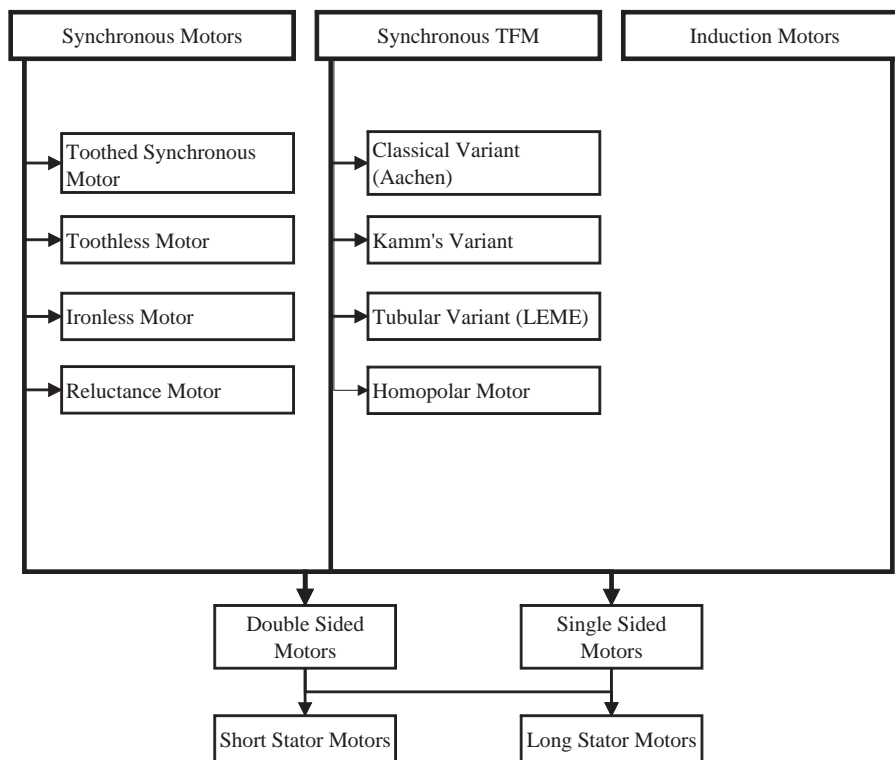


Figure 7.1: Considered motor variants and topologies for the MMS application.

All synchronous motors have been introduced in Chapter 1 except the homopolar linear motor which is the motor variant used for the Swissmetro project [85]. For the proposed TFMs, a short description is given in order to have a better overview.

The **classical variant** for the TFM motors is shown on Fig. 7.2. For this motor, the number of poles is given by the number of permanent magnets divided by two, because only half of the permanent magnet fluxes are active at each position when producing linkage flux. This characteristic requires that the motor must have an even number of permanent magnets to create a flux balance in the air gap. As an example, Figure 7.2 represents one pair of poles motor with four permanent magnets [86].

The linking flux, despite of the propulsion force, creates also an attractive force between both stators and the reactive track. This force can be annihilate by building a double sided motor.

The **Kamm's variant** has been introduced in Section 4.6.

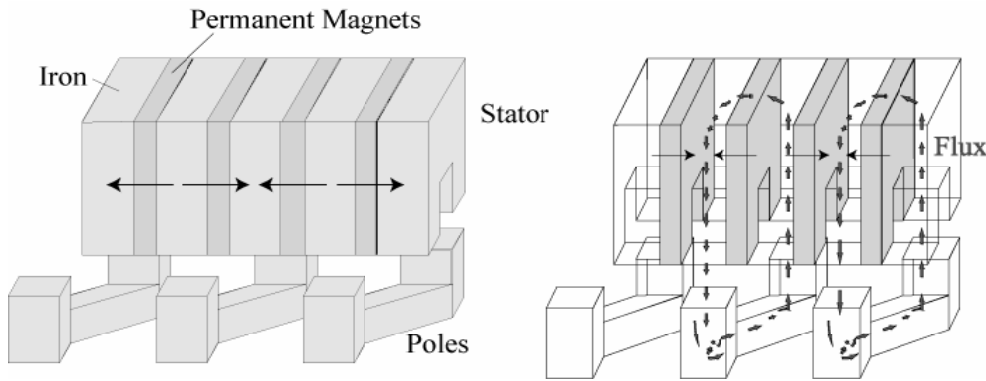


Figure 7.2: Transverse flux motor - Classical variant - one phase stack is shown [86].

The **LEME variant** starts as a simplification of the Kamm's variant. The design is shown on Fig. 7.3. Two main differences have been introduced to this variant:

1. it uses one single stack of permanent magnets and iron pieces;
2. the linking flux closes through the rotor and not through the stator.

The second characteristic avoids the two extra air gaps needed in Kamm's variant to close the linking flux.

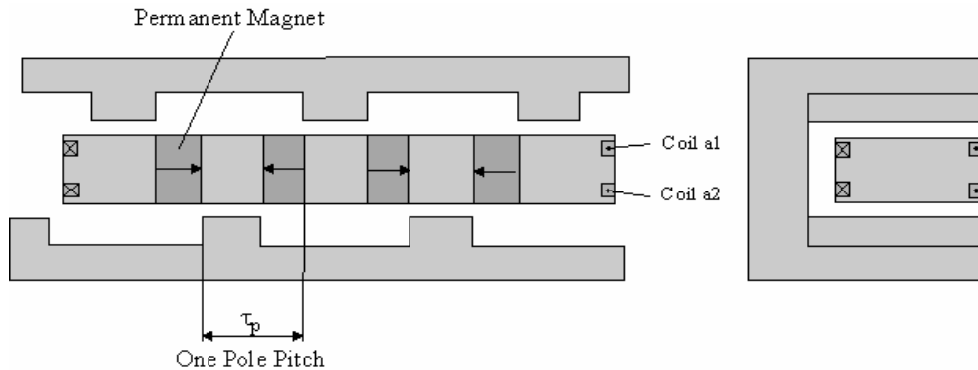


Figure 7.3: TFM - LEME Variant.

In order to further increase the active surface a tubular structure [87] can also be developed (Fig. 7.4), like rotor screw. It still needs to be proven whether this approach represents indeed an increase in active surface. In this case a rotational strength will also appear in addition to the propulsion force. The step of the screw will fix the ratio absolute value between the propulsion force and the rotation strength.

For all preselected motors the advantages and drawbacks regarding the MMS are presented in Table 7.2.

7.5 Linear Motor Preselection

7.5.1 First Motor Choice Imposed by the MMS

As presented in Chapter 3, the first motor choice is due to the application. The main figures of merit are:

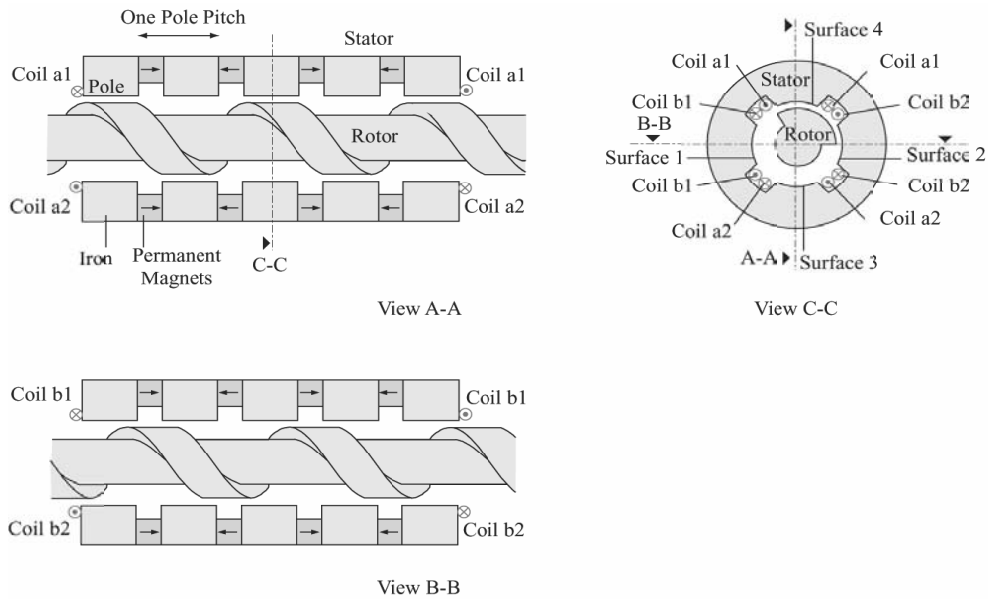


Figure 7.4: TFM - LEME Variant, screw solution [87].

- high efficiency;
- light moving mass (Energy consumption);
- to be able to work with a large air gap (3 mm);
- easy to manufacture;
- investment and exploitation costs.

With these factors, a first tree of decision (Fig. 7.5) is built. It has two options depending on the motor topology: short stator and long stator.

Three motor types, not dependent on the topology, are eliminated using the proposed criteria. These motors are the TFM LEME Variant, the TFM classical variant and the reluctance linear motor (RLM). Thereafter, the motor pre-selection process depends on the motor topology, ShS or LS.

For the ShS topology the most relevant figure of merit is the moving mass. Indeed, as the converter and a high power system of energy transmission must be embarked, the reduction of the moving weight is compulsory in order to reduce the needed power to move the cabin (up to 42 kW if the weight of the motor, the converter and the system of energy transmission are not taken into account). With this additional figure of merit, the homopolar motor (HLM) and the induction linear motor (ILM) can be eliminated.

For a LS topology the moving mass is not so relevant because the motor moving part weight will be relatively light for all motor cases. An important factor is the material cost. With this additional factor of merit, the homopolar motor and the TFM Kamm's variant are eliminated since with these topologies coils and magnets are mounted along the shaft leading to an expensive solution.

Therefore, four motors are preselected for each topology and they are listed in Table 7.3.

Table 7.2: Motor advantages and drawbacks for an MMS.

Toothed Synchronous Linear Motor	
Advantages	Drawbacks
Very high force density.	Expensive MaW. Very high attractive force between the motor and the MaW.
Synchronous Homopolar Linear Motor	
No rotor excitation is needed \Rightarrow passive track.	Small active surface \Rightarrow more iron \Rightarrow more weight.
Ironless Synchronous Linear Motor	
No attractive forces.	Low force density (large magnetic air gap)
Toothless Synchronous Linear Motor	
High force density.	Expensive MaW. Very high attractive force between the motor and the MaW.
Reluctance Synchronous Linear Motor	
Passive way is made of iron. No attractive force at no load.	Less interesting energy recovery. Needs a small air gap to achieve a high propulsion force density. Noisy.
Induction Linear Motor	
Easy to build (low cost). Passiv track. No attractive force ($I=0$).	Low power factor ($\cos \varphi$) and efficiency Less interesting energy recovery. Needs a small air gap to achieve a high propulsion force density.
TFM Classical Variant	
	Small propulsion force density. High reluctance force.
TFM Kamm's Variant	
High power density.	Two additional air gaps. In a long stator case, both the winding and magnets on the active part. Guidance problems.
TFM LEME Variant	
Produce a propulsion force and a rotary force	A big active surface is needed to produce the propulsion force, this means a weight increase. The rotor is difficult to manufacture.

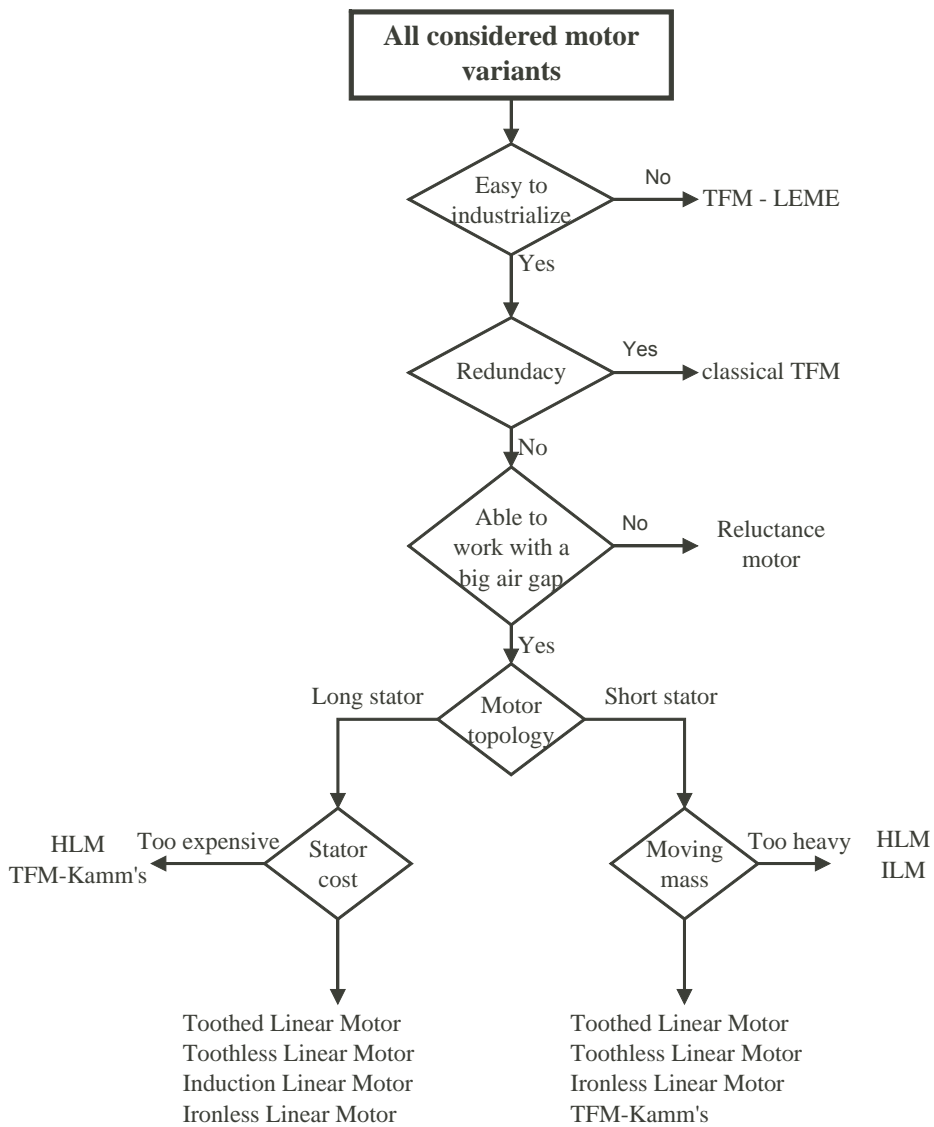


Figure 7.5: Considered motor variants and topologies for the MMS application.

Table 7.3: Preselected motors for each topology due to the application constraints.

Short Stator	Long Stator
Toothed synchronous motor	Toothed synchronous motor
Toothless synchronous motor	Toothless synchronous motor
Ironless synchronous motor	Ironless synchronous motor
Induction motor	TFM kamm's variant

7.5.2 Second Choice Imposed by Additional Choice Criteria

After this first choice, a comparative table is built in order to make the second choice based on more specific merit factors. The goal is to select only two motors per topology. The resulting effective active surface, for all the different designs, changes from one motor type to another, since they do not create the same propulsion force density due to their physical differences. The following points are considered:

- the force density is important to reduce the motor surface;
- the weight of the motor moving mass is also an important factor since it gives an idea of the additional needed energy consumption;
- if these two factors are combined such as to obtain a mass per force unit, then the most interesting motor, from an electrical point of view, is the one which has a low value of weight per force unit.

Nevertheless, the choice of the motor cannot only be made on these factors. The mechanical integration of the motor and especially the total investment costs must be analyzed. These two aspects depends naturally on the motor topologies. Table 7.4, presented in per unit [p.u.], gives the essential electromechanical figures of merit to design a motor for an MMS. This table is the result of many designs and simulations for the toothed synchronous motor, the toothless motor and the ironless motor and from experiments done with the TFM motor. The results for the induction motor are taken from the literature [13]. The reference for this analysis is a short stator toothed motor with mounted permanent magnets. In the case of the toothless motor, the number between brackets corresponds to a motor design with a speed of 3.5 m/s.

Table 7.4: Preselected motor comparison, second motor choice.

Motor variants	Force density [kN/cm ²]	Weight moving mass [kg/m ²]	Force per weight unit [kN/kg]	Attract. Force I=0 [N/cm ²]	Efficiency v _{max} , full cabin [%]	Air gap sensi- tivity (for the propulsion force)	Vibration force ripples	
Short stator	Toothed	1.00	1.00	1.00	90-95	Very high	Yes	
	Toothless	0.19 (0.35)	0.40	0.48 (0.95)	0.35	85-90	High	Yes (not important)
	Ironless	0.25	0.20	1.11	0.00	85-90	low	No
	TFM Kamm's	0.20	0.85	0.42	0.00	79.3 (V=1m/s)	low	Yes
Long stator	Toothed	1.00	0.25	4.00	1.00	90-95	Very high	Yes
	Toothless	0.19	0.30	0.66	0.35	85-90	High	Yes (not important)
	Ironless	0.25	0.60	0.44	0.00	85-90	low	No
	Induction	0.30	0.30	1.00	0.00	80	Very high	No

For the **ShS topology**, the table shows clearly that the TFM-Kamm's is not adapted since it has a high weight per force unit compared to the others. It means more energy to move the cabin which is a disadvantage. Mainly for this reason and since this motor is difficult to manufacture and to guide, it was decided to eliminate this solution. Another criterion was used to suppress the ironless motor. This motor has a low weight per force unit but it needs a lot of space and magnets leading to an expensive solution. Moreover, several motors must be mounted in parallel to produce the needed force. This could

bring guidance problems and hyperstatic mechanical problems. Therefore, this motor is not adapted for an MMS.

For the **LS topology**, the ironless motor is eliminated for the same reasons as in the ShS case. The induction motor has a worse efficiency than synchronous motors. Therefore, this motor will consume more electrical energy and as consequence, all the electronic parts should be more powerful. A long stator induction motor is therefore eliminated. For this topology, the toothed motor seems to be the most adapted. As a second solution, the toothless motor is appropriate since it has a high efficiency and an interesting weight per force unit. The induction motor has not a good efficiency. Moreover, this solution would be difficult to command at very low speed or at standstill.

After this second analysis it was decided, taking into account mechanical and electromechanical aspects and material costs, to keep only the toothless and toothed synchronous motors for each topology.

7.6 Considered Motor Topologies

For the two selected motor types several motor topologies are possible. They can be single or double sided and LS or ShS. The goal of this section is to define the topology which is best adapted for an MMS.

7.6.1 Double or Single Sided

The choice between single sided and double sided motors depends on mechanical considerations. Practically all motors can be either single sided or double sided. An exception is made with TFM Kamm's variant for which a double sided motor brings no additional advantages. The main reason to have a double sided motor is to reduce the attractive force between the magnetic way and the supply part and to have a more compact motor. In a Multi Mobile System, where the total attraction force is high, the use of a double sided motor is a must in order to compensate the attractive force. Figure 7.6 shows two different ways to build a double sided motor. The first is to build two independent motors in opposition. The red part on Fig. 7.6A can be small or big and plays no role in the motor operation. The second version consists in two complementary motors. In this case, the height between the coils is given by a mechanical constraint.

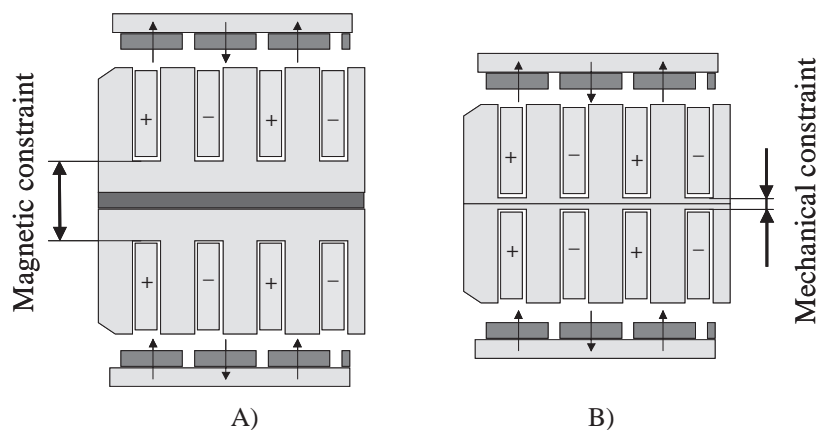


Figure 7.6: Double sided topology: A) two independent motors or B) two complementary motors.

For the project, the double sided motor with two complementary motors was chosen in agreement with the designers of the mechanical part since it is more compact.

Another choice to perform concerns the motor length. Regarding material cost, the motor length must be as long as possible in order to reduce the investment costs along the shaft. The choice of the motor

length should not disadvantage its efficiency. Figure 7.7 shows several motor possibilities for a same active surface. The stationary part along the shaft is in hell grey. The same active surface means that the investment costs for the moving part are about the same in the three presented cases (in reality, a small difference can appear if the moving mass changes). The first case on the Fig. 7.7 A) is a double sided motor with a short motor length. If for the same active surface, the motor is single sided as presented on Fig. 7.7 B), the investment costs would be reduced by a factor of 2. This single sided motor can be divided in two parts to build a double sided motor. These three pictures show the importance of the motor length in terms of investment costs.

If a double sided motor must be used to compensate the attractive force the solution shown on Fig. 7.7 C) would be the best solution in terms of investment costs, even if the efficiency is slightly worse. For this reason and due to the long stationary part along the shaft, the motor must be as long as possible in order to reduce the investment costs to the minimum.

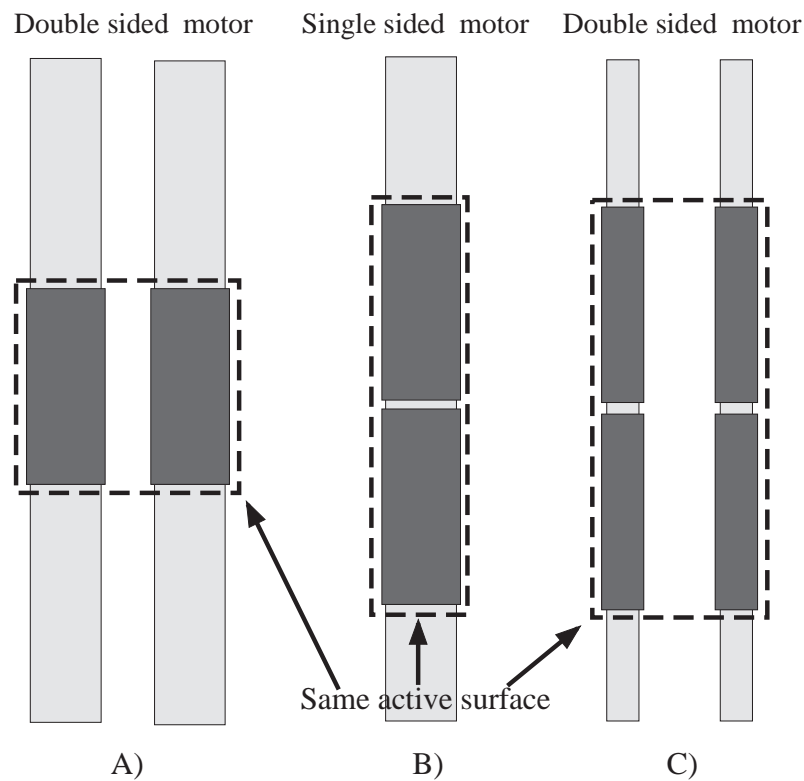


Figure 7.7: Various design topologies for the same active surface.

7.6.2 Short Stator Topologies

An important drawback of the short stator topology is the additional energy consumption due to the load of the energy transmission system to the cabin, the motor converter, the control and the cooling system. The corresponding additional mass can be up to 400 kg [88], versus the rated load of 650 kg, which implies an increase of the requested mechanical power. Moreover, the supply part of the linear motor is, in most cases, heavier than the long stator configuration. As all the electronic parts must be designed for the peak power, the investment costs will consequently increase. In terms of overheating, the ShS topology is very restricting because the motor must be designed for a duty cycle of 100%, contrary to the

LS topology which can be designed for a duty cycle less than 50 %, determined by the traffic analysis. Moreover, no water cooling can be considered on the cabin.

This motor topology seems well adapted for a counterweight solution, but not in an MMS case. To summarize, a short stator solution has the following drawbacks [78]:

- a higher energy consumption due to an additional weight of about 400 kg (motor and converter weights) and additional losses coming from the system of energy transmission;
- a system of energy transmission must be added. This system implies more weight and therefore additional investment costs. From a mechanical point of view, this extra system can bring additional problems and new maintenance costs. Moreover since a high power system is built along the shaft, a problem of security during the maintenance can appear;
- since the motor must be designed for a duty cycle of 100%, the motor weight becomes high. Furthermore, when the motor is at standstill and supplied, some heating points can appear on the system of energy transmission.
- The last main disadvantage is the fact that no water cooling system can be mounted on the cabin. The cooling system for a short stator is more important than for a long stator motor.

The advantages are:

- the motor efficiency is better;
- the complete system is more flexible in case of a breakdown since the cabin with its failed motorization can be "simply" taken off the shaft and the rest of the system can continue to work normally.

7.6.3 Long Stator Topologies

A motor with a long stator must be supplied by stator sections longer than the mobile MaW. Consequently, additional Joule losses are produced. On the other hand, this topology needs less installed mechanical power because a lower additional moving mass is on the cabin. Therefore, a compromise must be found between the stator length and the motor efficiency. This compromise is based on economical considerations (investment and exploitation costs).

From a heating point of view, the motor, divided in several segments, does not have to be engaged all the time during the cabin rise. Therefore, in the worst case, the motor duty cycle is equal to 50 %. This value will permit to increase the motor current and also to reduce the active surface (the active surface is proportional to the square root of the duty cycle). Therefore, for identical power dissipation, a smaller motor compared to a ShS motor can be designed.

The important drawback is probably the motor control and the traffic management.

To summarize, LS has the following advantages:

- significantly lighter than a ShS motor;
- no additional embarked weight;
- no high power system of energy transmission, implying a simpler system;
- duty cycle less than 50% → smaller motor;
- easy to cool.

The main drawbacks are:

- lower motor efficiency because of the longer supply part than the moving part;
- increased investment costs.

7.6.4 Motor Topology Choice

The double sided motor is a better solution than the single sided motor since it annihilates the resultant attractive force. Regarding the ShS and LS, the choice is more difficult and is made by analyzing not only the electromechanical part but also investment costs, mechanical parts and the complexity of the whole system.

The main drawback of the ShS topology is the increase of the installed power for the whole system and also the high power of energy transmission. Although technical solutions are possible (with or without contacts), it will considerably complicate the management of the power control and the cabin control. Therefore, mainly due to these two arguments, it was decided to chose a LS topology. This choice permits to concentrate on the propulsion drive and to put aside, in a first predesign approach, the energy transmission problems.

The choice of the propulsion system is a toothed or a toothless motor with a double sided long stator.

Once the LS motor is designed, it will be adapted to a ShS motor in order to compare these two solutions in terms of costs.

7.7 Motor Heating and Cooling System

Thermal models used to define the current density are the same for the toothless and the toothed motors. The following assumptions are made:

- there is no heat transfer between the MaW (moving part) and the supply part;
- losses in the MaW are thermal dissipated by forced convection due to the cabin speed. This heat transfer does not influence the motor design;
- the thermal conductivity of iron parts is assumed ideal ($k=\infty$).

For the supply part, the mean value of the iron and copper losses is taken into account using the motor duty cycle D_c . The motors will be designed with the upper value of $D_c = 0.5$ since it corresponds to the worst case. On the contrary, to evaluate the motor efficiency, all the losses (MaW and supply part) are summed without taking into account the motor duty cycle .

Finally, due to the motor duty cycle, it is decided to have *no additional cooling* for the application. Indeed, the motor duty cycle is comparable to a cooling since it allows to increase the current density. An additional cooling would have as consequence an increase of the current density and therefore a decrease of the efficiency. Furthermore, an additional cooling system will increase the investment costs.

Moreover, the temperature difference between the motor and the room will certainly generate an air circulation into the shaft. This aspect, equivalent to a forced convection, is not taken into account.

7.8 Supply Part

For a LS topology, the general electrical scheme is presented on Fig. 7.8. The supply part system was studied in details during the project and more information is given in [89]. The aim of this Section is to give the useful key points in order to have a better understanding of the whole propulsion system.

The power supply layout is composed of:

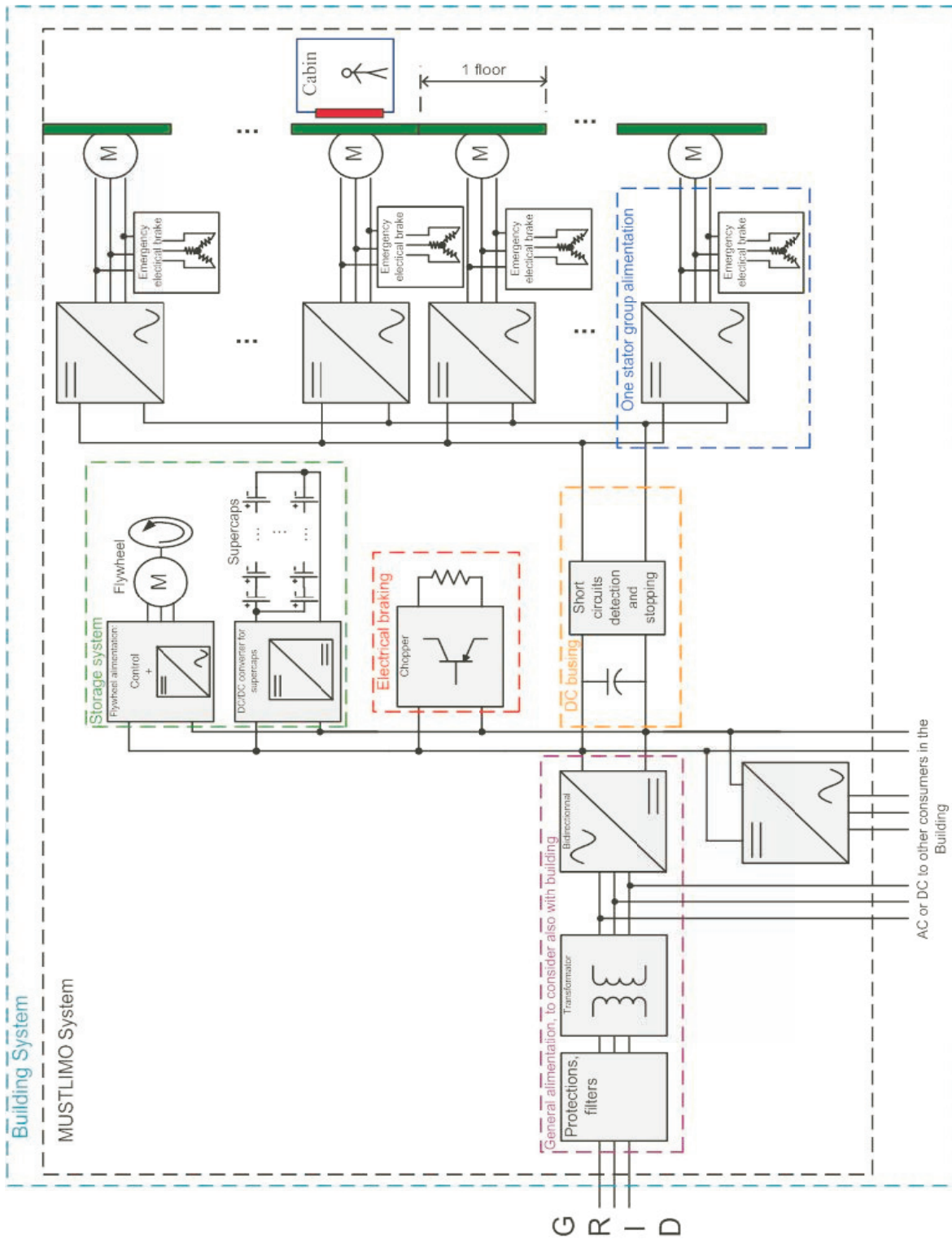


Figure 7.8: Power System General Scheme [89].

- the general alimentation of the building with its transformers and its bi-directional converters;
- an energy storage system;
- an electrical braking;
- a DC bus;
- motor supply parts with their bi-directional converters and their emergency electrical brakes.

In an MMS the regenerative braking of a cabin is compulsory because the power/energy required to lift a cabin without counterweight is significant. Therefore, the energy recuperation during down travel becomes important. The energy consumption of the MMS directly depends on the cabin weight. For cabin weight of 1100 kg, the energy consumption increases by ca. 2.5 times compared to conventional lift system to the cabin weight and the half of the rated load ($1100 + 1275/2 = 1737.5$ kg). A lighter cabin of 600 kg increases the energy consumption by ca 1.4 times compared to conventional systems with a counter weight equal to $430+630/2 = 745$ kg.

The ability to perform regenerative braking is given with a bidirectional inverter topology and the transmission of the power in the whole system is done through a DC bus. Several scenarios for using the regenerated energy are possible and they are listed by priority:

1. the energy obtained by the descent of a cabin is used to lift the others;
2. if no other cabins are going up at the same time or less power is required, the energy can be provided to other users in the building;
3. if no power is needed in the building, a storage system is used to save energy and re-inject it later;
4. the energy can be given back to the grid under precise conditions defined by the energy supplier;
5. if the grid cannot accept the energy, it must be destroyed in a dedicated device, such as a resistive system.

Regarding the DC bus, its voltage is determined by the motor characteristics. The condition on the DC bus voltage, such as to obtain sinusoidal currents at the level of the motor phase, is given in [89].

A special attention must be paid to the supplied motor length. This supplied motor length called a sector is composed by several motor modules in series (As introduced in Section 6.4, the motor modules have a length of about 0.5 m and are the following $((N_p/N_s)_{\text{number of layers}})$: $(14/15)_2, (17/18)_1, (17/18)_2, (20/21)_2, (22/24)_1$ and $(22/24)_2$). For LS, the length of the stator sector to be energized has a direct impact on the number of converters and on the resulting efficiency. Therefore, a compromise must be found between the traffic performances and the investment costs.

First, to assure the independence of the cabins, one converter must control only one cabin at the same time. There must always be at least the distance of a stator sector between two consecutive cabins. The distance between two consecutive cabins is equal to one floor when the cabins are travelling and equal to 0.4 m when they are stopped, as presented on Fig. 7.9.

Second, as several modules must be supplied in series in order to move the cabin, a high induced voltage will appear. Furthermore, more modules are supplied more losses are produced. This has as consequence to reduce the motor efficiency. On the other hand, if each module has its own converter, the investment costs will increase dramatically, as presented in [90].

To find the better compromise between investment costs and motor performances, a simulation of the whole system was made by ETHZ by the use of a dedicated software (MULTIMOBIL-Bus-Sim). Several conclusions as result of the simulation can be made:

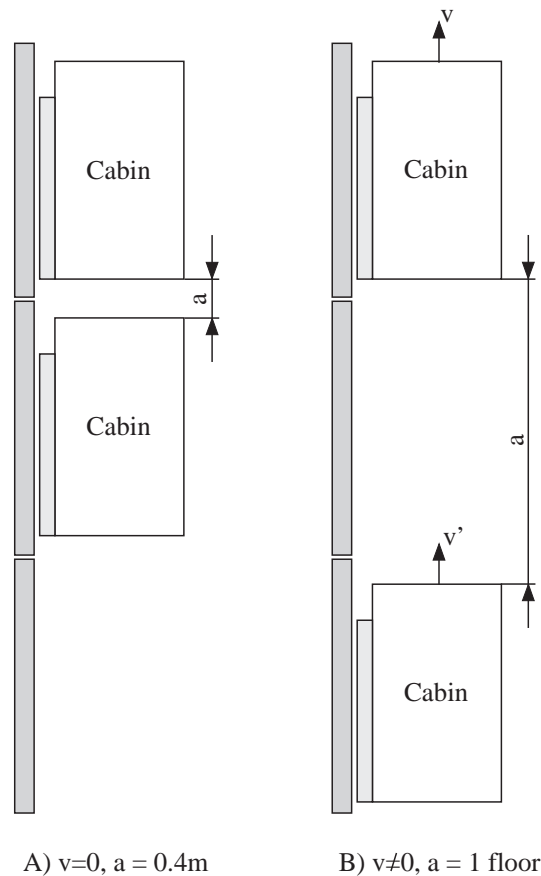


Figure 7.9: Minimal distance between two consecutive cabins, A) at standstill, B) during the cabin movement.

- there is a smarter structure to find. At bottom of the building where there is more traffic density, there could be shorter stator sectors to reduce distance and in the rest of the building longer ones. This configuration would optimize the number of inverters for a given traffic density. The total number of inverters would change only for a few units for the bottom and top;
- having longer stator lengths decreases the number of needed inverters (i.e. investment costs). However, there is an energetic aspect in the use of the stator sectors. To supply a long stator sector gives more losses than to supply a short one (exploitation costs). The optimal configuration should consider both: the investment costs and the exploitation costs.

Therefore, in order to go further in the motor design and to build a reference example it was chosen to have *one converter for each of the three first floors and one converter per two floors for the rest.*

7.9 Preselected Motor Design

For the toothless LS motors, two winding solutions are promising: 240 edeg and 300 edeg. Since these windings are very similar, only one winding with the maximum coil opening of 240 edeg will be analyzed.

For the toothed LS motors, the same strategy is applied as for the toothless motor. Two windings will be first studied and if this motor is more adapted than the toothless motor, other windings will be

analyzed. It was decided to analyze only a two layer winding since they produce less iron losses and they have a lower coil mmf than a one layer winding. Therefore, for the windings proposed at Section 6.4 the windings $(17/18)_2$ and $(22/24)_2$ are selected.

7.9.1 Assumptions and Constraints Relative to the Application

The constraints to design the motors are given in Table 7.5.

Table 7.5: Motor constraints due to the Application.

		Toothed motor	Ironless motor
a	Motor acceleration	1.2 m/s ²	1.2 m/s ²
a_{empty}	Maximum acceleration, empty cabin	5.8 m/s ²	5.8 m/s ²
B_r	Remanent flux density of PM	1.23 T	1.23 T
B_t, B_{ys}	Flux density in iron parts	1.4-1.8 T	1.4-1.8 T
D_c	Motor duty cycle	0.5	0.5
f	Motor supply frequency	<100 Hz	<100 Hz
k_{cu}	Copper filling factor	0.55-0.6	0.6
h_{coil}	Coil height	-	2-10 mm
h_s/l_s	slot height constraint	<4.5	-
h_{pm}	PM height	2-10 mm	2-10 mm
l_{int}	Inner coil length	l_t (tooth length)	≥ 4 mm
v	Motor speed	3.5 m/s	3.5 m/s
w_{pm}	PM width (Active width)	<150 mm	<150 mm
δ	Air gap height	3 mm	3 mm
τ_p	Pole pitch	17.5-50 mm	17.5-50 mm
T_{coil}	Coil temperature	<120°C	<120°C
T_∞	Room temperature	20°C	20°C

As introduced in Table 7.5, a higher acceleration for an empty cabin could be required in order to increase the traffic capacity.

Since the propulsion force is dependent on the motor embarked part, an iterative process during the motor design is needed. This iterative process for both ShS and LS solutions, is presented on Fig. 7.10. The design process ends once the condition ε_e is obtained. This condition is defined as:

$$\varepsilon_e < \frac{F_i - F_{i-1}}{F_i} \quad (7.1)$$

F_i is the propulsion force for the last design last and F_{i-1} is the propulsion force for the next to last design.

This iterative process is difficult to solve in a determinist approach. On contrary, by using the optimization software Pro@design, it can be solved with an implicit function.

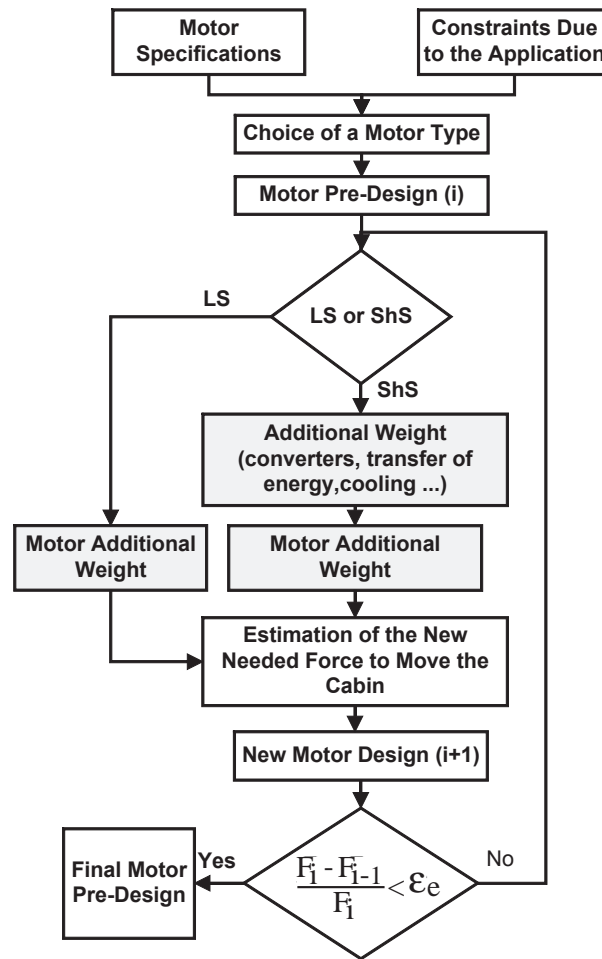


Figure 7.10: Iterative process on the propulsion force due to the embarked motor part [83].

7.9.2 First Optimization - First Selection

The first optimization is made in order to choose the motor types. The objective function is the material cost and the constraints given in Table 7.5 are applied. The results of these optimizations are presented in Table 7.6. All motors are double sided. For the toothed motors, four motors $(17/18)_2$ and four motors $(22/24)_2$ are assembled in series. For the toothless motor, it was decided to mount eighteen motor modules of three coils shifted by 240 edeg in series. Moreover, in order not to have a magnet width larger than $w_{pm} = 150$ mm the motor is formed by 4 double sided motors. These motors in series form a motor of a length of 2.2 m.

The first conclusion is that toothless motor has a lower efficiency than toothed as given in Table 7.3. Moreover, the solution with a toothless motor requires more embarked weight. Therefore, the solution to move the cabin with a toothless motor is less promising than with a toothed motor. To confirm that toothless motor is not adapted, several additional optimizations with the material costs as objective function are made depending on the motor efficiency. The results are shown on Fig. 7.11.

These four curves show clearly than toothless motor is not appropriate for an MMS. The main reasons are:

- a high embarked weight corresponding to at least about 50% of the cabin weight;

Table 7.6: Optimization results with the investment costs as an objective function.

		Toothed motor 4·(22/24) ₂	Toothed motor 4·(17/18) ₂	Toothless motor 18·(240 edeg)
Total motor power (v=3.5 m/s)	[kW]	43.6	43.8	48.8
Total motor embarked weight	[kg]	52.3	56.1	187.2
Total losses (v=3.5 m/s)	[kW]	3.5	3.1	8.6
Motor efficiency (coil @ 20°C)	[%]	0.94	0.95	0.89
Motor efficiency (coil @ 120°C)	[%]	0.92	0.93	0.85
Motor constant k_m	[N/√W]	226	237.5	150.1
Current density	[A/mm ²]	3.45	2.9	6.5
Magnet height	[mm]	3.7	4.2	6.8
Magnet width	[mm]	150	127	125
Pole pitch	[mm]	25	32.3	30.5
Motor length	[m]	2·2.2	2·2.2	8·2.2
Material costs for the reference building	[CHF]	2.6·10 ⁶	2.3·10 ⁶	4.2·10 ⁶

- a low efficiency;
- several motors in parallel;
- an expensive solution.

In the following section, the choice between the different motor windings proposed for the toothed motor, i.e. (14/15)₂, (17/18)₁, (17/18)₂, (20/21)₂, (22/24)₁, (22/24)₂ is discussed.

7.9.3 Second Optimization - Winding Selection

In order to make the first choice concerning the winding, the losses produced by a supplied sector of 4.2 m length for different motor powers are minimized. For such an application, where the motor must produce a force to move the load and its own weight, it is preferred to speak about losses rather than motor efficiency. To perform these optimization, a new constraint on the material cost of the whole motorization (without the supply part, i.e. converters, captors, etc.) is introduced. It is limited to 300'000 CHF. This cost constraint comes from a cost analysis presented by ETHZ [90]. The results of the minimization of the power losses of a supplied sector of 4.2 m as a function of the motor power are presented on Fig. 7.12. The increase of the motor power means an increase of the MaW weight.

For a given motor power and a supplied part length equal to 4.2 m, the windings producing less losses are the following: (20/21)₂, (22/24)₁, (22/24)₂. The winding (14/15)₂ has for a given motor length longer PM l_{pm} than the others. Therefore, a higher yoke h_{ys} is needed. As a consequence, the magnet volume becomes smaller in order to keep the same embarked weight as other windings. The decrease of magnet volume must be compensated by a higher current density producing therefore more losses. The same reasoning can be made for the windings (17/18). Furthermore, as the speed required for this application is not so high the copper losses are more important than iron and PM losses. Therefore, the motors with a high number of PM are preferred, leading to the solutions: (20/21)₂, (22/24)₁, (22/24)₂. These windings are studied in the following Section in order to find the best winding for an MMS.

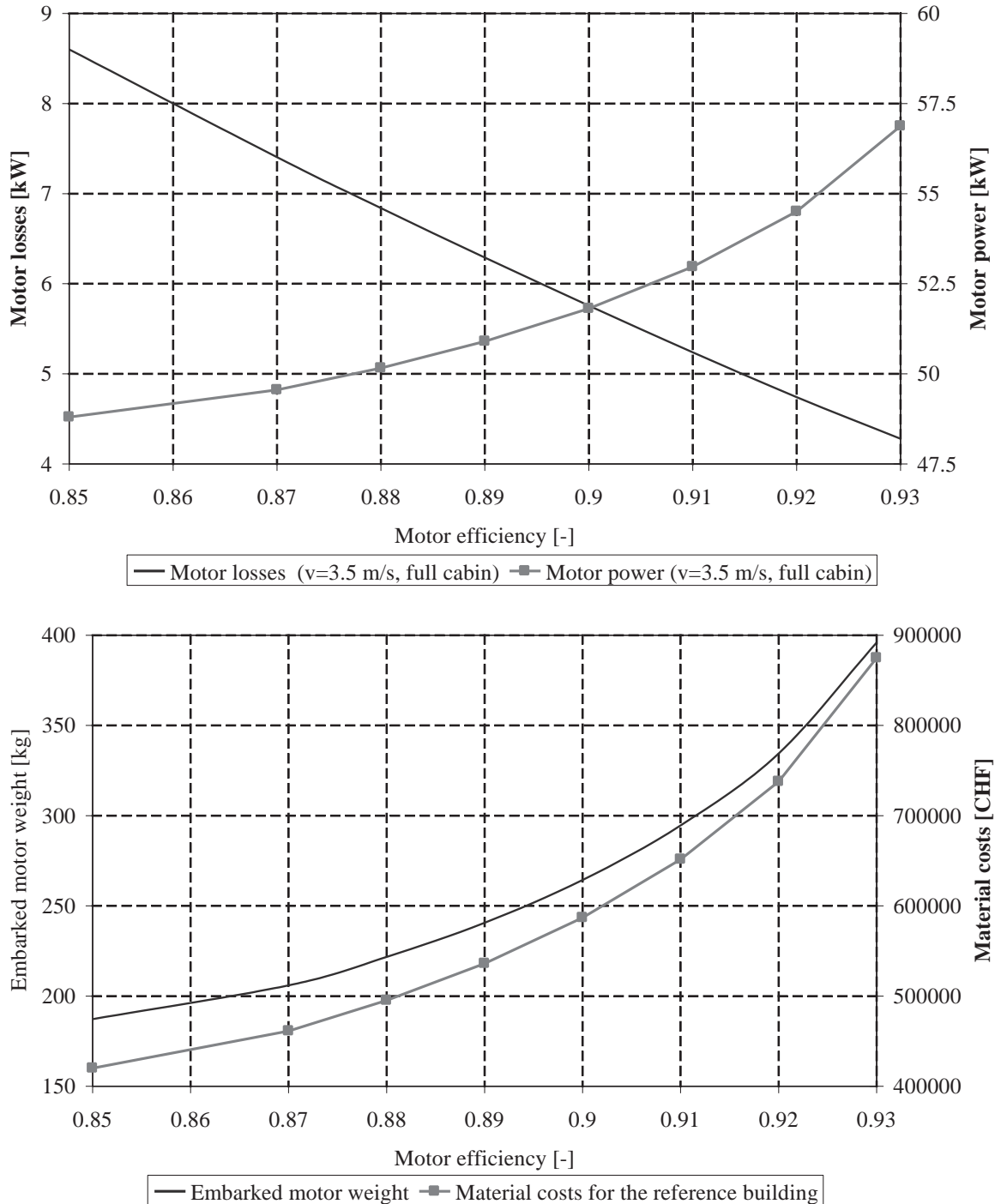


Figure 7.11: Results of the toothless motor optimizations with the material costs of the whole system (3 shafts, 16 cabins, 21 floors) as an objective function and with several imposed motor efficiencies.

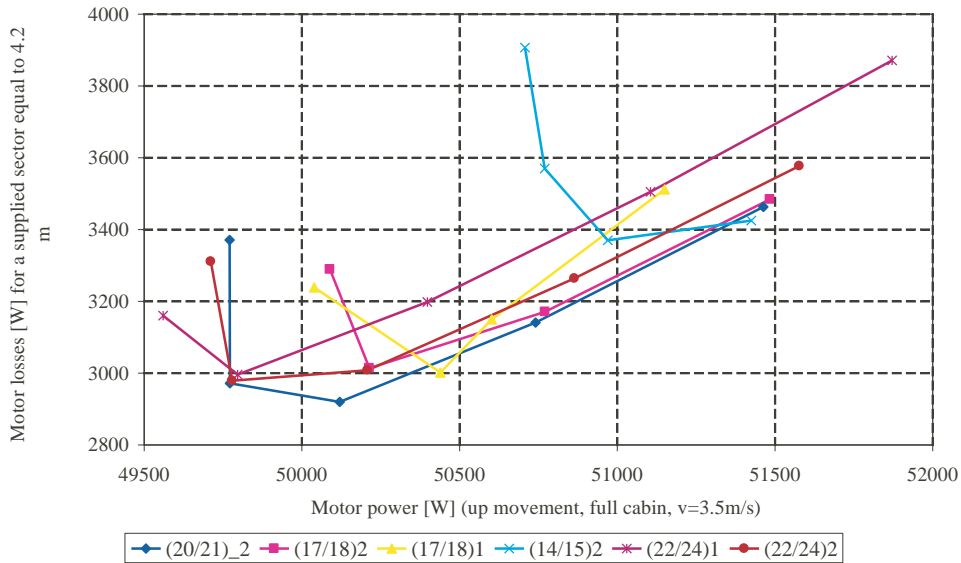


Figure 7.12: Minimized motor losses as a function of the motor power for the selected windings.

7.10 Final Motor Choice

As presented in Section 6.4.2, the total motor losses vary for a fixed motor length as a function of the number of poles. As the motor will be supplied by sectors longer than the reactive part, it is interesting to study the copper losses per meter and the total losses for a supplied part equal to one floor (4.2m). Therefore, the total losses for a supply part of 4.2 m length were minimized for different motor powers. The corresponding Pareto curves are presented on Fig. 7.13 for two different material costs constraints as a function of the motor power.

These two graphs lead to several conclusions:

1. the motors with a higher number of poles can have a lower motor power than motors with a smaller number of poles. This comes from an increase of the embarked weight due to the yoke height h_{ys} . A lower power is very important in order to reduce the installed power of electrical components such as transformers, converters, etc. ;
2. the waveform of the curve of the copper losses as a function of the motor power on the Fig. 7.13 A) has a minimum. This comes from the fact that for a low motor power, the embarked weight (i.e. the magnet volume) must be minimized leading to an increase of the copper losses. On the contrary, for high motor power, the embarked weight becomes higher leading to more total losses. Therefore, a minimum value is situated between these two points;
3. the difference between the winding (22/24) with one layer and two layers can be explained although these motors are very similar. For the same motor dimensions, except the winding characteristics, the motor (22/24)₁ can produce a higher propulsion force than the motor (22/24)₂ due to its higher winding factor 1k_w and copper filling factor k_{cu} . This aspect was studied in Section 6.4.2. Therefore, for a same motor power (i.e. a same embarked weight) the motor with the winding (22/24)₁ requires a smaller PM width w_{pm} . This reduction of the PM width is not enough to compensate the higher copper volume due to the higher end windings and the higher copper

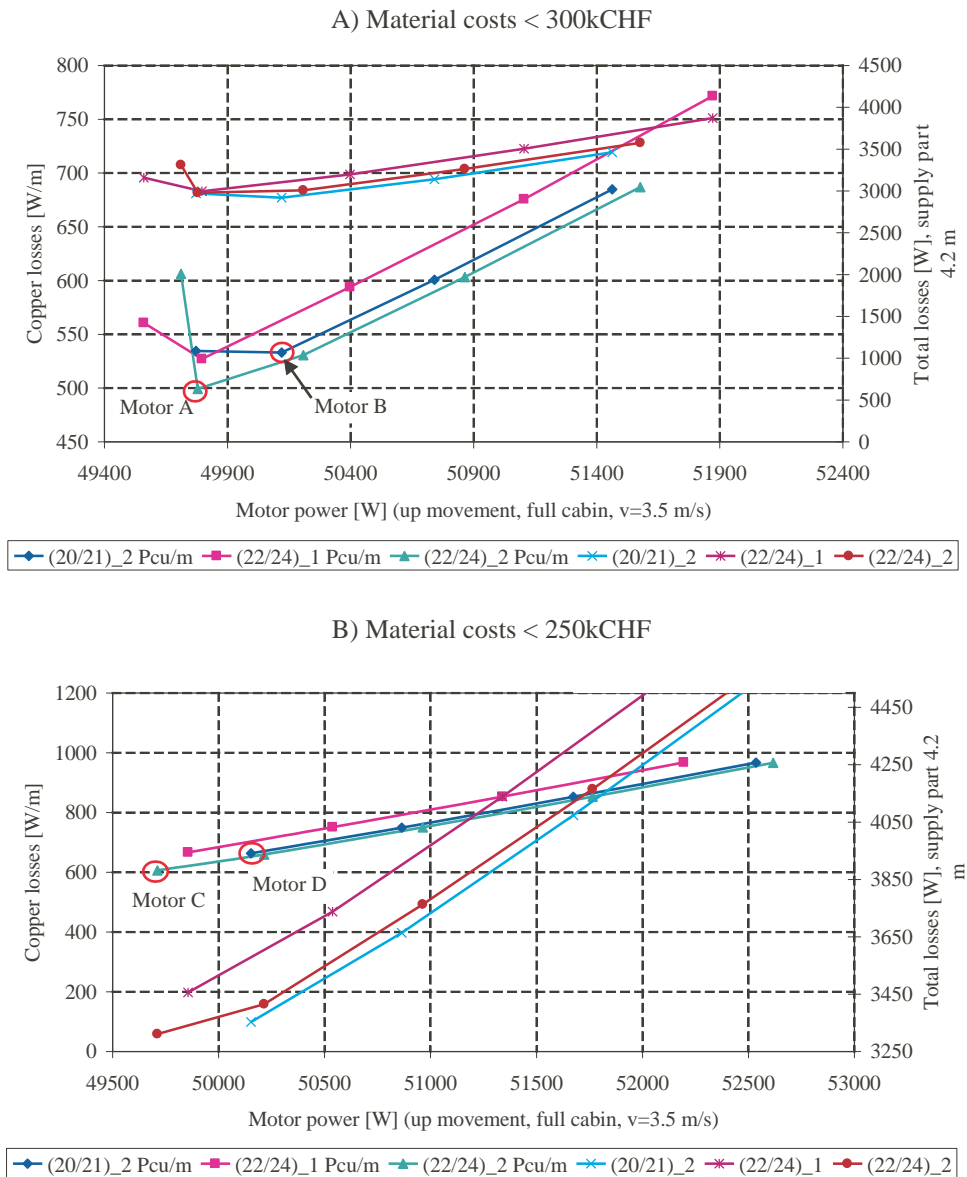


Figure 7.13: Copper losses and total losses for a supplied sector of 4.2 m long as a function of different motor power. A) material cost <300'000 CHF, B) material cost <250'000 CHF

filling factor. Therefore, in this case, the motor $(22/24)_1$ produces more copper losses per meter than the motor $(22/24)_2$;

- the material cost for the reference building has a direct impact on the motor width as it is presented in Section 7.6.1. More the material costs are constrained, more the motor width decreases. For this reason, the copper losses increase while the material costs decrease.

Although all values presented on the Fig. 7.13 are similar, a choice of the motor winding must be made. Therefore, the winding $(22/24)_1$ is eliminated since it has the highest total losses and highest copper losses per meter. The two resting solutions: $(20/21)_2$ and $(22/24)_2$ are analyzed more in details for the two proposed material costs. The motor power is chosen for both windings on the minimum of the curves presented on Fig. 7.13, i.e. a motor power of about 49700 W (motor A) and about 51000 W (motor B) for the windings $(22/24)_2$ and $(20/21)_2$, respectively and a maximum material cost of 300'000 CHF. The motor C and D corresponding to a maximum material cost of 250'000 CHF of the Fig. 7.13 are also analyzed.

For these four motor designs, the copper losses per meter and a function giving an image of the energy balance are analyzed as a function of the motor speed. The function representative of the energy balance is defined as the difference of the power needed to supply a motor sector of 4.2 m with a full cabin travelling up at the speed v and the recovery of the potential energy in the same condition (full cabin at the speed v).

For these motors the power balance is minimized for the two material cost constraints. Once these optima are obtained, the copper losses per meter as a function of the speed are calculated and presented on Fig. 7.14.

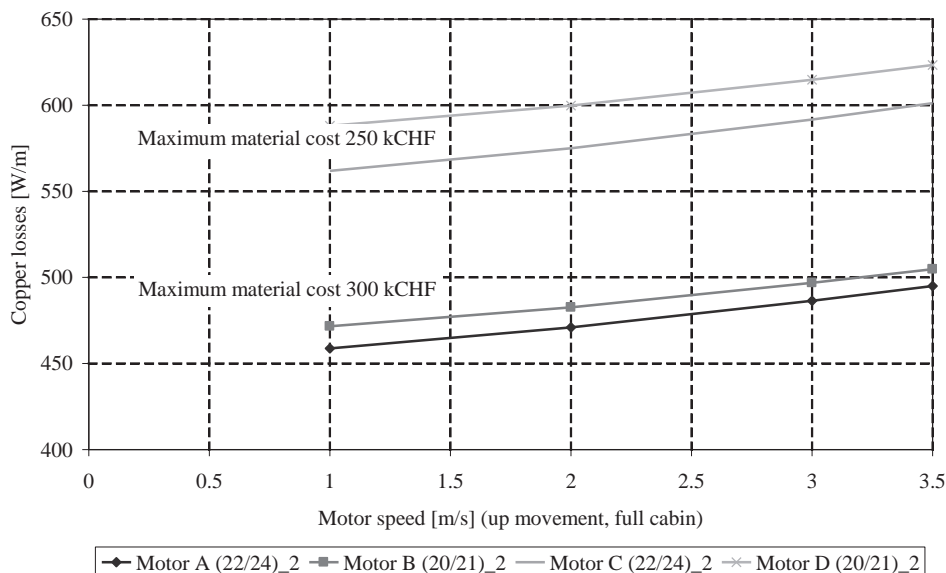


Figure 7.14: Copper losses per meter as a function of the motor speed for the four selected motors.

The slightly slope of the curve is due to the iron losses which have an impact on the coil temperature and therefore on the coil resistance. The copper losses per meter gives an idea of the losses for different supply part length. Figure 7.15 shows the power balance for each motor as a function of the motor speed. These graphs take into account the iron losses and are made for different material cost constraints.

As presented on the last graphs, the motor performances are very similar and the choice is really depends in fact on the building height and also on the commercial strategy. For the presented application

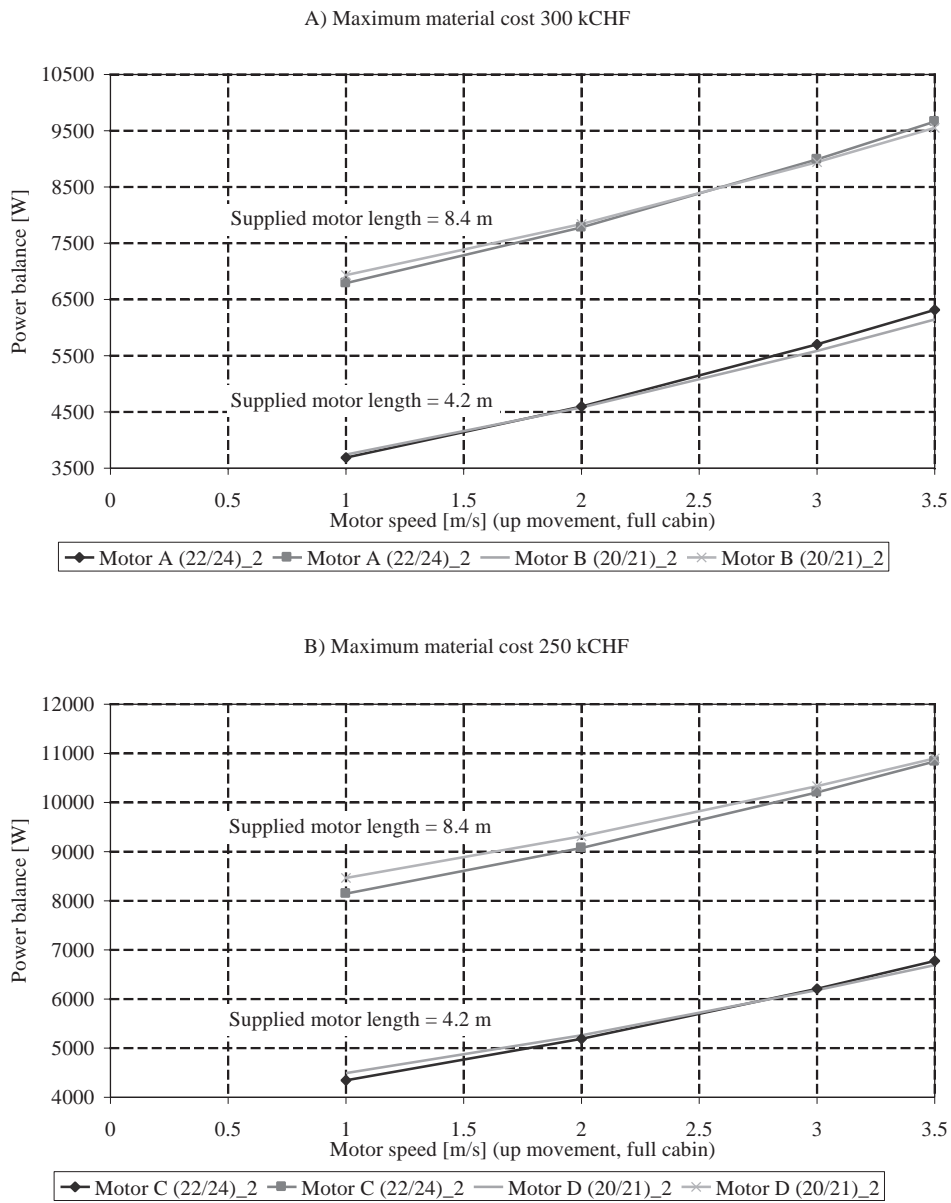


Figure 7.15: Power balance for the four selected motors as a function of the motor speed. A) Maximum material cost for the reference building of 300 kCHF, B) Maximum material cost for the reference building of 300 kCHF.

a typical cabin displacement during an up peak movement is given in Table 7.7 and are defined in [83]. It is assumed that the trapezoidal movement profile, which is the case needing a minimum energy as presented in Section 4.9.3, is adopted each time when it is possible.

Table 7.7: Typical cabin displacement [83].

Start floor	End floor	Numbers of passengers [-]	Travel time [s]	Travel distance [m]	Maximum acceleration [m/s ²]	Maximum speed [m/s]	Trapeze speed profile
-1	0	0	4.5	4.2	0.93	1.4	Yes
0	3	7	7.2	12.6	1.09	2.6	Yes
3	6	6	7.2	12.6	1.09	2.6	Yes
6	10	4	8.4	16.8	1.07	3	Yes
10	16	3	10.8	25.2	0.97	3.5	Yes
16	18	1	6	8.4	1.05	2.1	Yes
18	-1	0	26.4	79.8	0.52	4.5	No

This table shows that the maximum motor speed is only reached for long strokes. Therefore the winding $(22/24)_2$ is preferred since it has a better power ratio at low speed and since this difference increases with the reduction of the material costs. On the contrary, for a higher building for which the speed of 3.5 m/s will be more often reached, the winding $(21/22)$ could be more adapted.

This choice to use this winding type $(22/24)$ is more or less made by appreciation and it can be therefore arguable. This choice is only made by electrical considerations and more particularly on energy consumption. In an industrial process, the choice of the winding must be discussed with the manufacturing partner in order to underline the manufacturing advantages and drawbacks of each winding possibilities and also to plan its manufacturing costs. This aspect is not discussed here since it depends on many parameters imposed by the manufacturer.

7.11 Final Motor Design

For the chosen winding, the energy balance is minimized as a function of the material cost. The resulting Pareto curve is shown on Fig. 7.16. It shows the compromise which must be made between the investment and the exploitation costs. This choice related to these parameters must be made by the manufacturer.

Nevertheless, the choice to favor the power balance rather than the motor material cost was made. The solution with a material cost of 270 kCHF is finally chosen. The final motor pre-design is obtained by optimizing the power balance and by constraining the material cost up to 270 kCHF. Several other objective functions, also based on the motor losses such as the power balance for a supplied sector of 8.2m, the sum of the losses produced by several working point of the motor, etc. have been analyzed and all obtained results were similar.

This motor design method by optimization algorithms differ from a conventional determinist motor design. Indeed, in a conventional motor design, the first step is to define the winding in relation with the motor power and to fix a flux density in the air gap. Thereafter, the other geometrical quantities can be defined in order to obtain a motor fulfilling the specifications. On the contrary for the presented method only the constraints are given and no quantities are chosen in advance. This approach allows to find more efficiently the best motor which fulfills the specifications.

Figures 7.17 and 7.18 present the impact of the PM height and the current density on the reference building material costs and the motor power balance, respectively. As the magnet height is linked to the

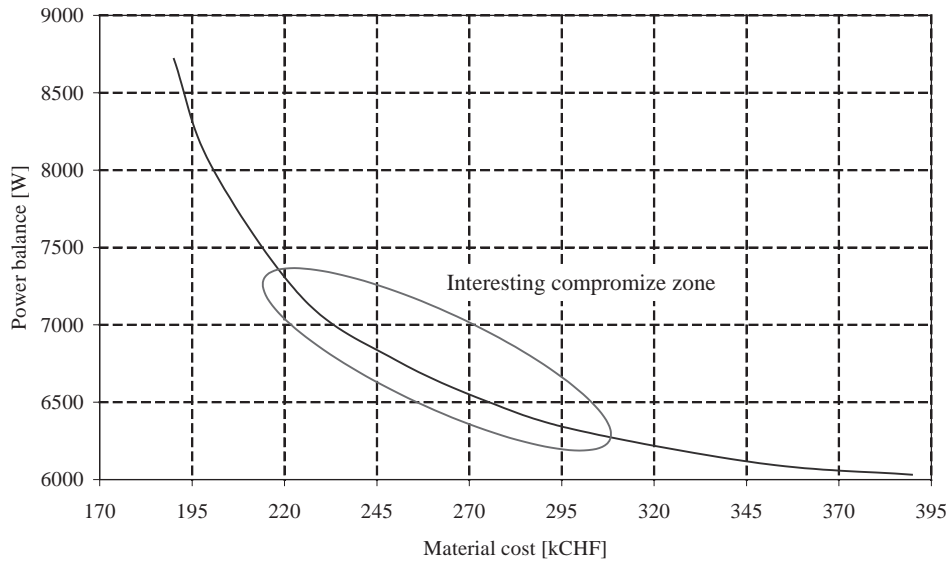


Figure 7.16: Power balance as a function of the material cost.

magnet width by the implicit function (iterative process presented on Fig. 7.10), its variation has a low influence on the reference building material costs and the power balance. On the other hand, the current density has a higher influence on these parameters. Figure 7.19 shows the PM width as a function of the PM height.

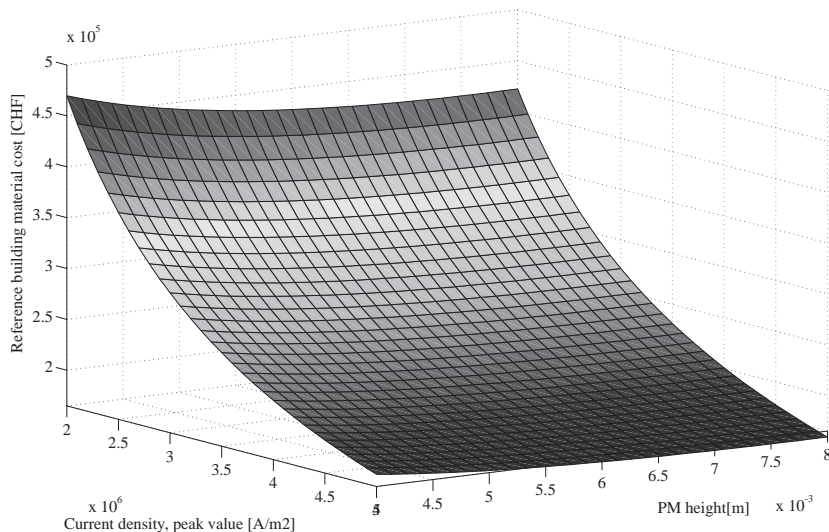


Figure 7.17: Reference building material costs as a function of the PM height and the current density.

Before finalizing the optimization, the induced voltage and more particularly the number of turns per coil and the copper wire diameter as well as the electrical connection between the motor modules must be discussed. Since the supplied part is longer than the MaW, all the motor modules along one side (the motor is double sided) must be connected in series in order to ensure that all the motor modules have the

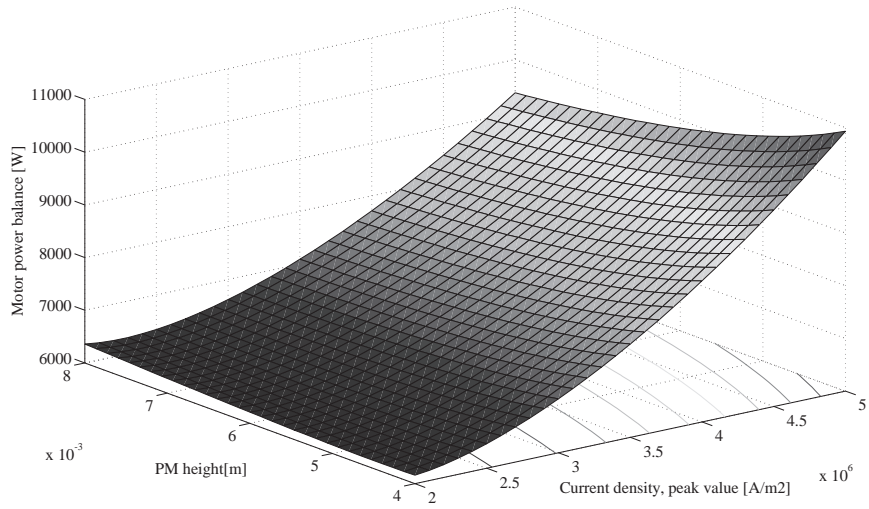


Figure 7.18: Motor power balance as a function of the PM height and the current density.

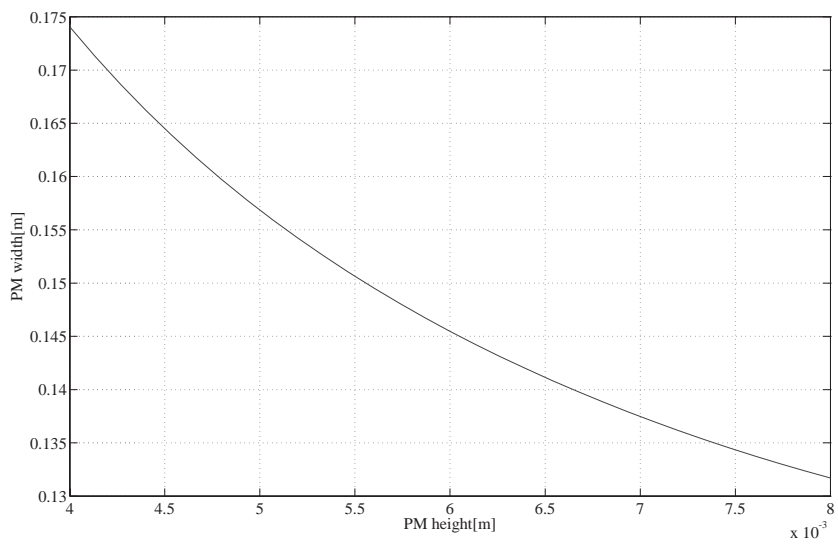


Figure 7.19: PM width as a function of the PM height due to the iterative process of the Fig. 7.10 with $\delta = 3$ mm.

same current. On the contrary, the opposite motor modules on the second side of the double sided motor, are connected in parallel in order to decrease as much as possible the induced voltage. Figure 7.20 shows the electrical connections between four motor modules. This four motor modules form a motor sector (double sided) of a length equal to two motor modules.

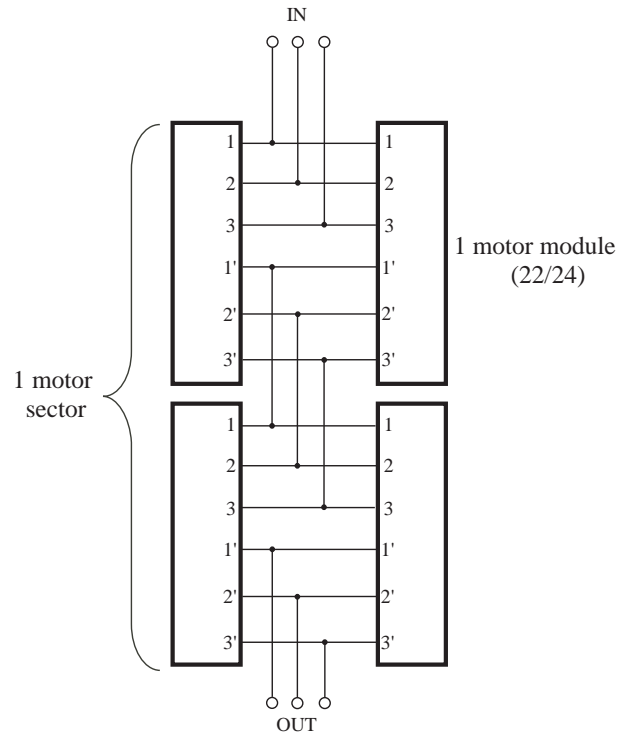


Figure 7.20: Motor sector connection between four motor modules (2 motor modules per side).

The maximum voltage constraint of the motor was imposed by the manufacturer to 3×460 V (line to line), meaning a supply voltage of about 265 V per phase. In order to command correctly the motor, the induced voltage is arbitrary limited to 210 V. For an MMS, a motor sector has always eight motor modules engaged to move the cabin. Therefore, as four motor segments are in series, the induced voltage for one motor segment ($(22/24)_2$) is limited to 52.5 V. This value gives a number of turns per coil equal to $N = 14$ with a copper wire diameter of $d_{cu} = 4.3$ mm. Therefore, for this supply part. However, for this supply part, a copper wire surface of $S_{cu} = 14.5$ mm² is required.

For this design the yoke heights are very thin and it can be increased for the supply part in order to have a more rigid motor without changing its performances. The teeth length are also tight but are nevertheless admissible. The optimization process, due to the objective function, has the tendency to make the teeth length as small as possible in order to increase the copper volume. Higher the copper volume, smaller will be the current density leading to a decrease of the copper losses.

This design is validated by FEM as it is presented in the following section.

7.11.1 Final Motor Design - FEM Comparison

The FEM simulation was performed in order to validate the motor design. The cogging force due to the end effect of the MaW and the interaction between teeth and PM was also analyzed.

The first quantity to check is the propulsion force. The result obtained with FEM ($F=1520$ N) is similar to the analytical value (1582). This indicates that in terms of propulsion force, the chosen analytical

Table 7.8: Motor module (22/24)₂ sizes and performances resulting from the optimization process.

Motor quantities		Units	Value
Propulsion force	F	[N]	1582
Attractive force	F_{att}	[N]	9800
Pole pitch	τ_p	[mm]	25
Magnet height	h_{pm}	[mm]	5.3
Magnet length	l_{pm}	[mm]	23
Magnet width	w_{pm}	[mm]	143
Air gap height	δ	[mm]	3
Yoke height	h_y	[mm]	8.3
Tooth pitch	τ_n	[mm]	22.9
Tooth length	l_t	[mm]	8.3
Slot height	h_s	[mm]	50
Maximum current density	J	[A/mm ²]	2.3
Winding filling factor	k_{cu}	[-]	0.55
Winding factor	k_w	[-]	0.949
Number of turns per coil	N	[-]	14
Copper wire surface	S_{cu}	[mm ²]	14.5
Phase resistance (at 20°C)	R	[mΩ]	50
Phase inductance	L	[mH]	0.28
Cyclic inductance	L_c	[mH]	0.42
Flux density in the tooth	B_t	[T]	1.7
Flux density in the yokes	B_y	[T]	1.7
emf phase constant (peak value)	K_u	[$\hat{V}/(m/s)$]	21.2
Copper losses (v=3.5, full cabin)	P_{cu}	[W/m]	670
Iron losses (v=3.5, full cabin)	P_{ir}	[W/m]	320
PM losses (v=3.5, full cabin)	P_{PM}	[W]	10

model gives good results.

Thereafter, the induced voltage is analyzed. It is slightly lower than the analytical value. Its waveform is presented on Fig. 7.21.

The cogging force due to the interaction between the teeth and the PM is very difficult to obtain with an analytical method. Figure 7.22 gives the cogging force, obtained with a FEM, for both the interaction between PM and teeth and the reluctance force due to the MaW end effect. The cogging force has a period equal to one pole pitch (25mm). It means that the cogging force due to the MaW end is more important than the cogging force due to the interaction between the teeth and the PM. Nevertheless, the peak value of the cogging force is assumed to be negligible in comparison with the propulsion force.

Another comparison is made on the flux density in the iron parts, as presented on Fig. 7.23. It shows that the flux density at no load is close to the value of 1.7 T as given in Table 7.8.

Since the comparisons with FEM are satisfying, the motor pre design can be validated. Of course, all the proposed geometrical quantities must be discussed with the future manufacturer in order to check the feasibility of the proposed design. This aspect was not considered during the project.

7.11.2 Mechanical Integration

This aspect was studied by ETHZ [91] and Schindler. Here, only the key points to get a better overview of the MMS are given.

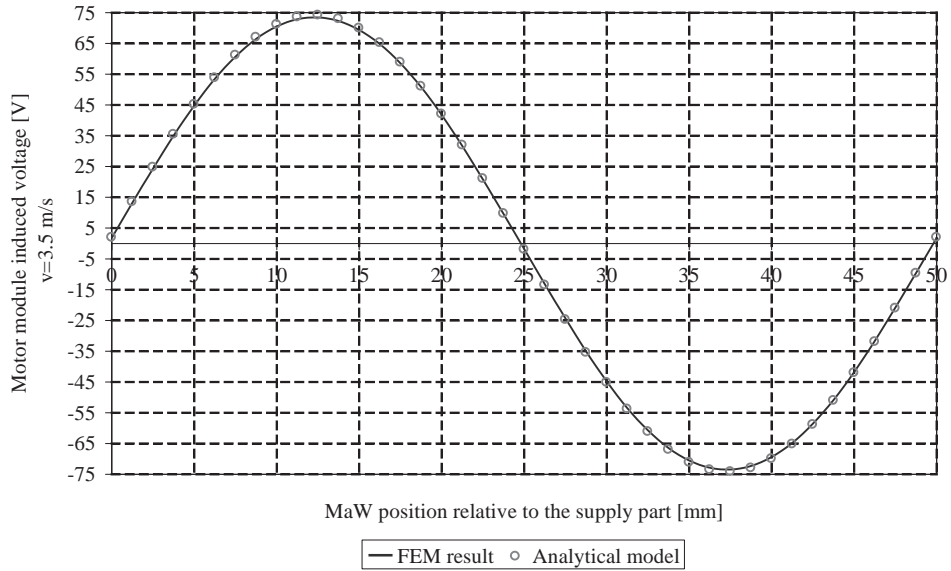


Figure 7.21: Comparison of the induced voltage on a motor module at the speed $v=3.5$ m/s.

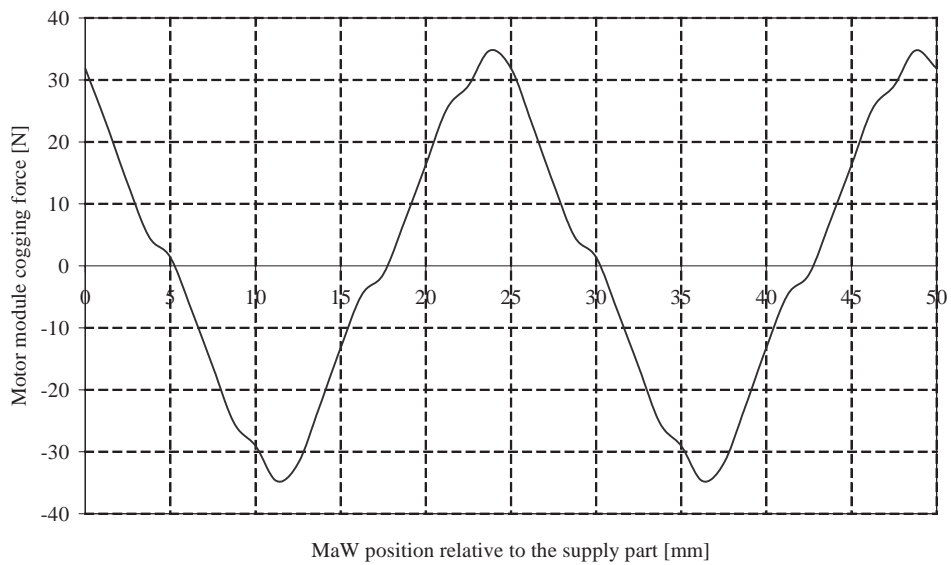


Figure 7.22: Cogging force for a motor module.

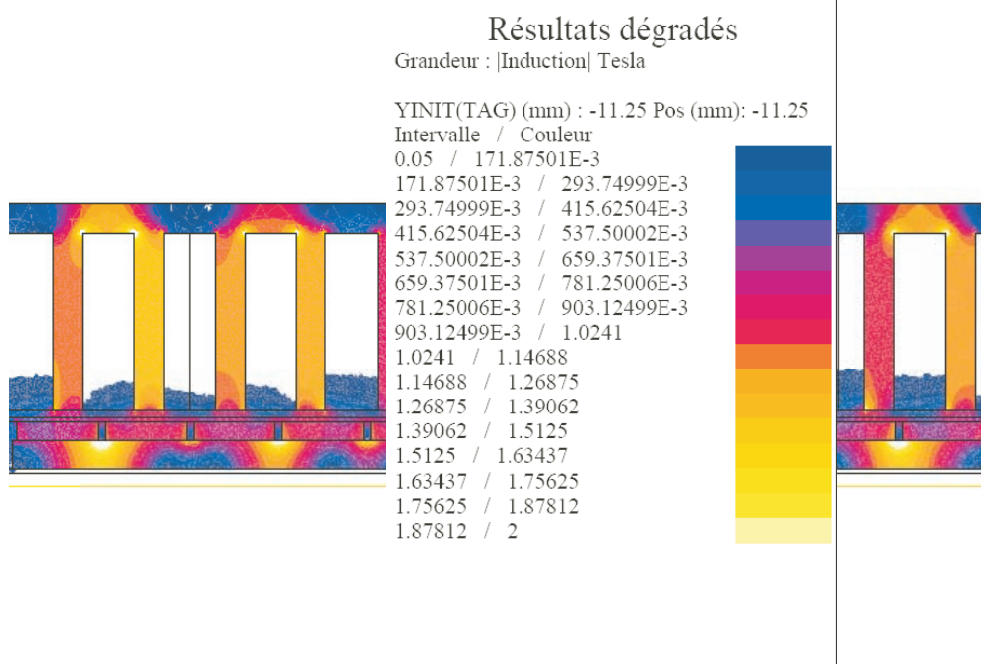


Figure 7.23: Flux density at no load.

To switch the cabin between two adjacent shafts, several movements were analyzed in order to have a minimal time transition. The first approach is to stop the cabin during the horizontal movement. It was put aside to favor a horizontal displacement while the cabin is moving vertically. To consider both continuous movements vertical and horizontal, a carriage, called the "sleigh", is designed. This sleigh, having a length of about 4 m, is longer than the cabin. During this movement, the missing sleigh in the shaft is replaced, as soon as possible, with another sleigh. This implies to have more sleighs than shafts in the floors where these horizontal displacements are possible. The cabin travels using tires along the shaft. To avoid a hyper static system all cabin corners will not have their own tires. Having the tires in a diagonal could be more appropriate. The double sided linear motor is guided by wheels. For the sleigh, wheels are proposed. The guidance has to offer a high stiffness and a silent movement. After the horizontal displacement, a high precision sensor to stop the sleigh in the right position is needed. This sleigh concept is presented on Fig. 7.24.

7.12 Conclusions

The proposed motor design methodology was successfully applied to the presented innovative application: a multi mobile system.

The choice of the motor topology (long double sided stator) was made by several criteria as presented in Section 7.6. A comparison is presented in order to show the difference, in terms of energy and material costs, between ShS and LS. For this comparison, the design given in Table 7.8 is adapted to a ShS. It is assumed that the additional embarked weight due to the converter and the energy transfer system is equal to 300 kg. The consequence is an increase of the magnet width to $w_{pm} = 208$ mm. The comparison is presented in Table 7.9.

If the motor has less losses in the ShS case, the global losses are higher than a LS motor since the losses due to the system of energy transmission must be taken into account. In terms of material costs,

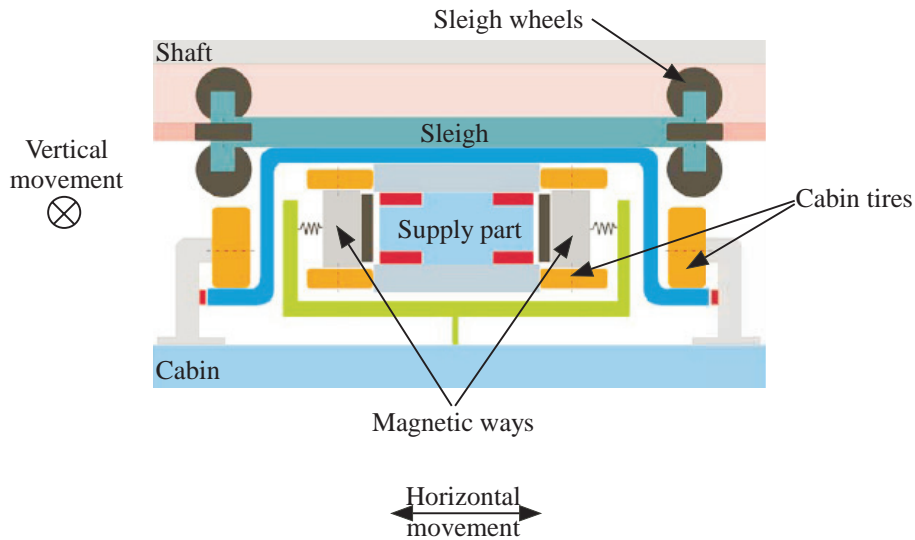


Figure 7.24: Sleigh bottom cut: horizontal movement [91].

Table 7.9: ShS and LS comparison, full cabin $v=3.5$ m/s.

	ShS	LS
Propulsion force [kN]	18	12.7
Motor power [kW]	63.5	45
Motor losses [kW]	3.1	3.5
Energy transmission losses ($\eta = 0.99$)	630	-
Material cost for the reference building [kCHF]	700	270

the ShS topology is more expensive. Although this topology needs less converters, this solution is not competitive compared to LS motor for the reference building. Therefore, for the studied case, the LS seems better adapted.

The choice of the winding is very difficult to make since the performances of each winding are very similar. Therefore, for other constraints than those introduced in Table 7.5, the winding choice can differ.

Finally, the design of the propulsion system for an MMS shows that an optimization process can be successfully applied to such a multi disciplinary project. Indeed, the predesign motor is validated by comparison with FEM. The difference between the analytical method and FEM shows that the chosen model is adapted to perform an analytical optimization.

The increase of the investment costs due to the use of a linear motor compared with a conventional lift with rotative motor is compensated by the increase of the rented surface in the building. A cost synthesis concludes that from a building height of 5 floors or more, an MMS is competitive in terms of return of investment. Therefore, such a lift system is a real possibility for future lift systems in high rise buildings.

An important drawback is the increase of the complexity compared with a conventional lift system. Therefore, the problem of security and reliability must be studied more in details in order to have a better overview of a MMS.

The proposed method to predesign a motor is very interesting since it is not also time consuming than the optimization with FEM. Nevertheless, such an approach has the drawback to not take into account the cogging force due to the end effect of the motor. This aspect can be added in a future step.

Chapter 8

Conclusions

This thesis deals with linear motor modelling and analytical optimization. Motor design is not a new research field. However, more work has been dedicated to rotative than to linear motors. This opens the possibility to investigate different aspects specific to linear motors.

Nevertheless, the main innovative contribution of this thesis results from the possibility to use new optimization softwares applied to linear motor designs. These optimization programs are based on different algorithms which use either numerical or analytical models. The specific optimization program used for this thesis is PRO@DESIGN and it is based on an Sequential quadratic programming (SQP) algorithm. This software requires analytical models. These analytical equations must be as far as possible analytically derivable. In this way motors or MaW comparison becomes straightforward.

The design software using optimization technics differ to the determinist methods (direct methods) in which some parameters have to be fixed (e.g. the flux density in the air gap and in the iron parts) in order to determine the other motor sizes. The obtained motor is then adapted in order to find a motor fulfilling the specification. The design method proposed in this thesis differs to this common approach since it is not any more necessary to fix parameters to perform a motor design but constraints or domains of parameter validity. The proposed methodology does not only take into account the motor design but introduces also a way to perform a relevant motor comparison. The main steps to perform a motor design for a given application using an optimization program and a comparison process are summarized below:

- study of the specifications, constraints and objectives;
- selection of the motorization possibilities;
- predesign of the selected motors;
- introduction of the figures of merit chosen for the application;
- motor variant comparison and choice;
- optimization of the selected motor(s);
- eventual final selection and design verification.

Although this approach is applied to linear motor using an SQP algorithm, the proposed motor design is introduced like a general approach and can therefore be extended to rotative motors or to another optimizer algorithms.

To perform the optimization, several analytical models have been developed. The linear motor models are mainly based on rotative motor models, which have been suitably modified. The particularity of linear motors to have an even or an odd number of poles is used in order to introduce a global method

for the choice of the windings. This method introduces also the mmf harmonics generated by a concentrated windings. In most cases, these harmonics do not have a high influence on the propulsion force mean value but they can generate additional losses in the iron parts and in the PM. Several magnetic way models based on the substitution of the PM by point currents are given. The drawbacks and advantages of each magnetic way are deduced using these models.

The advantage of motor models developed in the thesis is that they can be used to study several motors by assembling the windings, the MaW and the motor type models. These block models are completed with a thermal model which is compulsory to perform a motor design, with a mechanical model and with a power supply model. The thermal models are steady state models and the thermal capacities can be introduced if requested by the application. Nevertheless in most cases the presented static models are adequate. This is the case for the application studied in the thesis: an MMS.

The analytical motor models are also used to compare several motors and MaW. The use of analytical models is interesting to perform comparisons since they have the advantage to be not time consuming and they are precise enough. The comparisons presented in this thesis are useful to predict the motor performances and to choose the motor type and topology in relation to the application. These comparisons must be performed for the same constraints and objectives.

The presented methodology to design and to compare linear motors is successfully applied to an innovative application which deals with a lift system in high rise buildings. The particularity of this new lift is to allow the movement of several cabins in the same shaft. This concept reduces the total lift area since the lift performances are increased, permitting the increase of the usefull surface. The proposed design methodology has shown than the toothed synchronous motor is the most adapted one. Moreover, the choice to have a double sided long stator motor was confirmed since it has less losses and is less expensive in terms of material costs. The choice of winding type is more difficult to do. Indeed, most preselected motors are very similar and the choice is done regarding the proposed reference building and a typical cabin displacement. The optimized design obtained with the analytical model has been checked by FEM. The results obtained by optimization are close to those obtained by FEM and therefore the predesign is adopted. In order to valid it, the final design must still be discussed with the industrial partner,

The originality and the pertinent features of this thesis can be summarized as follows:

- the proposed motor design methodology takes into account the comparison of different motor types. This introduces the figure of merits and the definition and different possibilities to formulate an objective function. The comparisons based on the MMF of different MaW is also an interesting point;
- the global analysis of the motor windings and more particularly the distribution factor of the turns k_{zc} ;
- the motor design by an optimization based on an indirect method and its result analysis;
- the thermal model of the air gap by a rectangular cavity, ;
- the innovative application;
- the developed analytical models contribute also to the thesis originality.

Some different topics discussed in this thesis could be completed by a more extended study. Future works can be done to complete some topics and improve results. They are listed below:

- the impact of the winding harmonics on the motor losses could be investigated;

- the software Pro@design has introduced the possibility to work with integer number. This allows to introduce the winding in the optimization process;
- the transient thermal behavior of the motor can also be introduced in the model;
- the motor comparison proposed with concentrated winding could be completed with distributed windings.

This list is not exhaustive and depends on the interest and the objectives imposed by a new application.

Appendix A

Fourier Transformation

All periodic functions $f(x)$ of period $T = 2\pi$ may be expanded in a Fourier series consisting of an infinite sum of the circular sine and cosine functions according to:

$$f(x) = \frac{a_0}{2} + \sum_{k=1}^{\infty} [a_k \cos(kx) + b_k \sin(kx)], \quad (\text{A.1})$$

in which the constant coefficients, or amplitudes, a_k and b_k are determined as follows:

$$a_k = \frac{1}{\pi} \int_{-\pi}^{\pi} f(x) \cdot \cos(kx) dx, \quad (\text{A.2})$$

$$b_k = \frac{1}{\pi} \int_{-\pi}^{\pi} f(x) \cdot \sin(kx) dx, \quad (\text{A.3})$$

with $k=0,1,2,\dots$.

If $f(x)$ is an even function ($f(-x) = f(x)$), then $b_k = 0$ and similarly if $f(x)$ is an odd function ($f(-x) = -f(x)$), then $a_k = 0$.

Three Fourier transformations of odd functions used during the thesis are presented in Fig. A.1.

The Fourier transformation for these functions are (A.4) for the square form, (A.5) for the trapeze form and (A.6) for the pulsed form.

$$y = \frac{4a}{\pi} \left[\sin(x) + \frac{\sin(3x)}{3} + \frac{\sin(5x)}{5} + \dots \right] \quad (\text{A.4})$$

$$y = \frac{4a}{\alpha \cdot \pi} \left[\sin(\alpha) \sin(x) + \frac{\sin(3\alpha) \sin(3x)}{3^2} + \frac{\sin(5\alpha) \sin(5x)}{5^2} + \dots \right] \quad (\text{A.5})$$

$$y = \frac{4a}{\pi} \left[\cos(\alpha) \sin(x) + \frac{\cos(3\alpha) \sin(3x)}{3} + \frac{\cos(5\alpha) \sin(5x)}{5} + \dots \right] \quad (\text{A.6})$$

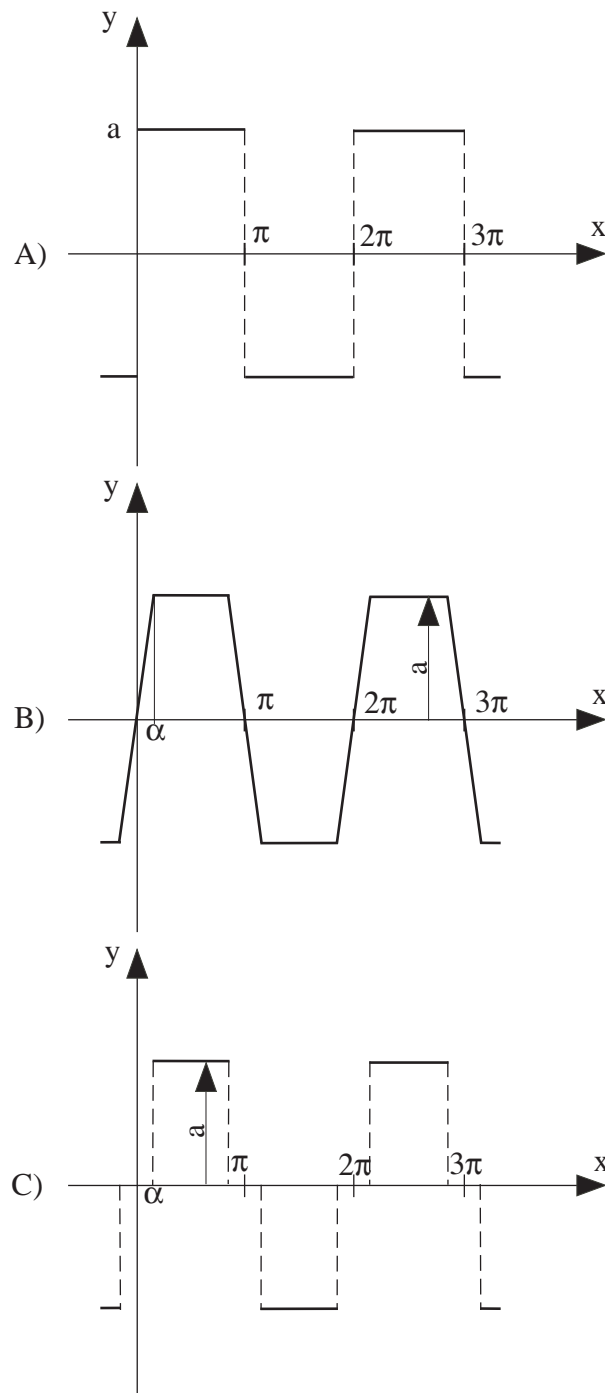


Figure A.1: Three wave form Fourier analysis; A) square form, B) trapeze form and C) pulsed form.

Appendix B

BH Curve Model

This appendix is based on [72] and therefore only the key points are given.

Motors are designed for working in the central part of the B-H curve presented in Fig.B.1, i.e. between $B_1 < B_f < B_3$, B_f being the flux density in the iron. Indeed, if the flux density in the motor is situated under the point B_1 , the iron is misused since the iron volume becomes very important. Contrary, if the flux density in the iron is located upper the point B_3 , the iron loses its characteristic of guiding the flux.

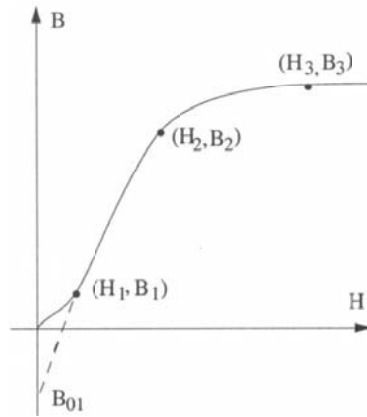


Figure B.1: B-H curve.

The basic curve and its reverse function are given by (B.1) and (B.2):

$$B_f = \frac{H_f - H_{0f}}{\eta_f + \xi_f \cdot (H_f - H_{0f})} \quad (\text{B.1})$$

$$H_f = \frac{\eta_f \cdot B_f}{1 - \xi_f \cdot B_f} + H_{0f} \quad (\text{B.2})$$

The three points, which defined the curve are:

- (H_1, B_1) smallest B amplitude
- (H_2, B_2) middle of the curve knee
- (H_3, B_3) highest B amplitude

For the central part $B_1 < B_f < B_3$, the definition of the three points permits to find constants used in equations (B.1) and (B.2):

$$\xi_f = \frac{(H_1 \cdot B_2 - H_2 \cdot B_1) \cdot (B_1 - B_3) - (H_1 \cdot B_3 - H_3 \cdot B_1) \cdot (B_1 - B_2)}{B_1 \cdot B_2 \cdot (B_1 - B_3) \cdot (H_1 - H_2) - B_1 \cdot B_3 \cdot (B_1 - B_2) \cdot (H_1 - H_3)} \quad (\text{B.3})$$

$$H_{0f} = \frac{\xi_f \cdot B_1 \cdot B_2 \cdot (H_1 - H_2) - H_1 \cdot B_2 + H_2 \cdot B_1}{B_1 - B_2} \quad (\text{B.4})$$

$$\eta_f = \frac{H_1 - H_{0f} - \xi_f \cdot B_1 \cdot (H_1 - H_{0f})}{B_1} \quad (\text{B.5})$$

For the other parts of the saturation curve, more details are given by [72]. These parts are not related here since the flux density is always constraint in order to be situated in the central part of the saturation curve.

Appendix C

Winding Factors

C.1 Concentrated Windings

Appendix D

Modulation Functions

Two modulation functions are presented in this appendix. These functions are used to model the flux density which interacts with the plane by multiplying these function by the flux density produced by the MW. These modulation functions are presented in Fig. D.1.

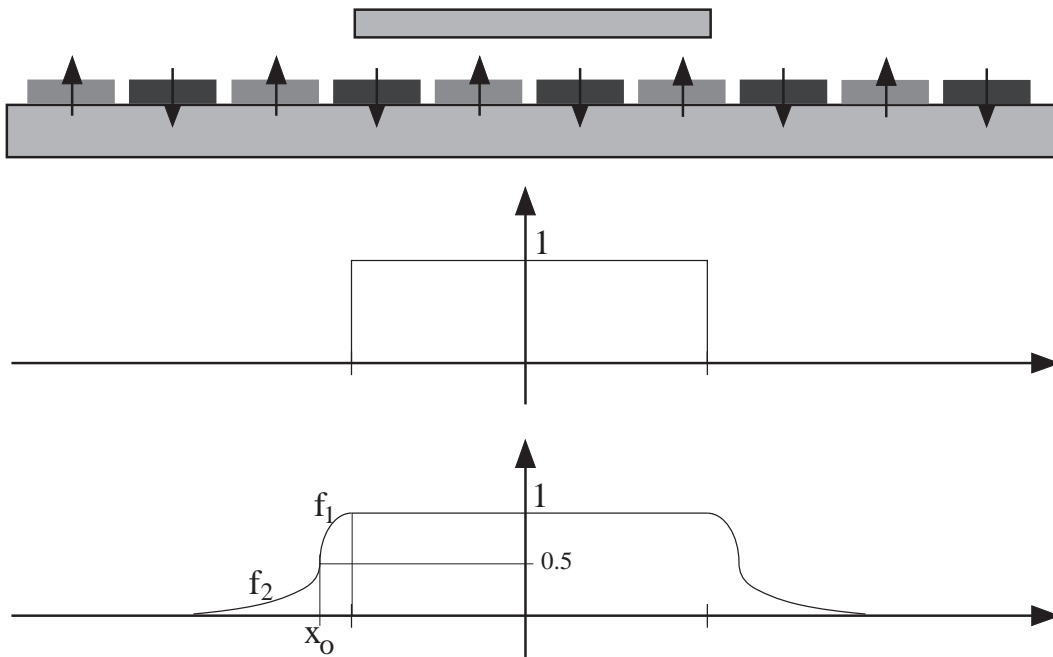


Figure D.1: Two modulation functions giving the relative permeability of a plane of a length l_{plane} ; Square function and cos-exp function

For the square function, the function is equal to:

$$w(x) = \begin{cases} 1 & \text{for } x \leq |l_{plane}/2| \\ 0 & \text{for } x > |l_{plane}/2| \end{cases} \quad (\text{D.1})$$

The second function [58] is defined by two functions, the first part is modelled by a cosine function $f_1(x)$ and the second by an exponential function $f_2(x)$ as follows:

$$f_1(x) = \frac{1}{2} \left(1 + \cos \left(\frac{\pi^2}{4\delta} x \right) \right), \quad (\text{D.2})$$

$$f_2(x) = \frac{1}{2} \exp\left(-\frac{\pi^2}{4\delta}(x - x_o)\right), \quad (\text{D.3})$$

with:

$$x_o = \frac{2\delta}{\pi}. \quad (\text{D.4})$$

Therefore, the second modulation equation is equal to:

$$w(x) = \begin{cases} 0 & \text{for } |x| < l_{plane}/2 \\ f_1(x) & \text{for } l_{plane}/2 \leq |x| \leq l_{plane}/2 + x_o \\ f_2(x) & \text{for } |x| > l_{plane}/2 + x_o \end{cases} \quad (\text{D.5})$$

Appendix E

TFM Geometry Parameters

The geometry and the geometrical constraints of the TFM are introduced in this Appendix. The motor consists on four parts: the magnet stack, the supply part yoke, the coil and the way.

E.1 Magnet Stack

The magnet stack is composed of seven magnets and eight iron parts permitting to concentrate the magnetic flux in the air gap. These iron parts are laminated in order to reduce the Eddy currents. The geometrical parameters are given on Fig. E.1.

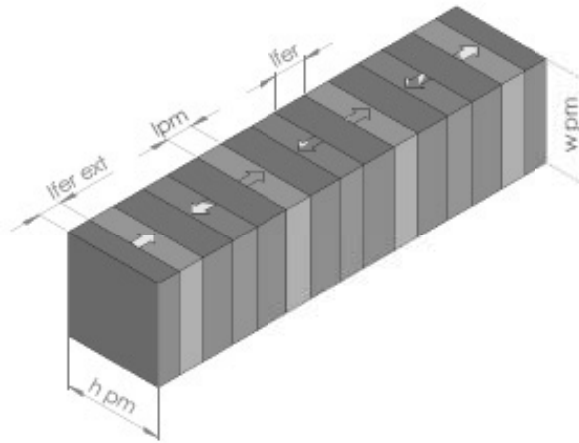


Figure E.1: Geometrical parameters of the magnet stack.

The pole pitch is defined as:

$$\tau_p = l_{pm} + l_{fer} \quad (\text{E.1})$$

The iron part at the end of the magnet stack does not necessary have the same length than the middle iron parts.

E.2 Supply Part Yoke

The yoke supports the coil. The geometrical quantities are given on Fig. E.2.

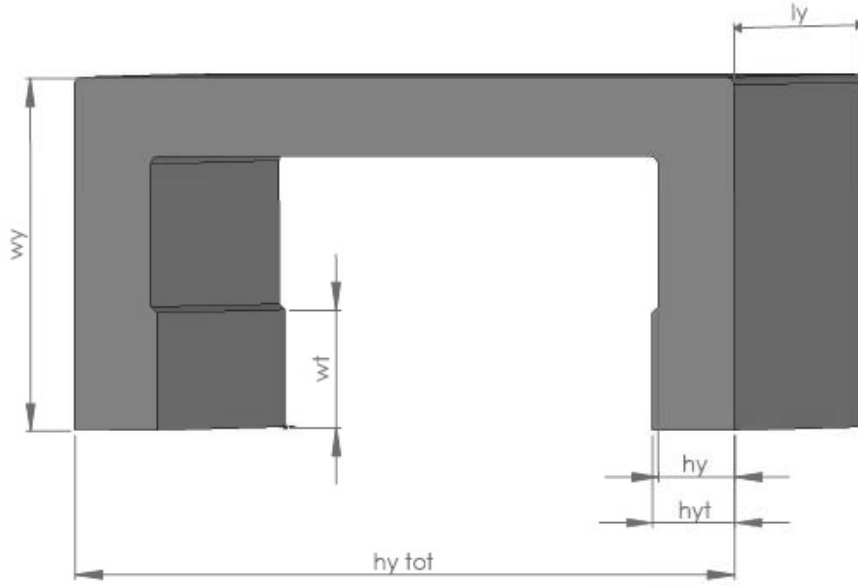


Figure E.2: Geometrical parameters of supply part yoke.

Some geometrical constraints are introduced: the length of the yoke is equal to the magnet stack length as:

$$l_y = 7 \cdot l_{pm} + 6 \cdot l_{fer} + 2 \cdot l_{fere\ ext}. \quad (E.2)$$

Moreover the distance of the yoke height is given by:

$$h_{y\ tot} = 6 \cdot \delta + 2 \cdot h_{pm} + 4 \cdot h_t + 3 \cdot h_{ys} + 2 \cdot h_{yt} \quad (E.3)$$

This motor has six air gaps of equal distance. Two extra air gaps are needed to close the flux. As a consequence, the magnetic flux produced by the magnets in the air gap is reduced. This is a disadvantage of this motor.

E.3 Coil

The sizes of the coil are presented on Fig. E.3. Moreover, the coil is characterized by the number of turns N and the wire diameter d_{cu} .

The geometrical constraints on the coil size are the following:

$$l_{int} < l_y \quad (E.4)$$

$$w_{int} < h_y \quad (E.5)$$

$$\frac{w_{ext} - w_{int}}{2} < w_y - w_t \quad (E.6)$$

$$h_{coil} < h_{y\ tot} - 2 \cdot h_y \quad (E.7)$$

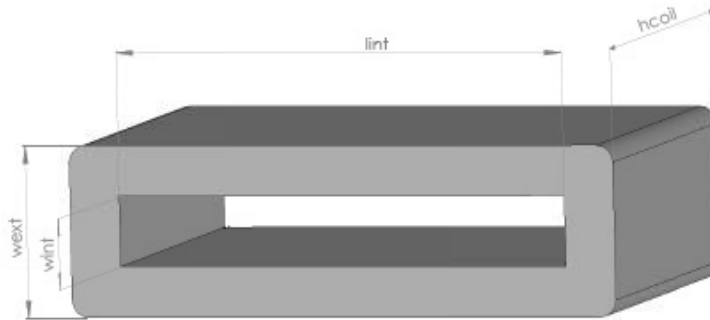


Figure E.3: Geometrical parameters of the TFM coil.

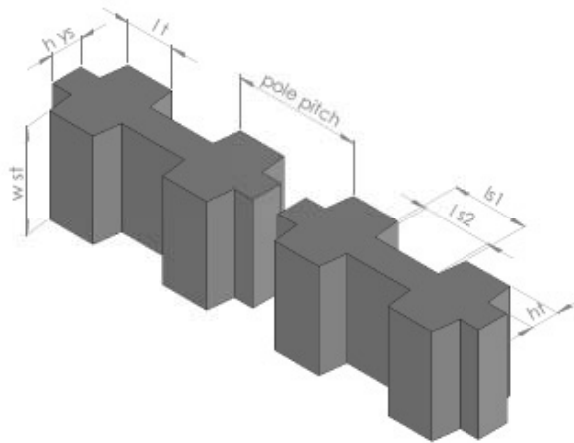


Figure E.4: Geometrical parameters of the reactive part.

E.4 Way: Reactive Part

The reactive part is laminated. The sizes of the reactive part are indicated on Fig. E.4 To achieve good results, the following geometrical constraints must be respected:

$$\tau_p = l_{pm} + l_{fer} = l_{s1} + l_t \tag{E.8}$$

$$w_t = w_{st} = w_{pm} \tag{E.9}$$

$$l_t > l_{fer} \tag{E.10}$$

E.5 Motor Sizes and Performances

The motor sizes are given in Table E.1. The ShS moving part has a weight of about 130kg.

E.5.1 Lumped Magnetic scheme

Due to its structure, only one module can be magnetically studied and modeled. This motor model differs in comparison with the other motor models since it is based on a lumped magnetic circuit. The use of this technic is due to the reluctance topology specific to TFM. Since one module has a symmetry,

Table E.1: Studied motor sizes.

Geometrical parameter		Unit	Value
Copper wire diameter	d_{cu}	[mm]	2.2
External iron lamination length of the stack	$l_{fer\ ext}$	[mm]	7
Length of the intern turn of the coil	l_{int}	[mm]	136
PM length	l_{pm}	[mm]	8
Iron lamination length of the stack	l_{fer}	[mm]	10
Slot length of the reactive part, external value	l_{s1}	[mm]	22
Slot length of the reactive part, internal value	l_{s2}	[mm]	20
Reactive part tooth length	l_t	[mm]	14
Coil height	h_{coil}	[mm]	128
Tooth height of reactive part	h_t	[mm]	8
PM height	h_{pm}	[mm]	30
Supply part yoke height	h_y	[mm]	20
Reactive part yoke height	h_{ys}	[mm]	9
Supply part tooth height	h_{yt}	[mm]	21.5
Supply part total height	$h_{y\ tot}$	[mm]	113
Number of turns per coil	N	[-]	170
Width of the extern turn of the coil	w_{ext}	[mm]	21
Width of the intern turn of the coil	w_{int}	[mm]	58
PM width	w_{pm}	[mm]	30
Reactive part tooth width	w_{st}	[mm]	30
Tooth width	w_t	[mm]	30
Yoke width	w_y	[mm]	30
Mechanical air gap	δ	[mm]	2
Pole pitch	τ_p	[mm]	18

the lumped magnetic scheme can modelize only one magnet stack travelling between two tracks. The equivalent lumped magnetic scheme is presented on Fig. E.5. All permeances are obtained using the circle-line method to model the flux path [22] and by assuming a constant relative permeability of the iron.

In order to obtain the characteristic of the motor, the permeance of the magnetic scheme must be defined for all positions of the magnet stack between $0 \leq x \leq \tau_p$. The origin of the magnet stack position is presented on Fig. E.6.

Therefore, all the following permeance values: Λ_1 , Λ_2 , Λ_4 , Λ_5 , Λ_6 and Λ_8 are variable. On the contrary, $\Lambda_{\delta 1}$ which models the extra air gap, Λ_9 which models the coil yoke, Λ_7 which models the passive track yoke and Λ_{pm} which models the PM are constant. All the variable permeance are the combination of the eventual track tooth, the air gap and the iron part of the magnet stack. The permeance variation as a function of the stack position are given on Fig.E.7, E.8, E.9 for Λ_1 and Λ_2 , Λ_4 , and Λ_6 , Λ_5 and Λ_8 , respectively.

The permeance $\Lambda_{\delta 1}$ must be calculated with a length of the flux tube equal to $\delta/2$.

The other permeances are straightforward to calculate.

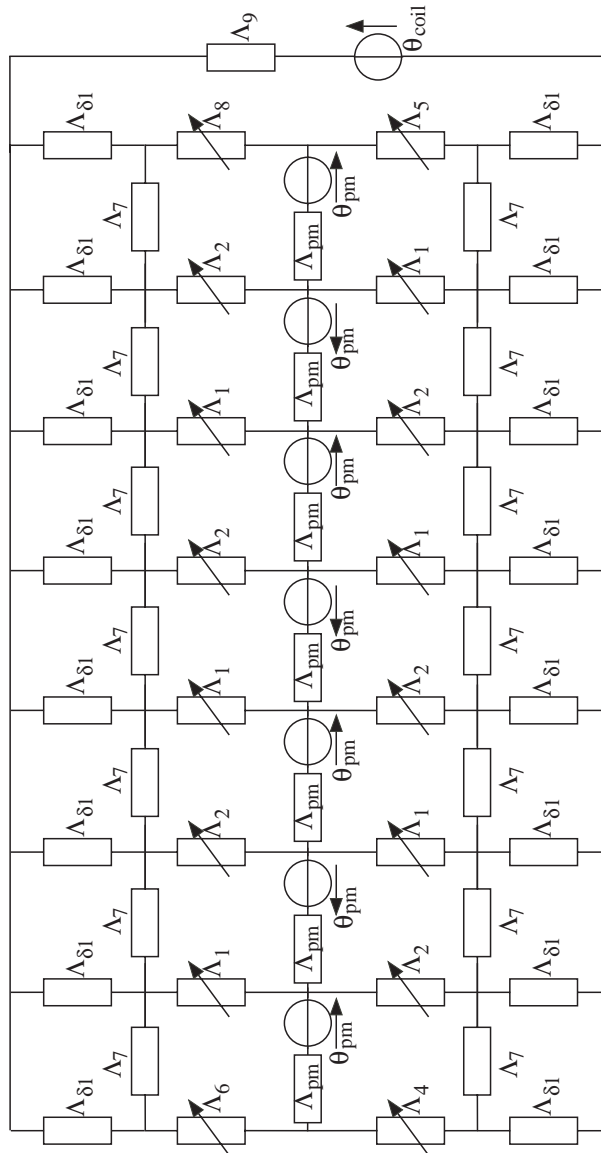


Figure E.5: Lumped magnetic scheme of a half motor module.

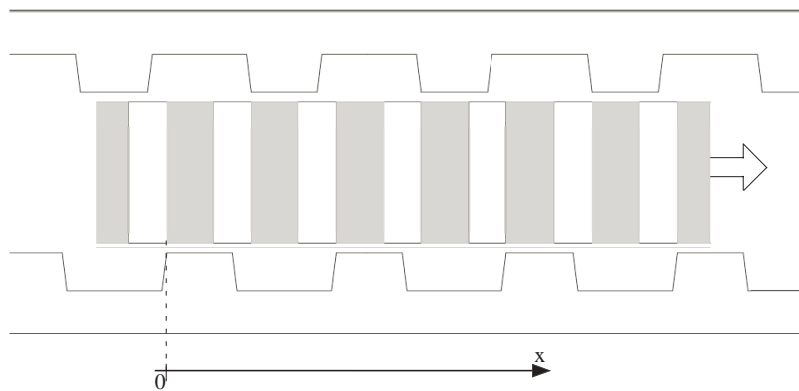


Figure E.6: Origin of the magnet stack position.

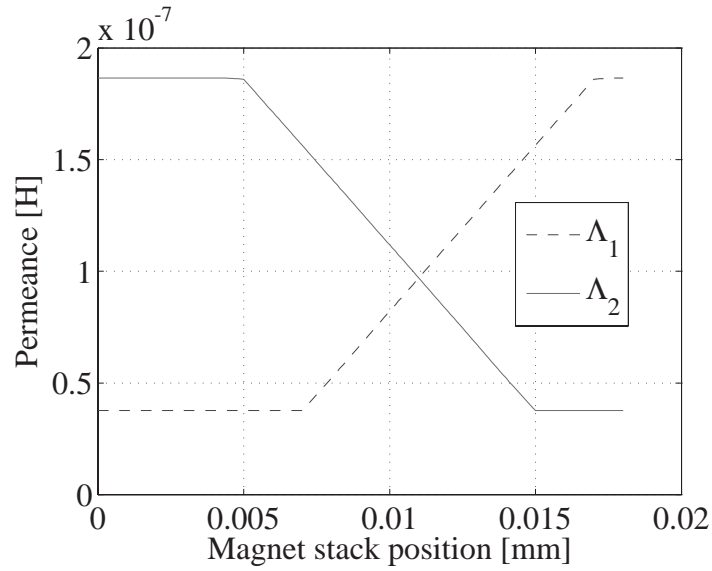


Figure E.7: Permeance variation (Λ_1, Λ_2) as a function of the stack position.

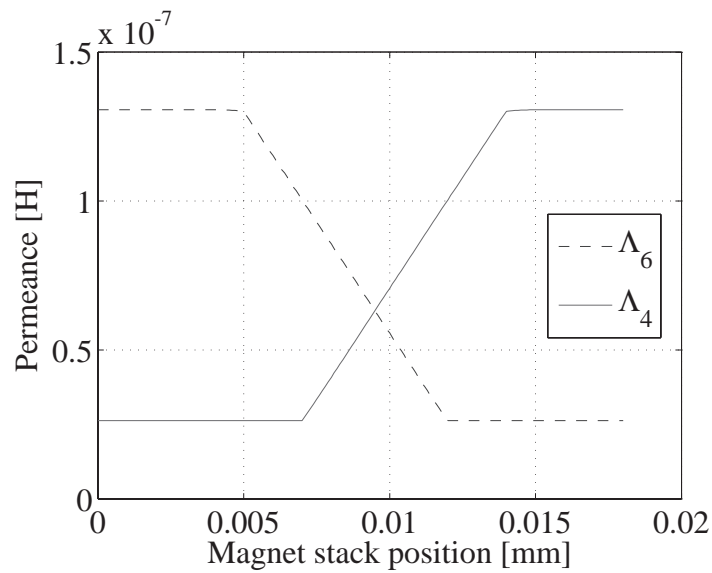


Figure E.8: Permeance variation (Λ_4, Λ_6) as a function of the stack position.

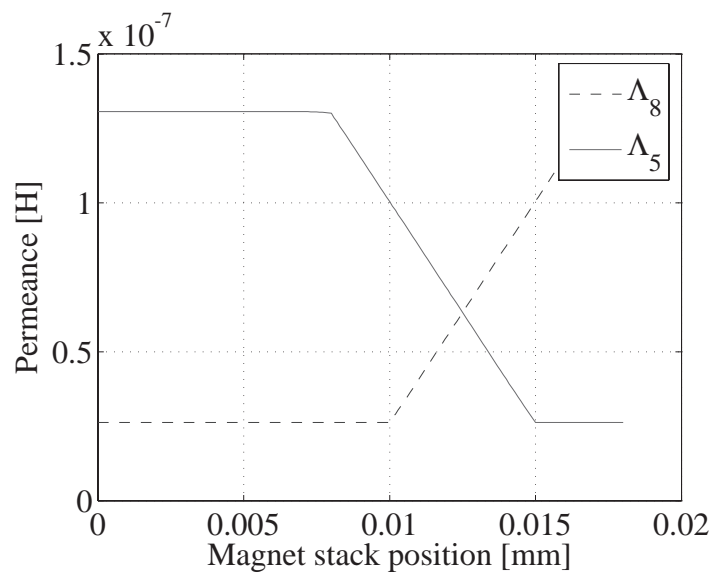


Figure E.9: Permeance variation (Λ_5, Λ_8) as a function of the stack position.

Appendix F

List of Symbols

The three dimensions, length, width and height are defined in the Fig. F.1.

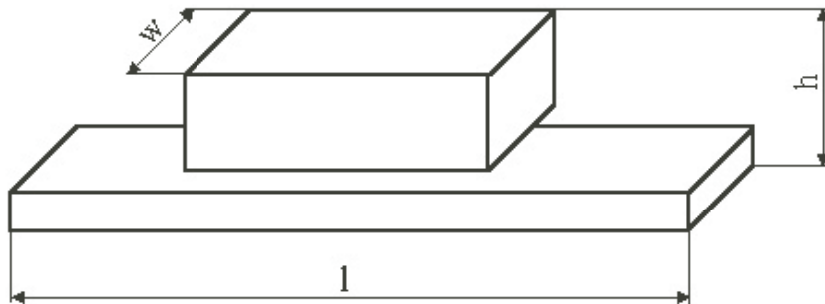


Figure F.1: Definition of the dimensions of the motor

a	Acceleration	[m/s ²]
A	Magnetic potential vector	[Wb/m]
B	Flux density	[T],[Vs/m ²]
B_r	Remanent flux density	[T],[Vs/m ²]
c	Thermal capacitance	[J/K]
cs	Coil shortening	[# slots]
d	Magnetic air gap (including magnet height)	[m]
d_{cu}	Copper wire diameter	[m]
D	Electric displacement	[C/m ²]
D_c	Duty cycle	[-]
E	Electric field	[V/m]
emf	Induce voltage	[V]
f	Supply frequency	[s ⁻¹]
g	gravitational acceleration	[m/s ²]
F	Force	[N]
F_{cu}	Copper losses figure of merit	[m ⁻¹]
h	Height	[m]
h_c	Convection heat transfer coefficient	[W/m ² K]
h_r	Radiation heat transfer coefficient	[W/m ² K]
H	Magnetic field	[A/m]
H_c	Coercitive field	[A/m]
I	Current	[A]
J	Current density	[A/m ²]
J_s	Surface current density	[A/m ²]
k	Thermal conductivity	[W/mK]
k_c	Carter factor	[-]
k_{cogg}	Number of cogging period	[-]
k_{cu}	Slot copper filling factor	[-]
k_{dem}	Demagnetization factor	[-]
k_f	Stacking factor	[-]
k_m	Motor constant	[N/W ^{0.5}]
k_s	Pitch factor	[-]
k_{sat}	Saturation coefficient	[-]
k_{sk}	Skewing factor	[-]
k_z	Distribution factor of the turns	[-]
k_{zc}	Distribution factor of the coil	[-]
k_u	emf phase constant	[$\hat{V}/(m/s)$]
k_w	Winding factor	[-]
k_{weight}	Weighting factor	[-]
k_θ	Heating factor	[m ² °C/As]
L	Inductance	[H]
L_c	Cyclic inductance	[H]
l	Length	[m]
l_{coil}	Length of the coil	[m]
l_{int}	Length of the intern turn of coil	[m]
m	Number of phases	[-]
m	Mass	[Kg]
M	Magnetization vector	[A/m]

N	Number of turns per coil	[-]
N_{cp}	Number of coils per phase	[-]
N_{cs}	Number of coils in serie per phase	[-]
N_p	Number of poles	[-]
N_s	slot number	[-]
Nu	Nusselt number	[-]
P	Active power	[W]
Pr	Prandtl number	[-]
P_{cu}	Copper losses	[W]
q	Number of slots per pole and per phase	[-]
q	heat rate	[W]
R	Electrical Resistance	[Ω]
R_{th}	Thermal resistance	[K/W]
Ra	Rayleigh number	[-]
Re	Reynolds number	[-]
s	coil opening	[m]
S	Surface	[m ²]
S_t	Stroke	[m]
t	Time	[s]
T_m	Maxwell stress tensor	[N/m ²]
T	Electrical period	[s]
T	Temperature	[K]
T_s	Temperature on the surface s	[K]
T_∞	Room Temperature	[K]
U	Voltage	[V]
v	speed	[m/s]
V	Electrical potential	[V]
V	Volume	[m ³]
w	Width	[m]
W	Energy	[J]
α	Convection coefficient	[W/m K]
α_d	Pole pitch	[edeg]
α_r	Radiation coefficient	[W/m ² K]
γ	Distance between two consecutive turns	[m]
δ	Mechanical air gap	[m]
ϵ	Emissivity	[-]
ϵ_e	End condition	[-]
Φ	Magnetic flux	[Vs], [Wb]
η	Efficiency	[-]
Λ	Permeance	[H]
μ_0	Air permeability	[Vs/Am]
μ_r	Relative permeability	[-]
ν	Harmonic order	[-]
θ	Magnetic source	[A]
ρ	Electrical resistivity	[$\Omega \cdot m$]

ρ_c	Volume charge density	[C/m ³]
ρ_m	Density	[kg/m ³]
σ	Electrical conductivity	[$\Omega^{-1} \cdot \text{m}^{-1}$]
σ_f	Leakage factor	[-]
σ_{sb}	Stefan Boltzmann constant	[-]
τ	Time constant	[s]
τ_n	Tooth pitch	[m]
τ_p	Pole pitch	[m]
Ψ	Total magnetic flux	[Vs]
ω	Electrical pulsation	[rad/s]

Indexes:

<i>a</i>	Active dimensions
<i>cu</i>	Relative to the copper
<i>ir</i>	Relative to the iron
<i>m</i>	Relative to the motor
<i>n</i>	Normal component
<i>pm</i>	Relative to the magnet
<i>s</i>	Relative to the slot
<i>t</i>	Relative to the tooth
<i>tg</i>	Tangential component
<i>x</i>	Relative to the x direction
<i>y</i>	Relative to the y direction
δ	Relative to the air gap
σ	Relative to the leakage
∞	Relative to an infinite condition

Abbreviations:

CTI	The innovation promotion agency	
edeg	electrical degrees	[°]
emf	electro magnetic force	[V]
FEM	Finite elements method	
GCD	Greatest common divisor	
HA	Halbach array	
HVT	Horizontal vertical transportation	
LCM	Least common multiple	
LS	Long stator	
mmf	Magnetic motrice force	[A]
MMS	Multi Mobile System	
MaW	Magnetic way	
NdFeB	Neodymium Iron Bore	
PM	Permanent magnet	
rms	Root mean square	
ShS	Short stator	
SQP	Sequential quadratic programming	
TFM	Transverse Flux Motor	
THD	Total harmonic distortion	

References

- [1] T. Ishii. Elevators for skyscrapers. *IEEE Spectrum*, 1994.
- [2] H. Jappsen. Rise elevators for the 21th century. *Elevcon*, 2002.
- [3] <http://www.magnemotion.com>.
- [4] S. Chevailler and A. Cassat. Multi mobile system with linear motors: Linear motors - synthesis report. Technical report, EPFL, 2005.
- [5] Project cti nř5729.1: Multi mobile system with linear motors. Technical report, 2003.
- [6] Project cti nř6900.1: Multi mobile system with linear motors. Technical report, 2005.
- [7] H.B. Hamed, M. Antunes, P.E. Cavarec, J. Lucidarme, B. Multon, L. Prévond, and B. Salamand. Généralités sur les actionneurs linéaires. *Satie ENS Cachan*, 2002.
- [8] P.-E. Cavarec, H. Ben Ahmed, and B. Multon. Actionneurs électromécaniques. *Techniques de l'ingénieur, traité Génie électrique*, D3 412.
- [9] A. Cassat, N. Corsi, R. Moser, and N. Wavre. Direct linear drives: Market and performance status. In *LDIA*, 2003.
- [10] <http://www.physikinstrumente.de/products/index.php>.
- [11] G. Duriaux. Etude comparative des variantes d'excitation pour moteurs linéaires. Technical report, EIVD, 2003.
- [12] M. Andriollo, G.Baccini, G.Martinelli, A.Morini, and A.Tortella. Design optimisation of slotless linear pm motors. *LDIA*, 2003.
- [13] I. Boldea and S.A. Nasar. *Linear Electric Actuators and Generators*. Cambridge University Press, 1997.
- [14] R. Martinez. Etude d'un moteur à flux transversal. Technical report, EIVD, 2004.
- [15] J.Y. Lee, J.P. Hong, and D.H. Kang. Analysis of pm type transverse flux linear motor by couplig 2d finite element method on 3d equivalent magnetic circuit network method. *IAS*, 2004.
- [16] M. Poloujadoff. *The Theory of Linear Induction Machinery*. Oxford University Press, 1980.
- [17] J.A. Stratton. *Electromagnetic Theory*. The Maple Press Compagny, 1941.
- [18] D.K. Cheng. *Field and Wave Electromagnetics*. Addison-Wesley Publishing Company, 1989.

- [19] M. Krasnov, A. Kissélev, G. Makarenko, and E. Chikine. *Mathématiques supérieures Tome II*. De Boeck Université, 1993.
- [20] H. Woodson. *Electromechanical Dynamics*. Wiley, New York, 1968.
- [21] L. Parsa and H.A. Toliyat. Five-phase interior permanent magnet motor with low torque pulsation. In *IEEE-IAS*, Hong Kong, 2005.
- [22] M. Jufer. *Electromécanique*, volume TE IX. Presses Polytechniques et Universitaires Romandes, 1998.
- [23] <http://www.vacuumschmelze.de>.
- [24] C. Koechli. *Contribution à l'étude des moteurs synchrones monophasés*. PhD thesis, EPFL, 1999.
- [25] C. Besson. Matériaux. Technical report, Cours EIVD, 2005.
- [26] R.N. Hasanha. *A Contribution to Energy Saving in Induction Motors*. PhD thesis, EPFL, 2005.
- [27] M. Klauz and D.G. Dorrell. Estimation of coefficients for exponential and fourier series representation of bh and magnetization curves.
- [28] M. Jufer. B-h curve approximation - iron and pm. *Rapport interne 96/237a*, 1996.
- [29] F. Wurtz. *Une nouvelle approche pour la conception sous contraintes de machines électriques*. PhD thesis, Institut national polytechnique de Grenoble, 1996.
- [30] M. Caldora Costa. *Optimisation de dispositifs électromagnétiques dans un contexte d'analyse par la méthode des éléments finis*. PhD thesis, Institut national polytechnique de Grenoble, 2001.
- [31] <http://www.webopedia.com>.
- [32] N. Bianchi and S. Bolognani. Design optimisation of electric motors by genetic algorithms. *IEE. Proc.-Electr. Power Appl.*, 145, 1998.
- [33] <http://www.designprocessing.com>.
- [34] G. Dayer. Synchronous linear motor with permanent magnets. Technical report, EPFL-Master project, 2005.
- [35] E. Fitani, F. Messine, and B. Nogarède. The electromagnetic actuator design problem: A general and rational approach. *IEEE Transactions on Magnetics*, 40(3), 2004.
- [36] D. Zarko. *A Systematic Approach to Optimized Design of Permanent Magnet Motors with Reduced Torque Pulsations*. PhD thesis, University of Wisconsin-Madison, 2004.
- [37] Y. Perriard and V. Nguyen. Transducer design with global parametric optimization. 2001.
- [38] S. Chevailler, M. Markovic, M. Jufer, and Y. Perriard. Linear motor optimization using an analytical model. *ICEM*, 2004.
- [39] L. Albert. *Modélisation et optimisation des alternateurs à griffes. Application au domaine automobile*. PhD thesis, INPG, 2004.
- [40]

- [41] S. Chevailler and T. Duenser. Multi mobile system with linear motors: General figures of merit. Technical report, 2003.
- [42] C. Paroz. *Contribution à l'optimisation des entraînements électrique*. PhD thesis, EPFL, 2003.
- [43] K.J. Binns, P.J. Lawrenson, and C.W. Trowbridge. *The Analytical and Numerical Solution of Electric and Magnetic Fields*. John Wiley and Sons.
- [44] B. Hague. *The Principles of Electromagnetism Applied to Electrical Machines*. Dover Publications, INC, 1962.
- [45] M. Markovic. *Magnetic Field Analysis in Electric Motors Using Conformal Mapping*. PhD thesis, EPFL, 2004.
- [46] S.-M. Jang, S.-H. Lee, and I.K. Yoon. Design criteria for detent force reduction of permanent-magnet linear synchronous motors with halbach array. *IEEE Transactions on Magnetics*, 38, 2002.
- [47] M. Jufer. Polyphase windings. *Rapport interne 93/230*, 1993.
- [48] M. Kostenko and L. Piotrovski. *Machines électriques, tome II*. Editions Mir, Moscou, 1969.
- [49] F. Magnussen and C. Sadarangani. Winding factors and joule losses of pm machines with concentrated windings. *IEEE*, 2003.
- [50] J.-J. Simond. *Machines électriques: 1ère partie: Régimes permanents*. EPFL, support de cours, 1993.
- [51] M. Cheng, K.T. Chau, and C.C. Chan. Design and analysis of a new doubly salient permanent magnet motor. *IEEE Transactions on Magnetics*, 37, 2001.
- [52] D. Ishak, Z.Q. Zhu, and D. Howe. Comparative study of pm brushless motors with all teeth and alternative teeth windings. *The Institution of Electrical Engineers (IEE)*, 2004.
- [53] A. M. EL-Refaie and T. M. Jahns. Comparison of synchronous pm machine type for wide constant-power speed range operation. *IEEE-IAS*, 2005.
- [54] R. Oberholzer. *Konstruktion leektrischer Maschinen*. Zentralschweizerischen Technikum Luzern.
- [55] Z.Q. Zhu and D. Howe. Influence of design parameters on cogging torque in pm machines. *IEEE Transactions on Energy Conversion*, 15(4), December 2000 2000.
- [56] A.G. Jack, B.C. Mecrow, P.G. Dickinson, D. Stephenson, J.S. Burdess, N. Fawcett, and J.T. Evans. Permanent magnet machines with powered iron cores and pressed windings. *IEEE Transactions on Industry Applications*, 36(4), 2000.
- [57] F. Magnussen and H. Lendenmann. Parasitic effects in pm machines with concentrated windings. In *IEEE-IAS*, 2005.
- [58] N. Wavre. *Etude harmonique tridimensionnelle des moteurs linéaires asynchrones a bobinages polyphases quelconques*. PhD thesis, EPFL, 1975.
- [59] Z.Q. Zhu, Z.P. Xia, D. Howe, and P.H. Mellor. Reduction of cogging force in slotless linear permanent magnet motors. *IEE Proc.-Electr. Appl.*, 144(4), 1997.

- [60] M. Jufer. Performances limites des entraînements directs. ENS Cachan, 1999.
- [61] K. Richter. *Elektrische Maschinen*, volume Band 1. Springer Verlag, 1963.
- [62] N. Boules. Design optimization of permanent magnet dc motors. *IEEE Transactions on Industry Applications*, 26(4), 1990.
- [63] H. Polinder. Modeling of a linear pm machine including magnetic saturation and end effects: Maximum force-to-current ratio. *IEEE Transactions on Industry Applications*, 39(6), 2003.
- [64] J. Chatelain. *Machines électriques*, volume X. Presses Polytechniques et Universitaires Romandes, 1989.
- [65] M. Jufer. Brushless dc motors - gap permeance and pm-mmf distribution analysis. *Proceedings IMCSD*, 1987.
- [66] N. Wavre. Permanent magnet linear synchronous motor, united states patent, 5,910,691, 1999.
- [67] B.E. Hasubek. *Analysis and Design of Passive Rotor Transverse Flux Machines with Permanent Magnets on the Stator*. PhD thesis, University of Calgary, 2000.
- [68] D.H. Kang, Y.H. Chun, and H. Weh. Analysis and optimal design of transverse flux linear motor with pm excitation for railway traction. *IEE. Proc.-Electr. Power Appl.*, 150, 2003.
- [69] S. Chevailler and A. Cassat. Double sided reference motor. Technical report, EPFL, 2004.
- [70] N. Scheidegger. Simulation du flux d'énergie dans une voiture solaire. Technical report, Travail de semestre EPFL, 2005.
- [71] F.P. Incropera and D.P. De Witt. *Fundamentals of Heat and Mass Transfer*. John Wiley and Sons, 2002.
- [72] C. Kuert. *Modélisation de moteurs pas à pas hybrides*. PhD thesis, EPFL, 2000.
- [73] Y. Bertin. Refroidissement des machines électriques tournantes. *Techniques de l'ingénieur, traité Génie électrique*, D3 460.
- [74] M. Kudelski. *Analyse et conception de moteurs synchrones chemisés à commutation électronique*. PhD thesis, EPFL, 1998.
- [75] C. Besson. Puissance, couples et rendement. systèmes de refroidissement. Technical report, Cours EIVD, 2005.
- [76] H. Polinder and M.J. Hoeijmakers. Eddy-current losses in the segmented surface-mounted magnets of a pm machine. *IEE Proc.-Electr. Power Appl.*, 146, 1999.
- [77] S. Chevailler, A. Cassat, and M. Jufer. High acceleration applications: Design optimization and comparison between different toothless motors. In *LDIA*, Japan, 2005.
- [78] S. Chevailler and A. Cassat. Multi mobile system with linear motors: Linear motors - comparison long-short stator. Technical report, EPFL, 2003.
- [79] T. J. Harned and S. R. Huard. To slot or not to slot. *Motion control*, 1995.
- [80] T. Duenser, R. Deplazes, and M. Meier. A new elevator system and its implementation. In *MAGLEV*, Lausanne, 2002.

- [81] S. Chevailler, A. Cassat, A. Dos Santos, R. Deplazes, and M. Jufer. Integration of possible motor variants in domotic lifts without rope. In *LDIA*, 2003.
- [82] T. Duenser. Multi mobile system with linear motors: Traffic organization and exploitation. Technical report, 2003.
- [83] S. Chevailler, T. Duenser, H. Kocher, Y. Perriard, and M. Jufer. Linear motors for multi mobile systems. In *IEEE - IAS*, Hong Kong, 2005.
- [84] T. Duenser and S. Chevailler. Multi mobile system with linear motors: Specifications. Technical report, 2004.
- [85] A. Cassat and M. Jufer. Maglev projects technology aspects and choices. *IEEE Transactions on Applied Superconductivity*, 12(1), 2002.
- [86] A. dos Santos. Polyphase transverse flux linear motor. Technical report, EPFL, 2002.
- [87] A. dos Santos, A. Cassat, and S. Chevailler. Transverse flux linear motor leading to a tubular configuration. In *LDIA*, Birmingham, 2003.
- [88] S. Chevailler and A. Cassat. Multi mobile system with linear motors: Long stator vs. short stator. Technical report, 2003.
- [89] P.-O. Moix. Supply and control of a ropeless multimobile elevator system with synchronous linear motor. Technical report, LEI-EPFL, 2003.
- [90] T. Duenser. Mms with linear motors: Cost synthesis. Technical report, 2004.
- [91] A. Hofmann. Konstruktion und visualisierung eines schachtwechselmechanismus. Technical report, Master ETHZ, 2005.

Curriculum Vitae

Name: Samuel CHEVAILLER
Date of birth: 18. June 1975
Marital status: Married, 1 child
Nationality: Swiss

Formation

07/1990 - 07/1994 Apprenticeship as a mechanic-electrician Von Roll SA, Delémont
11/1994 - 01/1998 Bachelor's Degree in Electrical Engineering HES Engineer school of Yverdon
11/1997 - 03/2001 Master's Degree in Electrical Engineering, EPFL
04/2002 - 06/2006 Ph.D. Student in electrical machines and teaching assistant

Publications

A. Dos Santos, S. Chevailler, A. Cassat, "Transverse Flux Linear Motor Leading to a Tubular Configuration", Linear Drive Industry Application (IEE-LDIA), Birmingham, 2003
S. Chevailler, A. Dos Santos, A. Cassat, R. Deplazes, M. Jufer, "Integration of Possible Motor Variants in Domestic Lifts Without Rope", Linear Drive Industry Application (IEE-LDIA), Birmingham, 2003
S. Chevailler, M. Markovic, Y. Perriard, M. Jufer, "Linear Motor Optimization Using an Analytical Model", International Conference on Electrical Machines (ICEM), Krakow, 2004
S. Chevailler, T. Duenser, Y. Perriard, H. Kocher, M. Jufer, "Linear Motors for Multi Mobile Systems", Industry Application Society (IEEE-IAS), Honk-Kong, 2005
S. Chevailler, A. Cassat, M. Jufer, "High Acceleration Applications: Design Optimization and Comparison between Different Toothless Motors", Linear Drives for Industry Applications (IEE-LDIA), Awaji Yumebutai (Jp), 2005

Working Experience

05/2001 - 12/2003 Research and development engineer in the motors R&D group, ETEL SA.